

GOLD NANOPARTICLES IN SOME CHEMICAL AND PHOTOTHERMAL
APPLICATIONS OF CANCER THERAPY

A Dissertation
Presented to
The Academic Faculty

By

Megan A. Mackey

In Partial Fulfillment
Of the Requirements for the Degree
Doctor of Philosophy in the School of Chemistry and Biochemistry

Georgia Institute of Technology

December 2013

Copyright © Megan A. Mackey 2013

GOLD NANOPARTICLES IN SOME CHEMICAL AND PHOTOTHERMAL
APPLICATIONS OF CANCER THERAPY

Approved by:

Dr. Mostafa A. El-Sayed
Advisor
School of Chemistry and Biochemistry
Georgia Institute of Technology

Dr. Bridgette A. Barry
School of Chemistry and Biochemistry
Georgia Institute of Technology

Dr. Adegboyega K. Oyelere
School of Chemistry and Biochemistry
Georgia Institute of Technology

Dr. Christine K. Payne
School of Chemistry and Biochemistry
Georgia Institute of Technology

Dr. Ingeborg Schmidt-Krey
School of Biology
Georgia Institute of Technology

Date Approved: August 9, 2013

To the two most influential and supportive people in my life

Mom and Dad

Without you, this would not have been possible.

Thank you

ACKNOWLEDGEMENTS

First and foremost, I would like to thank my advisor, Dr. Mostafa A. El-Sayed for his support, guidance and funding during my time at Georgia Tech. Dr. El-Sayed has always been so supportive of me in both my research and other aspects of my career as a scientist. He has taught me never stop learning and never stop asking questions. He has been a great mentor over the years, ultimately making me into the scientist that I am today. I would also like to thank my undergraduate research advisor, Dr. Pamela St. John for igniting my passion for research.

I would also like to thank the many collaborators to which I have had the honor to work with. Dr. Oyelere and his research group have been essential to my accomplishments throughout my research, along with my collaborators at Emory University, Dr. Shin, Dr. Chen, Dr. Peng and Dana Ray. Our collaboration and success over the past years has helped excel the field of nanomedicine and each individual has played a crucial role in achieving that. Also, thank you to those who manage the IBB Core Facilities, Steve Woodard, Nadia Boguslavsky and Andrew Shaw, for your patience and expertise in the various methods and instruments utilized in every aspect of my research.

I must also thank my thesis committee members, Dr. Barry, Dr. Payne, Dr. Oyelere and Dr. Schmidt-Krey. They have been great mentors throughout my time at Georgia Tech and have always pushed me to excel and I know that they will continue to support me in my future endeavors as a scientist. I have also had the honor to work with many other scientists who have significantly contributed to my thesis work. Thank you to Dr.

Xiaohua Huang, Dr. Erik Dreaden, Dr. Steven Hayden, Dr. Rachel Near, Dr. Bin Kang, Dr. Chun-wan Yen, Dr. Mahmoud A. Mahmoud, Lauren Austin, Marwa Affifi, Justin Bordley, Adam Poncheri, Brian Snyder, Daniel O'Neil, Mena Aioub and Batyr Garlyyev. They have all not only contributed to my knowledge and skills as a scientist, but have also been a pleasure to work with over the years. Also, I would like to thank Mike Riley and Paul Ficklin-Alred for always making sure everything in the building/lab is taken care of and always having the answers.

A special thank you is warranted for those I have worked with side-by-side in the biolab. Lauren Austin, Marwa Affifi and Bin Kang. Their constructive brainstorming and constant support have been such a crucial component to the research presented in this thesis.

My family and friends have supported me from day one. There has never been a moment when they have wavered and for that I grateful. My mom and dad especially, have taught me the value of hard work and perseverance. They have also not only taught me, but shown me, that enjoying life is more important than anything. They have lead by example ever since I can remember and I can only hope that one day I could be half as amazing as they are. I would also like to thank my brother who has always been supportive and never doubted my ability to do anything I put my mind to. I must also thank my best friend Whitney, for always being there and picking me back up when I was down. And last, but certainly not least, I would like to thank Tad. He has been such an important part of my life for the last 5 years and without him, I might not have been able to do this. He has never once questioned why I do what I do, instead he has allowed me to chase my dreams, no matter how much of a struggle it might be.

TABLE OF CONTENTS

Dedication	iii
Acknowledgements	iv
List of Tables	xii
List of Figures	xiii
List of Abbreviations and Symbols	xxv
Summary	xxvi
Chapter 1: Introduction	1
1.1. Gold Nanoparticles: Design and Biocompatibility	2
1.1.1. Gold Nanoparticle Synthesis	2
1.1.2. Gold Nanoparticle Conjugation	4
1.1.3. Gold Nanoparticle Accumulation, Uptake and Clearance	7
1.2. Intrinsic Properties of Gold Nanoparticle Conjugates	12
1.2.1. Anti-Proliferative Effects	12
1.2.2. Cell Cycle Regulation	13
1.3. Extrinsic Properties of Gold Nanoparticle Conjugates	14
1.3.1. Optical Properties	14
1.3.2. Photothermal Contrast Agents	15

1.4. Conclusions and Future Outlook	23
1.5. References	24
Chapter 2: Detailed Experimental Methods	30
2.1. Methods of Gold Nanoparticle Design	30
2.1.1. Gold Nanosphere Synthesis	30
2.1.2. Gold Nanocage Synthesis	31
2.1.3. Gold Nanorod Synthesis	33
2.1.3.1. Seed-mediated growth method	33
2.1.3.2. Seedless growth method	35
2.1.4. Gold Nanoparticle Functionalization	38
2.1.4.1. Conjugation with polyethylene glycol	39
2.1.4.2. Conjugation with peptides	39
2.2. Cell Biology and Imaging Methods	40
2.2.1. Cell Culture	40
2.2.2. Intracellular Localization and Nanoparticle Uptake	40
2.2.2.1. Dark Field Imaging of Fixed Cells	40
2.2.2.2. Live-Cell Dark Field Imaging	41
2.2.2.3. Nuclear Localization with Confocal Imaging	42
2.2.2.4. Spectrophotometric Measurements of Relative Uptake	43
2.2.3. Cell Viability Assays	46
2.2.3.1. Mitochondrial Activity (XTT)	46
2.2.3.2. ATP Production	51
2.2.4. Flow Cytometry	53

2.2.4.1. Cell Cycle Analysis	53
2.2.4.2. Detection of Apoptosis and Necrosis	57
2.2.5. Confocal Microscopy	60
2.2.5.1. Detection of DNA Double Strand Breaks	60
2.2.5.2. Detection of Reactive Oxygen Species	61
2.3. References	62
Chapter 3: Intrinsic Properties of Gold Nanoparticle Conjugates	64
3.1. Nuclear Localization of Gold Nanoparticles in Cancer Cells Induces DNA Damage, Causing Cytokinesis Arrest and Apoptosis	64
3.1.1. Introduction	65
3.1.2. Experimental Methods	66
3.1.2.1. Cell Culture	66
3.1.2.2. Gold Nanoparticle Synthesis and Peptide Conjugation	66
3.1.2.3. Dark Field Imaging	68
3.1.2.4. Live-Cell Dark Field Imaging	68
3.1.2.5. Cell Synchronization	70
3.1.2.6. Flow Cytometry	70
3.1.2.7. Confocal Microscopy DNA Damage Detection	70
3.1.3. Results and Discussion	71
3.1.4. Conclusions and Future Outlook	80
3.1.5. References	81
3.2. Inducing Cancer Cell Death by Targeting its Nucleus:Solid Gold Nanospheres versus Hollow Gold Nanocages	84
3.2.1. Introduction	85

3.2.2.	Experimental Methods	87
3.2.2.1.	Cell Culture	87
3.2.2.2.	Gold Nanoparticle Synthesis and Peptide Conjugation	87
3.2.2.3.	Gold Nanoparticle Internalization	91
3.2.2.4.	Nuclear Localization of Gold Nanoparticles	92
3.2.2.5.	Flow Cytometry Cell Cycle Analysis	92
3.2.2.6.	ATP Assay	93
3.2.2.7.	Flow Cytometry Analysis of Apoptosis and Necrosis	93
3.2.2.8.	Confocal Acquisition of ROS	94
3.2.2.6.	Statistical Analysis	95
3.2.3.	Results and Discussion	95
3.2.3.8.	Nanoparticle-Induced Disruption of Cellular Functions	98
3.2.3.6.	Possible Mechanism for Enhance Nanoparticle Induced Cell Death by the Gold Nanocages	102
3.2.4.	Conclusions and Future Outlook	108
3.2.5.	References	110
3.3.	Varying the Silver Content of Gold Nanocages Impacts Apoptosis and Necrosis	116
3.3.1.	Introduction	117
3.3.2.	Experimental Methods	118
3.3.2.1.	Cell Culture	118
3.3.2.2.	Gold Nanocage Synthesis and Peptide Conjugation	118
3.3.2.7.	Flow Cytometry Analysis of Apoptosis and Necrosis	121
3.3.2.6.	Statistical Analysis	121
3.3.3.	Results and Discussion	122
3.3.4.	Conclusions and Future Outlook	128
3.3.5.	References	129

3.4. Enhancing 5-Fluorouracil Drug Efficacy by Gold Nanoparticle Cell Cycle Regulation	133
3.4.1. Introduction	134
3.4.2. Experimental Methods	135
3.4.2.1. Cell Culture	135
3.4.2.2. Gold Nanoparticle Synthesis and Peptide Conjugation	135
3.4.2.3. Treatment of Cells with AuNPs and 5-Fluorouracil	139
3.4.2.4. Flow Cytometry Cell Cycle Analysis	140
3.4.2.5. Cell Viability Assay	140
3.4.2.6. Apoptosis and Necrosis Detection via Flow Cytometry	141
3.4.2.7. Statistical Analysis	141
3.4.3. Results and Discussion	142
3.4.3.1. Gold Nanoparticle Induced Cell Cycle Regulation	142
3.4.3.2. Enhanced 5-Fluorouracil Chemosensitivity	145
3.4.4. Conclusions and Future Outlook	151
3.4.5. References	152

Chapter 4 : Extrinsic Properties of Gold Nanoparticle Conjugates155

4.1. The Most Effective Gold Nanorod Size for Plasmonic Photothermal Therapy: Theory and Experiment.....	155
4.1.1. Introduction	157
4.1.2. Experimental Methods	161
4.1.2.1. Gold Nanorod Synthesis and PEG Conjugation	161
4.1.2.2. Photothermal Heating of Gold Nanorods in Solution	163
4.1.2.3. Gold Nanorod Heating in Cell Culture and Cell Viability Assay	163
4.1.2.4. Statistical Analysis	164
4.1.2.5. DDA Calculations	164

4.1.3.	Results and Discussion	165
4.1.3.1.	Size-Dependent Photothermal Heat Conversion: Experiment ...	165
4.1.3.2.	Size-Dependent Electromagnetic Field: Theory	167
4.1.3.3.	Size-Dependent Absorbance:Scattering Ratio: Theory	170
4.1.3.4.	Size-Dependent Absorbance:Scattering Ratio: Experiment	172
4.1.3.5.	Size-Dependent <i>in Vitro</i> Plasmonic Photothermal Efficacy in HSC-3 Cancer Cells	174
4.1.4.	Conclusions and Future Outlook	177
4.1.5.	References	180
4.2.	Decreasing Gold Nanorod Size for Plasmonic Photothermal Therapy in a Mouse Model	185
4.2.1.	Introduction	186
4.2.2.	Experimental Methods	187
4.2.2.1.	Gold Nanorod Synthesis and Conjugation	187
4.2.2.2.	Circulation Half-Life and Biodistribution	189
4.2.2.3.	Tumor Inoculation and Nanorod Injection	190
4.2.2.4.	Near-Infrared Laser Exposure	191
4.2.3.	Results and Discussion	191
4.2.4.	Conclusions and Future Outlook	196
4.2.5.	References	198
Appendix A : Chapter 3 Additional Figures		201
Appendix B : Chapter 4 Additional Figures		210
Curriculum Vitae		212

LIST OF TABLES

Table 3.1	90
Zeta potential measurements for functionalized AuNSs and AuNCs used throughout this study.	
Table 3.2	123
Various AuNCs synthesized with different surface plasmon peak positions and their corresponding ratio of Ag to Au.	
Table 3.3	139
Dynamic light scattering measurements of the hydrodynamic diameter and zeta potential for various AuNPs used in this study.	
Table B.1	210
Additional temperature measurements taken for experimental photothermal heat conversion.	

LIST OF FIGURES

- Figure 1.1.....4**
Transmission electron microscopy (TEM) images of common biomedically relevant gold nanostructures. (A) Gold nanospheres synthesized via citrate reduction. (B) Gold nanorods synthesized via seed-mediated growth. (C) Gold nanocages synthesized via galvanic replacement. Scale bar: 100 μm .
- Figure 1.2.....8**
Graphic illustrating enhanced permeability and retention (EPR) effect exploited by gold nanoparticle conjugates to achieve selective accumulation at tumor sites. Gold nanoparticle conjugates penetrate leaky vasculature of blood vessels and diminished lymphatic drainage allows for retention of gold nanoparticle conjugates within the tumor interstitium.
- Figure 1.3.....10**
Size-dependent receptor-mediated endocytosis of IgG-gold nanoparticle conjugates by breast cancer cells. (Left) Schematic illustrating that 2 nm particles do not bind multiple receptors and therefore are not efficiently internalized by cells, as shown by fluorescence images of nanoparticles on surface of cell. (Middle) 40 nm particles do bind multiple receptors and are therefore efficiently taken up via endocytosis, as shown in fluorescence images. (Right) 70 nm particles also exhibit simultaneous binding to multiple receptors, but are too large for efficient internalization by cells, as shown in fluorescence images. In fluorescence images, the nuclei are stained blue and the particles are represented by red fluorescence. Scale bar: 10 μm .
- Figure 1.4.....17**
Wavelength range (650-900 nm) of the near-infrared (NIR) tissue transmission window. (A) Absorption from physiologic components, such as oxy/deoxyhemoglobin and water is minimal in this range. (B) This allows for maximum NIR laser penetration depths. Photothermal contrast agents are designed to absorb in this wavelength range to allow for maximum penetration depth of external radiation through biological tissues.

Figure 1.5	20
<i>In vivo</i> near-infrared (NIR) laser plasmonic photothermal therapy utilizing gold nanorod contrast agents. PEGylated gold nanorods were intravenously and locally injected in carcinoma-bearing nude mice. (A) NIR imaging indicated significantly increased NIR extinction of gold nanorods accumulated at the tumor sites, with direct injection showing higher accumulation of AuNRs than tail vein injection. (B) The change in tumor volume was determined over the course of two weeks, after single NIR laser exposure, and exhibits a significant decrease in tumor volume for the nanorod-treated tumors compared with the controls.	
Figure 2.1	31
Gold nanospheres synthesized via citrate reduction of H _{AuCl} ₄ . TEM images (left), size distribution histograms (middle) and UV-Vis spectrum (right) of 30 nm AuNSs (A) and 15 nm AuNSs (B).	
Figure 2.2	33
Gold nanocages synthesized via galvanic replacement. UV-Vis spectra (left), schematic (middle) and TEM images (right) of AuNCs with about a 40 nm wall length and increasing addition of Au salt (from A to C).	
Figure 2.3	34
Schematic representation of AuNR synthesis via seed-mediated growth. The three main steps involved are the preparation of a seed solution (A), preparation of a growth solution (B) and growth of AuNRs by the addition of the seed to growth solution (C).	
Figure 2.4	35
TEM image (top) of 38 x 11 nm AuNRs synthesized by seed-mediated growth. UV-Vis spectrum (bottom) showing these AuNRs have a surface plasmon resonance around 740 nm. Scale bar: 60 nm.	
Figure 2.5	37
Schematic representation of AuNR synthesis via seedless growth. The two main steps involved are the preparation of a growth solution (A) and growth of AuNRs by the addition of sodium borohydride to the growth solution (B).	
Figure 2.6	38
TEM image (top) of 28 x 8 nm AuNRs synthesized by seedless growth. UV-Vis spectrum (bottom) showing these AuNRs have a surface plasmon resonance around 770 nm. Scale bar: 60 nm.	
Figure 2.7	42
Schematic representing the homemade setup for live-cell dark field imaging of cells treated with gold nanoparticles. A dark field light scattering imaging microscope with a side-illumination arrangement is combined with an environmental cell incubation chamber for real time studies of live cells.	

Figure 2.8	44
Example of 96-well plate configuration when treating cells for uptake. Wells 1/A-H contain cells and are loaded with 100 μ L of cell culture medium containing nanoparticle A (A+). Wells 2/A-H contain cells and are loaded with 100 μ L of cell culture medium containing gold nanoparticle B (B+). Wells 3/A-H contain cells and are loaded with 100 μ L of cell culture medium containing gold nanoparticle C (C+). Wells 4-6/A-H do not contain cells and are loaded with 100 μ L of cell culture medium containing gold nanoparticles A, B, and C (A-, B-, C-, respectively).	
Figure 2.9	45
Example of 96-well plate configuration after transferring gold nanoparticle containing medium to new wells. Gray wells represent those that originally contained gold nanoparticles. White wells represent the 75 μ L of nanoparticle containing transferred from the original wells.	
Figure 2.10	47
Example of 96-well plate configuration when treating cells for cell viability assay. Wells 1/A-H are loaded with 100 μ L of cell culture medium (C). Wells 2/A-H are loaded with 100 μ L of cell culture medium containing lowest concentration of treatment (X1). Wells 3-12/A-H are loaded with 100 μ L of cell culture medium containing increased concentrations of treatment (X2-X12).	
Figure 2.11	48
Example of 96-well plate after incubating treated cells with XTT. Wells C/A-C contain cells that were not treated with the cytotoxic agent and demonstrate the highest intensity of orange color (<i>i.e.</i> formazan produced by reduction of XTT by succinate dehydrogenases in viable cells). Wells X1-X8/A-C contain cells that were treated with increasing concentrations of the cytotoxic agent and demonstrate a gradual decrease in intensity of orange color, which indicates a decrease in the number of viable cells present.	
Figure 2.12	49
Example of exported data recorded from Biotek Synergy H4 multi-mode plate reader. Top panel contains the corrected absorbance values at 450 nm. Bottom panel contains the corrected absorbance values at 690 nm (background).	
Figure 2.13	50
Example of how the cell viability is determined based on the data recorded from Biotek Synergy H4 multi-mode plate reader. Control, X1, X4 and X8 represent samples shown in Figure 2.xx. In Excel, basic mathematical functions (average, standard deviation, etc.) are used to calculate the % cell viability and its % relative standard deviation (% rsd).	

Figure 2.14	51
Cell viability graph representing data and results determined by calculations shown in Figure 2.13. The % cell viability is plotted as a function of increasing concentration of the cytotoxic agent. The error bar represents the % cell viability (normalized to the control) \pm % relative standard deviation (% rsd).	
Figure 2.15	54
Example of 12-well plate configuration when treating cells for flow cytometry. (C) Wells loaded with 500 μ L of cell culture medium. (X1) Wells loaded with 500 μ L of cell culture medium containing lowest concentration of treatment. (X2-X5) Wells loaded with 500 μ L of cell culture medium containing increased concentrations of treatment.	
Figure 2.16	56
Screenshot of BD FACSDiva (software used for flow cytometry analysis) displaying settings and typical results for cell cycle analysis via flow cytometry.	
Figure 2.17	59
Screenshot of BD FACSDiva (software used for flow cytometry analysis) displaying settings and typical results for analysis of apoptosis and necrosis via flow cytometry.	
Figure 3.1	67
(A) UV-Vis spectrum of AuNPs exhibiting a maximum absorption at 528 nm. (B) UV-Vis spectrum of RGD/NLS-AuNPs exhibiting a maximum absorption at 532 nm. (C) TEM image of AuNPs about 30 nm in diameter.	
Figure 3.2	69
Schematic setup of real-time light scattering imaging system for live cell studies. A dark field light scattering imaging microscope with a side-illumination arrangement is combined with an environmental cell incubation chamber for real time studies of live cells.	
Figure 3.3	72
Dark field light scattering images of cytoplasm and nuclear targeting AuNPs. (A) RGD-AuNPs located in the cytoplasm of cancer cells. (B) RGD/NLS-AuNPs located at the nucleus of cancer cells. (C) RGD-AuNPs located in the cytoplasm of normal cells. (D) RGD/NLS-AuNPs located at the nucleus of normal cells. The cancer and normal cells were incubated in the presence of these AuNPs at a concentration of 0.4 nM for 24 h and these images clearly display the efficient uptake of AuNPs in cancer cells compared with normal cells. Scale bar: 10 μ m.	

Figure 3.4	73
Real-time images of cancer cell division showing an apparent cytokinesis arrest (B4) followed by binucleat cell formation (B6, B7) in the presence of 0.4 nM nuclear-targeting gold nanoparticles (RGD/NLS-AuNPs). This phenomenon was not observed in untreated cancer cells (A1-7) or cancer cells under other conditions (see Appendix A, Figure A.1). Red stars indicate the nuclei. Scale bar: 10 μ m.	
Figure 3.5	74
DNA damage induced in cancer cells by 0.4 nM nuclear-targeting gold nanoparticles (RGD/NLS-AuNPs) is indicated by the bright green fluorescence in (C). Cancer cells (A) in the absence of AuNPs and (B) with AuNPs in the cytoplasm, no DNA damage was observed. Scale bar: 10 μ m.	
Figure 3.6	76
(top) M phase (mitosis phase of cell division) accumulation of cancer cells in the presence of 0.4 nM nuclear-targeting gold nanoparticles (RGD/NLS-AuNPs) suggests complete cell division (cytokinesis) has not taken place. (bottom) Data for normal cells. Nocodazole synchronization and release techniques were used in this experiment (see Experimental section) and the cell cycle was measured at different times of release (120 and 360 min).	
Figure 3.7	78
Percentages of cells in each phase of the cell cycle show the appearance of a DNA-deficient cell population (subG1, yellow) for cancer cells in the presence of 0.4 nM nuclear-targeting gold nanoparticles (RGD/NLS-AuNPs), suggesting apoptosis.	
Figure 3.8	79
Number of normal cells (left) and cancer cells (right) counted using flow cytometry after incubation of cells with different AuNPs for 24 h.	
Figure 3.9	89
UV-Vis absorption spectra of (A) PVP-AuNCs and (B) citrate-AuNSs before (black) and after (red) conjugation with PEG. Transmission electron micrograph of (C) 45 nm PVP-AuNCs and (D) 35 nm citrate-AuNSs.	
Figure 3.10	96
Cellular internalization and nuclear localization of peptide-conjugated AuNPs by HSC cells after 48 h, determined as the percent uptake (A), as well as the with plasmonic dark field light scattering imaging (B) of internalized nanoparticles before and after etching of extracellular nanoparticles. Scale bar: 20 μ m	
Figure 3.11	97
Confocal microscopy images of FITC (green) labeled RGD/NLS-AuNCs (left) and AuNSs (right) co-localized with the nuclei (blue) of HSC cells. Scale bar: 20 μ m.	

Figure 3.12	99
Cell cycle changes induced by peptide-conjugated AuNPs, compared to control (HSC cells treated with nanoparticle-free culture medium). RGD/NLS-AuNSs (A), and RGD/NLS-AuNCs (B), at concentrations of 0.4 nM, both generate an increase in G0/G1 phase, a decrease in S phase and a decrease in G2/M phase populations when incubated with HSC cells for 48 h. Values expressed as mean \pm standard deviation of three independent experiments. Statistical significance, with respect to control, indicated by * ($p < 0.05$).	
Figure 3.13	100
ATP depletion induced by peptide-conjugated AuNPs (0.1 and 0.4 nM), normalized to the control (HSC cells treated with nanoparticle-free medium) after 48 h. The combination of RGD and NLS peptides conjugated to the nanoparticles allows for the greatest reduction in ATP in the case of the AuNSs (A) and AuNCs (B). Values expressed as mean \pm standard deviation of three independent experiments. Statistical significance, with respect to control (0.0 nM), indicated by * ($p < 0.05$).	
Figure 3.14	102
Cell death, via apoptosis (A) and necrosis (B), induced in HSC cells after 48 h treatment with 0, 0.1, and 0.4 nM peptide-conjugated AuNSs (purple) and AuNCs (blue). The RGD/NLS-AuNCs, at 0.4 nM treatment concentrations, induce the greatest amount of cell death. Values expressed as mean \pm standard deviation of three independent experiments. Statistical significance, with respect to control (above each bar) and between AuNSs and AuNSs (above each line) indicated by * ($p < 0.05$).	
Figure 3.15	103
Cell death induced, via apoptosis (yellow) and necrosis (grey), in HSC cells after 48 h treatment with varying concentrations AgNO_3 (<i>i.e.</i> Ag^+ ions), as well as free peptides in culture medium (3.2 μM RGD and 4 μM NLS). Values expressed as mean \pm standard deviation of three independent experiments. Statistical significance, with respect to control, indicated by * ($p < 0.05$).	
Figure 3.16	105
UV-Vis spectra of AuNCs in water (left) and DMEM, cell culture medium (right). A 51 nm shift in the surface plasmon of the AuNCs in DMEM is observed after 48 h at physiological conditions indicating the oxidation of silver atoms to Ag_2O on the inner cavity of the AuNC	

Figure 3.17	107
Reactive oxygen species (ROS) generation detected by confocal microscopy for 0.4 nM RGD/NLS-AuNSs and AuNCs. DAPI panel (left) shows the nuclei of HSC cells stained blue. FITC panel (middle) represents green fluorescence indicative of ROS generated inside cells. DAPI/FITC overlay (right) shows the combination of both nuclei and ROS. Control (cells treated with nanoparticle-free medium) exhibits minimal FITC fluorescence, along with the 0.4 nM RGD/NLS-AuNSs. 100 μ M H ₂ O ₂ shows high FITC fluorescence, used as a positive control for ROS generation. The 0.4 nM RGD/NLS-AuNCs display FITC fluorescence, indicating ROS are generated in HSC cells with this nanoparticle treatment. Scale bar: 20 μ m	
Figure 3.18	120
UV-Vis spectra (A) and TEM images of 40 nm AuNCs (B-D) synthesized with varying ratios of Ag to Au. As more gold salt is deposited onto the silver nanocube template, the surface plasmon peak redshifts (A). Scale bar: 40 μ m.	
Figure 3.19	122
Synthesis of AuNCs via galvanic replacement. Stoichiometrically, three Ag atoms of the Ag nanocube template are oxidized by one Au ³⁺ ion of the Au salt, which is subsequently reduced and deposited onto the Ag template. This results in hollow cage structure with porous faces and residual Ag on the inner cavity.	
Figure 3.20	125
Surface plasmon peak shifts observed for the oxidation of various RGD/NLS-AuNCs incubated in cell culture medium for up to 48 h. (A) Sample 1 (2.56 Ag: Au) exhibits an 84 nm redshift after 48 h. (B) Sample 2 (2.34 Ag: Au) exhibits a 63 nm redshift after 48 h. (C) Sample 3 (1.78 Ag: Au) exhibits a 37 nm redshift after 48 h.	
Figure 3.21	127
Apoptosis and necrosis induced in HSC cells by 48 h treatment of 0.1 nM RGD/NLS-AuNCs with varying porosity and Ag content (Samples 1-3). All nanocage-treated samples have statistically higher levels of apoptotic and necrotic cells ($p < 0.05$) than the untreated cells (control). Remaining data are considered statistically significant if $p < 0.05$, and is indicated by * above bars.	
Figure 3.22	137
TEM images of AuNPs synthesized via citrate reduction of HAuCl ₄ . (A) AuNPs with diameter of 29 ± 4 nm, inset showing size distribution histogram. (B) AuNPs with diameter of 14 ± 1 nm, inset showing size distribution histogram	

Figure 3.23.....	143
Cell cycle analysis of HSC-3 cells after treatment with various AuNPs (0.4 nM, 24 h) and 5-FU (100 μ M, 48 h). Cells that were not treated (white), cells treated with AuNPs alone (yellow), cells treated with 5-FU alone (light gray) and cells treated with combination of AuNPs and 5-FU (dark gray). Comparison between AuNP size: (A) 30 nm NLS-AuNPs versus (B) 15 nm NLS-AuNPs. Comparison between AuNP surface functionalization: (A) 30 nm NLS-AuNPs versus (C) 30 nm RGD-AuNPs.	
Figure 3.24.....	145
5-FU efficacy in HSC-3 cells after treatment with various AuNPs (0.4 nM, 24 h) and 5-FU (100 μ M, 48 h). Control represents cells that were not treated with any AuNPs. Cells that were not treated with 5-FU (light gray) and cells that were treated with 5-FU (red). 5-FU efficacy defined as % cells in S phase divided by % cells in G2/M phase of the cell cycle.	
Figure 3.25.....	147
Cell viability determined by an XTT assay of HSC-3 cells after treatment with various AuNPs (0.4 nM, 24 h) and 5-FU (10-500 μ M, 48 h). Cells that were only treated with 5-FU (control, black) and cells treated with a combination of AuNPs and 5-FU (red). Comparison between AuNP size: (A) 30 nm NLS-AuNPs versus (B) 15 nm NLS-AuNPs. Comparison between AuNP surface functionalization: (A) 30 nm NLS-AuNPs versus (C) 30 nm RGD-AuNPs. Statistical significance between cells treated with only 5-FU and cells treated with combination of AuNPs and 5-FU is indicated by * ($p < 0.05$).	
Figure 3.26.....	150
Flow cytometry analysis of HSC-3 cell death after treatment with 0.4 nM NLS-AuNPs (24 h), 150 μ M 5-FU (48 h) or 0.4 nM NLS-AuNPs (24 h) followed by 150 μ M 5-FU (48 h). Right panel shows necrotic cells (red), late apoptotic cells (dark blue), early apoptotic cells (light blue) and live cells (green) for cells that were untreated (c), treated with 150 μ M 5-FU for 48 h (5-FU), treated with 0.4 nM 30 nm AuNPs for 24 h (Au) and treated with 150 μ M 5-FU (48 h) after 24 h pre-treatment with 0.4 nM 30 nm NLS-AuNPs (Au + 5-FU). Statistical significance with respect to the control is indicated by * ($p < 0.05$) within the bars of the graph. Statistical significance with respect to different treatment groups indicated by * ($p < 0.05$) above graph.	
Figure 4.1.....	162
UV-Vis spectra of AuNRs (black) as well as the NIR cw laser spectrum (red) (with corresponding TEM images, scale bar: 60 nm). (A) 38 x 11 nm AuNRs with longitudinal plasmon resonance at 740 nm. (B) 28 x 8 nm AuNRs with longitudinal plasmon resonance at 770 nm (C) 14 x 5 nm AuNRs with longitudinal plasmon resonance at 755 nm.	

Figure 4.2.....	166
Photothermal heat conversion factor determined, per particle, for 17 x 5 nm AuNRs (17 nm, blue), 28 x 8 nm AuNRs (28 nm, yellow) and 38 x 11 nm AuNRs (38 nm, gray) at increasing NIR laser irradiation time. All initial temperatures were 24 ± 1 °C. Statistical significance ($p < 0.05$) indicated by *.	
Figure 4.3.....	168
Field contour plots for the longitudinal mode of the different AuNRs, with particle dimensions indicated and the field decaying to 1.25 at the extremities of each plot. (A) The field maximum of the 38 x 10 nm AuNR (calculated at 804 nm) is 3500. (B) The field maximum of the 25 x 7 nm AuNR (calculated at 761 nm) is 5220. (C) The field maximum of the 18 x 4 nm AuNR (calculated at 875 nm) is 5480	
Figure 4.4.....	171
DDA extinction (black dots), absorption (red line) and scattering (green line, and shown in inset) spectra for the longitudinal mode of the different AuNRs in water. (A) The 38 x 10 nm AuNR has an absorbance:scattering ratio of 63.8. (B) The 25 x 7 nm AuNR has an absorbance:scattering ratio of 204. (C) The 18 x 4 nm AuNR has an absorbance:scattering ratio of 921.	
Figure 4.5.....	173
Temperature change induced by plasmonic photothermal heating of different AuNRs (17, 28 and 38 nm in length) at different optical densities (0.5 and 1.5) and increasing NIR laser irradiation times. All initial temperatures were 24 ± 1 °C. Statistical significance between different sized AuNRs and optical densities at 2 min laser irradiation ($p < 0.5$) is indicated by *.	
Figure 4.6.....	175
Temperature change of cell culture medium containing different AuNRs. AuNRs 38 nm in length at OD 0.5 (light gray), AuNRs 28 nm in length at OD 0.5 (yellow), AuNRs 17 nm in length at OD 0.5 (blue) and AuNRs 38 nm in length at OD 1.5 (dark gray) were all exposed to upon NIR laser irradiation at increasing lengths of time. All initial temperatures were 32 ± 1 °C. . Statistical significance between different sized AuNRs and optical densities ($p < 0.5$) is indicated by * above bars.	
Figure 4.7.....	177
Cell viability determined for HSC cells treated with different AuNRs and subjected to PPTT via NIR laser irradiation. Cells treated with AuNRs 38 nm in length at OD 0.5 shown in light gray, AuNRs 28 nm in length at OD 0.5 shown in yellow, AuNRs 17 nm in length at OD 0.5 shown in blue and AuNRs 38 nm in length at OD 1.5 shown in dark gray. Statistical significance ($p < 0.05$) indicated by *. Statistical significance with respect to control (no AuNRs) indicated inside bars. Statistical significance between different treatments indicated above bars.	

Figure 4.8	188
TEM image (A), size distribution (B), and UV-Vis spectrum (C) of AuNRs about 27 nm in length and 8 nm in width, with a surface plasmon resonance around 760 nm	
Figure 4.9	189
Structure of HNSCP peptide conjugated to AuNRs for specific targeting of squamous cell carcinoma of the head and neck. Peptide provided by Raftery, E. and Sotimehin, A. (Georgia Tech).	
Figure 4.10	192
Pharmacokinetic properties, in terms of the blood circulation half-life ($t_{1/2}$) in healthy mice. (A) The $t_{1/2}$ is 12.8 h for PEG-AuNRs and (B) 8.5 h for HNSCP-AuNRs, as calculated by fitting the data to a one-phase decay model. Conjugated particles were provided by Mackey, M.A. and Ali, M.R.K. (Georgia Tech). Circulation half-life measurements were provided by Peng, X. (Emory University).	
Figure 4.11	193
Biodistribution profile of PEG-AuNRs and HNSCP-AuNRs 24 h following iv injection to nude mice bearing Tu212 xenografts. (A) Accumulation of AuNRs in brain, heart, lung, kidney and tumor. (B) Uptake of AuNRs by RES (<i>i.e.</i> accumulation in the liver and spleen). Conjugated particles were provided by Mackey, M.A. and Ali, M.R.K. (Georgia Tech). Biodistribution profile was provided by Peng, X. (Emory University).	
Figure 4.12	195
Tumor volume measurements with respect to time after treatment of nude mice bearing Tu212 xenografts. Control (black) mice (n = 3) were directly injected with 100 uL of PBS. Laser control (red) mice (n = 3) were directly injected with 100 uL of PBS and exposed to NIR radiation (5.8 W/cm ² , 2 min). HNSCP-AuNR control (blue) mice (n = 3) were directly injected with 100 uL of HNSCP-AuNRs, such that final concentration in tumor was 2.25 nM. HNSCP-AuNR laser treatment (green) mice (n = 6) were directly injected with 100 uL of HNSCP-AuNRs, such that final concentration in tumor was 2.25 nM and exposed to NIR radiation (5.8 W/cm ² , 2 min). Conjugated particles were provided by Mackey, M.A. and Ali, M.R.K. (Georgia Tech). Photothermal treatment and tumor size were provided by Mackey, M.A. (Georgia Tech) and Peng, X. (Emory University).	
Figure A.1	201
Real time imaging of cancer cells incubated with 0.4 nM cytoplasm targeting gold nanoparticles (RGD-AuNPs) (a) and 0.1 nM nuclear targeting gold nanoparticles (RGD/NLS-AuNPs) (b) show no apparent cytokinesis arrest.	

Figure A.2	202
Cell cycle time of cancer cells and normal cells with treatment of AuNPs. The cell cycle of cancer cells was extended by about 4 h with treatment of 0.1 nM RGD/NLS-AuNPs; but no changes with RGD-AuNPs treatment. The cell cycle time of normal cells have no change under both RGD-AuNPs and RGD/NLS-AuNPs. For cancer cells, 0.4 nM RGD/NLS-AuNPs induced cell cycle arrest, which make the whole cell cycle observation unavailable. The cell cycle time here is defined from the division of parent cells to the division of 2 nd generation cells (daughter cells). Four individual cell cases were taken for each data point to obtain an average value. The * indicates $p < 0.05$ and NS indicates <i>not significant</i> .	
Figure A.3	203
Release dynamics of cancer cells (left) and normal cells (right) initially synchronized at prometaphase. Cells are synchronized to prometaphase with nocodazole and then released in fresh medium. At different time points of release, DNA content was measured using flow cytometry.	
Figure A.4	204
Apoptosis induced by the presence of AuNPs at the nucleus of cancer cells. Cells were incubated with AuNPs for 24 h before analysis. The red box indicates sample with subG1 cell population (i.e. apoptotic cells).	
Figure A.5	205
Cell cycle changes induced by 0.1 and 0.4 nM peptide-conjugated gold nanoparticles in HSC cells after 48 h treatment with RGD-AuNSs (A), NLS-AuNSs (B), RGD-AuNCs (C) and NLS-AuNCs (D). Values expressed as mean \pm standard deviation of three independent experiments. Statistical significance, with respect to control, indicated by * ($p < 0.05$).	
Figure A.6	206
Raw data obtained from flow cytometry cell cycle analysis for all nanoparticle treatments tested in this work. Cell cycle histograms, not filled in, represent the raw data, including the subG1 population, indicative of an apoptotic population. SubG1 populations appear in HSC cells treated with 0.1 nM RGD-AuNC, 0.4 nM RGD-AuNC, 0.4 nM RGD-AuNS, 0.4 nM NLS-AuNS, 0.4 nM RGD/NLS-AuNS, and the greatest subG1 population in 0.4 nM RGD/NLS-AuNC. Cell cycle histograms, filled in, represent how the data was fit, after gating single cells and eliminating the subG1 populations, to obtain G0/G1 (green), S (yellow) and G2/M (blue) phase populations.	
Figure A.7	207
Peptide-conjugated gold nanoparticle-induced cell death, via apoptosis (A) and necrosis (B), in HSC cells after 48 h treatment with RGD-AuNSs, RGD-AuNCs, NLS-AuNSs, and NLS-AuNCs. Values expressed as mean \pm standard deviation of three independent experiments. Statistical significance, with respect to control, indicated by * ($p < 0.05$).	

Figure A.8.....207

HaCat cell death via apoptosis (left) and necrosis (right) induced by all nanoparticle formulations. All nanoparticle formulations induce minimal cell death in the HaCat cells compared with the HSC cells. This was expected, as the HaCat cells do not overexpress the alpha beta integrins on their surface.¹ Values expressed as mean \pm standard deviation of three independent experiments. Statistical significance, with respect to control, indicated by * ($p < 0.05$).

Figure A.9.....208

ROS generation detected by confocal microscopy for 0.4 nM RGD-AuNCs, RGD-AuNSs, NLS-AuNCs, and NLS-AuNSs. DAPI panel (left) shows the nuclei of HSC cells stained blue. FITC panel (middle) represents green fluorescence indicative of ROS generated inside cells. DAPI/FITC overlay (right) shows the combination of both nuclei and ROS. The 0.4 nM RGD-AuNCs and NLS-AuNCs display FITC fluorescence, indicating ROS are generated in HSC cells with this nanoparticle treatment. Scale bar: 20 μm .

Figure A.10.....209

Uptake analysis of 5-Fluorouracil (5-FU) in HSC-3 cells after cells were pre-treated with 15 nm NLS-AuNPs (light gray) or 30 nm NLS-AuNPs (dark gray). 5-FU uptake was determined by measuring the optical density (OD) of cell culture medium containing 5-FU, after 48 h treatment, with a Biotek Synergy H4 multi-mode plate reader. The measured OD was converted to a concentration by multiplying by the extinction coefficient, $39,290 \text{ M}^{-1} \text{ cm}^{-1}$ (determined by measuring various concentrations of 5-FU in cell culture medium). This concentration was then subtracted from the treatment concentration initially added to cells. Pre-treatment with NLS-AuNPs does not appear to enhance the uptake of 5-FU by HSC-3 cells.

Figure B.1.....210

Field contour plots at the resonance wavelength for the longitudinal mode of (A) a $38 \times 10 \text{ nm}$ AuNR at a wavelength of 786. The field maximum is 5560. (B) A $25 \times 7 \text{ nm}$ AuNR at a wavelength of 757 nm. The field maximum is 5320. (C) An $18 \times 4 \text{ nm}$ AuNR at a wavelength of 865 nm, The field maximum is 5760. For all cases, the particle dimensions are indicated on the axes and the field has decayed to a value of 1.25 at the extremities of the plot. At the resonance condition, there is less than 10% difference between the maximum field enhancement values for the different sized AuNR, not corresponding to the experimental results.

LIST OF ABBREVIATIONS AND SYMBOLS

Ag	silver
Au	gold
AuNC	gold nanocage
AuNP	gold nanoparticle
AuNR	gold nanorod
AuNS	gold nanosphere
DMEM	Dulbecco's modified eagle's medium
EGFR	epidermal growth factor
EPR	enhanced permeability and retention
FITC	fluorescein isothiocyanate
HD	hydrodynamic diameter
LSPR	localized surface plasmon resonance
NIR	near-infrared
PBS	phosphate buffered saline
PEG	poly(ethylene) glycol
PPTT	plasmonic photothermal therapy
RES	reticuloendothelial system
TEM	transmission electron microscopy
UV-Vis	ultraviolet-visible

SUMMARY

Gold nanoparticles exhibit an array of properties, both intrinsic and extrinsic, that can be exploited for their use in cancer therapeutics. Owing to their size and ease with which they can be functionalized with various ligands, gold nanoparticles represent a class of highly functional biomedically relevant nanostructures. **Chapter 1** introduces the reader to the synthesis and functionalization of various gold nanostructures. Intrinsic properties of these gold nanostructures are also discussed in this chapter, to lead to **Chapter 3**, where the recent exploration of these properties is presented. Extrinsic properties of gold nanostructures are also introduced, to prepare the reader for **Chapter 4**, in which recent developments in the exploitation of these properties are presented. **Chapter 2** presents the reader with a detailed explanation of experimental protocols for the various *in vitro* methods utilized throughout our work.

Chapter 3 discusses recent developments in the use of gold nanoparticles as intrinsic antineoplastic agents, with their ability to cause DNA damage and cytokinesis arrest (**Chapter 3.1**), to suppress tumor growth (**Chapter 3.2**), to induce apoptosis in a metallic composition-dependent manner (**Chapter 3.3 and 3.4**), as well as their ability to enhance sensitivity to chemotherapy by regulation of the cell cycle (**Chapter 3.5**).

In **Chapter 4**, the extrinsic properties of gold nanoparticles are examined, in detail, through both theoretical and experimental assessment (**Chapter 4.1**) for their use as photothermal contrast agents *in vitro*. Based on this assessment, the gold nanoparticles are tested in the plasmonic photothermal therapy of head and neck cancer in a mouse model (**Chapter 4.2**).

CHAPTER 1

INTRODUCTION

On December 23rd, 1971, US President Nixon declared a “War on Cancer,” with the signing of the National Cancer Act, which aims to eradicate cancer as a major cause of death through increased research to develop more effective treatments and improvements in the understanding of cancer biology. One research area that is currently being used to achieve this is that of understanding the interactions between materials and cellular/molecular components on the most elemental level of biology, also referred to as nanotechnology. The heart and soul behind this area of research is US National Cancer Institute’s Alliance for Nanotechnology in Cancer. With this program, new nanotechnologies are being developed and, through active collaborations between researchers, they are being successfully applied in the diagnosis and treatment of cancer.[1] Many, in fact, have already been approved or are in the pre-clinical and clinical trial stages of development.[2, 3]

Among the many types of nanotechnologies, gold nanoparticles, in particular, exhibit unique properties that can be utilized in this “War on Cancer.” When conjugated with specific ligands, they exhibit properties distinctive from both the particle scaffold and their parent molecule. Gold nanoparticle conjugates can show increased binding affinity and targeting selectivity when functionalized with multiple targeting groups,[4] as well as tumor-selective uptake due to their size.[5] These particles can be delivered systemically, demonstrating minimum immunogenic responses[6] and long circulatory half-lives.[7] They also possess unique optical and electronic properties which can be exploited in cancer-selective photothermal therapeutic applications[8-12] or non-invasive diagnostic

imaging.[13-16] Their intrinsic size, shape, and surface reactivity can further be used to direct and selectively modify cellular processes associated with malignant progression.[17-20] Gold nanoparticles represent a versatile, potent, selective, and highly multi-functional anti-cancer nanotechnology.

1.1. Gold Nanoparticles: Design and Biocompatibility

1.1.1. Gold Nanoparticle Synthesis

Common applications of gold nanoparticles involve the use of spherical gold nanoparticles in drug delivery and antineoplastic treatment applications. Small (10 nm in diameter) gold nanospheres are synthesized from the citrate reduction of aqueous chloroauric acid. A representative TEM image of gold nanospheres is shown in Figure 1.1A. The synthesis of colloidal gold, first observed by Faraday[21] in 1857, generally involves the reduction of a metal salt in the presence of a stabilizing agent. Following the advent of the transmission electron microscope (TEM), Turkevich later surveyed a variety of synthetic methods to obtain gold nanoparticles[22] and in 1973, Frens systematically developed methods for synthesizing gold nanospheres of varying diameter via the citrate reduction method.[23] The resulting nanoparticle sizes are controlled by the stoichiometric ratio of gold to reducing agent, with larger ratios leading to larger diameters. In this case, citrate also acts as an anionic capping agent which stabilizes the colloidal solution by electrostatic repulsion.

Gold nanorods, similar to those shown in Figure 1.1B, are synthesized via seed-mediated growth.[24] In this method, small seeds (3-5 nm in diameter), capped by an

amphiphilic, cationic surfactant are synthesized from the reduction of aqueous chloroauric acid by borohydride. An aqueous chloroauric acid growth solution, containing silver nitrate and the cationic surfactant, is then mildly reduced from Au^{3+} to Au^+ by the addition of ascorbic acid. The seeds are then introduced into the growth solution, acting as nucleation sites for the anisotropic reduction of Au^+ ions onto the seeds, forming rod-shaped particles over the next several hours. Although the widths of the nanorods formed by this method are fairly constant, lengths can be extended by increasing the amount of silver nitrate. Murphy and coworkers and El-Sayed and coworkers further adapted and optimized the surfactant-directed method for solution-phase growth using the seed-mediated method.[25] Later, Murphy and coworkers developed a seedless growth method, which produced gold nanorods that were much smaller in size (length and width) than those synthesized via seed-mediated growth.[26] El-Sayed and coworkers further modified this method, by achieving simultaneous seed formation and nanorod growth using only sodium borohydride as a reducing agent. This method produces the smaller gold nanorods in large scale and high monodispersity.[27]

Gold nanocages, like those shown in Figure 1.1C, make up another class of biomedically-relevant gold nanoparticles. Over the past several years, Xia and coworkers have developed a variety of solution-phase techniques for the synthesis of hollow-core noble metal nanoparticles, based on the galvanic displacement method.[28, 29] This technique relies on the use of a metal nanoparticle template from which atoms are displaced for another metal. The precursor nanoparticle is comprised of a less noble metal, (e.g. Ag) such that the addition of ions of a more noble metal (e.g. Au, Pt, Pd) will spontaneously replace the ions of the precursor nanoparticle. Gold nanocages are

synthesized by reacting silver nanocubes with Au^{3+} ions. Because the reduction potential of gold is more positive (i.e. more energetically favorable) than silver, atoms from the silver nanocube are spontaneously oxidized (i.e. displaced) as gold ions are reduced onto the precursor nanoparticle surface. In this case, because gold reduction is a three electron process and silver oxidation is a one electron process, voids are created in the newly formed cuboid structure as three silver atoms are exchanged for one gold atom. Displacement proceeds according to the availability of surface sites on the template particle, forming a subsequent cage-like gold structure.

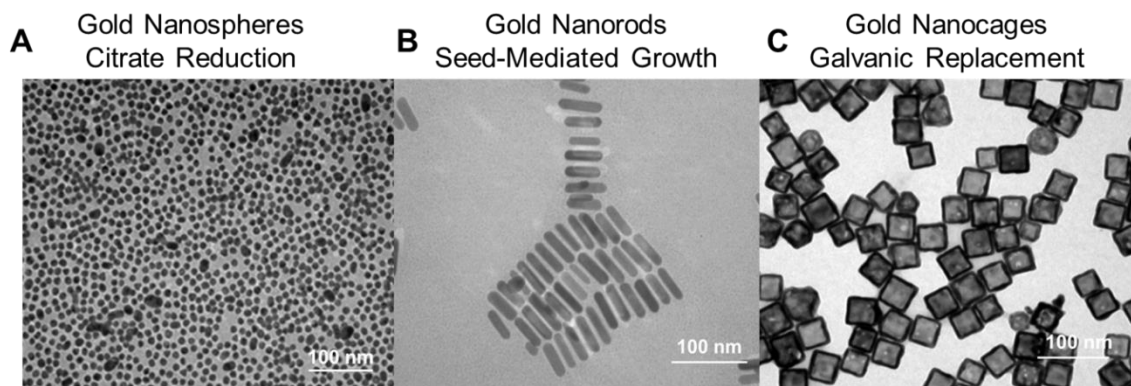


Figure 1.1. Transmission electron microscopy (TEM) images of common biomedically relevant gold nanostructures. (A) Gold nanospheres synthesized via citrate reduction. (B) Gold nanorods synthesized via seed-mediated growth. (C) Gold nanocages synthesized via galvanic replacement. Scale bar: 100 μm .

1.1.2. Gold Nanoparticle Conjugation

The gold nanoparticle surface represents one of the most stable and easily functionalized platforms for molecular conjugation. Au surfaces can be functionalized with a variety of organic self-assembled monolayers (SAMs) (e.g. thiolates, dithiolates, amines, carboxylates, cyanides, isothiocyanates, phosphines, etc.) to allow stable dispersion of particles in both aqueous and organic media. In most cases, ligation is

spontaneous at room temperature and occurs over the millisecond to minute time scale for commonly used alkanethiols.[30] Packing and reordering of the SAM can occur over several hours and place exchange of the monolayer can also be performed to functionalize gold nanoparticles with mixed monolayers or fully exchanged SAMs of targeting, therapeutic, or stabilizing ligands, as well as heterobifunctional linkers to which such molecules can also be appended. Molecular coverages on a gold surface can be as high as 1.5×10^{15} molecules/cm², however in practice, coverages are typically an order of magnitude less.[31] Multivalent nanoparticle conjugates exhibit cellular interactions distinct from their parent ligands or particles. Similar to antibodies, nanoconjugate binding affinity (K_d) can be enhanced by simply increasing the density of targeting ligands on the particle, in some cases increasing the affinity up to 4 orders of magnitude.[32] The circulatory half-life of hydrophobic drugs can also be significantly increased by functionalization with hydrophilic nanoparticles.[7] The intracellular transport rate of molecules which passively diffuse into the cell can be enhanced by endocytosis of their nanoparticle conjugates,[33] the intracellular localization of drugs can be directed by cell-penetrating peptides or nuclear localization sequences,[34] and endosomal accumulation or degradation can be circumvented by proton sponge groups or photothermal heating[35] of the particle. Targeting selectivity, tumor accumulation, and therapeutic response of the nanoparticle conjugate can be further enhanced using multiple targeting groups (i.e. multimodal targeting).

Biocompatibility of gold nanoparticle conjugates is also an important aspect of their design. Physiological environments exhibit high ionic and serum concentrations which can disrupt and diminish the stabilizing capacity of many nanoparticle ligands.

Nanoparticles are considered stably suspended if the working distance of their repulsive forces outweighs that of their attractive forces. Attractive forces are generally attributed to van der Waals interactions and repulsive forces are generally associated with charge–charge (i.e. electrostatic) or physical (i.e. steric) separation. Because of the high ionic concentration present in both physiologic fluids and cell growth media, electrostatic repulsion alone is often insufficient to overcome Debye charge screening and subsequent nanoparticle aggregation. Physical separation using hydrophilic polymer ligands is common practice and allows stable suspension of the particles in environments of both high ionic strength and serum concentration. Poly(ethylene glycol) (PEG) is the most common surface ligand used to stabilize nanoparticles, especially in the case of gold surfaces via thiol linker. PEG consists of hydrophilic poly(ethylene oxide) repeats and can be branched if increased stability and size are needed. Gold nanorods have, for example, exhibited circulatory half-lives as high as 17 h in nude mice when PEGylated.[7] Other common polymer stabilizers for gold nanoparticles include: poly(lysine) (PLL), poly-(styrene sulfonate) (PSS), starches, and poly(vinylpyrrolidone) (PVP). Functionalization with such polymers not only increases hydrophilicity, but also decreases immunogenic response from the nanoparticles, as well as their recognition and subsequent removal by the reticuloendothelial system (RES) through minimizing adsorption of proteins and molecules (i.e. opsonins) which initiate phagocytic uptake. Together, these strategies serve to maximize circulatory half-life and, thus, tumor accumulation by active or passive targeting strategies.

1.1.3. Gold Nanoparticle Accumulation, Uptake and Clearance

One particular advantage of anti-cancer gold nanoparticle conjugates is their size-selective accumulation at tumor sites due to the enhanced permeability and retention (EPR) effect.[36] Malignant cells require larger amounts of nutrients in order to sustain their accelerated growth and division. To meet this demand, solid tumors stimulate the production of new vasculatures through which increasing amounts of blood can be supplied (*i.e.* angiogenesis). In contrast to normal vessels, the angiogenic neovasculature is characterized by a highly disordered endothelium with large gaps that permit the penetration of nanosized conjugates. Characteristically diminished lymphatic drainage from the tumor interstitium also serves to increase retention of such compounds at the tumor site, resulting in both improved penetration and decreased clearance of circulating nanoparticle conjugates. These characteristics are demonstrated by the illustration shown in Figure 1.2.

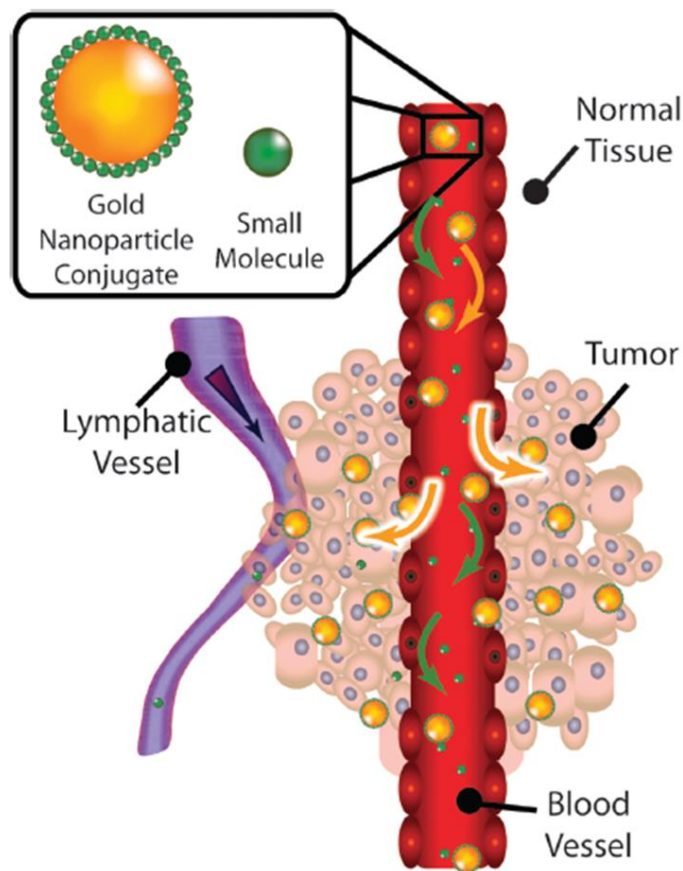


Figure 1.2. Graphic illustrating enhanced permeability and retention (EPR) effect exploited by gold nanoparticle conjugates to achieve selective accumulation at tumor sites. Gold nanoparticle conjugates penetrate leaky vasculature of blood vessels and diminished lymphatic drainage allows for retention of gold nanoparticle conjugates within the tumor interstitium. Adapted from Dreaden, et. al.[37]

The optimal size for EPR of a gold nanoparticle conjugate varies depending on the stage, location, and type of cancer, however particles with a hydrodynamic diameter (HD) greater than the renal clearance threshold (about 6 nm) and up to 2 μm in HD can be expected to exhibit preferential tumor accumulation. Passively[38, 39] (e.g. EPR) and actively[38-40] targeted gold nanoparticles, for example, have exhibited as much as 2–5% and 6–13% tumor accumulation, respectively, from systemically administered particles *in vivo*. Although most gold nanoparticle conjugates are capable of exhibiting

some degree of intracellular penetration, particle size, charge, and lipophilicity also play critical roles in determining the extent of uptake. Chan and coworkers have studied the size and shape dependent uptake of gold nanoparticles by cervical cancer cells (HeLa) and found that size dependent internalization peaked at a 50 nm diameter and that the uptake of colloidal nanorods decreased with increasing aspect ratio.[41] In another study, shown in Figure 1.3, using immunoglobulin G (IgG) antibody gold nanoparticle conjugates, they further found that multivalent functionalization of smaller gold nanoparticles did not enhance uptake due to their decreased ability to occupy multiple, receptor binding sites and that larger particles, although capable of multivalent receptor binding, were too large for membrane wrapping (*i.e.* engulfing) necessary for efficient endocytosis.[42] Particles conjugated to antibodies of an epidermal growth factor receptor (EGFR) exhibited the greatest uptake into breast cancer cells (SK-BR-3) and therapeutic response when 40–50 nm gold nanoparticles were used.

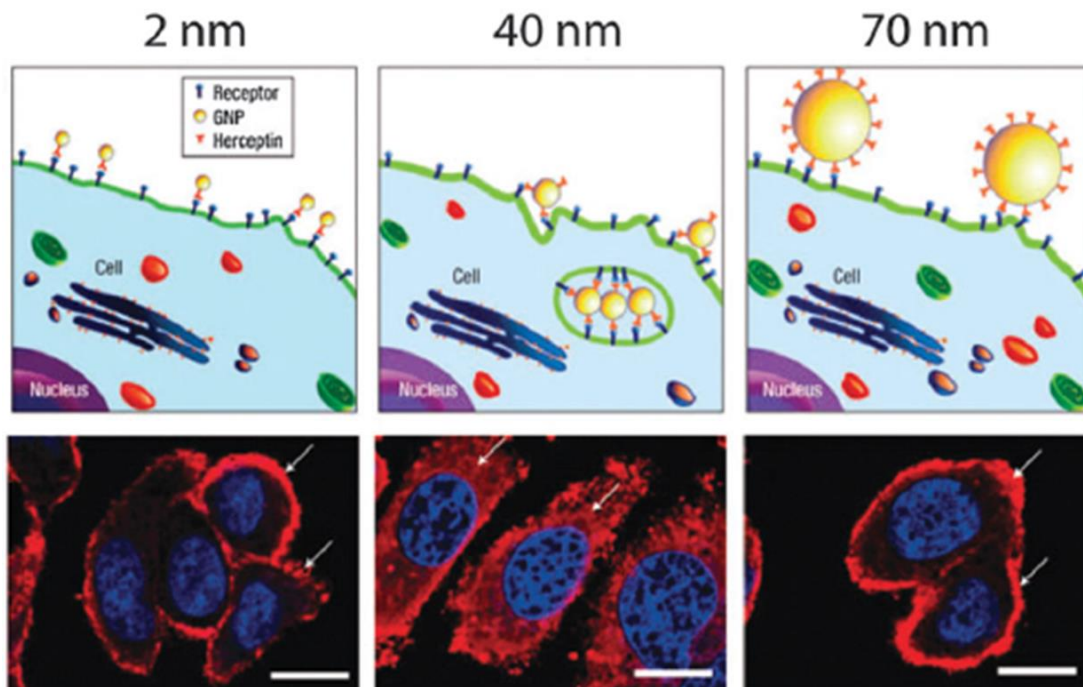


Figure 1.3. Size-dependent receptor-mediated endocytosis of IgG-gold nanoparticle conjugates by breast cancer cells. (Left) Schematic illustrating that 2 nm particles do not bind multiple receptors and therefore are not efficiently internalized by cells, as shown by fluorescence images of nanoparticles on surface of cell. (Middle) 40 nm particles do bind multiple receptors and are therefore efficiently taken up via endocytosis, as shown in fluorescence images. (Right) 70 nm particles also exhibit simultaneous binding to multiple receptors, but are too large for efficient internalization by cells, as shown in fluorescence images. In fluorescence images, the nuclei are stained blue and the particles are represented by red fluorescence. Scale bar: 10 μm . Adapted from Dreaden, et. al.[37]

Although the optimal particle size for intracellular penetration obviously varies depending on the cell size, type, receptor density, metabolic activity, as well as the specific targeting strategy employed, this study nonetheless highlights the importance of therapeutic nanoparticle conjugate size in determining subsequent transport kinetics and treatment efficacy. Cationic zeta potential (i.e. positive surface charge) can also promote the uptake of nanoparticle conjugates due to electrostatic attraction with anionic phospholipids on the cell surface. In some cases however, this attraction can result in significant cytotoxicity due to membrane disruption. The pharmacokinetic clearance of

circulating gold nanoparticle conjugates is also of key importance to subsequent efficacy.[43] Cationic nanoparticles exhibit high propensity for urinary (renal) clearance, due to electrostatic attraction with the net negative charge of the capillaries that separate circulating blood from urinary filtrates. Although efficient renal clearance is sometimes desirable, cationic nanoparticles can exhibit poor circulatory half-lives due to electrostatic attraction with the negatively charged laminar surfaces of the blood vessels. Anionic nanoparticles, on the other hand, often exhibit decreased cell penetration. Nanoparticle opsonization and phagocytic uptake are typically lowest when particles possess a neutral zeta potential and contain hydrophilic polymers which shield hydrophobic-hydrophobic and/or electrostatic interactions with antibodies and serum proteins.[44]

Circulating nanoparticles which cannot be filtered by the renal system are captured and degraded by Kupffer cells or allowed to proceed to the liver where they are metabolized by (or internalized by) hepatocytes and excreted into the bile. Cho et al. have recently studied the size-dependent *in vivo* accumulation and clearance of intravenously administered, PEGylated (5 kDa) gold nanoparticles in nude mice.[45] They found that larger gold nanoparticles (100 nm versus 4 and 13 nm in diameter) exhibited shorter circulatory half-lives and more rapid RES accumulation, accumulating predominantly in the liver and spleen, rapidly reaching maximum accumulation at 30 min and persisting for 6 months. In contrast, the smaller gold nanoparticles accumulated predominantly in the liver, spleen, and lung, reaching peak accumulation at 7 days and persisting up to 6 months. Very low urinary excretion of the small gold nanoparticles was shown over 1 day post-injection and only nominal renal clearance of the large particles was observed.

Very low biliary excretion was also shown for both large and small particles from 1–4 weeks, however the majority of the particles remained accumulated in the RES organs. Acute toxicity has been observed with the *in vivo* administration of polymer stabilized gold nanoparticles, but long term toxicological investigations, specifically with respect to maintenance of RES organ function, is urgently needed in order to accelerate the clinical translation of these therapeutic nanotechnologies.

1.2. Intrinsic Properties of Gold Nanoparticle Conjugates

1.2.1. Anti-Proliferative Effects

Gold nanoparticle conjugates can exhibit intrinsic antineoplastic properties, much like chemo- and radio-therapy. The selective regulation of cell growth and division by gold nanoparticles can serve as a potent anti-cancer treatment strategy. The extent of tumor growth and malignant progression is highly dependent on the formation of new blood vessels, angiogenesis, a process primarily mediated by signaling associated with vascular permeability factor/vascular endothelial growth factor 165 (VPF/VEGF-165). Selective inhibition of VPF/VEGF-165 activity is one method by which angiogenic growth can be mitigated in anti-cancer treatments. Mukhopadhyay and coworkers have recently studied the effects of spherical gold nanoparticles on VEGF-165-dependent proliferation in human umbilical vascular endothelial cells (HUVEC).[20] Their results showed that these gold particles significantly inhibited VEGF-165-induced cell proliferation of HUVEC cells (5 nm in diameter, citrate-capped, 335–670 nM, 24 h). Using X-ray photoelectron spectroscopy (XPS), they found that the gold nanoparticles bound directly

to the heparin-binding domain of VEGF-165 through sulfur and/or nitrogen bonds, an interaction which significantly inhibits VEGF-165's ability to associate with cell surface receptors necessary for angiogenic signaling and proliferation. Further, they showed that gold nanoparticles had no effect on signaling/proliferation associated with a non-heparin binding growth factor, VEGF-121. The group later explored the ability of gold nanoparticles to inhibit VEGF-165-induced angiogenesis and vascular permeability *in vivo*, observing a significant reduction of angiogenic activity in ovarian tumor-bearing nude mice when the gold nanoparticles were intradermally administered (2 x 10⁶ μL of 670 nM).[19] A significant decrease in vascular permeability was also observed following injection of the gold nanoparticle mixture, combined effects which could be potentially applied in future anti-cancer treatments.

1.2.2. Cell Cycle Regulation

Because malignant cells are increasingly sensitive to cell cycle disruption and also less capable of repairing such damages, gold nanoparticles can be used as cancer-selective cytotoxic agents for the selective modulation of the cell cycle. Xing and coworkers have explored changes in the cell cycle and sensitization to radiotherapy in a radiation-resistant human prostate carcinoma cells line (DU-145) treated with glucose-capped gold nanoparticles (10.8 nm in diameter) *in vitro*. [17] The glucose-gold nanoparticle conjugates were shown to arrest the prostate cancer cells at the G2/M phase of the cell cycle, the phase in which cells are most sensitive to radiation damage (15 nM, 2 h). Accumulation of the cells in G2/M was shown to result from upregulated expression of cyclin E protein, a promoter of the so-called cell cycle “checkpoint kinase”, which

regulates the transition from G1 to S and accelerates progression through G1 (1.2 fold upregulation, 24 h; 1.5 fold upregulation, 48 h). Radiosensitization of prostate cancer cells treated with glucose-gold nanoparticle conjugates is expected to increase the efficacy of subsequent radiotherapy treatments and to minimize adverse side-effects by lowering threshold exposure levels. Because cancer cells are increasingly sensitive to cell cycle disruption and DNA damage, gold nanoparticles which induce such effects can be selectively delivered to malignant cells or administered at dosages below that necessary to damage normal tissues to achieve oncologic effect.

1.3. Extrinsic Properties of Gold Nanoparticle Conjugates

1.3.1. Optical Properties

Metallic conductors are characterized by their delocalized free electrons whose density can vary in response to an externally applied electromagnetic field. Just as solid materials exhibit vibrational modes associated with the collective oscillations of their atoms, metallic solids also exhibit collective oscillatory modes of their free electrons (i.e. plasmon modes). Free electrons in noble metals exhibit plasmon oscillation frequencies in the mid- to far- UV, but the electrons on the nanometer scale are less restricted and can oscillate at near-UV, optical, NIR, and IR wavelengths. Incident electromagnetic fields (i.e. photons) can couple with surface plasmon modes of similar frequency, leading to their absorption or scattering. Surface plasmon resonance results in the local increase of resonant electromagnetic fields over several orders of magnitude. Surface plasmon absorption occurs rapidly, dephasing on the femtosecond time scale, dissipating absorbed

energy by coupling to adjacent electronic systems or to atomic lattice vibrations. Subsequent phonon–phonon relaxation occurs on the picosecond time scale and results in highly localized heat generation.[46] The wavelength of a nanoparticle’s surface plasmon resonance depends on the metal, as well as its size, shape, and dielectric environment. Plasmonic metals include Li, Na, K, Mg, Al, Fe, Cu, Ag, Pt, and Au. Of these, gold is the only nanoscale metal which exhibits both inert reactivity and plasmon resonance which is red shifted sufficient to avoid significant attenuation by tissues and fluids in physiological environments. Increased size can serve to red shift gold’s surface plasmon resonance, but with increasing size, absorption also diminishes due to increased scattering, a property which can often be disadvantageous. Although the dielectric environment surrounding circulating and tissue-accumulated nanoparticles is fairly constant, surface plasmon resonance can also red shift significantly with increasing dielectric permittivity and refractive index. By synthetically varying the shape of gold nanoparticles, the plasmon resonance can be shifted to higher tissue penetration wavelengths.

1.3.2. Photothermal Contrast Agents

Photothermal therapy (PTT) is a cancer treatment method which, like chemotherapy, relies on the selective application or the increasing sensitivity of cancer cells to cytotoxic damage-in this case from heat, or hyperthermia. A wide variety of electromagnetic radiation sources can be used in these treatments, applied in whole-body procedures or focused to specific regions of interest, where it is absorbed and dissipated as heat by physiologically relevant molecules, such as melanin and water, or by photothermal contrast agents which can be directly applied to solid tumors or intravenously

administered and accumulated at malignant sites by active and/or passive targeting. Although the methodology has gained some degree of popularity in Europe, it is not yet widely applied clinically in the US. Current clinical and preclinical PTT trials using gold nanoparticle contrast agents, however, are rapidly progressing (e.g. CytImmune, Nanospectra Biosciences). Photothermal therapies involving plasmonic gold nanoparticles can be categorized based on the mechanisms by which they achieve cell death. Mild temperature increases of 3–6 °C (i.e. hyperthermia) often trigger apoptotic pathways and are well known to alter a variety of normal cellular functions, resulting in denaturation of proteins/enzymes, induction of heat-shock proteins, metabolic signaling disruption, endothelial swelling, microthrombosis, diminished vascular supply, impaired receptor recognition, dysfunctional membrane transport, and inhibited nucleotide synthesis.[47, 48] In addition, the ability of malignant cells to repair such damages is also decreased, compared to normal cells. Larger, more rapid temperature increases, often termed “ablative” treatments, occur via necrotic cell death. In these cases, disruption of the cellular membrane is often predominant, with subsequent physical destruction of organelles also occurring. Gold nanoparticles are currently being explored as contrast agents for anti-cancer PTT (i.e. plasmonic photothermal therapy, PPTT) because their absorption cross sections and photostabilities are far superior to traditional molecules such as indocyanine green. Treatments can include focused and fiber optic-guided laser excitation of primary tumors, and can be particularly advantageous in treating tumors in areas poorly accessible by surgery. With absorption by physiological fluids and tissues (e.g. hemoglobin and water) being minimal in the near-infrared (NIR, 650–900 nm)

region, the absorption maxima of therapeutic and diagnostic gold nanoparticles are synthetically tuned to this “NIR window” shown in Figure 1.4).[49]

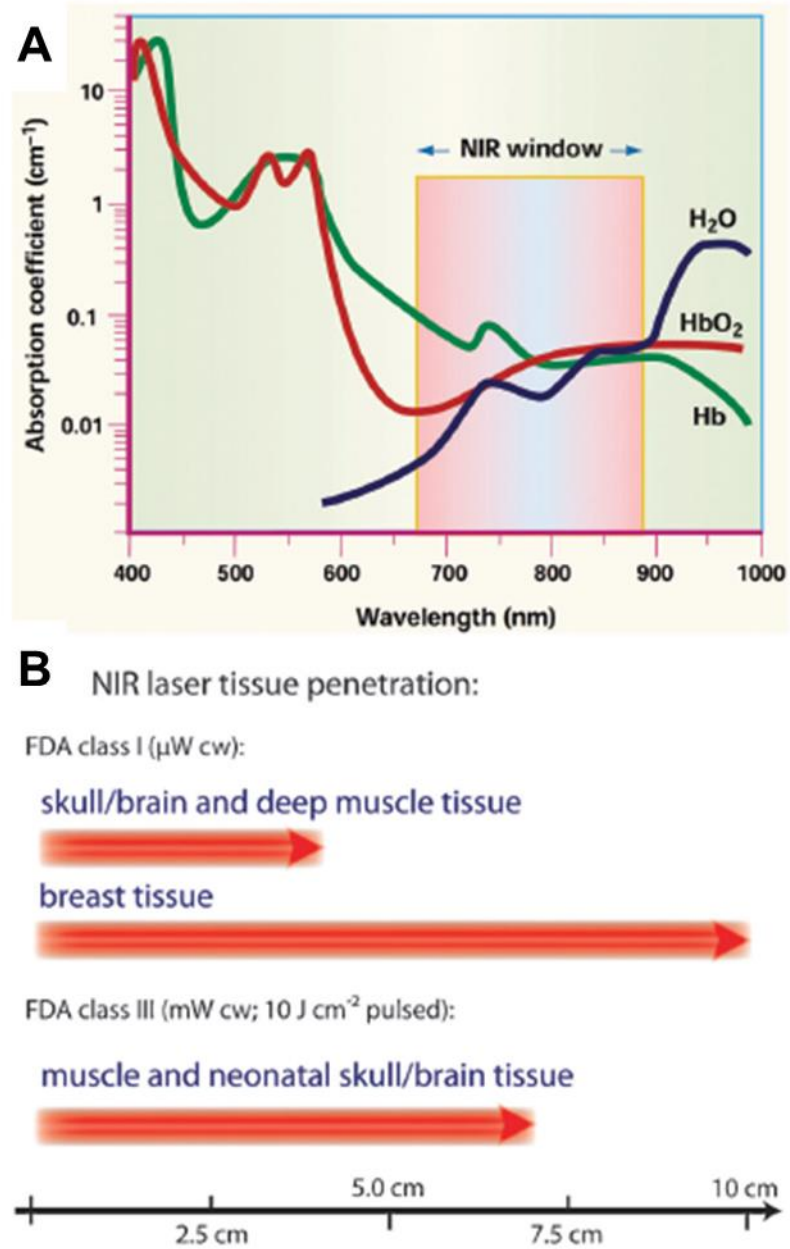


Figure 1.4. Wavelength range (650-900 nm) of the near-infrared (NIR) tissue transmission window. (A) Absorption from physiologic components, such as oxy/deoxyhemoglobin and water is minimal in this range. (B) This allows for maximum NIR laser penetration depths. Photothermal contrast agents are designed to absorb in this wavelength range to allow for maximum penetration depth of external radiation through biological tissues. Adapted from Dreaden, et.al.[37]

Microwatt NIR lasers (FDA class 1) can, for example, efficiently penetrate as much as 4 cm through the skull/brain and deep muscle tissue and up to 10 cm through breast tissue. Higher power lasers (FDA class 3) have exhibited 7 cm penetration depths through muscle and neonatal skull/brain tissue, as well. In PPTT applications, gold nanorod, nanoshell, and nanocage absorption is tuned by synthetically varying the aspect ratio, shell thickness:core radius, and the extent of galvanic displacement, respectively. PPTT using gold nanoparticles was first demonstrated *in vitro* by Lin and coworkers in 2003.[50] Here, spherical gold nanoparticles were conjugated with IgG antibodies that target CD8 receptors on peripheral blood lymphocyte cells. Using nanosecond pulsed visible laser exposure, 95% of cells containing as few as about 500 particles/cell were killed, due to apparent membrane disruption. Our lab later demonstrated the use of continuous wave visible laser exposure in PPTT of oral squamous cell carcinoma cells treated with spherical gold nanoparticle conjugates of EGFR IgG antibodies.[51] Benign cells were found to require more than twice the energies required to kill malignant cells due to increased antibody–nanoparticle conjugate labeling and PPTT response from the cancer cells. Halas and West later applied silica–gold core–shell nanoparticles (gold nanoshells) in near-infrared PPTT, correlating *in vitro* treatment response with *in vivo* efficacy.[52] Breast carcinoma cells specifically labeled with PEGylated gold nanoshells were shown to be efficiently destroyed by cw NIR laser exposure (7 min, 35 W/cm², 5 mm spot size). The nanoshells were later injected into the tumor interstitium of scid mice bearing sarcoma xenografts. Using magnetic resonance imaging (MRI), NIR laser exposure was directed about the tumor site (< 6 min, 4 W/cm², 5 mm spot size). Based on the temperature-dependent MRI frequency shift of protons in the tissues, intratumoral

temperature changes were three dimensionally mapped in real time, showing average temperature increases of 37.4 ± 6.6 °C in nanoshell treated PPTT, which resulted in significant coagulation, cell shrinkage, and loss of nuclear staining, as shown by histological analysis. NIR PPTT using systemically administered gold nanoshells was later demonstrated using a colon cancer model.[53] PEGylated gold nanoshells were intravenously injected in carcinoma-bearing nude mice and their tumors were exposed to cw NIR laser radiation after 6 h (3 min, 4 W/cm², 5.5 mm spot size). Tumors in nanoshell-treated mice were completely ablated after a single PPTT treatment and the animals appeared healthy and tumor free 490 days post treatment. In contrast, tumors in control animal groups continued to grow, with nearly 50% of the animals dying after 10 days. El-Sayed and coworkers later demonstrated *in vitro* NIR PPTT using gold nanorods which can more efficiently absorb photons to generate heat.[54] Anti-EGFR conjugates of gold nanorods were found by dark-field light scattering microscopy to selectively label oral squamous cell carcinoma cells which overexpress EGFR on their cell surface. Similar to experiments with gold nanospheres, cw laser NIR PPTT found that malignant cells required nearly half the energy necessary to kill nonmalignant cells, due to their increased nanoparticle labeling and subsequent membrane disruption from the treatments. As seen in Figure 1.5, The group later showed the use of both systemically and locally administered gold nanorods in *in vivo* NIR PPTT .[48]

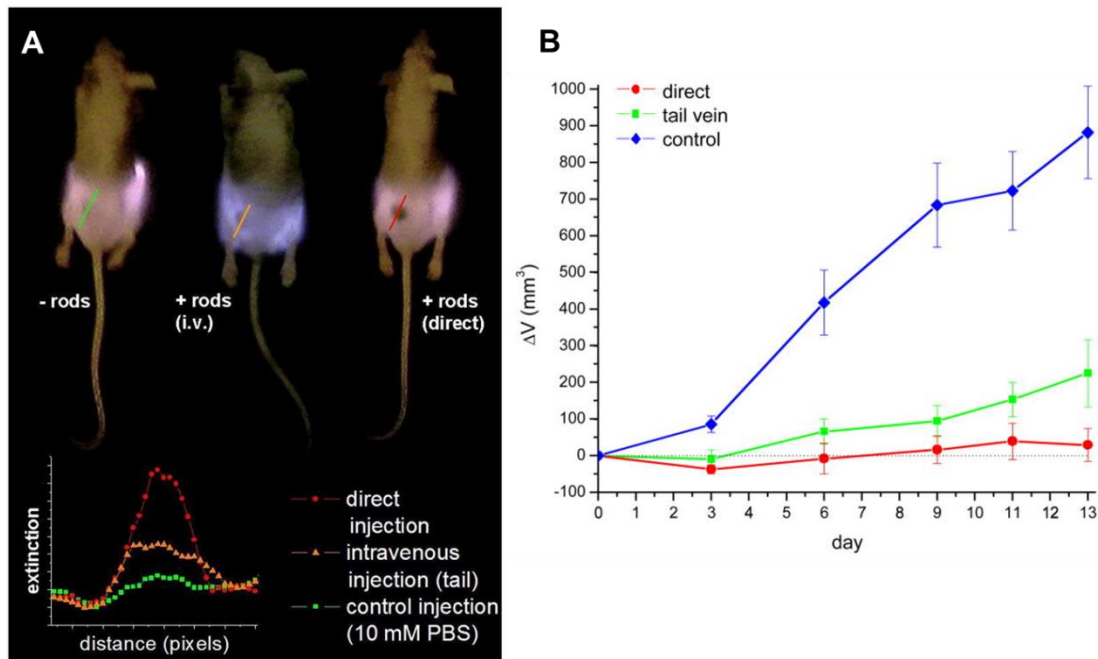


Figure 1.5. *In vivo* near-infrared (NIR) laser plasmonic photothermal therapy utilizing gold nanorod contrast agents. PEGylated gold nanorods were intravenously and locally injected in carcinoma-bearing nude mice. (A) NIR imaging indicated significantly increased NIR extinction of gold nanorods accumulated at the tumor sites, with direct injection showing higher accumulation of AuNRs than tail vein injection. (B) The change in tumor volume was determined over the course of two weeks, after single NIR laser exposure, and exhibits a significant decrease in tumor volume for the nanorod-treated tumors compared with the controls. Adapted from Dreaden, et.al.[37]

PEGylated gold nanorods were intravenously or interstitially administered in nude mice bearing squamous cell carcinoma tumors. The gold nanorods exhibited efficient accumulation and enhanced NIR absorption at the tumor site following administration by both methods. After a single cw NIR laser exposure, nanorod treated tumors exhibited dramatic growth remission (10 min, 1–2 W/cm², 6 mm spot size). Greater than 57% of the directly-injected tumors and 25% of the intravenously-treated tumors were completely resorbed after 13 days. Bahatia and coworkers later showed that the intrinsic X-ray absorbing properties of gold nanorods (double that of clinical iodine standards) can

be used to guide NIR PPTT and increase the treatment efficacy.[7] Using X-ray computed tomography (CT) and contrast from tumor-accumulated gold nanorods, they were able to noninvasively image and three-dimensionally reconstruct tumor xenograft margins in nude mice models. Subsequent NIR PPTT achieved complete tumor resorption and 100% survival of the nanoparticle treated group (1 min, 0.75 W/cm^2 , 1 cm spot size) while tumors in untreated control groups grew uncontrolled with less than 1 month survival. In 2007, Xia and coworkers first demonstrated the use of gold nanocages for contrast in *in vitro* NIR PPTT.[55] Nanocages conjugated to antibodies of the human epidermal growth factor receptor 2 (HER2) were used to selectively target breast cancer cells overexpressing HER2 on their cell surface. Cell destruction using pulsed NIR laser exposure was observed at a minimum power density of 1.5 W/cm^2 (5 min, 2 mm spot size). Using similarly synthesized hollow-core, spherical gold nanoparticles, Li and coworkers have studied *in vitro* NIR PPTT using anti-EGFR conjugates of the hollow gold nanoparticles, as well as their *in vivo* biodistribution following intravenous administration[40] Squamous cell carcinoma cells, overexpressing EGFR, were found to be selectively labeled and photothermally destroyed using cw NIR laser exposure (5 min, 40 W/cm^2 , 2 mm spot size). Intravenous administration in tumor bearing nude mice resulted in predominant RES organ (i.e. liver, spleen, and kidney) accumulation. Tumor accumulation was found to be as high as 6.5% of the initial dose with predominant perivascular localization. Targeted NIR PPTT of melanoma tumors using hollow gold nanoparticles was further studied in animal models by the same group using an agonist ligand of a melanocortin type-1 receptor, overexpressed by melanoma cells.[38] Biodistribution studies following 24 h of intravenous circulation found significantly

enhanced tumor accumulation by the active targeting strategy (13% versus 5%). Histological analysis following NIR laser exposure (1 min, 0.5 W/cm², 1 cm spot size) determined a significantly enhanced necrotic response from nanoparticle treated tumors (66% versus 8% in control). Positron emission tomographic (PET) imaging also indicated dramatically decreased metabolic activity in nanoparticle treated tissues, but not in sham or control tumors. Xia and Wang have further demonstrated that the NIR absorption properties of nanocages and other plasmonic gold nanoparticles can be used to noninvasively image tumors for surgical or PPTT guidance, as well as to assess the stage and location of primary melanoma tumors *in vivo* by photoacoustic tomographic imaging.[56] Also using a ligand of the melanocortin type-1 receptor, they showed that systemically administered nanocages can be preferentially targeted to melanoma tumors, allowing about 40% enhanced imaging contrast and actively targeted tumor accumulation.

Determining the optimal gold nanostructure for NIR PPTT can be highly subjective due to the numerous ways in which such analyses can be performed. Structures can be compared based on their absorption cross sections, absorption efficiencies, or thermal transduction efficiencies on a per particle, per unit gold, per unit mass, or per unit extinction basis. Gold nanorods have been shown to exhibit much larger and narrower NIR absorption cross sections and efficiencies than either nanoshells or nanocages.[57, 58] Experiments comparing NIR thermal transduction from solutions of equivalent optical density (i.e. extinction) found gold nanorods and AuS₂-Au nanoshells to be much more efficient photothermal contrast agents than SiO₂-Au nanoshells.[58] Per unit mass gold, nanorods have exhibited 1/3 the spectral bandwidth, about 3-fold higher extinction

cross section, and 6 times greater heating capability than SiO₂-Au nanoshells in NIR laser photothermal experiments.[7]

1.4. Conclusions and Future Outlook

Gold nanoparticles present tremendous opportunities for the design of next-generation, multimodal anti-cancer treatment strategies. Due to their multivalency and functional versatility, these particle conjugates can exhibit increased targeting selectivity, augmented binding affinity, long circulatory half-life, high biocompatibility, rapid transport kinetics, and size-enhanced tumor uptake. The optical and electronic properties of gold nanoparticles can further provide high contrast in photothermal therapeutic treatments. The intrinsic biomolecular interactions of gold nanoparticles can additionally provide cancer-selective cytotoxic activity. Together, these properties comprise a highly multifunctional platform on which increasingly selective and potent oncologic treatment methods can be designed. These new nanotechnologies will ultimately aid in fighting the “War on Cancer,” now and in the future.

1.5. References

1. US National Institutes of Health. National Cancer Institute. Nanotechnology in Clinical Trials. Available at URL: <http://nano.cancer.gov/learn/now/clinical-trials.asp> (July 30, 2013).
2. Wang, A. Z., Langer, R., and Farokhzad, O. C. (2012) Nanoparticle delivery of cancer drugs, *Annual review of medicine* 63, 185-198.
3. Zhang, L., Gu, F. X., Chan, J. M., Wang, A. Z., Langer, R. S., and Farokhzad, O. C. (2008) Nanoparticles in medicine: therapeutic applications and developments, *Clinical pharmacology and therapeutics* 83, 761-769.
4. Giljohann, D. A., Seferos, D. S., Daniel, W. L., Massich, M. D., Patel, P. C., and Mirkin, C. A. (2010) Gold nanoparticles for biology and medicine, *Angewandte Chemie* 49, 3280-3294.
5. Ghosh, P., Han, G., De, M., Kim, C. K., and Rotello, V. M. (2008) Gold nanoparticles in delivery applications, *Advanced drug delivery reviews* 60, 1307-1315.
6. Niidome, T., Yamagata, M., Okamoto, Y., Akiyama, Y., Takahashi, H., Kawano, T., Katayama, Y., and Niidome, Y. (2006) PEG-modified gold nanorods with a stealth character for in vivo applications, *Journal of Controlled Release* 114, 343-347.
7. von Maltzahn, G., Park, J. H., Agrawal, A., Bandaru, N. K., Das, S. K., Sailor, M. J., and Bhatia, S. N. (2009) Computationally guided photothermal tumor therapy using long-circulating gold nanorod antennas, *Cancer Res* 69, 3892-3900.
8. Dickerson, E. B., Dreaden, E. C., Huang, X. H., El-Sayed, I. H., Chu, H. H., Pushpanketh, S., McDonald, J. F., and El-Sayed, M. A. (2008) Gold nanorod assisted near-infrared plasmonic photothermal therapy (PPTT) of squamous cell carcinoma in mice, *Cancer Lett.* 269, 57-66.
9. El-Sayed, I. H., Huang, X. H., and El-Sayed, M. A. (2006) Selective laser photothermal therapy of epithelial carcinoma using anti-EGFR antibody conjugated gold nanoparticles, *Cancer Letters* 239, 129-135.
10. Chen, J. Y., Glaus, C., Laforest, R., Zhang, Q., Yang, M. X., Gidding, M., Welch, M. J., and Xia, Y. (2010) Gold Nanocages as Photothermal Transducers for Cancer Treatment, *Small* 6, 811-817.

11. Hirsch, L. R., Stafford, R. J., Bankson, J. A., Sershen, S. R., Rivera, B., Price, R. E., Hazle, J. D., Halas, N. J., and West, J. L. (2003) Nanoshell-mediated near-infrared thermal therapy of tumors under magnetic resonance guidance, *Proceedings of the National Academy of Sciences of the United States of America* 100, 13549-13554.
12. Huff, T. B., Tong, L., Zhao, Y., Hansen, M. N., Cheng, J. X., and Wei, A. (2007) Hyperthermic effects of gold nanorods on tumor cells, *Nanomedicine (Lond)* 2, 125-132.
13. Jain, P. K., Lee, K. S., El-Sayed, I. H., and El-Sayed, M. A. (2006) Calculated absorption and scattering properties of gold nanoparticles of different size, shape, and composition: Applications in biological imaging and biomedicine, *J Phys Chem B* 110, 7238-7248.
14. El-Sayed, I. H., Huang, X. H., and El-Sayed, M. A. (2005) Surface plasmon resonance scattering and absorption of anti-EGFR antibody conjugated gold nanoparticles in cancer diagnostics: Applications in oral cancer, *Nano letters* 5, 829-834.
15. Boisselier, E., and Astruc, D. (2009) Gold nanoparticles in nanomedicine: preparations, imaging, diagnostics, therapies and toxicity, *Chem Soc Rev* 38, 1759-1782.
16. Wang, H. F., Huff, T. B., Zweifel, D. A., He, W., Low, P. S., Wei, A., and Cheng, J. X. (2005) In vitro and in vivo two-photon luminescence imaging of single gold nanorods, *Proceedings of the National Academy of Sciences of the United States of America* 102, 15752-15756.
17. Roa, W., Zhang, X., Guo, L., Shaw, A., Hu, X., Xiong, Y., Gulavita, S., Patel, S., Sun, X., Chen, J., Moore, R., and Xing, J. Z. (2009) Gold nanoparticle sensitize radiotherapy of prostate cancer cells by regulation of the cell cycle, *Nanotechnology* 20, 375101.
18. Lee, K., Lee, H., Bae, K. H., and Park, T. G. (2010) Heparin immobilized gold nanoparticles for targeted detection and apoptotic death of metastatic cancer cells, *Biomaterials* 31, 6530-6536.
19. Mukherjee, P., Bhattacharya, R., Wang, P., Wang, L., Basu, S., Nagy, J. A., Atala, A., Mukhopadhyay, D., and Soker, S. (2005) Antiangiogenic properties of gold nanoparticles, *Clin. Cancer. Res.* 11, 3530-3534.
20. Bhattacharya R., M. P., Xiong Z., Atala A., Soker S., Mukhopadhyay. (2004) Gold Nanoparticles Inhibit VEGF165-Induced Proliferation of HUVEC Cells, *Nano Lett.* 4, 2479-2481.

21. Faraday, M. (1857) *Philosophical transactions of the Royal Society of London. Series B, Biological sciences* 147, 145-181.
22. J. Turkevich, P. C. S., J. Hillier. (1951) *Discuss. Faraday Soc.*, 55-75.
23. Frens, G. (1973) Controlled nucleation for regulation of particle-size in monodisperse gold suspensions, *Nature (London), Phys. Sci.* 241, 20-22.
24. Gole, A., and Murphy, C. J. (2004) Seed-mediated synthesis of gold nanorods: Role of the size and nature of the seed, *Chem Mater* 16, 3633-3640.
25. Huang, X. H., Neretina, S., and El-Sayed, M. A. (2009) Gold Nanorods: From Synthesis and Properties to Biological and Biomedical Applications, *Advanced Materials* 21, 4880-4910.
26. Jana, N. R., Gearheart, L., and Murphy, C. J. (2001) Wet chemical synthesis of high aspect ratio cylindrical gold nanorods, *J Phys Chem B* 105, 4065-4067.
27. Ali, M. R. K., Snyder, B., and El-Sayed, M. A. (2012) Synthesis and Optical Properties of Small Au Nanorods Using a Seedless Growth Technique, *Langmuir* 28, 9807-9815.
28. Chen, J., McLellan, J. M., Siekkinen, A., Xiong, Y., Li, Z. Y., and Xia, Y. (2006) Facile synthesis of gold-silver nanocages with controllable pores on the surface, *J Am Chem Soc* 128, 14776-14777.
29. Skrabalak, S. E., Chen, J., Sun, Y., Lu, X., Au, L., Cobley, C. M., and Xia, Y. (2008) Gold nanocages: synthesis, properties, and applications, *Acc Chem Res* 41, 1587-1595.
30. Love, J. C., Estroff, L. A., Kriebel, J. K., Nuzzo, R. G., and Whitesides, G. M. (2005) Self-assembled monolayers of thiolates on metals as a form of nanotechnology, *Chem Rev* 105, 1103-1169.
31. Bard, A. J., and Faulkner, L. R. (2001) *Electrochemical methods : fundamentals and applications*, 2nd ed., Wiley, New York.
32. Tassa, C., Duffner, J. L., Lewis, T. A., Weissleder, R., Schreiber, S. L., Koehler, A. N., and Shaw, S. Y. (2010) Binding affinity and kinetic analysis of targeted small molecule-modified nanoparticles, *Bioconjugate chemistry* 21, 14-19.
33. Dreaden, E. C., Mwakwari, S. C., Sodji, Q. H., Oyelere, A. K., and El-Sayed, M. A. (2009) Tamoxifen-poly(ethylene glycol)-thiol gold nanoparticle conjugates: enhanced potency and selective delivery for breast cancer treatment, *Bioconjugate chemistry* 20, 2247-2253.

34. Kang, B., Mackey, M. A., and El-Sayed, M. A. (2010) Nuclear targeting of gold nanoparticles in cancer cells induces DNA damage, causing cytokinesis arrest and apoptosis, *J Am Chem Soc* 132, 1517-1519.
35. Lu, W., Zhang, G., Zhang, R., Flores, L. G., 2nd, Huang, Q., Gelovani, J. G., and Li, C. (2010) Tumor site-specific silencing of NF-kappaB p65 by targeted hollow gold nanosphere-mediated photothermal transfection, *Cancer Res* 70, 3177-3188.
36. Iyer, A. K., Khaled, G., Fang, J., and Maeda, H. (2006) Exploiting the enhanced permeability and retention effect for tumor targeting, *Drug discovery today* 11, 812-818.
37. Dreaden, E. C., Mackey, M. A., Huang, X., Kang, B., and El-Sayed, M. A. (2011) Beating cancer in multiple ways using nanogold, *Chem Soc Rev* 40, 3391-3404.
38. Lu, W., Xiong, C., Zhang, G., Huang, Q., Zhang, R., Zhang, J. Z., and Li, C. (2009) Targeted photothermal ablation of murine melanomas with melanocyte-stimulating hormone analog-conjugated hollow gold nanospheres, *Clinical cancer research : an official journal of the American Association for Cancer Research* 15, 876-886.
39. Choi, C. H., Alabi, C. A., Webster, P., and Davis, M. E. (2010) Mechanism of active targeting in solid tumors with transferrin-containing gold nanoparticles, *Proceedings of the National Academy of Sciences of the United States of America* 107, 1235-1240.
40. Melancon, M. P., Lu, W., Yang, Z., Zhang, R., Cheng, Z., Elliot, A. M., Stafford, J., Olson, T., Zhang, J. Z., and Li, C. (2008) In vitro and in vivo targeting of hollow gold nanoshells directed at epidermal growth factor receptor for photothermal ablation therapy, *Molecular cancer therapeutics* 7, 1730-1739.
41. Chithrani, B. D., Ghazani, A. A., and Chan, W. C. (2006) Determining the size and shape dependence of gold nanoparticle uptake into mammalian cells, *Nano Lett* 6, 662-668.
42. Jiang, W., Kim, B. Y., Rutka, J. T., and Chan, W. C. (2008) Nanoparticle-mediated cellular response is size-dependent, *Nature nanotechnology* 3, 145-150.
43. Longmire, M., Choyke, P. L., and Kobayashi, H. (2008) Clearance properties of nano-sized particles and molecules as imaging agents: considerations and caveats, *Nanomedicine (Lond)* 3, 703-717.
44. Owens, D. E., 3rd, and Peppas, N. A. (2006) Opsonization, biodistribution, and pharmacokinetics of polymeric nanoparticles, *International journal of pharmaceutics* 307, 93-102.

45. Cho, W. S., Cho, M., Jeong, J., Choi, M., Han, B. S., Shin, H. S., Hong, J., Chung, B. H., Jeong, J., and Cho, M. H. (2010) Size-dependent tissue kinetics of PEG-coated gold nanoparticles, *Toxicology and applied pharmacology* 245, 116-123.
46. Link, S., and El-Sayed, M. A. (2003) Optical properties and ultrafast dynamics of metallic nanocrystals, *Annual review of physical chemistry* 54, 331-366.
47. Bert H., P. W., Olaf A., Annette D., Geetha S., Thoralf K., Roland F., Hanno R. (2002) *Crit. Rev. Oncol./Hematol.* 43, 33-56.
48. Dickerson, E. B., Dreaden, E. C., Huang, X., El-Sayed, I. H., Chu, H., Pushpanketh, S., McDonald, J. F., and El-Sayed, M. A. (2008) Gold nanorod assisted near-infrared plasmonic photothermal therapy (PPTT) of squamous cell carcinoma in mice, *Cancer Lett* 269, 57-66.
49. Weissleder, R. (2001) A clearer vision for in vivo imaging, *Nature biotechnology* 19, 316-317.
50. Pitsillides, C. M., Joe, E. K., Wei, X., Anderson, R. R., and Lin, C. P. (2003) Selective cell targeting with light-absorbing microparticles and nanoparticles, *Biophys J* 84, 4023-4032.
51. El-Sayed, I. H., Huang, X., and El-Sayed, M. A. (2006) Selective laser photothermal therapy of epithelial carcinoma using anti-EGFR antibody conjugated gold nanoparticles, *Cancer Lett* 239, 129-135.
52. Hirsch, L. R., Stafford, R. J., Bankson, J. A., Sershen, S. R., Rivera, B., Price, R. E., Hazle, J. D., Halas, N. J., and West, J. L. (2003) Nanoshell-mediated near-infrared thermal therapy of tumors under magnetic resonance guidance, *Proceedings of the National Academy of Sciences of the United States of America* 100, 13549-13554.
53. O'Neal, D. P., Hirsch, L. R., Halas, N. J., Payne, J. D., and West, J. L. (2004) Photo-thermal tumor ablation in mice using near infrared-absorbing nanoparticles, *Cancer Lett* 209, 171-176.
54. Huang, X., El-Sayed, I. H., Qian, W., and El-Sayed, M. A. (2006) Cancer cell imaging and photothermal therapy in the near-infrared region by using gold nanorods, *J Am Chem Soc* 128, 2115-2120.
55. Chen, J., Wang, D., Xi, J., Au, L., Siekkinen, A., Warsen, A., Li, Z. Y., Zhang, H., Xia, Y., and Li, X. (2007) Immuno gold nanocages with tailored optical properties for targeted photothermal destruction of cancer cells, *Nano Lett* 7, 1318-1322.

56. Kim, C., Cho, E. C., Chen, J., Song, K. H., Au, L., Favazza, C., Zhang, Q., Cobley, C. M., Gao, F., Xia, Y., and Wang, L. V. (2010) In vivo molecular photoacoustic tomography of melanomas targeted by bioconjugated gold nanocages, *ACS Nano* 4, 4559-4564.
57. Hu, M., Chen, J., Li, Z. Y., Au, L., Hartland, G. V., Li, X., Marquez, M., and Xia, Y. (2006) Gold nanostructures: engineering their plasmonic properties for biomedical applications, *Chem Soc Rev* 35, 1084-1094.
58. Cole J.R., M. N. A., Knight M.W., Goodrich G.P., Halas N.J. (2009) *J. Phys. Chem. C* 113, 12090-12094.

CHAPTER 2

DETAILED EXPERIMENTAL METHODS

2.1. Methods of Gold Nanoparticle Design

2.1.1. Gold Nanospheres

Spherical gold nanoparticles are synthesized via citrate reduction of HAuCl_4 , as developed by Frens[1] Briefly, 50 mL of a 0.01% (w/v) HAuCl_4 aqueous solution is brought to a boil, while stirring, followed by addition of a trisodium citrate aqueous solution. For gold nanospheres with about a 30 nm diameter and a surface plasmon resonance at about 530 nm (shown in Figure 2.1A), 1 mL of 1% (w/v) trisodium citrate is added to the HAuCl_4 solution, while for those 15 nm in diameter and a surface plasmon resonance at about 520 nm (shown in Figure 2.1B), 1 mL of 2% trisodium citrate (w/v) is added. Reaction completion is determined by the color changing from clear to a deep red/purple. The AuNSs are then purified by centrifugation at 6000 rpm for 15 min and redispersed in water.

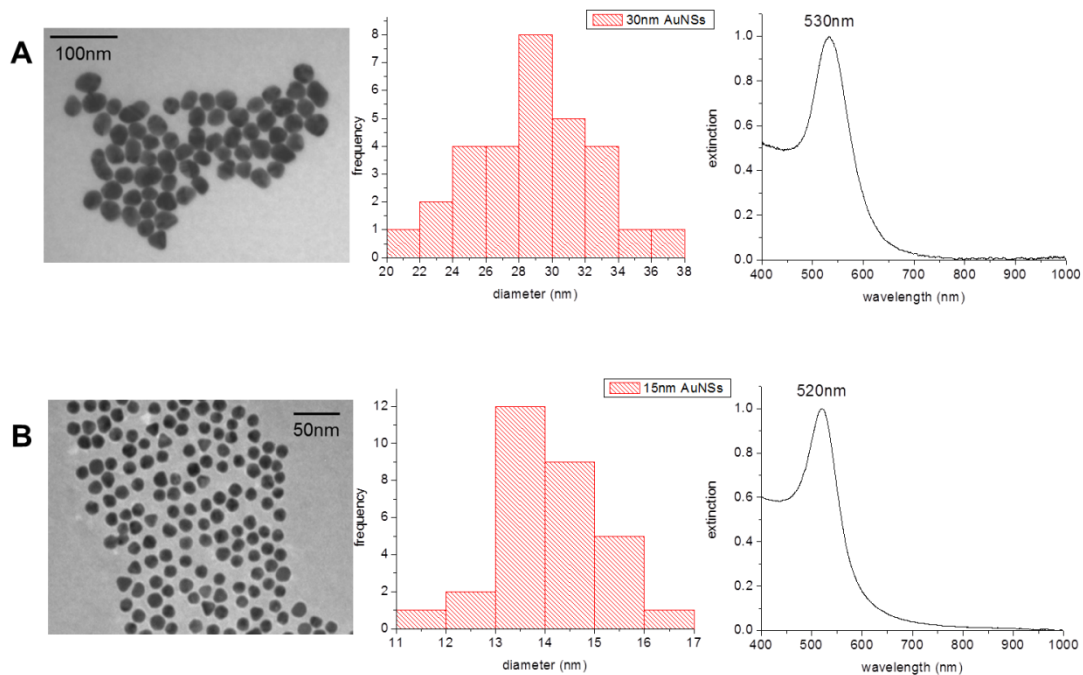


Figure 2.1. Gold nanospheres synthesized via citrate reduction of HAuCl_4 . TEM images (left), size distribution histograms (middle) and UV-Vis spectrum (right) of 30 nm AuNSs (A) and 15 nm AuNSs (B).

2.1.2. Gold Nanocages

Gold nanocages (AuNCs), with a wall length of about 40 nm, are synthesized via galvanic replacement reaction with silver nanocubes as a template, where silver atoms of a silver nanocube template are oxidized by Au^{3+} , which is subsequently reduced and deposited onto the surface of the template.[2] The silver nanocube template is prepared by a previously reported method.[3] Briefly, 70 mL of ethylene glycol (EG) is heated to 150°C for 1 h, followed by the addition of polyvinyl pyrrolidone (PVP, MW 55,000; 0.82 g dissolved in 5 mL EG). While still at 150°C , 0.7 mL of a 3 mM sodium sulfide solution (in EG) is added, followed by slow injection of 4 mL of a silver nitrate solution (0.48 g dissolved in 10 mL EG). [4, 5] The reaction is allowed to proceed to completion (10-15

min) resulting in the reduction of silver ions to silver nanocubes. The silver nanocubes are purified by adding a 1:2 acetone/water mixture at a volume two times that of the nanocube solution, centrifuging at 14,000 rpm for 5 min and redispersing the precipitate in 200 mL of DI water. The silver nanocube solution is brought to a boil under reflux, after which a 10 mg/L hydrogen tetrachloroaurate (HAuCl_4) solution is slowly injected and the UV-Vis spectrum of the solution is monitored until the absorption maximum redshifts from ca. 440 nm (silver nanocubes) to ca. 600 nm. Once the initial peak shift is observed, a 1 mg/L $\text{HAuCl}_4 \cdot 3\text{H}_2\text{O}$ solution is added drop wise until the peak redshifts and remains constant at desired the wavelength. Addition of the dilute HAuCl_4 solution causes a decrease in silver content (remaining silver on the inner cavity of the AuNC) due to the replacement of silver atoms with gold atoms.[4] Figure 2.2 displays the UV-Vis spectra for various AuNCs (A-C) after increasing addition of HAuCl_4 . The TEM images, as well as the schematic show the structure of these AuNCs. The AuNCs are then purified by centrifugation at 14,000 rpm for 5 min and redispersed in water.

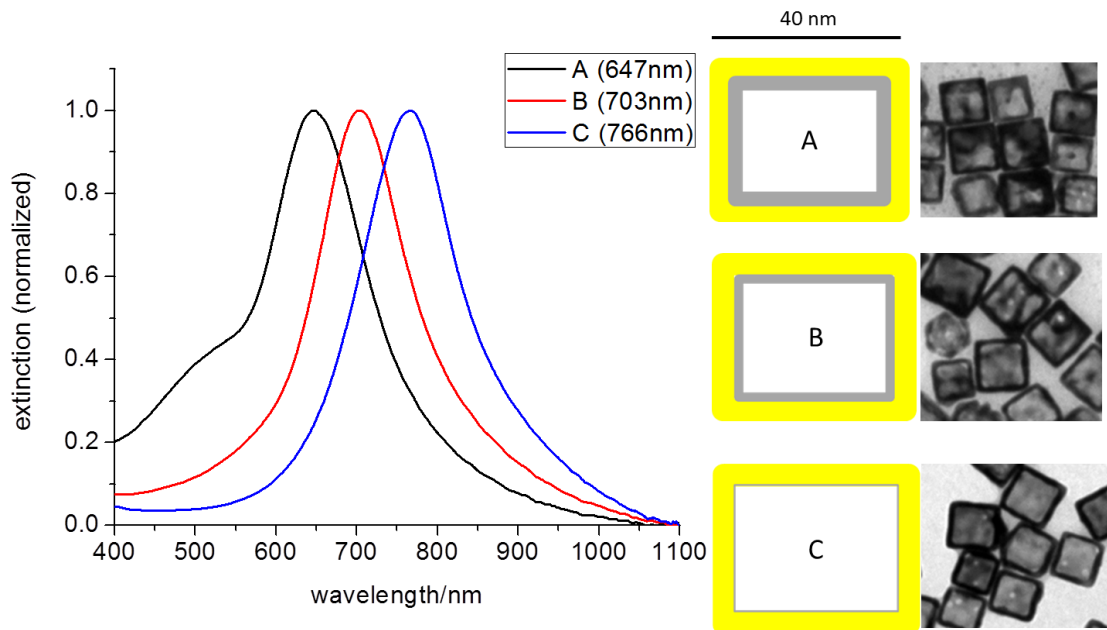


Figure 2.2. Gold nanocages synthesized via galvanic replacement. UV-Vis spectra (left), schematic (middle) and TEM images (right) of AuNCs with about a 40 nm wall length and increasing addition of Au salt (from A to C).

2.1.3. Gold Nanorods

2.1.3.1. Seed-Mediated Growth Method

Relatively large gold nanorods (AuNRs) are synthesized via the seed-mediated growth method.[6] A schematic representation of this method is shown in Figure 2.3. Briefly, a seed solution consisting of 7.5 mL of 0.2 M CTAB, 2.5 mL of 1.0 mM HAuCl₄ and 600 μ L 0.01 M NaBH₄ is prepared, followed by a growth solution containing 100 mL of 1.0 mM HAuCl₄, 100 mL of 0.2 M CTAB, 5 mL of 4.0 mM silver nitrate and 1.4 mL of 78.8 mM ascorbic acid. A 240 μ L volume of the seed solution is added to the growth solution, producing AuNRs approximately 38 nm in length and 11 nm in width, as displayed in Figure 2.4. The surface plasmon resonance (SPR) of these AuNRs is around 740 nm. These CTAB-stabilized AuNRs are purified by centrifugation at 14,000 rpm for 5 min and redispersed in DI water.

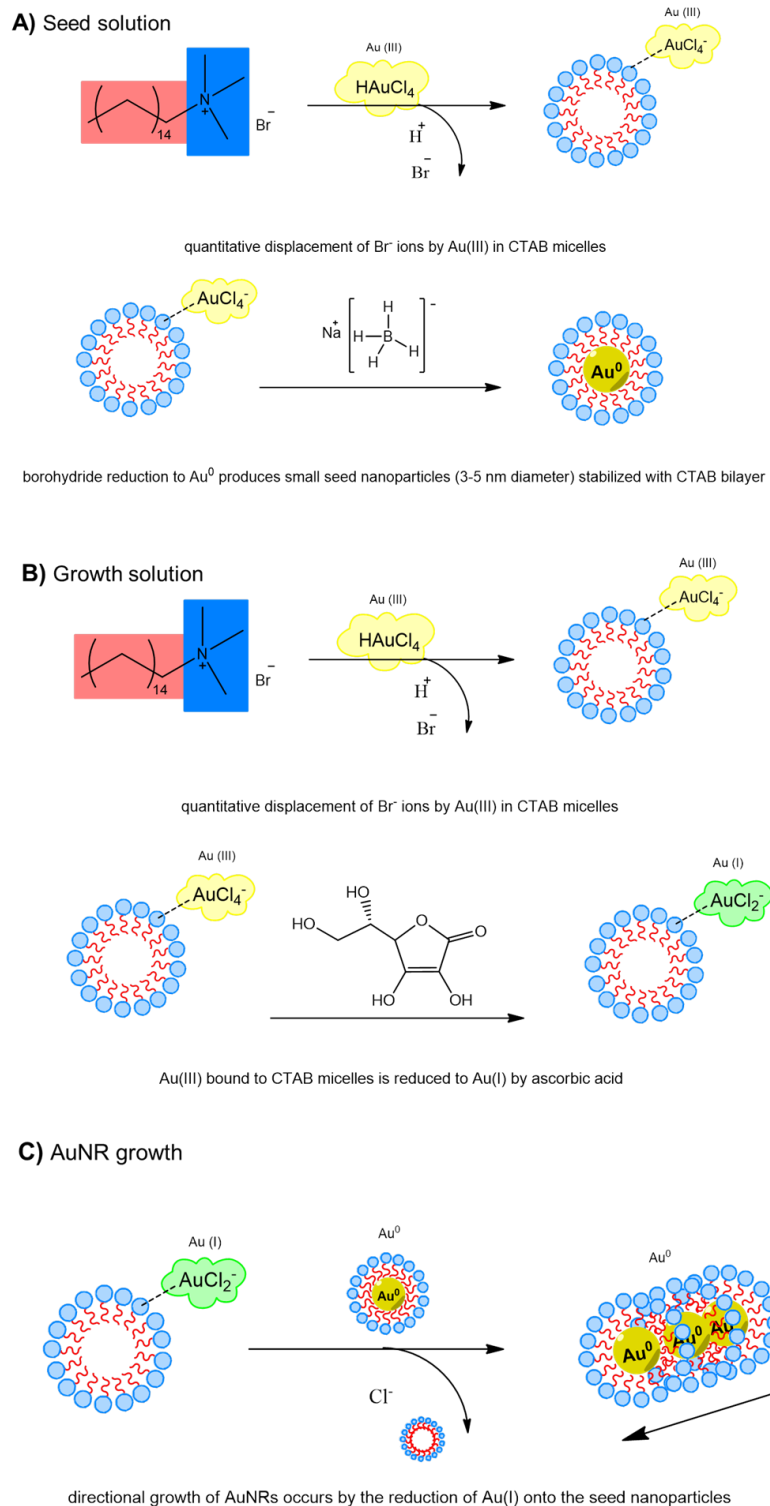


Figure 2.3. Schematic representation of AuNR synthesis via seed-mediated growth. The three main steps involved are the preparation of a seed solution (A), preparation of a growth solution (B) and growth of AuNRs by the addition of the seed to growth solution (C).

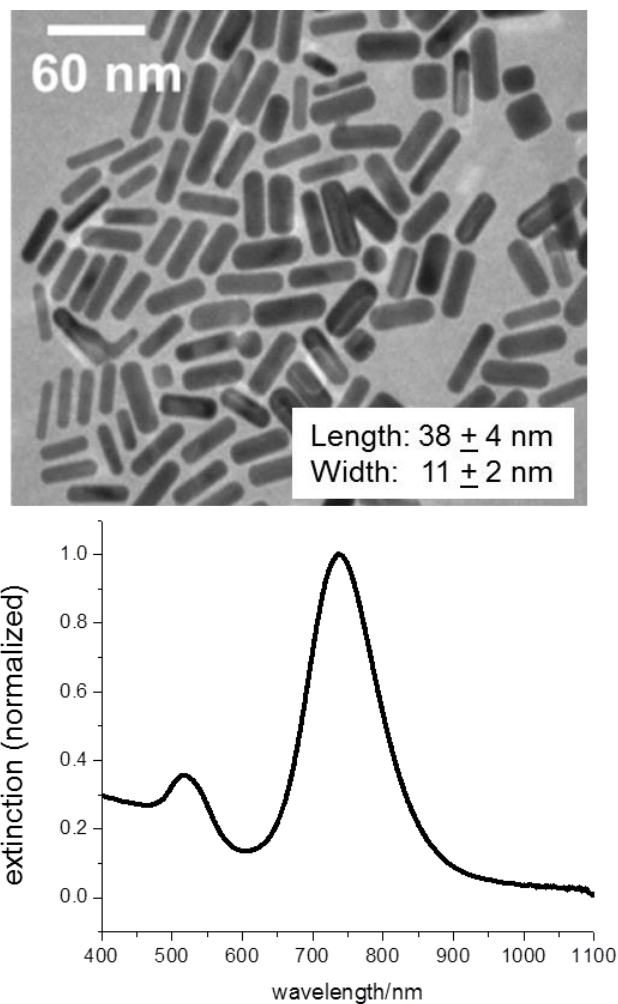


Figure 2.4. TEM image (top) of 38 x 11 nm AuNRs synthesized by seed-mediated growth. UV-Vis spectrum (bottom) showing these AuNRs have a surface plasmon resonance around 740 nm. Scale bar: 60 nm.

2.1.3.2. Seedless Growth Method

Relatively small AuNRs are synthesized by a seedless growth method.[7] A schematic representation of this method is shown in Figure 2.5. In this method, the growth solution is kept at an acidic pH and sodium borohydride is added instead of a seed solution, for simultaneous seed formation and AuNR growth. To obtain AuNRs

approximately 28 nm in length and 8 nm in width, shown in Figure 2.6, 300 μL of 0.01 M NaBH_4 was prepared and added to an acidic growth solution containing 160 μL of 37% HCl , 100 mL of 1.0 mM HAuCl_4 , 100 mL of 0.2 M CTAB, 5 mL of 4.0 mM silver nitrate and 1.4 mL of 78.8 mM ascorbic acid. The SPR of these AuNRs is around 770 nm. These CTAB-stabilized AuNRs were also purified by centrifugation at 14,000 rpm for 5 min and redispersed in DI H_2O .

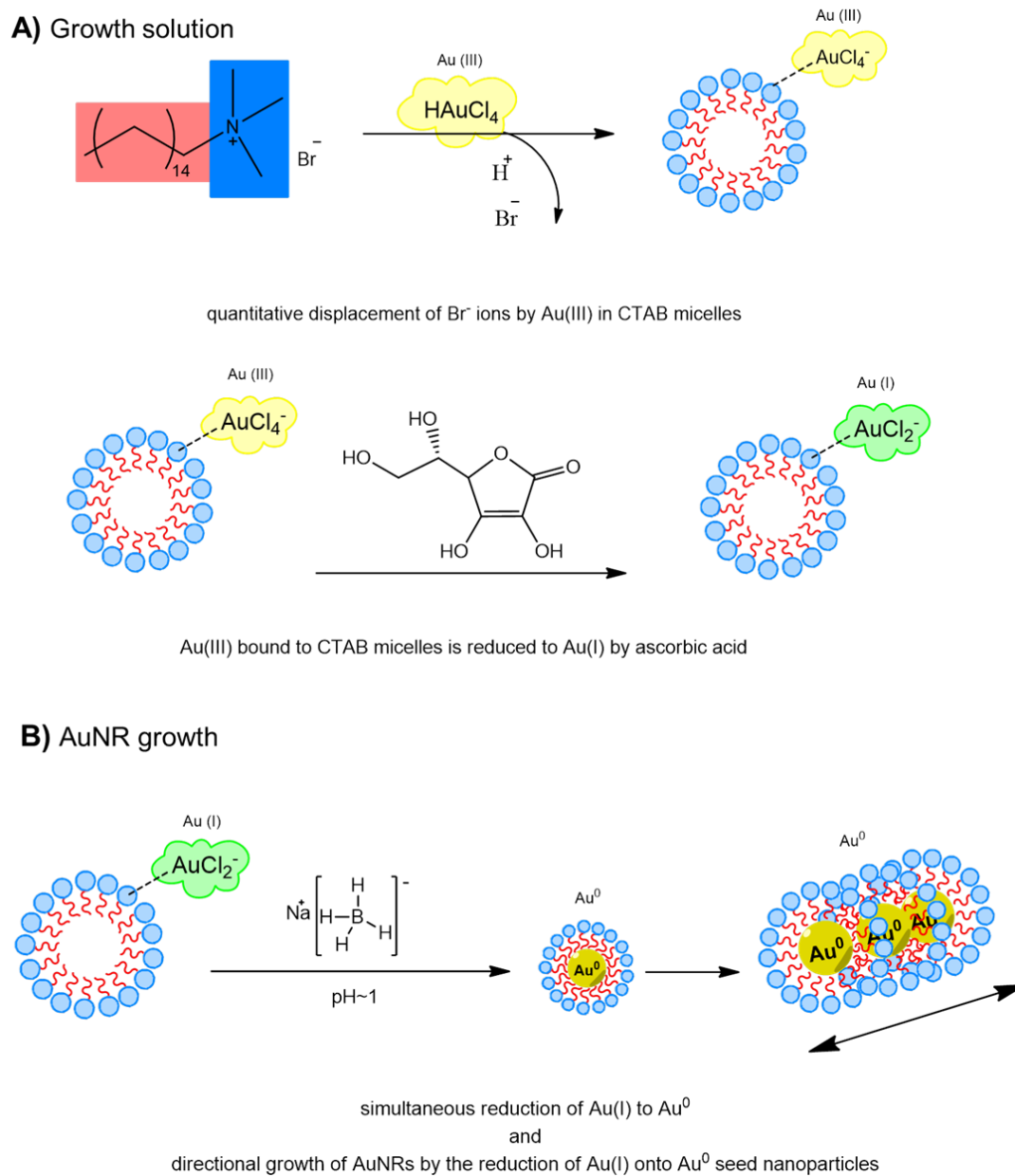


Figure 2.5. Schematic representation of AuNR synthesis via seedless growth. The two main steps involved are the preparation of a growth solution (A) and growth of AuNRs by the addition of sodium borohydride to the growth solution (B).

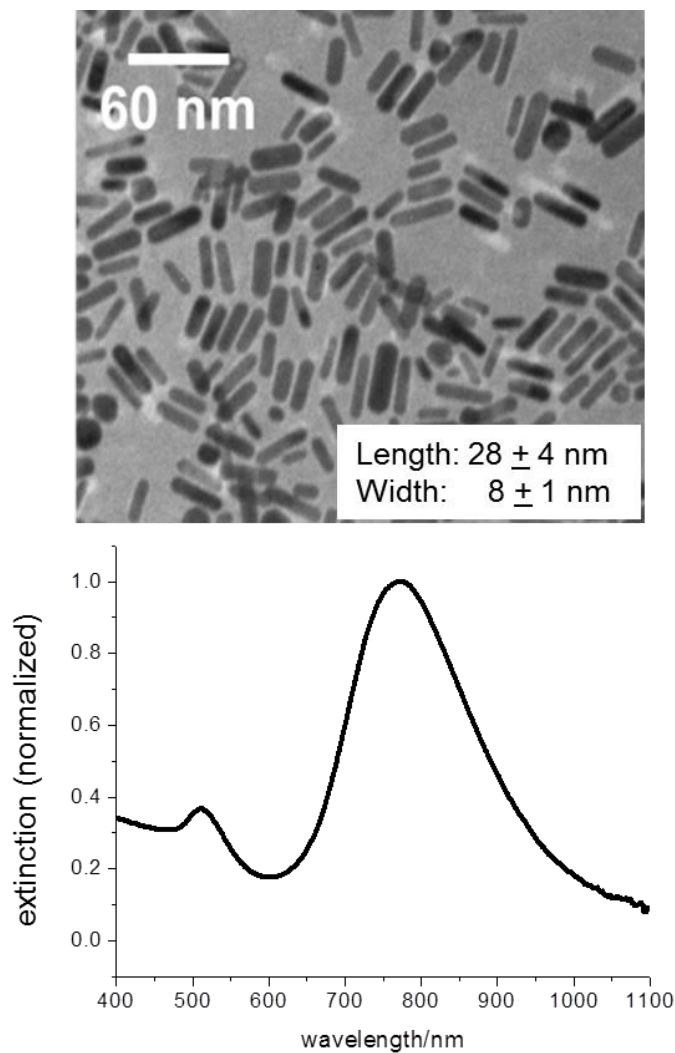


Figure 2.6. TEM image (top) of 28 x 8 nm AuNRs synthesized by seedless growth. UV-Vis spectrum (bottom) showing these AuNRs have a surface plasmon resonance around 770 nm. Scale bar: 60 nm.

2.1.4. Gold Nanoparticle Functionalization

Gold nanoparticles can be easily functionalized with sulfhydryl (SH) containing ligands through a gold-sulfur (Au-S) covalent bond. Formation of the Au-S bond occurs through creation of a thiyl radical via deprotonation of the SH group. The Au-S covalent bond is very strong, having a bond strength of around 44 kcal/mol (184 kJ/mol).[8] The presence of sulfhydryl groups on many different biocompatible molecules, including

polymers and peptides, allows for the facile attachment of biologically relevant compounds to the gold nanoparticle surface, as discussed below.

2.1.4.1. Conjugation with polyethylene glycol

Gold nanoparticles, of all types, are stabilized with thiol-terminated methoxy polyethylene glycol (mPEG-SH, MW 5000, Laysan Bio, Inc.) through a Au-S bond. This is done in order to prevent nonspecific adsorption of proteins to the particles in a physiological environment. A 1 mM aqueous solution of mPEG-SH is added to AuNPs at 10^4 molar excess, and left overnight. Particles are then purified by centrifugation and resuspended in water.

2.1.4.2. Conjugation with peptides

After PEGylation gold nanoparticles are further conjugated with custom peptides purchased from GenScript USA, Inc. Specifically, an RGD (CGPDGRDGRDGRDGR) peptide and an NLS (CGGGPKKKRKVGG) peptide, both with C-terminal amidation, were used in this work. Conjugation of peptides was achieved by addition of a 5 mM aqueous solution of peptide to the PEG-coated nanoparticles at 1×10^4 molar excess of NLS peptides and 8×10^3 molar excess of RGD peptides for 24 h, after which the peptide conjugated nanoparticles were centrifuged and redispersed in water. The hydrodynamic diameter of the peptide-conjugated gold nanoparticles was determined using dynamic light scattering (DLS). Further confirmation that the nanoparticle surface was modified during conjugation of PEG and peptides was achieved through zeta potential measurements.

2.2. Cell Biology and Imaging Methods

2.2.1. Cell Culture

Human oral squamous cell carcinoma (HSC-3) cells were utilized in this work as the malignant cell line and human keratinocytes (HaCat) were utilized in this work as the non-malignant (healthy) cell line. Both cell lines were maintained in Dulbecco's Modification of Eagle's Medium (DMEM, Mediatech, Cat# 10-013-CV), supplemented with 10% v/v fetal bovine serum (FBS, Mediatech, Cat# 35-010-CV) and 1% v/v antibiotic-antimycotic solution (Mediatech, Cat# 30-004-CI). Cells were grown in a 37°C, 5% CO₂ humidified incubator.

2.2.2 Intracellular Localization and Nanoparticle Uptake

2.2.2.1. Dark Field Imaging of Fixed cells

Cells are grown on 18 mm diameter glass coverslips (in bottom of well in 12-well tissue culture plate) overnight and incubated with gold nanoparticle solutions in culture medium for desired treatment time. After incubation, coverslips are rinsed with PBS buffer and fixed with 500 µL of 4% paraformaldehyde for 15 min. The coverslip is then placed on another coverslip containing a small drop of glycerin, and sealed with nail polish. Dark field images are taken using an inverted Olympus IX70 microscope utilizing a dark field condenser (U-DCW). A 100x/1.35 oil Iris objective (UPLANAPO) is used to collect the scattered light from the samples to produce the dark field images.

For I2/KI etching, cells are grown on 18 mm diameter glass coverslips (in bottom of well in 12-well plate) and incubated with gold nanoparticle solutions in culture medium

for desired treatment time. The nanoparticle-containing medium was removed and the cells are washed with PBS buffer. In order to remove nanoparticles that have not been internalized by the cells, a previously developed etching method is used.[9] Briefly, 1 mL of an aqueous solution containing a 1:6 molar ratio mixture of I₂ (0.34 mM) and KI is added to the cells and removed after 5 min. The coverslips are then washed with deionized water and placed on another coverslip containing a small drop of glycerin, followed by sealing with nail polish. The cells are then fixed with 500 μ L 4% paraformaldehyde for 15 min and dark field light scattering images are taken.

2.2.2.2. Live-Cell Dark Field Imaging

A homemade setup was modified based on an inverted Olympus IX70 microscope.[10] The incident white light emitted from the Fiber-Lite MI-150 Illuminator (Dolan-Jenner Industries) is delivered with an optical fiber and is focused into a tiny spot on the focal plane of the microscope objective by a condenser lens at the end of the optical fiber. The angle of the illuminating light is adjusted to prevent the incident illuminating light from entering the light collection cone of the microscope objective. A schematic representation of the setup is shown in Figure 2.7. The sample, nanoparticle-treated cells grown in the 35 mm culture plate, is placed in the homemade environmental mini cell chamber, which is mounted on the stage of the microscope. The environmental parameters inside the chamber, such as temperature, carbon dioxide concentration, and humidity, are well controlled. A long working distance 40x objective is used to collect only the scattered illuminating light from the sample. The dark field pictures are taken using the Nikon D200 digital camera automatically with an interval time of 2 min.

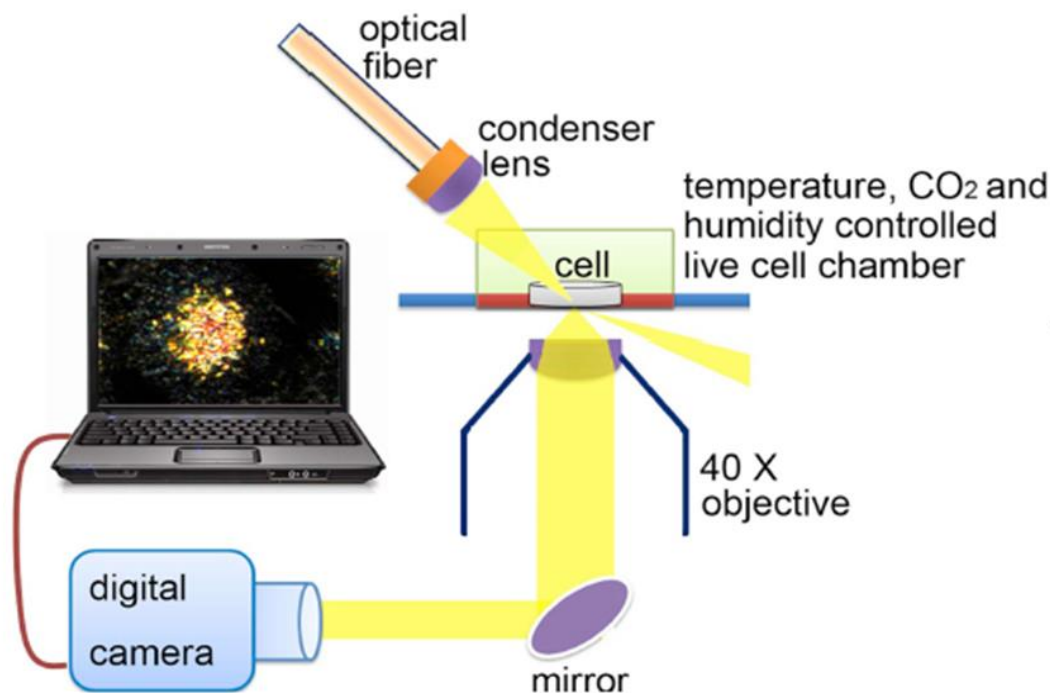


Figure 2.7. Schematic representing the homemade setup for live-cell dark field imaging of cells treated with gold nanoparticles. A dark field light scattering imaging microscope with a side-illumination arrangement is combined with an environmental cell incubation chamber for real time studies of live cells.

2.2.2.3. Nuclear Localization with Confocal Imaging

The nuclear-targeting of fluorescently-labeled gold nanoparticles can be visualized using confocal imaging. A simple way to fluorescently-label the gold nanoparticles, is to conjugate them with a FITC-PEG-SH (Nanocs, Inc. Cat. No. PG1-FC-5k) instead of PEG, prior to peptide conjugation (see Section 2.1.4). After nanoparticle functionalization with a FITC-PEG and peptides, cells are prepared for confocal imaging. Briefly, cells are grown on 18 mm diameter glass coverslips (in bottom of well in 12-well tissue culture plate) overnight and incubated with FITC-AuNP-containing culture medium for desired treatment time. After desired treatment time, the nanoparticle-containing media is removed and the cells are washed with PBS. Cells are then fixed with

500 μL of 4% paraformaldehyde for 15 min. In order to visualize the cell nuclei with confocal imaging, the nuclei must also be fluorescently-labeled. Therefore, the paraformaldehyde is removed, coverslips are washed with PBS, and 500 μL of 120 nM DAPI (4',6-Diamidino-2-phenylindole) (Life Technologies, Inc. Cat. No. C1306) is added. The plate is swirled gently for ~ 1 min, to allow for homogeneous staining of the cells on the coverslip, after which, the coverslip is rinsed with water 3 times. The coverslip is then placed on a microscope slide containing a small drop of 30% glycerin, sealed with nail polish and stored at 4°C until analysis. Fluorescence images are taken by multiphoton confocal microscopy using the Zeiss LSM 510 NLS META with 785 (DAPI) and 488 nm (FITC) excitation sources (IBB Core Facilities, Georgia Tech, contact Andrew Shaw).

2.2.2.4. Spectrophotometric Measurements of Relative Uptake

The relative uptake of nanoparticles can be spectrophotometrically measured. Cells are plated in a 96-well tissue culture plate and allowed to grow for 24 h. The culture media is then removed and replaced with 100 μL of culture medium containing gold nanoparticles. Figure 2.8 shows an example of the plate configuration.

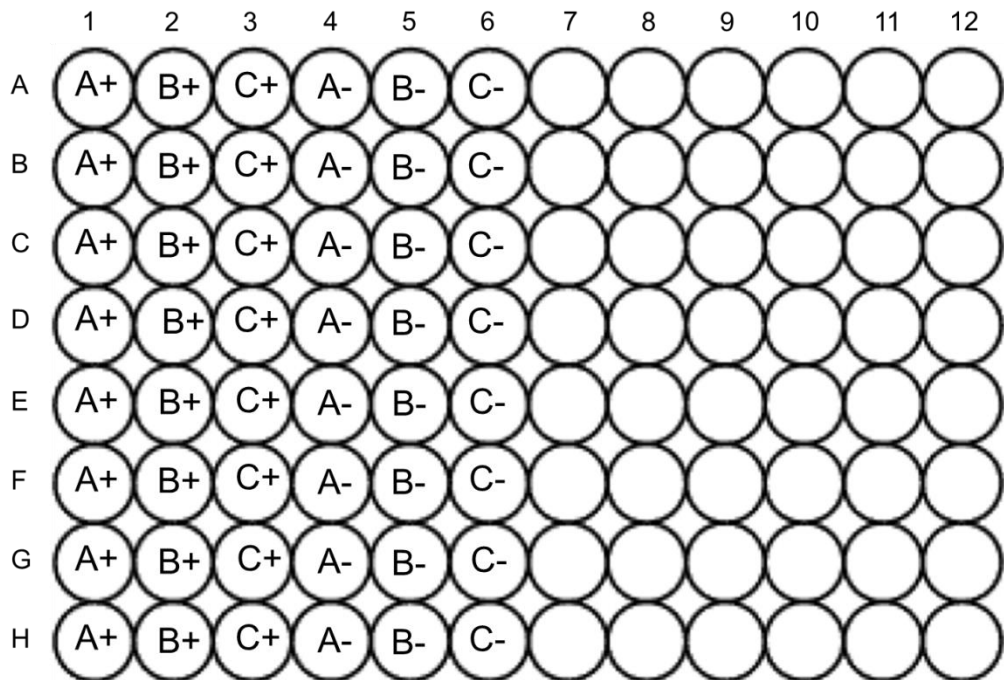


Figure 2.8. Example of 96-well plate configuration when treating cells for uptake. Wells 1/A-H contain cells and are loaded with 100 μL of cell culture medium containing nanoparticle A (A+). Wells 2/A-H contain cells and are loaded with 100 μL of cell culture medium containing gold nanoparticle B (B+). Wells 3/A-H contain cells and are loaded with 100 μL of cell culture medium containing gold nanoparticle C (C+). Wells 4-6/A-H do not contain cells and are loaded with 100 μL of cell culture medium containing gold nanoparticles A, B, and C (A-, B-, C-, respectively).

Cells (or wells containing no cells) are then incubated with nanoparticles for desired treatment time (*e.g.* 24, 48, 72 h). After desired incubation period with gold nanoparticles, 75 μL of the gold nanoparticle-containing media is removed and placed into new cell-free wells of the 96-well plate. Figure 2.9 shows an example of the plate configuration at this step.

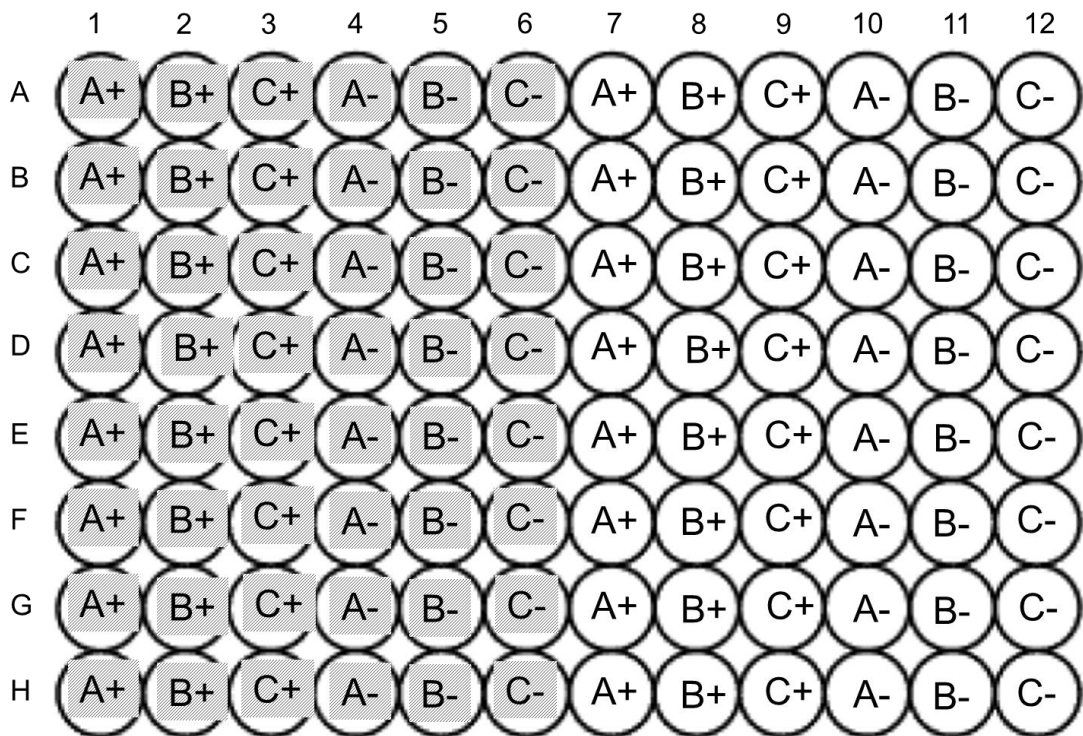


Figure 2.9. Example of 96-well plate configuration after transferring gold nanoparticle containing medium to new wells. Gray wells represent those that originally contained gold nanoparticles. White wells represent the 75 μ L of nanoparticle containing transferred from the original wells.

The optical density of the nanoparticle containing cell culture medium (wells 7-12/A-H in Fig. 2.9) is measured with a Biotek Synergy H4 multi-mode plate reader (IBB, Georgia Tech, contact Andrew Shaw). In the plate reader software, the settings are set to record absorbance of each well at the plasmon absorption wavelengths of each nanoparticle tested. After absorbance values (optical densities) are collected, data is exported to Microsoft Excel for further analysis. Once the data is exported to Excel, the recorded optical densities of wells A+, B+, and C+ are subtracted from the recorded optical densities of wells A-, B-, and C-, respectively (*i.e.* optical density of gold nanoparticle containing medium representing zero uptake). These values are then converted to an actual number of nanoparticles, or moles, to give the number of

nanoparticles taken up cells. The percentage of nanoparticle uptake can then be calculated by dividing the number of nanoparticles taken up by number of nanoparticles initially added (*i.e.* the number of nanoparticles present in wells A-, B-, and C-).

2.2.3. Cell Viability Assays

2.2.3.1. Mitochondrial Activity (XTT)

Mitochondrial activity (*i.e.* the mitochondrial respiratory chain) can be used for quantitative measurements of viable cells present in cell culture. During cellular respiration, the succinate dehydrogenase system is active, rendering succinate dehydrogenase activity as an ideal candidate for the measurement of cell viability. XTT (2,3-bis[2-methoxy-4-nitro-5-sulfopheny]-2H-tetrazolium-5-carboxyanilide inner salt) is a tetrazolium salt that can be cleaved/reduced by succinate dehydrogenase in the presence of an electron coupling reagent (PMS (N-methyl dibenzopyrazine methyl sulfate)) in the cell. Once cleaved/reduced, a formazan product is formed. This formazan is water-soluble and orange in color. The formazan can be spectrophotometrically measured at 450 nm and its absorbance is directly proportional to the number of viable cells present in the cell culture.[11-13]

Cells are plated in a 96-well tissue culture plate and allowed to grow for 24 h. The culture media is then removed and replaced with 100 μ L of culture medium containing the desired treatment. Figure 2.10 shows an example of the plate configuration.

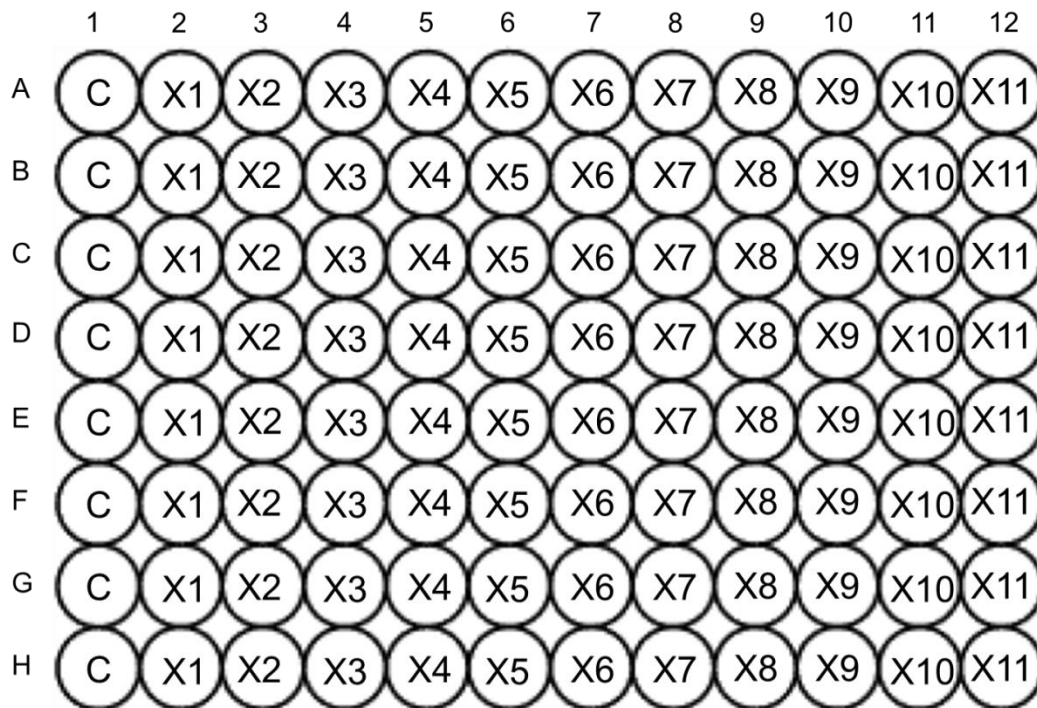


Figure 2.10. Example of 96-well plate configuration when treating cells for cell viability assay. Wells 1/A-H are loaded with 100 μ L of cell culture medium (C). Wells 2/A-H are loaded with 100 μ L of cell culture medium containing lowest concentration of treatment (X1). Wells 3-12/A-H are loaded with 100 μ L of cell culture medium containing increased concentrations of treatment (X2-X12).

Cells are then incubated with treatment for desired treatment time (*e.g* 24, 48, 72 h). Following treatment, the culture media is removed and cells are washed with 100 μ L of PBS. Immediately following this washing step, the XTT solution is added to each well at a volume of 125 μ L (a total volume of 12 mL for a 96-well plate). The 12 mL XTT solution is composed of 10.8 mL DMEM (without phenol red, supplemented with 10% FBS, and 1% antibiotic/antimycotic solution) and 1.2 mL of activated XTT reagent (Biotium, Inc. Cat. No. 30007). The activated XTT reagent is composed of 6 μ L of the electron coupling reagent (activation reagent) and 1.2 mL of the XTT reagent (ratio of XTT volume:PMS volume is 200). Upon addition of the XTT solution to the cells, the plate is returned to the incubator for 6-12 h. During the incubation period, succinate

dehydrogenases, active in viable cells, reduce the XTT (tetrazolium salt) into an orange formazan. Figure 2.11 shows an example of what the plate looks like after reduction of XTT by viable cells in a control (untreated) sample of cells (column C) as well as that of cells treated with increasing concentrations of a cytotoxic agent (columns X1-X8). It is clear, by visual inspection of the orange color intensity, that as the concentration of the cytotoxic agent is increased, the cell viability is decreased.

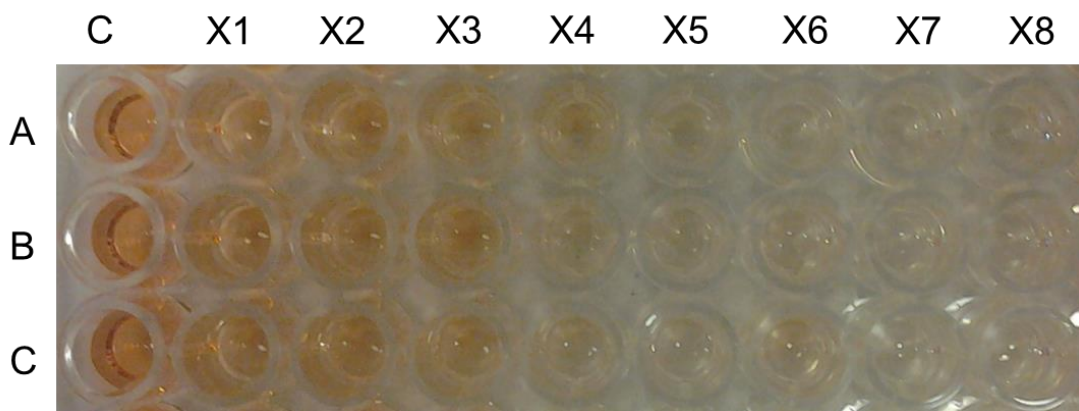


Figure 2.11. Example of 96-well plate after incubating treated cells with XTT. Wells C/A-C contain cells that were not treated with the cytotoxic agent and demonstrate the highest intensity of orange color (*i.e.* formazan produced by reduction of XTT by succinate dehydrogenases in viable cells). Wells X1-X8/A-C contain cells that were treated with increasing concentrations of the cytotoxic agent and demonstrate a gradual decrease in intensity of orange color, which indicates a decrease in the number of viable cells present.

In order to quantify the intensity of the orange formazan, the absorbance signal is measured spectrophotometrically with a Biotek Synergy H4 multi-mode plate reader (IBB Core Facilities, Georgia Tech, contact Andrew Shaw). In the plate reader software, the settings are set to record absorbance of each well at 450 and 690 nm, with the pathlength correction option selected. With the pathlength correction enabled, the microplate reader automatically calculates the pathlength of each sample (instead of

assuming 1 cm), thereby correcting the measured absorbance values accordingly. After corrected absorbance values are collected, data is exported to Microsoft Excel for further analysis. Figure 2.12 shows an example of how the data appears in Excel.

	1	2	3	4	5	6	7	8	9	10	11	12	
A	2.409	1.022	0.718	0.652	0.549	0.439	0.399	0.377	0.38	0.385	2.223	2.645	Corrected [450]
B	2.722	1.39	1.311	1.217	0.645	0.431	0.427	0.429	0.384	0.381	2.631	2.655	Corrected [450]
C	2.666	1.189	1.231	0.941	0.81	0.498	0.426	0.389	0.395	0.374	2.568	2.648	Corrected [450]
D	2.612	1.231	1.127	1.271	0.622	0.474	0.53	0.394	0.393	0.373	2.561	2.605	Corrected [450]
E	2.633	1.207	1.184	1.076	0.627	0.453	0.617	0.365	0.37	0.373	2.618	2.812	Corrected [450]
F	2.35	0.934	1.24	0.789	0.494	0.389	0.385	0.373	0.362	0.365	2.613	2.735	Corrected [450]
G	1.987	1.103	1.141	0.636	0.448	0.4	0.389	0.377	0.373	0.377	2.618	2.764	Corrected [450]
H	2.485	0.765	0.726	0.595	0.434	0.395	0.409	0.379	0.355	0.355	2.577	3.026	Corrected [450]
	1	2	3	4	5	6	7	8	9	10	11	12	
A	0.175	0.149	0.139	0.133	0.143	0.143	0.14	0.135	0.141	0.145	0.148	0.172	Corrected [690]
B	0.203	0.163	0.16	0.18	0.152	0.142	0.146	0.14	0.138	0.138	0.184	0.183	Corrected [690]
C	0.198	0.157	0.16	0.18	0.185	0.138	0.14	0.139	0.136	0.133	0.183	0.184	Corrected [690]
D	0.193	0.159	0.16	0.208	0.157	0.138	0.146	0.138	0.137	0.134	0.181	0.18	Corrected [690]
E	0.187	0.164	0.158	0.181	0.15	0.138	0.141	0.137	0.137	0.139	0.191	0.235	Corrected [690]
F	0.165	0.159	0.153	0.144	0.144	0.137	0.136	0.137	0.135	0.143	0.198	0.257	Corrected [690]
G	0.164	0.16	0.156	0.155	0.141	0.138	0.136	0.136	0.132	0.142	0.195	0.223	Corrected [690]
H	0.172	0.136	0.143	0.146	0.133	0.136	0.139	0.138	0.127	0.129	0.184	0.371	Corrected [690]

Figure 2.12. Example of exported data recorded from Biotek Synergy H4 multi-mode plate reader. Top panel contains the corrected absorbance values at 450 nm. Bottom panel contains the corrected absorbance values at 690 nm (background).

After data is exported to Excel, the cell viability can be calculated using basic mathematical functions, as shown in Figure 2.13. Briefly, all absorbance values are averaged (avg) and the standard deviation (sd) is calculated, along with the standard deviation squared (sd^2), to be used for further standard deviation calculations. After averaging, the background absorbance values (690 nm) are subtracted from the signal absorbance values (450 nm) and the standard deviation (sd) is calculated along with the relative standard deviation squared (rsd^2). The % cell viability can then be determined by dividing the values of each treated sample by the control sample and multiplying by 100, along with determining the % relative standard deviation (% rsd).

450 (corrected)	control	X1	X4	X8
A	2.631	1.39	0.549	0.38
B	2.666	1.189	0.645	0.384
C	2.612	1.231	0.622	0.395
D	2.633	1.207	0.627	0.393
avg	2.6355	1.25425	0.61075	0.388
sd	0.02242766	0.09212084	0.042335	0.007165
sd^2	0.000503	0.00848625	0.001792	5.13E-05
690 (corrected)	control	X1	X4	X8
A	0.203	0.149	0.143	0.141
B	0.198	0.163	0.152	0.138
C	0.193	0.157	0.157	0.136
D	0.187	0.159	0.15	0.137
avg	0.19525	0.157	0.1505	0.138
sd	0.00684957	0.00588784	0.005802	0.00216
sd^2	4.6917E-05	3.4667E-05	3.37E-05	4.67E-06
450-690	control	X1	X4	X8
avg	2.44025	1.09725	0.46025	0.25
sd	0.17110592	0.31306339	0.219402	0.096566
rsd^2	0.00491656	0.08140543	0.227245	0.1492
viability	control	X1	X4	X8
% viability	100	44.9646553	18.86077	10.24485
% rsd	9.91620989	13.2108876	9.087709	4.021886

Figure 2.13. Example of how the cell viability is determined based on the data recorded from Biotek Synergy H4 multi-mode plate reader. Control, X1, X4 and X8 represent samples shown in Figure 2.xx. In Excel, basic mathematical functions (average, standard deviation, etc.) are used to calculate the % cell viability and its % relative standard deviation (% rsd).

Upon determining the % cell viability and % rsd, the results are graphed using OriginPro8. Figure 2.14 displays the cell viability graph for the data and calculated

results shown in Figure 2.13. Upon graphing the results, it can be quantitatively concluded that by increasing the concentration of the cytotoxic agent, the cell viability decreases.

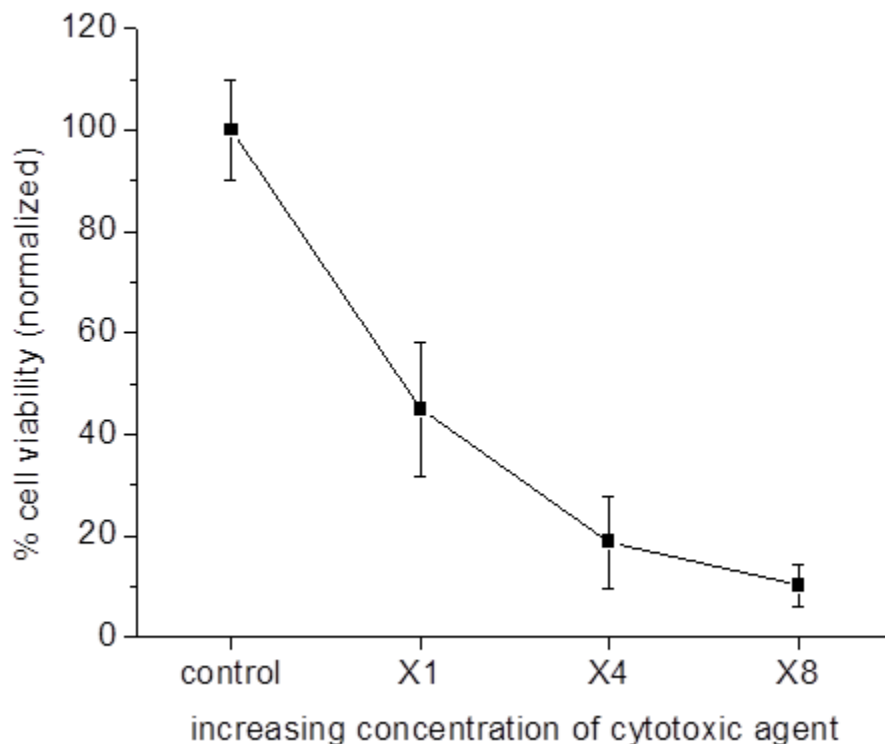


Figure 2.14. Cell viability graph representing data and results determined by calculations shown in Figure 2.13. The % cell viability is plotted as a function of increasing concentration of the cytotoxic agent. The error bar represents the % cell viability (normalized to the control) \pm % relative standard deviation (% rsd).

2.2.3.2. ATP Production

Cell viability can also be quantified by measuring the amount of ATP production in cells. The assay utilized for these measurements is the CellTiter-Glo® Luminescent Cell Viability Assay (Promega, Inc. Cat. No. G7570). This assay provides a quantitative

measurement of the amount of ATP in the cell culture, and can be used as a cell viability assay, as the luminescence signal is directly correlated to the number of metabolically active cells, based on their ATP production.[14]

Cells are plated in a white opaque-walled 96-well tissue culture plate and allowed to grow for 24 h. The culture media is then removed and replaced with 100 μ L of culture medium containing the desired treatment. Figure 2.10 shows an example of the plate configuration. Cells are then incubated with treatment for desired treatment time (*e.g.* 24, 48, 72 h). Following treatment, the 96-well plate is allowed to equilibrate to room temperature (\sim 30 min). The culture media is then removed and cells are washed with 100 μ L of PBS. Immediately following this washing step, 100 μ L of room temperature DMEM (without phenol red, supplemented with 10% FBS, and 1% antibiotic/antimycotic solution) is added to the wells, followed by 100 μ L of the room temperature CellTiter-Glo[®] Reagent is added to the wells. The CellTiter-Glo[®] Reagent is composed of the CellTiter-Glo[®] Buffer and the CellTiter-Glo[®] Substrate, mixed according to the manufacturer's protocol. The 96-well plate is then placed on an orbital shaker for 10 min to promote cell lysis. The luminescence is then measured with a Biotek Synergy H4 multi-mode plate reader (IBB Core Facilities, Georgia Tech, Contact Andrew Shaw). In the plate reader software, the settings are set to record luminescence. After luminescence values are collected, data is exported to Microsoft Excel for further analysis. Once the data is exported to Excel, the % ATP production can be calculated. Briefly, the luminescence values are averaged and the standard deviation is calculated, along with the relative standard deviation (rsd) squared. The % ATP can then be determined by dividing the average of each treated sample by that of the control sample and multiplying by 100,

along with determining the % rd. Upon determining the % ATP production and % rd, the results are graphed using OriginPro8. The graph should look similar to that of % cell viability, displayed in Figure 2.14. Upon graphing the results, it can be quantitatively concluded that by increasing the concentration of the cytotoxic agent, the % ATP production by cells decreases.

2.2.4. Flow Cytometry

2.2.4.1. Cell Cycle Analysis

Propidium iodide (PI) is a commonly used fluorescent dye for staining DNA in cells. Because it intercalates into the DNA, the fluorescence signal exhibited by PI is directly related to the amount of DNA within cells. Utilizing this method of DNA staining, fixed cells can be analyzed in terms of their DNA content. Since DNA content varies with respect to cell cycle phase, the percentages of cells in each phase of the cell cycle can be quantified by flow cytometry analysis of PI stained cells.

Cells are grown in a 12-well tissue culture plate for 24 h. The culture media is then removed and replaced with 500 μ L of culture medium containing the desired treatment, such that each treatment is administered to two wells. Figure 2.15 shows an example of the plate configuration.

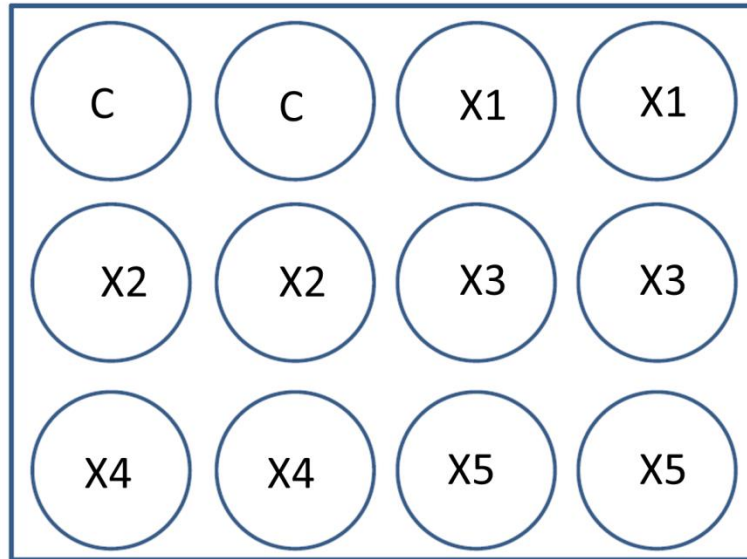


Figure 2.15. Example of 12-well plate configuration when treating cells for flow cytometry. (C) Wells loaded with 500 μ L of cell culture medium. (X1) Wells loaded with 500 μ L of cell culture medium containing lowest concentration of treatment. (X2-X5) Wells loaded with 500 μ L of cell culture medium containing increased concentrations of treatment.

After desired treatment time, the culture medium is removed, cells are washed with 1 mL of PBS and then trypsinized by adding 400 μ L of trypsin (Trypsin EDTA 1x, Mediatech, Cat# 25-031-CI) to each well. When all cells are removed from the plate, 400 μ L of cell culture medium is added to each well and like samples are combined into 15 mL centrifuge tubes. The cell suspension is then centrifuged at 1500 rpm for 7 min. The supernatant is then removed and the cell pellet is redispersed in 600 μ L of PBS, followed by addition of 2.9 mL of 95% ice cold ethanol, for fixing cells in 80% ethanol. Cells must be fixed in order to permeabilize the cell membrane for efficient dye loading of the relatively impermeable PI dye. The fixed cells can then be stored at -20°C for up to two weeks.

The fixed cells are centrifuged at 2000 rpm for 9 min. The supernatant containing the ethanol mixture is then removed and the cell pellet is redispersed in 750 μ L of PBS. RNase treatment of cells is achieved by adding 5 μ L of 2 mg/mL RNase (Sigma) to the cell suspension and incubating at 37°C for 30 min. RNase treatment is required since PI can also bind RNA, which would skew the cell cycle analysis, which is based on DNA content only. After RNase treatment, 75 μ L of the fluorescent nucleic acid stain, propidium iodide (PI, 1 mg/mL) is mixed with the cell suspension and left at room temperature for 15 min. After dye-loading, cells are passed through a 40 μ m sterile filter and analyzed via flow cytometry. Samples consisting of 10,000 cells, in triplicate, are analyzed using the BD LSR II (BD Biosciences) with a 488 nm excitation (IBB Core Facilities, Georgia Tech, contact Nadia Boduslavsky). Figure 2.16 displays a typical view of the flow cytometry software, BD FACSDiva, when using the BD LSR II for cell cycle analysis. Using the flow cytometry analysis software, FlowJo, DNA content and subsequent cell cycle analyses are carried out.

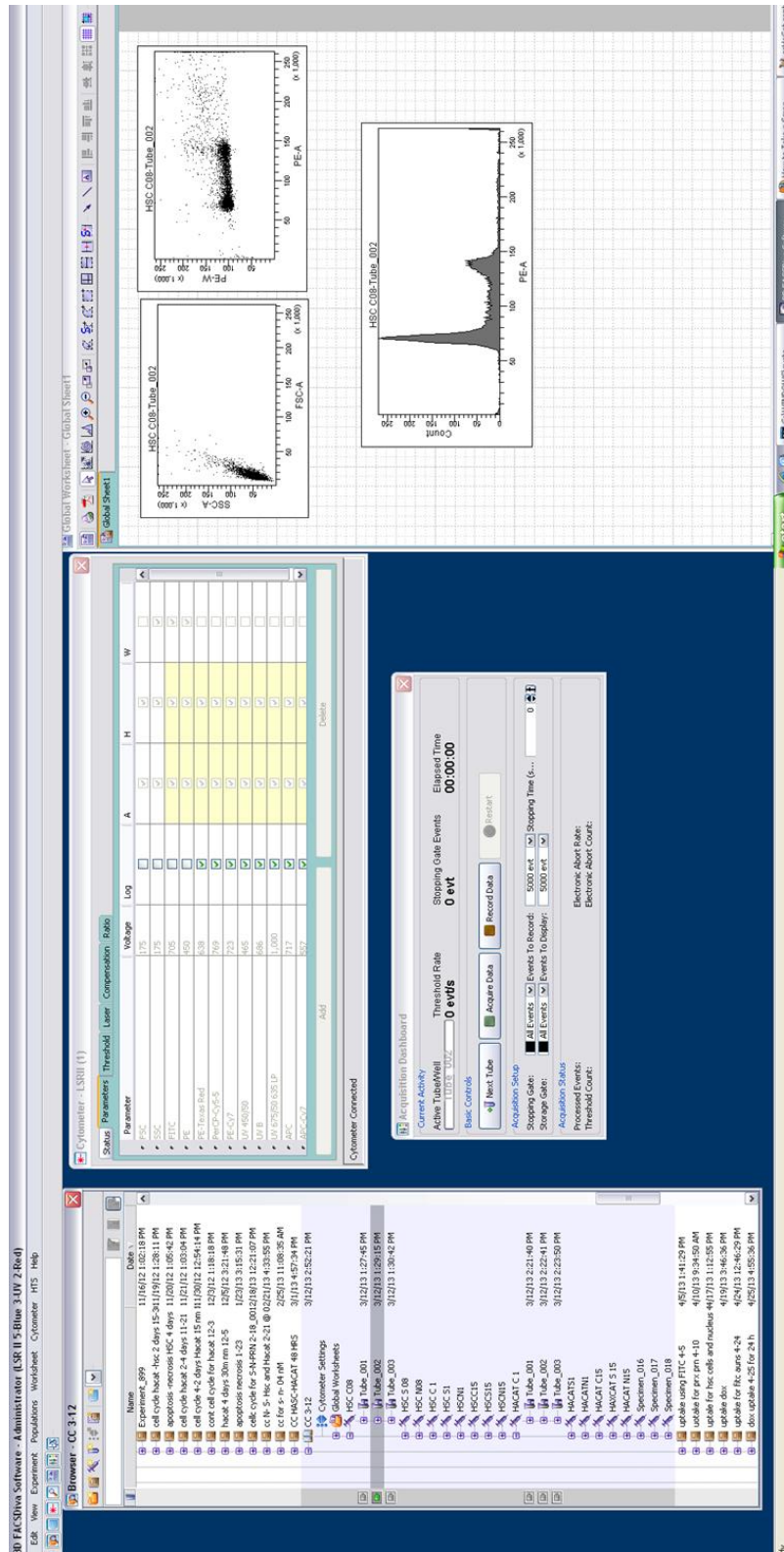


Figure 2.16. Screenshot of BD FACSDiva (software used for flow cytometry analysis) displaying settings and typical results for cell cycle analysis via flow cytometry.

2.2.4.2. Detection of Apoptosis and Necrosis

One of the earliest events to take place during apoptosis is the exposure of phosphatidylserine (PS) residues on the outer leaflet of the cell membrane. These PS residues have a high affinity for the phospholipid binding protein annexin-V. Therefore, by exposing cells to fluorescently labeled annexin-V, apoptosis can be quantified by the fluorescence intensity measured using flow cytometry.[15] The apoptotic population can be distinguished from the necrotic population with the addition of propidium iodide, which binds nucleic acids in cells only once the membrane becomes permeable (*i.e.* necrosis). In order to quantify the amount of apoptosis and necrosis induced in cells by various nanoparticle treatments, the *ApoTarget*[™] Annexin-V FITC Apoptosis Kit (Invitrogen, Inc. Cat. #PHN1010) was utilized.

Cells are grown in a 12-well tissue culture plate for 24 h. The culture media is then removed and replaced with 500 μ L of culture medium containing the desired treatment, such that each treatment is administered to two wells. Figure 2.15 shows an example of the plate configuration. After desired treatment time, the culture medium is removed, cells are washed with 1 mL of PBS and then trypsinized by adding 400 μ L of trypsin (Trypsin EDTA 1x, Mediatech, Cat# 25-031-CI) to each well. When all cells are removed from the plate, 400 μ L of cell culture medium is added to each well and like samples are combined into 15 mL centrifuge tubes. The cell suspension is then centrifuged at 1500 rpm for 7 min. The supernatant is removed and the pellet is redispersed in 500 μ L of 1x Annexin binding buffer, 2 μ L of 100 μ g/mL PI and 5 μ L of Annexin-V-FITC, followed by incubation at room temperature for 15 min after which the remaining volume 1x Annexin binding buffer is added (493 μ L) and the cells are passed through a 40 μ m

sterile filter. Cells are analyzed immediately using the BD LSR II (BD Biosciences) with a 488 nm excitation on 10,000 cells, in triplicate (IBB Core Facilities, Georgia Tech, contact Nadia Boduslavsky). Figure 2.17 displays a typical view of the flow cytometry software, BD FACSDiva, when using the BD LSR II for analysis of apoptosis and necrosis. Using the flow cytometry analysis software, FlowJo, the FITC and PI intensities are gated and percentages of live, early apoptotic, late apoptotic and necrotic cells are quantified.

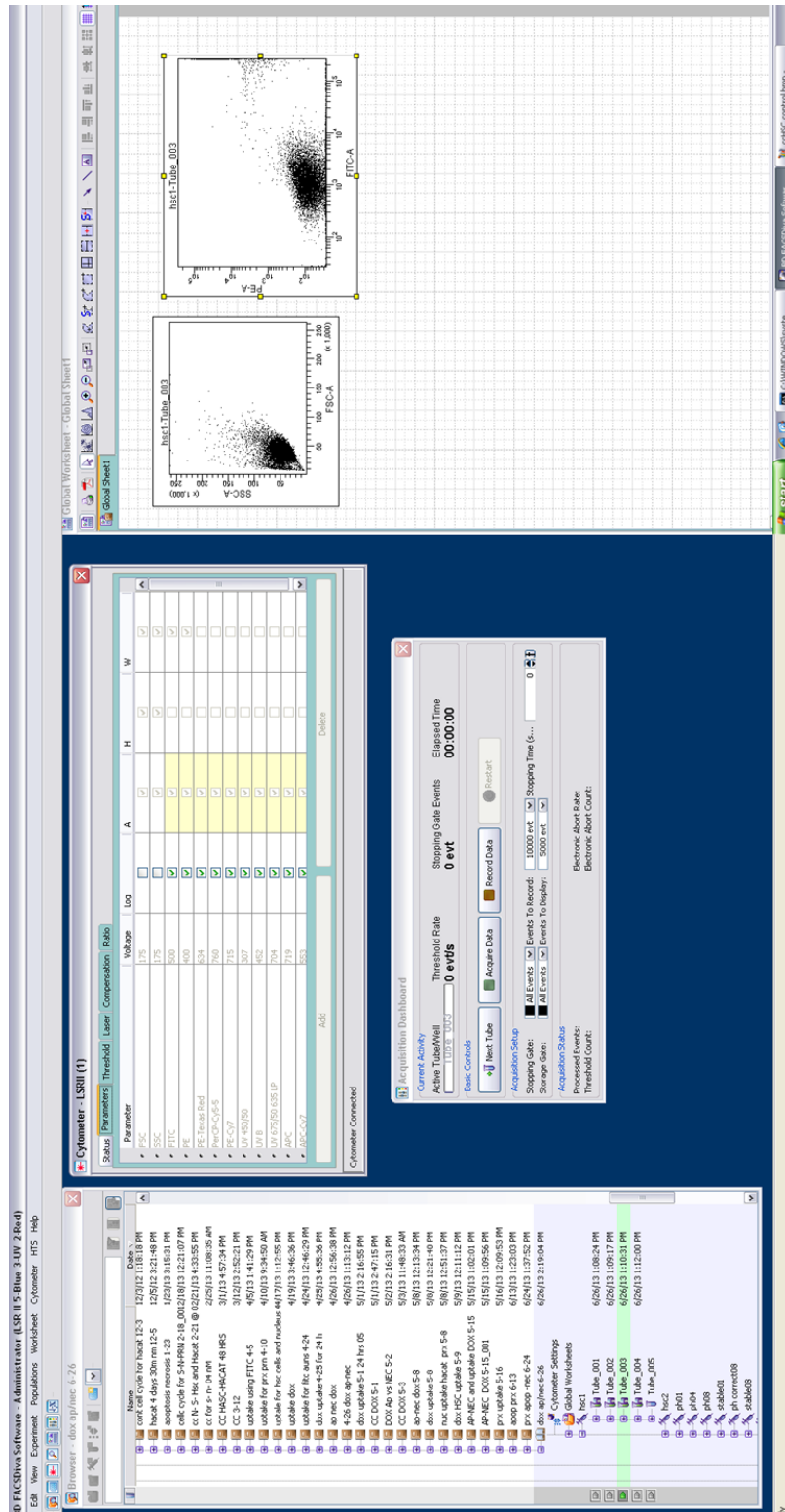


Figure 2.17. Screenshot of BD FACSDiva (software used for flow cytometry analysis) displaying settings and typical results for analysis of apoptosis and necrosis via flow cytometry.

2.2.5. Confocal Microscopy

2.2.5.1. Detection of DNA Double Strand Breaks

One of the earliest steps in the cellular response to double-strand breaks (DSBs) is the phosphorylation of serine-139 of H2AX, a subclass of eukaryotic histone proteins that are part of the nucleoprotein structure of chromatin.[16] Using a fluorescently labeled antibody specific for the phosphorylated form of H2AX (γ -H2AX) discrete nuclear foci can be visualized at the sites of DSBs.[17] For confocal imaging, cells are grown on 18 mm diameter glass coverslips (in bottom of well in 12-well tissue culture plate) overnight and incubated with gold nanoparticle solutions in culture medium for desired treatment time. After desired treatment time, cells are fixed in 500 μ L of 4% paraformaldehyde for 15 min, washed in PBS three times, permeabilized for 5 min on ice in 0.2% Triton X-100, and blocked by washing with PBS, containing 1% BSA, three times at room temperature. The coverslips are incubated with anti- γ -H2AX antibody (Bethyl Laboratories, Inc) for 1 h, washed with PBS, containing 1% BSA, three times, and incubated with FITC-conjugated goat anti-rabbit secondary antibody (Bethyl Laboratories, Inc) for 1 h at room temperature. Cells are washed with PBS three times and the nuclei are stained with DAPI (500 μ L, 120 nM) DAPI. The plate is swirled gently for ~ 1 min, to allow for homogeneous staining of the cells on the coverslip and rinsed with water 3 times. The coverslip is then placed on a microscope slide containing a small drop of 30% glycerin, sealed with nail polish and stored at 4°C until analysis. Fluorescence images are taken by multiphoton confocal microscopy using the Zeiss LSM 510 NLS META with 785 (DAPI) and 488 nm (FITC) excitation sources (IBB Core Facilities, Georgia Tech, contact Andrew Shaw).

2.2.5.2. Detection of Reactive Oxygen Species

Generation of reactive oxygen species (ROS) is common for some cytotoxic agents. In order to detect ROS within cells, a cell permeant compound, 2',7'-dichlorodihydrofluorescein diacetate (H2DCFDA), that is converted to a highly fluorescent compound, 2'7'-dichlorofluorescein (DCF), in the presence of ROS, is loaded into cells. If ROS are indeed present, FITC fluorescence can be visualized by confocal microscopy.

Cells are grown on 18 mm diameter glass coverslips (in bottom of well in 12-well tissue culture plate) overnight and incubated with gold nanoparticle solutions in culture medium for desired treatment time. After desired treatment time, the culture medium is removed and the cells are washed with PBS, after which the cells are stained with a 10 μ M (500 μ L) solution of H2DCFDA (6-carboxy-2',7'-dichlorodihydrofluorescein diacetate, Invitrogen, C2938) and left to incubate at 37°C for 30 min. After dye loading, the cells are washed with PBS and fixed with 500 μ L of 4% paraformaldehyde for 15 min, followed by nuclear staining with DAPI (500 μ L, 120 nM) and swirling gently for ~ 1 min, to allow for homogeneous staining of cells on the coverslip. The coverslip is then rinsed with water 3 times and placed on a microscope slide containing a small drop of 30% glycerin. Coverslip is sealed with nail polish and stored at 4°C until analysis. Fluorescence images are taken by multiphoton confocal microscopy using the Zeiss LSM 510 NLS META with 785 (DAPI) and 488 nm (FITC) excitation sources (IBB Core Facilities, Georgia Tech, contact Andrew Shaw).

2.3. References

1. Frens, G. (1973) Controlled Nucleation for Regulation of Particle-Size in Monodisperse Gold Suspensions, *Nature-Phys Sci* 241, 20-22.
2. Chen, J. Y., Wiley, B., Li, Z. Y., Campbell, D., Saeki, F., Cang, H., Au, L., Lee, J., Li, X., and Xia, Y. (2005) Gold nanocages: Engineering their structure for biomedical applications, *Adv. Mater.* 17, 2255-2261.
3. Mahmoud, M. A., Snyder, B., and El-Sayed, M. A. (2010) Surface Plasmon Fields and Coupling in the Hollow Gold Nanoparticles and Surface-Enhanced Raman Spectroscopy. Theory and Experiment, *J. Phys. Chem. C* 114, 7436-7443.
4. Siekkinen, A. R., McLellan, J. M., Chen, J. Y., and Xia, Y. N. (2006) Rapid synthesis of small silver nanocubes by mediating polyol reduction with a trace amount of sodium sulfide or sodium hydrosulfide, *Chem. Phys. Lett.* 432, 491-496.
5. Yen, C. W., Mahmoud, M. A., and El-Sayed, M. A. (2009) Photocatalysis in gold nanocage nanoreactors, *J. Phys. Chem. A* 113, 4340-4345.
6. Huang, X. H., Neretina, S., and El-Sayed, M. A. (2009) Gold Nanorods: From Synthesis and Properties to Biological and Biomedical Applications, *Advanced Materials* 21, 4880-4910.
7. Ali, M. R. K., Snyder, B., and El-Sayed, M. A. (2012) Synthesis and Optical Properties of Small Au Nanorods Using a Seedless Growth Technique, *Langmuir* 28, 9807-9815.
8. Dubois, L. H., and Nuzzo, R. G. (1992) Synthesis, Structure, and Properties of Model Organic-Surfaces, *Annual review of physical chemistry* 43, 437-463.
9. Chithrani, B. D., and Chan, W. C. W. (2007) Elucidating the mechanism of cellular uptake and removal of protein-coated gold nanoparticles of different sizes and shapes, *Nano Lett.* 7, 1542-1550.
10. Qian, W., Huang, X., Kang, B., and El-Sayed, M. A. (2010) Dark-field light scattering imaging of living cancer cell component from birth through division using bioconjugated gold nanoprobe, *J Biomed Opt* 15, 046025.
11. Scudiero, D. A., Shoemaker, R. H., Paull, K. D., Monks, A., Tierney, S., Nofziger, T. H., Currens, M. J., Seniff, D., and Boyd, M. R. (1988) Evaluation of a Soluble Tetrazolium Formazan Assay for Cell-Growth and Drug Sensitivity in

Culture Using Human and Other Tumor-Cell Lines, *Cancer Research* 48, 4827-4833.

12. Weislow, O. S., Kiser, R., Fine, D. L., Bader, J., Shoemaker, R. H., and Boyd, M. R. (1989) New Soluble-Formazan Assay for Hiv-1 Cytopathic Effects - Application to High-Flux Screening of Synthetic and Natural-Products for Aids-Antiviral Activity, *J Natl Cancer I* 81, 577-586.
13. Roehm, N. W., Rodgers, G. H., Hatfield, S. M., and Glasebrook, A. L. (1991) An Improved Colorimetric Assay for Cell-Proliferation and Viability Utilizing the Tetrazolium Salt Xtt, *Journal of Immunological Methods* 142, 257-265.
14. Crouch, S. P. M., Kozlowski, R., Slater, K. J., and Fletcher, J. (1993) The Use of Atp Bioluminescence as a Measure of Cell-Proliferation and Cytotoxicity, *J. Immunol. Methods* 160, 81-88.
15. van Engeland, M., Nieland, L. J. W., Ramaekers, F. C. S., Schutte, B., and Reutelingsperger, C. P. M. (1998) Annexin V-affinity assay: A review on an apoptosis detection system based on phosphatidylserine exposure, *Cytometry* 31, 1-9.
16. Rogakou, E. P., Pilch, D. R., Orr, A. H., Ivanova, V. S., and Bonner, W. M. (1998) DNA double-stranded breaks induce histone H2AX phosphorylation on serine 139, *The Journal of biological chemistry* 273, 5858-5868.
17. Chen, H. T., Bhandoola, A., Difilippantonio, M. J., Zhu, J., Brown, M. J., Tai, X., Rogakou, E. P., Brotz, T. M., Bonner, W. M., Ried, T., and Nussenzweig, A. (2000) Response to RAG-mediated VDJ cleavage by NBS1 and gamma-H2AX, *Science* 290, 1962-1965.

CHAPTER 3

INTRINSIC PROPERTIES OF GOLD NANOPARTICLE CONJUGATES

3.1. Nuclear Targeting of Gold Nanoparticles in Cancer Cells Induces DNA Damage, Causing Cytokinesis Arrest and Apoptosis [1]

Unique properties of plasmonic gold nanoparticles have been successfully exploited for potential use in anticancer drug delivery systems and photothermal cancer treatment, both in vitro and in animal models. Here, we report the use of gold nanoparticles alone as a cancer treatment. By properly conjugating gold nanoparticles with specific peptides, we can selectively transport nanoparticles to the nucleus of cancer cells. Confocal microscopy images of DNA double strand breaks show that localization of gold nanoparticles at the nucleus of cancer cells damages the DNA. Using gold nanoparticle dark field imaging of live cells in real time, the nuclear-targeting gold nanoparticles are observed to specifically induce a cytokinesis arrest in cancer cells, where binucleate cell formation occurs after mitosis takes place. Flow cytometry results indicate that this failure to complete cell division leads to programmed cell death (apoptosis) in cancer cells. These results suggest that gold nanoparticles properly bound to nuclear- and cancer-targeting ligands can be effective anticancer agents and have implications in understanding the interaction between nanomaterials and living systems.

3.1.1. Introduction

Understanding how nanomaterials affect live cell functions, controlling such effects, and using them for disease therapeutics are now the principal aims and most challenging aspects of nanobiotechnology and nanomedicine. Gold nanoparticles (AuNPs), nanorods, and nanoshells with unique properties [2-5] have been shown to be of potential use in anticancer drug delivery systems [6] and photothermal cancer treatment agents.[7-12] Although such applications have shown promising potential in cancer treatment, the fundamental interactions and effects of nanomaterials in living systems for the most part still remain unknown.

To address these fundamentals, many studies to assess the effect of introducing AuNPs into the cytoplasm of the cell have been done, [13-15] yet little is known about the effect of AuNPs at the nucleus of the cell. The cell nucleus functions to maintain all processes that occur within the cell, and any disruptions within the nucleus would subsequently affect the cell's DNA, thereby disturbing the highly regulated cell cycle.

Here we report the use of nuclear targeting of AuNPs to selectively disturb the division of cancer cells by the observation of cytokinesis arrest. Cytokinesis arrest was observed by AuNP dark-field imaging of live cells in real time, [16] which showed binucleate cell formation at late stages of mitosis, leading to the failure to complete cell division. Confocal microscopy and flow cytometry gave evidence that DNA damage and programmed cell death (apoptosis), respectively, accompany the observed cytokinesis arrest.

3.1.2. Experimental Methods

3.1.2.1. Cell Culture

One malignant epithelial cell line, HSC-3 (human oral squamous cell carcinoma), and one nonmalignant epithelial cell line, HaCat (human keratinocytes) were cultured in Dulbecco's Modified Eagle's Medium (DMEM, Mediatech) supplemented with 4.5 g/L glucose and sodium pyruvate, 10% v/v fetal bovine serum (FBS, Mediatech) and 1% antimycotic solution (Mediatech). Cell cultures were kept at 37°C in a 5% CO₂ humidified incubator.

3.1.2.2. Nanoparticle Synthesis and Peptide Conjugation

Gold nanoparticles (AuNPs) were synthesized via the citrate reduction of HAuCl₄ method developed by Frens.[17] The measured absorption maximum of these particles was at 528nm. TEM showed an average particle size of about 30nm (Figure 3.1 A, C).

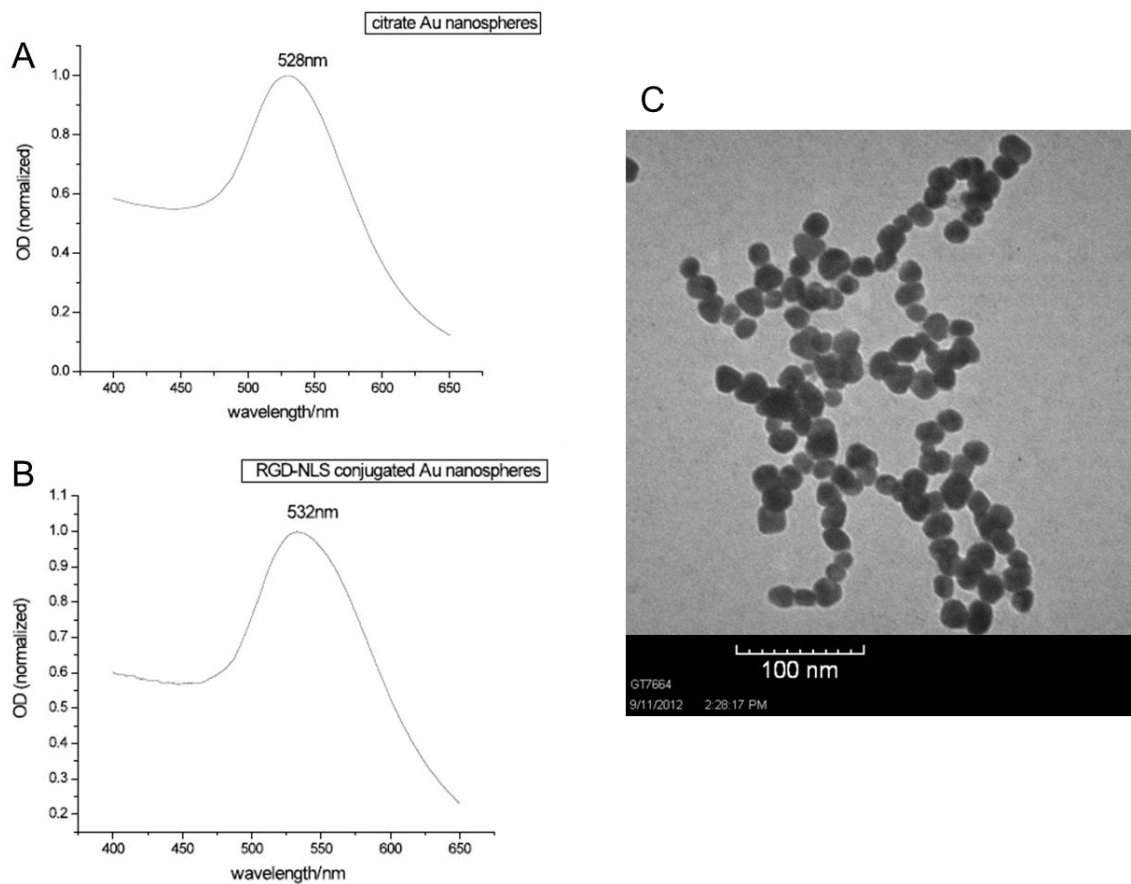


Figure 3.1. (A) UV-Vis spectrum of AuNPs exhibiting a maximum absorption at 528 nm. (B) UV-Vis spectrum of RGD/NLS-AuNPs exhibiting a maximum absorption at 532 nm. (C) TEM image of AuNPs about 30 nm in diameter.

For pegylation necessary to prevent aggregation of AuNPs, a 1 mM solution of mPEG-SH 5000 (Laysan Bio, Inc.) in DI water was added to a volume of AuNPs to make the concentration of mPEG-SH 10^3 times that of the AuNPs. The mixture was left to react for 2 h, excess mPEG-SH was removed by centrifugation at 6000 rpm for 15 min and the particles were dispersed in PBS. For conjugation of peptides to the PEG-AuNPs, a previous established method was used.[18] Briefly, for conjugation of RGD peptides to the PEG-AuNPs, a 1 mM solution of RGD in DI water was added to a volume of PEG-

AuNPs to make the concentration of RGD 10^5 times that of the PEG-AuNPs. The mixture was left to react for 48 h, excess RGD peptide was removed by centrifugation at 6000 rpm for 15 min and particles were dispersed in PBS. For conjugation of RGD and NLS peptides to PEG-AuNPs, a 1 mM solution of RGD in DI water and a 1 mM solution of NLS in DI water were added to a volume of PEG-AuNPs to make the concentrations 10^5 times and 10^6 times that of the PEG-AuNPs, respectively. The mixture was left to react for 48 h, excess RGD and NLS were removed by centrifugation at 6000 rpm for 15 min and the particles were dispersed in PBS. A redshift of 5 nm was observed upon conjugation of peptides to Au (Figure 3.1 B), characteristic of the change in dielectric of the surrounding environment of the nanoparticles. Upon conjugation of peptides to AuNPs and dispersion in PBS, the peptide-AuNPs were further diluted in DMEM culture medium, described above, to concentrations of 0.1 and 0.4 nM.

3.1.2.3. Dark Field Imaging

For fixed cells, cells were cultured on 18 mm diameter glass coverslips coated with collagen and incubated with peptide-AuNP solutions in DMEM for 24 h. After incubation, coverslips were rinsed with PBS buffer and fixed with 4% paraformaldehyde. Dark field images were taken using an inverted Olympus IX70 microscope utilizing a dark field condenser (U-DCW). A 100x/1.35 oil Iris objective (UPLANAPO) was used to collect the scattered light from the samples to produce the dark field images.

3.1.2.4. Live Cell Imaging

The homemade setup (Figure 3.2) was modified based on an inverted Olympus IX70 microscope.[16] The incident white light emitted from the Fiber-Lite MI-150 Illuminator (Dolan-Jenner Industries) was delivered with an optical fiber and was focused into a tiny

spot on the focal plane of the microscope objective by a condenser lens at the end of the optical fiber. The angle of the illuminating light was adjusted to prevent the incident illuminating light from entering the light collection cone of the microscope objective. The sample, cells grown in the 35 mm culture plate, was placed in the homemade environmental mini cell chamber, which was mounted on the stage of the microscope. The environmental parameters inside the chamber, such as temperature, carbon dioxide concentration, and humidity, were well controlled. A long working distance 40x objective was used to collect only the scattered illuminating light from the sample. The dark field pictures were taken using the Nikon D200 digital camera automatically with an interval time of 2 min.

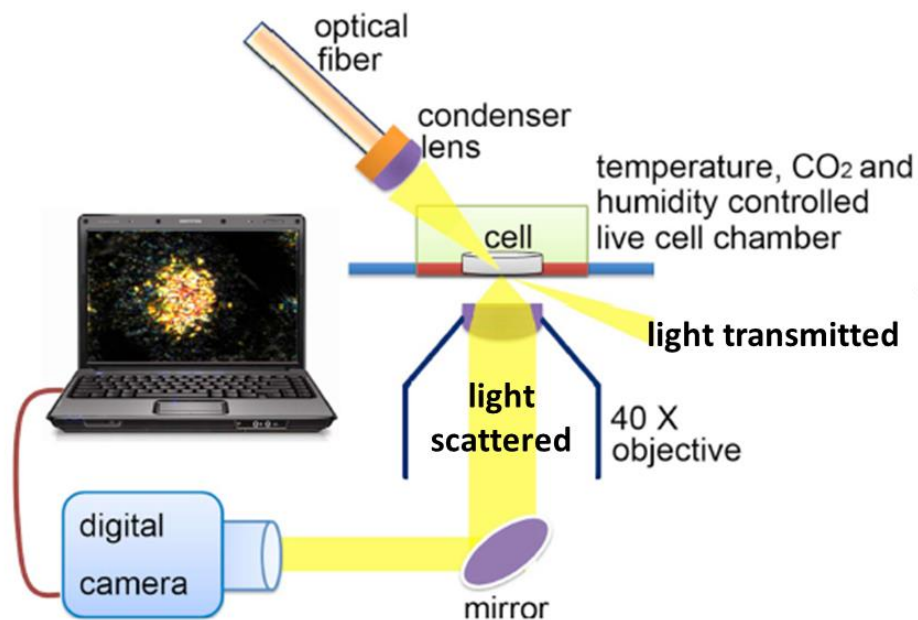


Figure 3.2. Schematic setup of real-time light scattering imaging system for live cell studies. A dark field light scattering imaging microscope with a side-illumination arrangement is combined with an environmental cell incubation chamber for real time studies of live cells.

3.1.2.5. Cell Synchronization

Cells were synchronized in prometaphase via nocodazole block. Briefly, cells were grown for 14 h in the presence of 80 ng/mL nocodazole. Mitotic cells, obtained by shake-off, were released in fresh culture medium containing different concentrations of peptide-AuNPs. Cells were then harvested at indicated time points, washed three times in PBS, and fixed with -20°C ethanol for further analysis.

3.1.2.6. Flow Cytometry

For flow cytometry analysis, all fixed cell suspensions were centrifuged and the pellet was rinsed with PBS. The cells were then treated with 200 µg/mL RNase (Sigma) at 37°C for 30 min, followed by DNA staining with propidium iodide (Sigma) at room temperature for 15 min. Flow cytometry was done using the BD LSR II (BD Biosciences) with a 488 nm excitation laser and fluorescence detection in the PE channel. Cell cycle analysis of the data was done using FlowJo (flow cytometry analysis software). For cell number counting, the cell samples were run out on the flow cytometer and the single cell populations were gated in a PE-A/PE-W window.

3.1.2.7. Confocal Microscopy DNA Damage Detection

One of the earliest steps in the cellular response to double-strand breaks (DSBs) is the phosphorylation of serine-139 of H2AX, a subclass of eukaryotic histone proteins that are part of the nucleoprotein structure of chromatin.[19] Using a fluorescently labeled antibody specific for the phosphorylated form of H2AX (γ -H2AX) discrete nuclear foci can be visualized at the sites of DSBs.[20] For confocal imaging, cells on coverslips were fixed in 4% paraformaldehyde for 15 min, washed in PBS three times, permeabilized for 5 min on ice in 0.2% Triton X-100, and blocked by washing with PBS, containing 1%

BSA, three times at room temperature. The coverslips were incubated with anti- γ -H2AX antibody (Bethyl Laboratories, Inc) for 1 h, washed with PBS, containing 1% BSA, three times, and incubated with FITC-conjugated goat anti-rabbit secondary antibody (Bethyl Laboratories, Inc) for 1 h at room temperature. Cells were washed with PBS three times and then stained with 4, 6 diamidino-2-phenylindole (DAPI). Fluorescence images were captured using a Zeiss LSM 510 NLS META multi-photon excitation confocal microscope.

3.1.3. Results and Discussion

In order to selectively transport the AuNPs to the cancer cell nucleus, 30 nm AuNPs coated with polyethylene glycol (PEG) were bioconjugated with an arginine-glycine-aspartic acid peptide (RGD) and a nuclear localization signal (NLS) peptide. RGD is known to target α v β integrins on the cell surface and enter the cytoplasm via receptor-mediated endocytosis.[21] NLS, which has a lysine-lysine-lysine-arginine-lysine (KKKRK) sequence, is known to associate with karyopherins (importins) in the cytoplasm, after which translocation to the nucleus occurs.[22] AuNPs conjugated with RGD only (RGD-AuNPs) exhibit cancer-cell-specific targeting, and AuNPs conjugated with RGD and NLS (RGD/NLS-AuNPs) exhibit cancer cell nucleus-specific targeting. In this study, human oral squamous cell carcinoma (HSC) having α v β integrins overexpressed on the cell surface[23] was used as the cancer cell model, and human keratinocytes (HaCat) were used as the normal cell model. The RGD-AuNPs specifically target the cytoplasm of cancer cells over that of normal cells, and the RGD/NLS-AuNPs specifically target the nuclei of cancer cells over those of the normal cells (Figure 3.3).

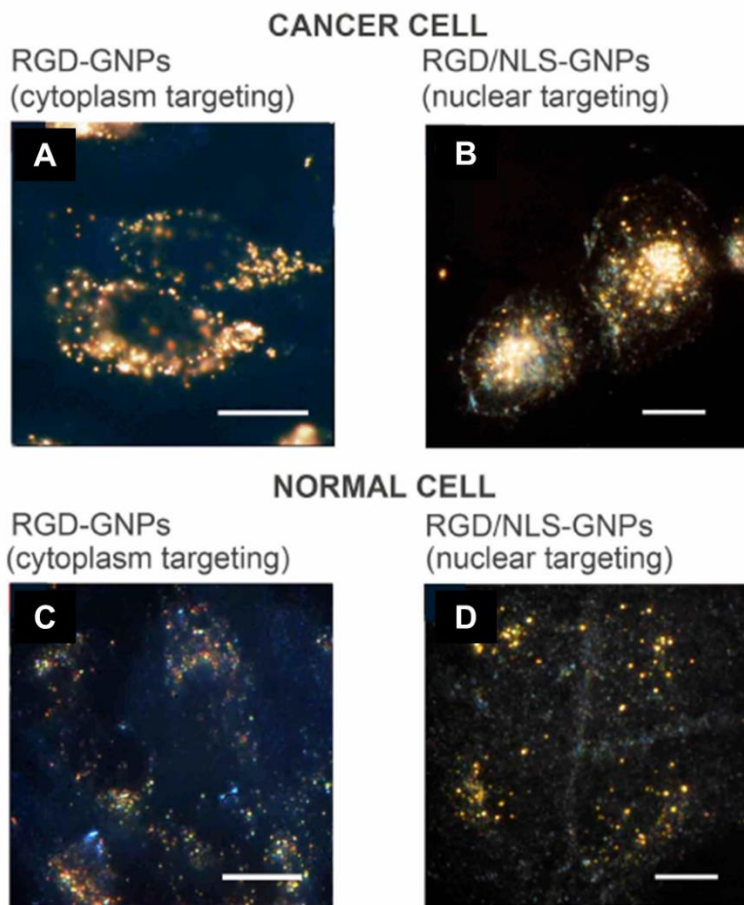


Figure 3.3. Dark field light scattering images of cytoplasm and nuclear targeting AuNPs. (A) RGD-AuNPs located in the cytoplasm of cancer cells. (B) RGD/NLS-AuNPs located at the nucleus of cancer cells. (C) RGD-AuNPs located in the cytoplasm of normal cells. (D) RGD/NLS-AuNPs located at the nucleus of normal cells. The cancer and normal cells were incubated in the presence of these AuNPs at a concentration of 0.4 nM for 24 h and these images clearly display the efficient uptake of AuNPs in cancer cells compared with normal cells. Scale bar: 10 μ m.

To look at the effects of the specific nuclear localization of AuNPs in cancer cells, a full investigation of the cell cycle was carried out under various conditions. Cell cycle arrest was determined by studying the full cell cycle time and the dynamics of cell division in the presence of AuNPs by using long-term live-cell gold plasmonic scattering

imaging on a homemade setup (Fig. 3.2). Figure 3.4 displays typical snapshots of the movies taken of cancer cell division.

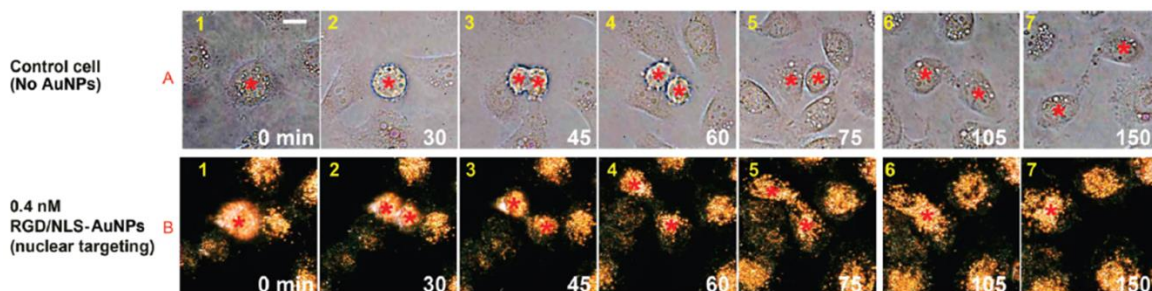


Figure 3.4. Real-time images of cancer cell division showing an apparent cytokinesis arrest (B4) followed by binucleate cell formation (B6, B7) in the presence of 0.4 nM nuclear-targeting gold nanoparticles (RGD/NLS-AuNPs). This phenomenon was not observed in untreated cancer cells (A1-7) or cancer cells under other conditions (see Appendix A, Figure A.1). Red stars indicate the nuclei. Scale bar: 10 μ m.

In the absence of AuNPs (Fig 3.4A), cancer cells begin the process of cytokinesis at 45 min (Fig. 3.4A3). After complete cleavage furrow contraction, daughter cells were linked together by a cytoplasmic bridge, which was extended over time with the midbody at its center (Fig. 3.4A6). Abscission occurred after 2 h, and the two daughter cells separated completely to form independent cells (Fig. 3.4A7). A similar process was observed for cells incubated with 0.4 nM RGD-AuNPs (see Appendix A, Figure A.1) and 0.1 nM RGD/NLS-AuNPs (see Appendix A, Figure A.1), with 0.1 nM RGD/NLS-AuNPs extending the full cell cycle time by about 4 h (see Appendix A, Figure A.2). However, for cells incubated with 0.4 nM RGD/NLS-AuNPs, complete cell division was not observed (Fig. 3.4B). The onset of cytokinesis proceeded with the same kinetics as in the untreated cells (Fig 3.4B1-4), but when the cleavage furrow was fully contracted, the cytoplasmic bridge did not extend (Fig. 3.4B5-6); instead the contractile ring relaxed, and

the daughter cells fused back together to form a binucleate cell (Fig 3.4B7). Cytokinesis arrest was not observed in any normal cell groups here. This observation clearly demonstrates that a 0.4 nM concentration of AuNPs targeting the nucleus of cancer cells causes disruption of cytokinesis, thereby inhibiting these cells from completing cell division.

Within the present work, cytokinesis arrest was observed only in cancer cells treated with 0.4 nM RGD/NLS-AuNPs, suggesting that a disruption within the nucleus is the cause. To test this possibility, we investigated DNA double-strand breaks (DSBs) in cancer cells incubated with AuNPs. Figure 3.5 shows confocal images of cancer cells in which the cell nuclei are stained blue with DAPI and the DSB foci are seen as bright green FITC fluorescence.

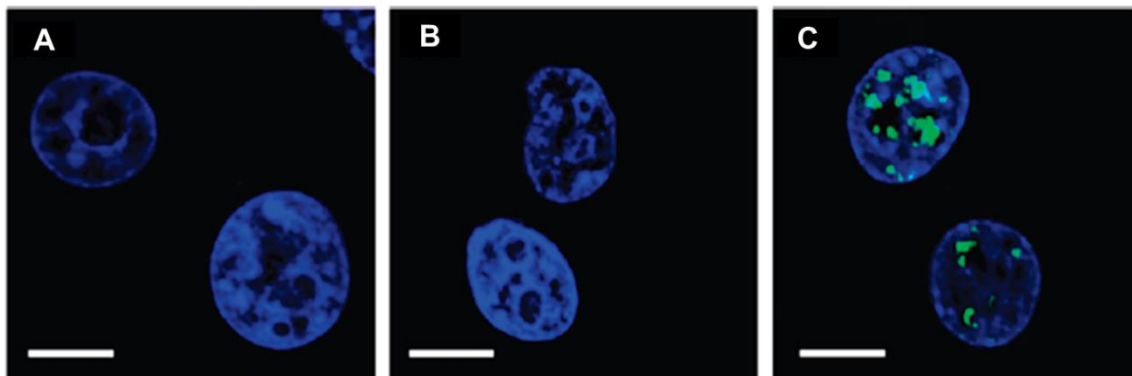


Figure 3.5. DNA damage induced in cancer cells by 0.4 nM nuclear-targeting gold nanoparticles (RGD/NLS-AuNPs) is indicated by the bright green fluorescence in (C). Cancer cells (A) in the absence of AuNPs and (B) with AuNPs in the cytoplasm, no DNA damage was observed. Scale bar: 10 μ m.

For untreated cells (Fig. 3.5A) and cells with AuNPs present in the cytoplasm (Fig. 3.5B), no DSBs were observed in the cell nuclei. However, for cells treated with 0.4 nM nuclear-targeted AuNPs (RGD/NLS-AuNPs) (Fig. 3.5C), bright green DSB foci were

observed in the cell nuclei. DSBs can induce many different defects of cellular function and could be one reason for cell cycle disruption, specifically cytokinesis arrest and subsequent apoptosis, as observed here.

The observations seen with imaging techniques occurred in only a few cases. In order to prove this phenomenon on a larger scale, flow cytometry was carried out on a large number of cells. Both cancer cells and normal cells were first synchronized at prometaphase with nocodazole and then released in fresh medium containing different concentrations of RGD-AuNPs and RGD/NLS-AuNPs. The flow cytometry cell cycle results are shown in Figure 3.6 (see Appendix A, Figure A.3 for cell cycle histograms).

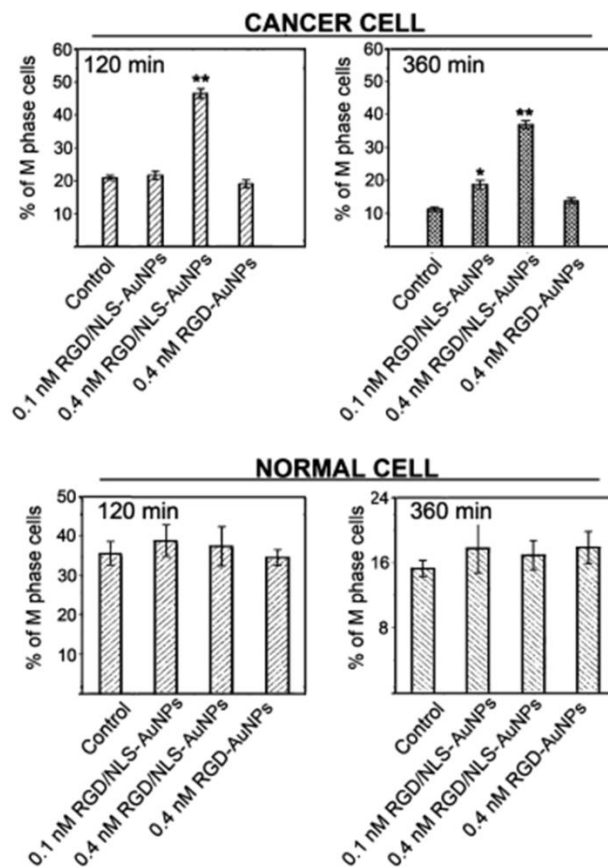


Figure 3.6. (top) M phase (mitosis phase of cell division) accumulation of cancer cells in the presence of 0.4 nM nuclear-targeting gold nanoparticles (RGD/NLS-AuNPs) suggests complete cell division (cytokinesis) has not taken place. (bottom) Data for normal cells. Nocodazole synchronization and release techniques were used in this experiment (see Experimental section) and the cell cycle was measured at different times of release (120 and 360 min).

In the absence of AuNPs, 90% of the cancer cell population was synchronized in the M phase at time zero. At 120 min, more than 75% of the cell population had exited mitosis. Finally, at 360 min, more than 90% of the cell population was at the G1 phase. In the presence of 0.1 nM RGD/NLS-AuNPs, the process of cell division was slightly disrupted, as indicated by the dynamics compared with the untreated cancer cells, but more than 80% of the cell population was able to go through mitosis and enter the G1 phase. In contrast, in the presence of 0.4 nM RGD/NLS-AuNPs, 60% of the cell

population was at the M phase after 120 min, suggesting mitotic delay. At 360 min, 35% of the cell population was still arrested at the M phase, indicating that the cancer cells were unable to proceed through mitosis. As for the normal cells, all of the AuNP-treated groups showed no contrast to the untreated cells. Normal cells in all cases were able to proceed through mitosis.

As the last step of cell division, cytokinesis is very complex and highly regulated.[24] Errors in the cytokinesis process could potentially cause apoptosis. To further investigate the result of the observed cytokinesis arrest, a complete cell cycle analysis via flow cytometry and subsequent identification of a subG1 cell population (apoptotic cells) was carried out and is shown in Figure 3.7 (see Appendix A, Figure A.4 for cell cycle histograms).

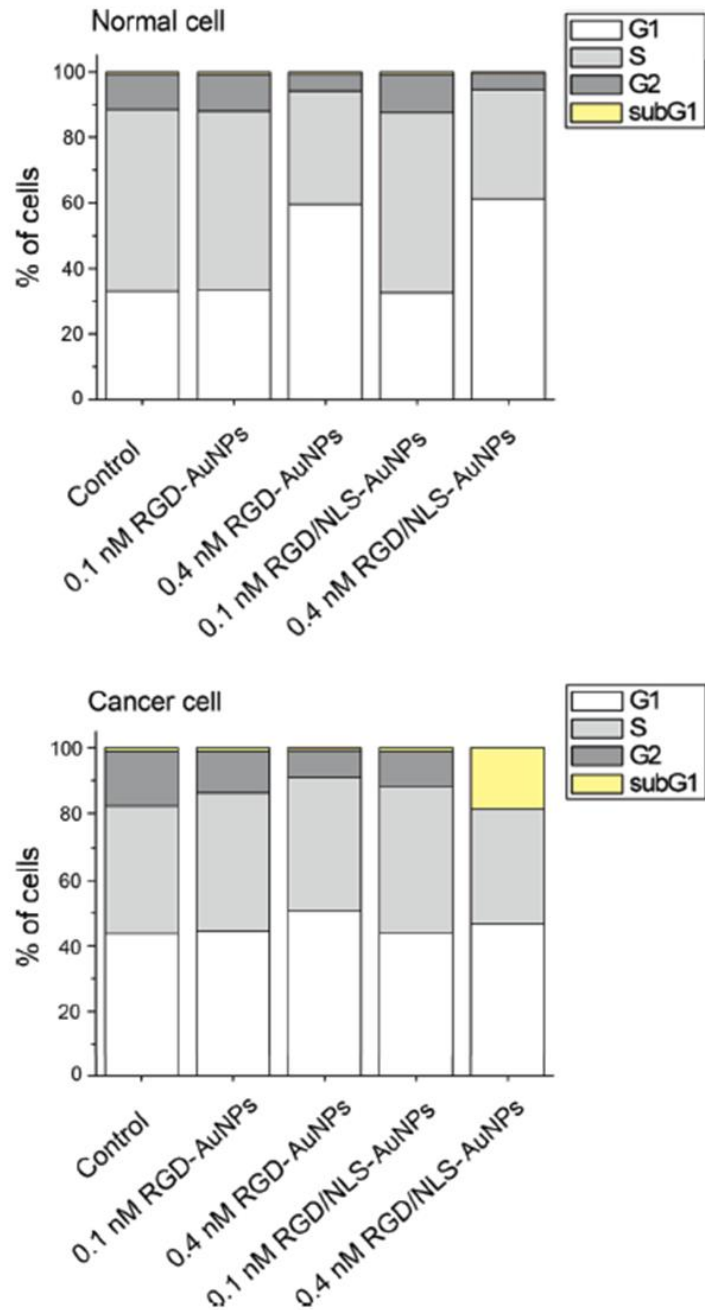


Figure 3.7. percentages of cells in each phase of the cell cycle show the appearance of a DNA-deficient cell population (subG1, yellow) for cancer cells in the presence of 0.4 nM nuclear-targeting gold nanoparticles (RGD/NLS-AuNPs), suggesting apoptosis.

Cancer cells and normal cells were grown in the presence of different concentrations of RGD-AuNPs and RGD/NLS-AuNPs for 24 h before cell cycle analysis was carried out (see Experimental section for details). For cancer cells incubated with 0.4 nM RGD/NLS-AuNPs, about 20% of the cell population was apoptotic (yellow in Figure 3.7). This particular attribute was not observed in the untreated cancer cells, the other AuNP-treated cancer cells, or any of the normal cell cases (treated or untreated). In the normal cell group, cells treated with a 0.4 nM concentration of AuNPs showed accumulation of cells at the G1 phase, indicating a disruption of the G1-to-S transition in the cell cycle, but the AuNPs did not cause apoptosis, as indicated by the absence of a subG1 cell population. In control groups treated with free peptides, neither M-phase arrest nor G1 disruption were observed (see Appendix A, Figure A.5).

Upon observation of an apoptotic cell population, absolute cell numbers were counted under each condition, shown in Figure 3.8 below.

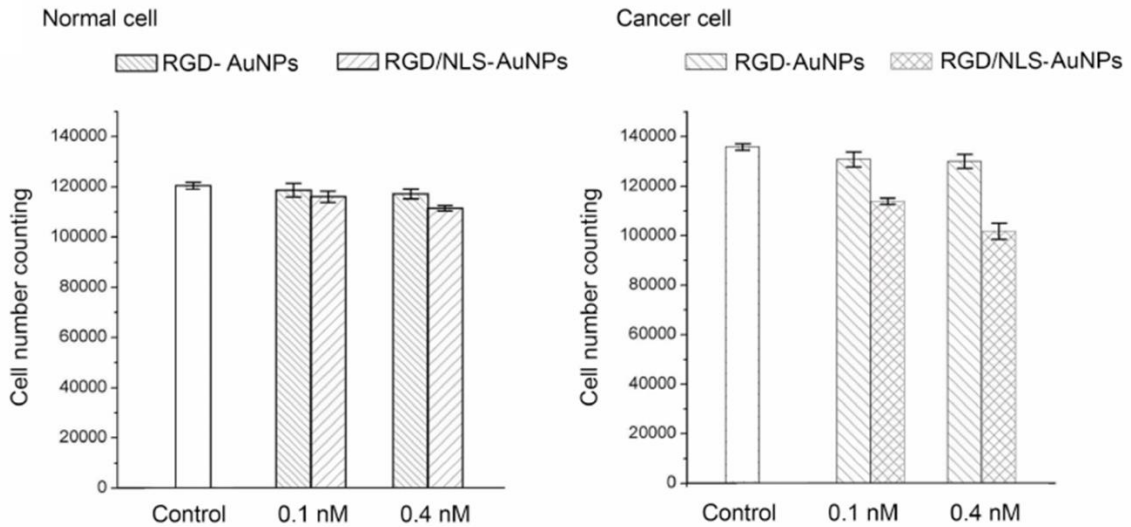


Figure 3.8. Number of normal cells (left) and cancer cells (right) counted using flow cytometry after incubation of cells with different AuNPs for 24 h.

The cancer cell number did not significantly change with AuNPs in the cytoplasm (RGD-AuNPs), but a significant decrease in the cell number (30%) was observed in the presence of 0.4 nM RGD/NLS-AuNPs. The normal cell number did not significantly change upon treatment with AuNPs. Here, both the subG1 cell population (20%) and cell number decrease (30%) were observed in only the cancer cells treated with 0.4 nM RGD/NLS-AuNPs. These results clearly show that the cytokinesis arrest observed in the live-cell imaging and synchronized cell flow cytometry for cancer cells in the presence of 0.4 nM RGD/NLS-AuNPs results in apoptosis.

3.1.4. Conclusions and Future Outlook

In conclusion, we have demonstrated that nuclear targeting of gold nanoparticles in cancer cells causes cytokinesis arrest, leading to the failure to complete cell division and thereby resulting in apoptosis. This work shows evidence that nanomaterials localized at the cell nucleus can specifically affect cellular function. A detailed mechanism has not been established, yet the results shown here are still significant. These observations have implications in understanding the basic interactions between nanomaterials and live systems and have a huge impact on the fields of nanomedicine and nanobiology. These results might even propose a new method by which AuNPs can be used alone as an anticancer therapeutic material if conjugated to the proper nuclear-targeting ligands. The cytokinesis arrest observed here could be a general effect for other types of nanoparticles that can selectively target the nuclei of cancer cells.

3.1.5. References

1. Kang, B., Mackey, M. A., and El-Sayed, M. A. (2010) Nuclear Targeting of Gold Nanoparticles in Cancer Cells Induces DNA Damage, Causing Cytokinesis Arrest and Apoptosis, *J. Am. Chem. Soc.* *132*, 1517-1519.
2. El-Sayed, M. A. (2001) Some interesting properties of metals confined in time and nanometer space of different shapes, *Acc Chem Res* *34*, 257-264.
3. Burda, C., Chen, X., Narayanan, R., and El-Sayed, M. A. (2005) Chemistry and properties of nanocrystals of different shapes, *Chem Rev* *105*, 1025-1102.
4. Link, S., and El-Sayed, M. A. (2003) Optical properties and ultrafast dynamics of metallic nanocrystals, *Annual review of physical chemistry* *54*, 331-366.
5. Boisselier, E., and Astruc, D. (2009) Gold nanoparticles in nanomedicine: preparations, imaging, diagnostics, therapies and toxicity, *Chem Soc Rev* *38*, 1759-1782.
6. Paciotti, G. F., Myer, L., Weinreich, D., Goia, D., Pavel, N., McLaughlin, R. E., and Tamarkin, L. (2004) Colloidal gold: a novel nanoparticle vector for tumor directed drug delivery, *Drug delivery* *11*, 169-183.
7. Hirsch, L. R., Stafford, R. J., Bankson, J. A., Sershen, S. R., Rivera, B., Price, R. E., Hazle, J. D., Halas, N. J., and West, J. L. (2003) Nanoshell-mediated near-infrared thermal therapy of tumors under magnetic resonance guidance, *Proceedings of the National Academy of Sciences of the United States of America* *100*, 13549-13554.
8. O'Neal, D. P., Hirsch, L. R., Halas, N. J., Payne, J. D., and West, J. L. (2004) Photo-thermal tumor ablation in mice using near infrared-absorbing nanoparticles, *Cancer Lett* *209*, 171-176.
9. Loo, C., Lowery, A., Halas, N. J., West, J., and Drezek, R. (2005) Immunotargeted nanoshells for integrated cancer imaging and therapy, *Nano Lett* *5*, 709-711.
10. El-Sayed, I. H., Huang, X., and El-Sayed, M. A. (2006) Selective laser photo-thermal therapy of epithelial carcinoma using anti-EGFR antibody conjugated gold nanoparticles, *Cancer Lett* *239*, 129-135.
11. Huang, X., El-Sayed, I. H., Qian, W., and El-Sayed, M. A. (2006) Cancer cell imaging and photothermal therapy in the near-infrared region by using gold nanorods, *J Am Chem Soc* *128*, 2115-2120.

12. Dickerson, E. B., Dreaden, E. C., Huang, X., El-Sayed, I. H., Chu, H., Pushpanketh, S., McDonald, J. F., and El-Sayed, M. A. (2008) Gold nanorod assisted near-infrared plasmonic photothermal therapy (PPTT) of squamous cell carcinoma in mice, *Cancer Lett* 269, 57-66.
13. Chithrani, B. D., Ghazani, A. A., and Chan, W. C. (2006) Determining the size and shape dependence of gold nanoparticle uptake into mammalian cells, *Nano Lett* 6, 662-668.
14. Chithrani, B. D., and Chan, W. C. (2007) Elucidating the mechanism of cellular uptake and removal of protein-coated gold nanoparticles of different sizes and shapes, *Nano Lett* 7, 1542-1550.
15. Jiang, W., Kim, B. Y., Rutka, J. T., and Chan, W. C. (2008) Nanoparticle-mediated cellular response is size-dependent, *Nature nanotechnology* 3, 145-150.
16. Qian, W., Huang, X., Kang, B., and El-Sayed, M. A. (2010) Dark-field light scattering imaging of living cancer cell component from birth through division using bioconjugated gold nanoprobe, *J Biomed Opt* 15, 046025.
17. Frens, G. (1973) Controlled nucleation for regulation of particle-size in monodisperse gold suspensions, *Nature (London), Phys. Sci.* 241, 20-22.
18. Oyelere, A. K., Chen, P. C., Huang, X., El-Sayed, I. H., and El-Sayed, M. A. (2007) Peptide-conjugated gold nanorods for nuclear targeting, *Bioconjugate chemistry* 18, 1490-1497.
19. Rogakou, E. P., Pilch, D. R., Orr, A. H., Ivanova, V. S., and Bonner, W. M. (1998) DNA double-stranded breaks induce histone H2AX phosphorylation on serine 139, *The Journal of biological chemistry* 273, 5858-5868.
20. Chen, H. T., Bhandoola, A., Difilippantonio, M. J., Zhu, J., Brown, M. J., Tai, X., Rogakou, E. P., Brotz, T. M., Bonner, W. M., Ried, T., and Nussenzweig, A. (2000) Response to RAG-mediated VDJ cleavage by NBS1 and gamma-H2AX, *Science* 290, 1962-1965.
21. Gao, H., Shi, W., and Freund, L. B. (2005) Mechanics of receptor-mediated endocytosis, *Proceedings of the National Academy of Sciences of the United States of America* 102, 9469-9474.
22. Nakielnny, S., and Dreyfuss, G. (1999) Transport of proteins and RNAs in and out of the nucleus, *Cell* 99, 677-690.
23. Xue, H., Atakilit, A., Zhu, W., Li, X., Ramos, D. M., and Pytela, R. (2001) Role of the alpha(v)beta6 integrin in human oral squamous cell carcinoma growth in vivo and in vitro, *Biochem Biophys Res Commun* 288, 610-618.

24. Scholey, J. M., Brust-Mascher, I., and Mogilner, A. (2003) Cell division, *Nature* 422, 746-752.

3.2. Inducing Cancer Cell Death by Targeting its Nucleus: Solid Gold Nanospheres versus Hollow Gold Nanocages [1]

Recently, we have shown that targeting the cancer cell nucleus with solid gold nanospheres, using a cancer cell penetrating/pro-apoptotic peptide (RGD) and a nuclear localization sequence peptide (NLS), inhibits cell division, thus leading to apoptosis. In the present work, flow cytometric analysis revealed an increase in cell death, via apoptosis and necrosis, in HSC cells upon treatment with peptide-conjugated hollow gold nanocages, compared to those treated with the peptide-conjugated solid gold nanospheres. This is consistent with a G0/G1 phase accumulation, S phase depletion and G2/M phase depletion, as well as reduced ATP levels. Here, we investigate the possible causes for the observed enhanced cell death with the use of confocal microscopy. The fluorescence images of HSC cells treated with gold nanocages, indicate the presence of reactive oxygen species, known to cause apoptosis. The formation of reactive oxygen species observed is consistent with a mechanism involving the oxidation of metallic silver on the inner cavity of the nanocage (inherent to the synthesis of the gold nanocages), to silver oxide. This oxidation is confirmed by an observed redshift in the surface plasmon resonance of the gold nanocages in cell culture medium. The silver oxide, a semiconductor known to photochemically generate hydroxyl radicals, a form of reactive oxygen species, is proposed as a mechanism for the enhanced cell death caused by gold nanocages. Thus, the enhanced cell death, via apoptosis and necrosis, observed with peptide-conjugated hollow gold nanocage-treated cells is considered to be a result of the metallic composition (silver remaining on the inner cavity) of the nanocage.

3.2.1. Introduction

Gold nanostructures and their interactions with biological systems are growing increasingly important, especially in biomedical research. Due to their unique optical properties, gold nanoparticles exhibit extrinsic activation as photothermal contrast agents, ultimately enabling the photothermal ablation of tumors by use of core-shell nanoparticles,[2, 3] gold nanorods,[4-6] gold nanocages,[7] and spherical gold nanoparticles.[6, 8] As our group has recently demonstrated, using peptide-conjugated gold and silver nanoparticles to target cancer cells *in vitro*,[9, 10] nanostructures also exhibit intrinsic antineoplastic capabilities. These targeted nanoparticles not only cause changes in the cell cycle and induce apoptosis, but their location in the cell can also be determined using plasmonic imaging, due to their high scattering cross-section, as was first demonstrated by El-Sayed and coworkers.[11] By utilizing polyethylene glycol (PEG) to minimize non-specific uptake, as well as an RGD (arginine-glycine-aspartic acid) sequence peptide and an NLS (nuclear localization sequence) peptide, nanoparticles are targeted to alpha v beta integrins on the cancer cell surface[12-15] and translocated to the nuclear pore complex,[16-18] respectively. Not only does the RGD peptide target integrins on the cell surface to serve as a cell penetration peptide, but it has also been characterized as a pro-apoptotic peptide, which induces rapid autoprocessing of the caspase-3 proenzyme, via interactions with an RGD-binding motif, causing subsequent caspase-3 activation.[19, 20] Previous reports of RGD and NLS peptides having the ability to target gold nanoparticles to the nucleus of cancer cells,[17, 21, 22] as well as the extensive studies done on the fundamental and applied properties of gold nanocages,[7, 23-26] provide an excellent platform for further investigation of the

antineoplastic properties of gold nanostructures, both solid gold nanospheres and hollow gold nanocages. One such property exhibited by gold nanostructures is the ability to modulate the cell cycle in malignant cells, which have characteristic sensitivities to cell cycle disruption, and, due to inherently compromised repair mechanisms, malignant cells can undergo subsequent apoptosis.[9, 10]

In the present work, we compare the efficacy at which nuclear-targeting gold nanostructures, of different shapes, induce disruptions in the cellular functions of HSC (human oral squamous carcinoma) cells. We specifically detect cell cycle disruptions, ATP depletion, and apoptotic and necrotic cell populations induced by both solid gold nanospheres and hollow gold nanocages. We found that the gold nanocages are much more effective in disrupting cellular functions and causing cell death than the gold nanospheres. This is shown to result from the presence of reactive oxygen species (ROS) species, known to cause apoptosis in living cells.[27] From our previous work using gold nanocages for the destruction of pollutant azo dyes,[26] we concluded that the silver remaining on the inner cavity of the gold nanocages, inherent to their synthesis, is photochemically oxidized to silver oxide, which produces reactive oxygen species. Therefore, the different metallic compositions are proposed to be the cause of different cellular disruptions observed between the nanospheres and nanocages.

3.2.2. Experimental Methods

3.2.2.1. Cell culture

Human oral squamous cell carcinoma (HSC-3) cells were maintained in Dulbecco's modified Eagle's medium (DMEM, Mediatech) supplemented with 10% v/v fetal bovine serum (FBS, Mediatech) and 1% v/v antimycotic solution (Mediatech) in a 37°C, 5% CO₂ humidified incubator.

3.2.2.2. Nanoparticle synthesis and peptide conjugation

Gold nanocages (AuNCs), with a 45 nm wall length and a 5 nm wall thickness, were prepared via galvanic replacement reaction with silver nanocubes as a template.[23] Silver nanocubes were prepared by a previously reported method.[25] Briefly, 70 mL of ethylene glycol (EG) was heated to 150°C for 1 h, followed by the addition of polyvinyl pyrrolidone (PVP, MW 55,000; 0.82 g dissolved in 5 mL EG). While still at 150°C, 0.7 mL of a 3 mM sodium sulfide solution (in EG) was added, followed by slow injection of 4 mL of a silver nitrate solution (0.48 g dissolved in 10 mL EG). [26, 28] The reaction was allowed to proceed to completion (10-15 min) resulting in the reduction of silver ions to silver nanocubes. The silver nanocubes were purified by adding a 1:2 acetone/water mixture at a volume two times that of the nanocube solution, centrifuging at 14,000 rpm for 5 min and redispersing the precipitate in 200 mL of water. The silver nanocube solution was brought to a boil under reflux, after which a 10 mg/L hydrogen tetrachloroaurate (HAuCl₄) solution was slowly injected and the UV-Vis spectrum of the solution was monitored until the absorption maximum red-shifted and remained constant at about 720 nm.[28] The AuNCs were then purified by centrifugation at 14,000 rpm for 5 min and redispersed in water. The surface plasmon absorption spectrum of the PVP-

AuNCs can be found in Figure 3.9A (black). Transmission electron microscopy (TEM) reveals the AuNCs synthesized here are between 40 and 50 nm in wall length (Fig. 3.9C).

Gold nanospheres (AuNSs), with a 35 nm diameter, were synthesized based on the method developed by Frens.[29] Briefly, 20 mL of a 1 mM HAuCl₄ solution was brought to a boil, under reflux, while stirring, followed by addition of 0.5 mL of a 1% trisodium citrate solution. Reaction completion was determined by the color changing from clear to a deep red/purple. The UV-Vis spectrum of the solution showed the absorption maximum to be around 535 nm for the AuNSs. The AuNSs were then purified by centrifugation at 6000 rpm for 15 min and redispersed in water. The surface plasmon absorption spectrum of the citrate-AuNSs can be found in Figure 3.9B (black). Transmission electron microscopy (TEM) reveals the AuNSs synthesized here are between 30 and 40 nm in diameter (Fig. 3.9D).

Prior to peptide conjugation, the AuNCs and AuNSs were coated with thiol-terminated polyethylene glycol (mPEG-SH 5000) through a Au-S bond. This was done in order to prevent nonspecific adsorption of proteins to the particles in a physiological environment. A 1 mM aqueous solution of PEG was added to AuNPs at 10⁴ molar excess, and left overnight. Particles were then purified by centrifugation at 6000 rpm for 15 min and resuspended in water. The surface plasmon absorption spectrum of the PEG-AuNCs and PEG-AuNSs can be found in Figure 3.13A,B (red), respectively.

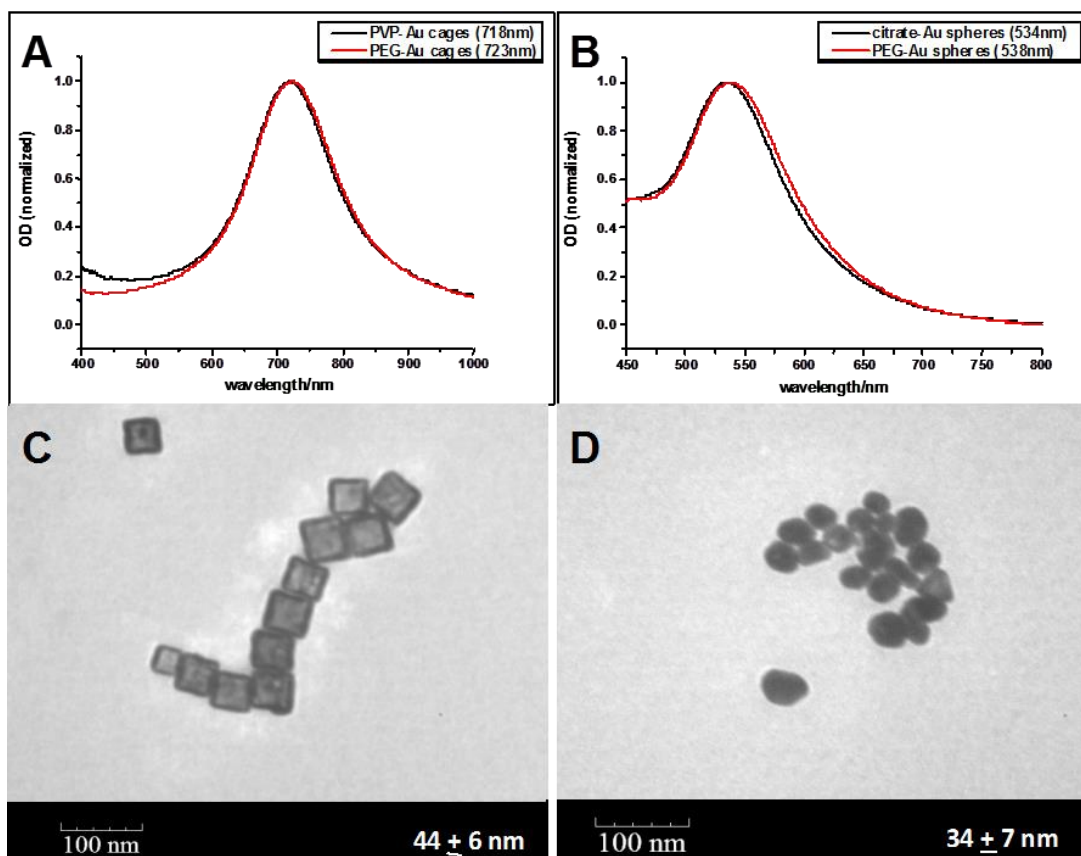


Figure 3.9. UV-Vis absorption spectra of (A) PVP-AuNCs and (B) citrate-AuNSs before (black) and after (red) conjugation with PEG. Transmission electron micrograph of (C) 45 nm PVP-AuNCs and (D) 35 nm citrate-AuNSs.

After PEGylation the AuNCs and AuNSs were further conjugated with custom peptides purchased from GenScript USA, Inc. Specifically, an RGD (RGDRGDRGDRGDPGC) peptide and an NLS (CGGGPKKKRKVGG) peptide, both with C-terminal amidation, were used in this work. Conjugation of peptides was achieved by addition of a 5 mM aqueous solution of peptide to the PEG coated nanoparticles at 1×10^4 molar excess of NLS peptides/nanoparticle and 8×10^3 molar excess of RGD peptides/nanoparticle for 24 h, after which the peptide conjugated nanoparticles were centrifuged at 6000 rpm for 15 min and redispersed in water to render RGD-AuNCs, RGD-AuNSs, NLS-AuNCs, NLS-AuNSs, RGD/NLS-AuNCs, and RGD/NLS-AuNSs.

The hydrodynamic diameter of the peptide-conjugated gold nanoparticles was determined using dynamic light scattering (DLS). The hydrodynamic diameter of the PEG-conjugated and peptide-conjugated AuNSs and AuNCs is drastically different although the actual gold nanoparticle size varies only by 10 nm. Upon conjugation with PEG, and RGD and NLS peptides, the hydrodynamic diameter of AuNCs increases to 96 nm while the RGD/NLS-AuNSs have a hydrodynamic diameter of 42 nm. The size increase to almost 100 nm observed in the case of the conjugated AuNCs is in agreement with the hydrodynamic diameter measurements previously observed, by Xia and coworkers[30], for PEG conjugated AuNCs. Further confirmation that the nanoparticle surface was modified during conjugation of PEG and peptides was achieved through zeta potential measurements, shown in Table 3.2.

Table 3.2. Zeta potential measurements for functionalized AuNSs and AuNCs used throughout this study.

	zeta potential (mV)	\pm
PEG-AuNSs	-11	2
NLS-AuNSs	-2	3
RGD-AuNSs	-4	3
RGD/NLS-AuNSs	1	3
PEG-AuNCs	-10	2
NLS-AuNCs	2	2
RGD-AuNCs	-1	3
RGD/NLS-AuNCs	-3	1

The peptide conjugated AuNCs and AuNSs were further diluted in DMEM to 0.1 and 0.4 nM, for treatment of HSC-3 cells. The gold nanoparticle concentrations were

determined using $\varepsilon = 5.0 \times 10^9$ (AuNCs), which was calculated based on ICP measurements, and $\varepsilon = 5.3 \times 10^9$ (AuNSs), which is based on previous reports.[31] ICP analysis was done by dissolving the AuNC solution in aqua regia (1 part HNO₃ to 3 parts HCl).

3.2.2.3. Gold nanoparticle internalization

Two different methods were used to determine nanoparticle uptake by HSC-3 cells. First, to determine the percentage of nanoparticles taken up by HSC-3 cells, a previously utilized spectroscopic method was used[10]. Specifically, the cells were grown in 96-well tissue culture plates overnight. The growth media was then removed and replaced with growth media containing gold nanoparticles. After a 48 h incubation period with gold nanoparticles, the gold nanoparticle-containing media was removed and placed into a cell-free 96-well plate. The optical density was analyzed on a Biotek Synergy H4 multi-mode plate reader at wavelengths of 723 and 538 nm (plasmon absorption for the AuNCs and AuNSs, respectively). In order to determine nanoparticle uptake, the recorded optical density was subtracted from the optical density of the gold nanoparticle-containing growth media initially added to the cell culture. This value was then converted to a percentage of what was initially added to the cell culture. Second, to visualize the nanoparticles inside HSC-3 cells by plasmonic dark field light scattering imaging, cells were grown on coverslips for 24 h, after which the culture medium was removed and replaced with nanoparticle-containing medium. HSC-3 cells were then grown in the presence of 0.4 nM peptide-conjugated gold nanoparticles for 48 h. The nanoparticle-containing medium was removed and the cells were washed with PBS buffer. In order to remove nanoparticles that have not been internalized by the HSC-3 cells, a previously

developed etching method was used.[32] Briefly, 1 mL of an aqueous solution containing a 1:6 molar ratio mixture of I₂ (0.34 mM) and KI was added to the cells and removed after 5 min. The coverslips were then washed with deionized water. The cells were then fixed with 4% paraformaldehyde. Dark field images were taken using an inverted Olympus IX70 microscope utilizing a dark field condenser (U-DCW) and a 100x/1.35 oil Iris objective (UPLANAPO).

3.2.2.4. Nuclear localization of nanoparticles by confocal microscopy

For FITC labeling, nanoparticles were conjugated with FITC-PEG-SH prior to peptide conjugation. After nanoparticle functionalization, HSC cells were prepared for confocal imaging. Briefly, HSC-3 cells were grown on coverslips overnight. The growth media was then removed and replaced with growth media containing FITC-PEG-RGD/NLS-AuNCs and AuNSs. After a 24 h incubation period with gold nanoparticles, the gold nanoparticle-containing media was removed and the cells were washed with PBS. Cells were then fixed with 4% paraformaldehyde for 15 min, followed by nuclear staining with DAPI (4',6-Diamidino-2-phenylindole, Dihydrochloride, Invitrogen) and washing with water. Fluorescence images were taken by multiphoton confocal microscopy using the Zeiss LSM 510 NLS META with 785 (DAPI) and 488 nm (FITC) excitation sources.

3.2.2.5. Flow cytometry cell cycle analysis

HSC-3 cells were grown in 12-well tissue culture plates overnight. The growth media was then removed and replaced with growth media containing gold nanoparticles. After cells were treated with gold nanoparticles for 48 h, they were fixed in 70% ethanol, centrifuged, washed, and resuspended in phosphate buffered saline (PBS). Cells were

then treated with 10 µg/mL RNase (Sigma) at 37°C for 30 min, after which they were stained with 100 µg/mL of propidium iodide (PI), fluorescent DNA stain, for 15 min at room temperature. Samples, consisting of 10,000 cells, in triplicate, were analyzed using the BD LSR II (BD Biosciences) with a 488 nm excitation. Using the flow cytometry analysis software, FlowJo, DNA content and subsequent cell cycle analyses were carried out.

3.2.2.6. ATP assay

HSC-3 cells were grown in white opaque-walled 96-well tissue culture plates overnight, after which the growth media was replaced with gold nanoparticle-containing media. Upon 48 h treatment with nanoparticles, the CellTiter-Glo® Luminescent Cell Viability Assay was used according to the manufacturer's protocol. Briefly, the CellTiter-Glo® Reagent was prepared by mixing the CellTiter-Glow® Buffer with the CellTiter-Glo® Substrate. After 48 h gold nanoparticle treatment, the cells were rinsed with PBS, 100 µL of fresh media was added, and the plate was allowed to equilibrate to room temperature. 100 µL of the CellTiter-Glo® Reagent was then added to the cells and the plate was mixed on an orbital shaker for 2 min to promote cell lysis. Luminescence was then recorded on a Biotek Synergy H4 multi-mode plate reader. This method provides a quantitative measurement of the amount of ATP in the cell culture, and can be used as a cell viability assay, as the luminescence signal is directly correlated to the number of metabolically active cells, based on their ATP production.[33]

3.2.2.7. Flow cytometry analysis of apoptosis and necrosis

HSC-3 cells were grown in 12-well tissue culture plates overnight, after which the growth media was removed and replaced with growth media containing gold

nanoparticles. After cells were treated with gold nanoparticles for 48 h, an Alexa Fluor 488 annexin-V/Dead Cell Apoptosis kit for flow cytometry (Invitrogen) was used for the detection of apoptosis and necrosis. The standard protocol was optimized for our experimental conditions. Briefly, cells were centrifuged, washed, and resuspended in 1 mL of 1X annexin-binding buffer. After which 5 μ L of Alexa Fluor 488 annexin-V and 2 μ L of 100 mg/mL propidium iodide (PI) were added to the cell suspension and left to incubate at room temperature for 15 min. Upon completion of dye loading, 1 mL of 1X annexin-binding buffer was added. Cells were analyzed immediately using the BD LSR II (BD Biosciences) with a 488 nm excitation on 10,000 cells, in triplicate. Using the flow cytometry analysis software, FlowJo, the Alexa Fluor 488 and PI intensities were gated based on a negative control (HSC-3 cells in nanoparticle-free media) and a positive control for apoptosis (HSC-3 cells treated with 10 μ M camptothecin for 4 h).

3.2.2.8. Confocal acquisition of ROS

HSC-3 cells were grown on coverslips overnight. The growth media was then removed and replaced with growth media containing gold nanoparticles. After a 24 h incubation period with gold nanoparticles, the gold nanoparticle-containing media was removed and the cells were washed with PBS, after which the cells were stained with a 10 μ M solution of H2DCFDA (6-carboxy-2',7'-dichlorodihydrofluorescein diacetate, Invitrogen, C2938) and left to incubate at 37°C for 30 min. After dye loading, the cells were washed with PBS and fixed with 4% paraformaldehyde for 15 min, followed by nuclear staining with DAPI (4'-6-Diamidino-2-phenylindole, Dihydrochloride, Invitrogen) and washing with water. Fluorescence images were taken by multiphoton confocal

microscopy using the Zeiss LSM 510 NLS META with 785 (DAPI) and 488 nm (FITC) excitation sources.

3.2.2.9. Statistical analysis

All results are expressed as the mean \pm standard deviation of three independent experiments. Statistical significance (*i.e.* p-value) was calculated using a *t-test calculator* (GraphPad Software, Inc.) and the data is considered statistically significant (indicated by *) when $p < 0.05$.

3.2.3. Results and Discussion

HSC cells were treated with gold nanoparticles of different shape: solid gold nanospheres (AuNSs, ~35 nm diameter) and hollow gold nanocages (AuNCs, ~45 nm wall length) as shown in Figure 3.13. These two distinctly shaped gold nanoparticles were stabilized with polyethylene glycol thiol (mPEG-SH, MW 5000) in order to prevent any nonspecific interactions that might take place with these nanoparticles in the physiological environment. The PEGylated gold nanoparticles were then functionalized with specific peptides: an RGD (arginine-glycine-aspartic acid) sequence peptide and an NLS (nuclear localization sequence) peptide. The RGD peptide provides for receptor-mediated uptake of nanoparticles by cancer cells, as it mimics extracellular matrix proteins and targets alpha v beta integrins that are overexpressed on the cell surface of HSC cells,[13, 34] while also exhibiting pro-apoptotic capabilities.[19, 20] The NLS peptide from the simian virus (SV) large T antigen, having a KKKRK (lysine-lysine-lysine-arginine-lysine) sequence, provides for nuclear localization of nanoparticles, by binding importin alpha in the cytoplasm of the cell, which subsequently binds importin

beta located on the cytoplasmic side of the nuclear membrane.[35-39] Peptide conjugation was exploited to give rise to six different types of gold nanoparticles, RGD-AuNSs NLS-AuNSs, RGD/NLS-AuNSs, RGD-AuNCs, NLS-AuNCs, and RGD/NLS-AuNCs. Each nanoparticle type exhibited cellular internalization, with the NLS peptide-conjugated nanoparticles showing subsequent nuclear localization. Cellular internalization (*i.e.* nanoparticle uptake) is shown in Figure 3.10A.

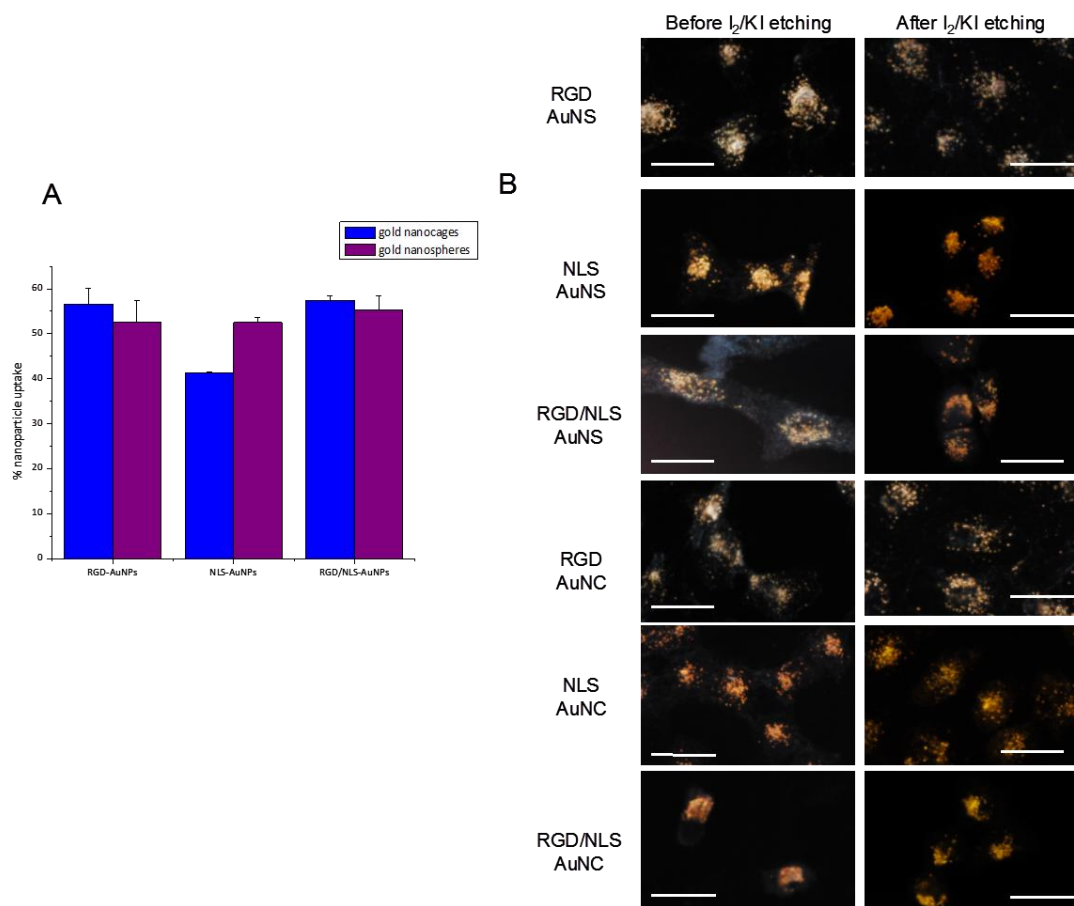


Figure 3.10. Cellular internalization and nuclear localization of peptide-conjugated AuNPs by HSC cells after 48 h, determined as the percent uptake (A), as well as the with plasmonic dark field light scattering imaging (B) of internalized nanoparticles before and after etching of extracellular nanoparticles. Scale bar: 20 μ m

Overall, each nanoparticle formulation exhibits about 50% uptake by HSC cells over 48 h. In order to confirm the internalization of the nanoparticles, plasmonic dark field imaging and a previously developed etching technique were employed.[32] With this technique, it can be seen that the plasmonic dark field light scattering images, shown in Figure 3.10B, before and after the removal of extracellular nanoparticles by I₂/KI etching, are the same, suggesting nanoparticle internalization by HSC cells has occurred. Also, these images suggest the nuclear localization of the nanoparticles conjugated with the NLS peptide, while those without appear to be more dispersed throughout the cytoplasm of the cell, as we have shown previously with similar nanoparticle formulations.[9] Co-localization of the RGD/NLS-AuNSs and RGD/NLS-AuNCs with the nucleus was also confirmed with confocal imaging, as shown in Figure 3.11.

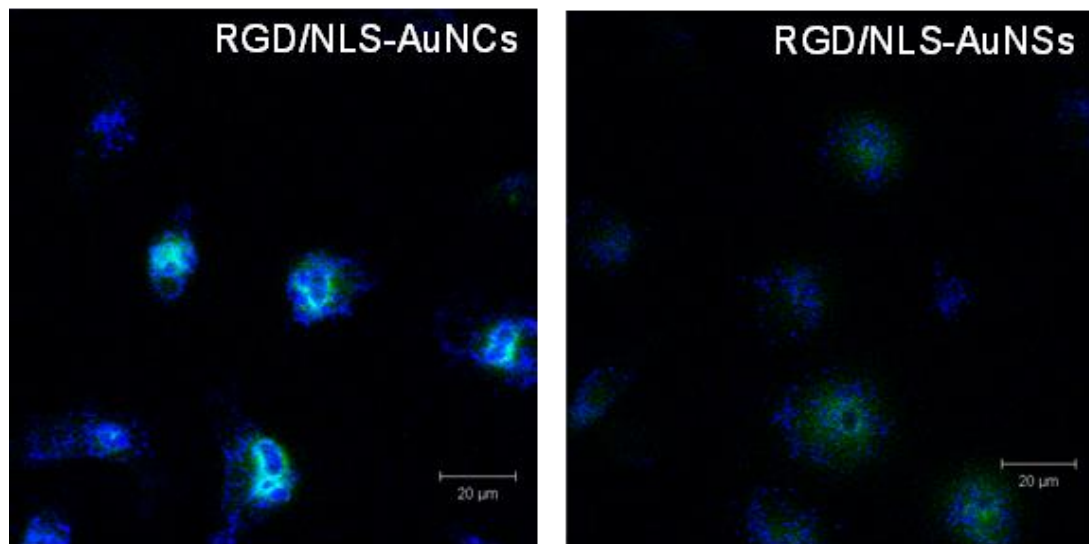


Figure 3.11. Confocal microscopy images of FITC (green) labeled RGD/NLS-AuNCs (left) and AuNSs (right) co-localized with the nuclei (blue) of HSC cells. Scale bar: 20 μm.

Upon confirmation of nuclear and cytoplasmic localization, all nanoparticles were examined in terms of their effects on HSC cellular functions, as well as their ability to induce cell death via apoptosis and necrosis.

3.2.3.1. Nanoparticle-induced disruption of cellular functions

Cell cycle analysis was utilized in order to compare the dependence of cell cycle disruption on nanoparticle shape (solid sphere or hollow cage), as well as nanoparticle concentration (0.1 or 0.4 nM). The most significant changes seen for all of the nanoparticle formulations occur when HSC cells are treated with a 0.4 nM concentration. With this high concentration, HSC cells experience cell cycle disruptions that have been previously linked to apoptosis.[40] The cell cycle changes observed for the RGD/NLS-AuNSs and RGD/NLS-AuNCs, as shown in Figure 3.12 (A and B, respectively), are an increased G0/G1 phase population (16% by AuNCs and 19% by AuNSs), a decreased S phase population (10% by AuNCs and 2% by AuNSs) and a decreased G2/M phase population (100% by both AuNCs and AuNSs).

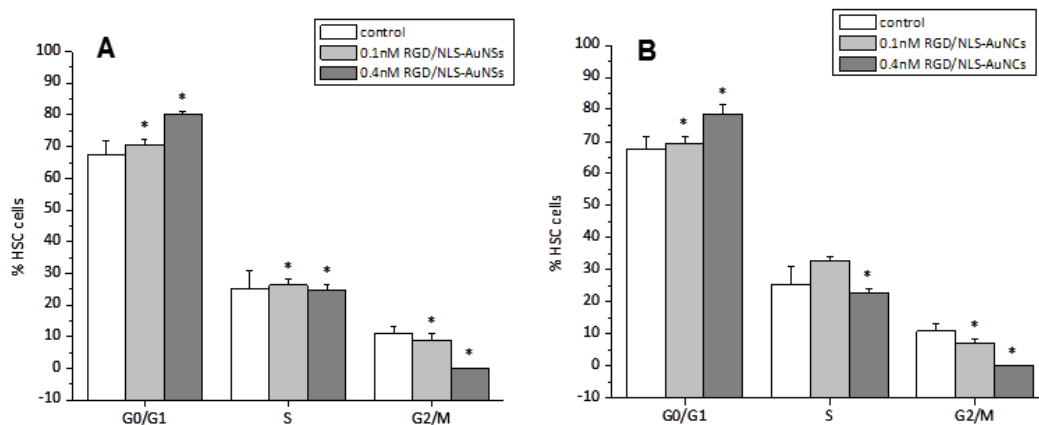


Figure 3.12. Cell cycle changes induced by peptide-conjugated AuNPs, compared to control (HSC cells treated with nanoparticle-free culture medium). RGD/NLS-AuNSs (A), and RGD/NLS-AuNCs (B), at concentrations of 0.4 nM, both generate an increase in G0/G1 phase, a decrease in S phase and a decrease in G2/M phase populations when incubated with HSC cells for 48 h. Values expressed as mean \pm standard deviation of three independent experiments. Statistical significance, with respect to control, indicated by * ($p < 0.05$).

Similar trends are seen with the RGD-conjugated and NLS-conjugated gold nanoparticles, shown in Appendix A, Figure A.5, except when HSC cells are treated with 0.1 nM RGD-AuNCs. In this case, a prominent G2/M arrest is observed, which has been correlated to cytokinesis arrest and apoptosis.[9] The more common trend observed here, G0/G1 phase accumulation and subsequent S phase depletion, has been attributed to a decrease in cellular ATP, as demonstrated using mitochondrial function disrupting agents.[41] Therefore, a direct quantitative measure of the ATP in gold nanoparticle-treated HSC cells was carried out. As shown in Figure 3.13, the amount of ATP present in cells is reduced with increased nanoparticle treatment concentrations for all nanoparticle formulations.

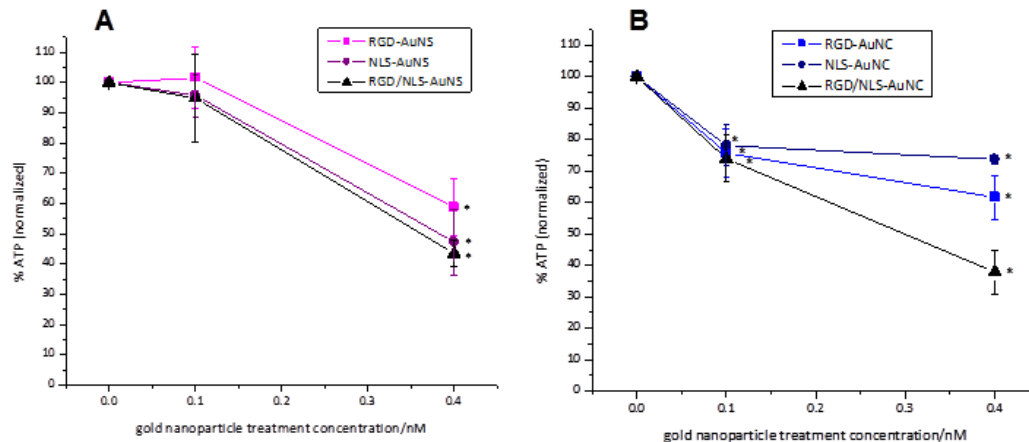


Figure 3.13. ATP depletion induced by peptide-conjugated AuNPs (0.1 and 0.4 nM), normalized to the control (HSC cells treated with nanoparticle-free medium) after 48 h. The combination of RGD and NLS peptides conjugated to the nanoparticles allows for the greatest reduction in ATP in the case of the AuNSs (A) and AuNCs (B). Values expressed as mean \pm standard deviation of three independent experiments. Statistical significance, with respect to control (0.0 nM), indicated by * ($p < 0.05$).

The greatest reduction in ATP is observed with 0.4 nM RGD/NLS-AuNCs and RGD/NLS-AuNSs, as would be expected, based on the cell cycle changes observed for these two nanoparticle treatments (Fig. 3.12). When HSC cells are treated with 0.4 nM RGD/NLS-AuNCs, ATP production is reduced to about 38%, which is slightly lower than the 43% ATP production observed with 0.4 nM RGD/NLS-AuNS-treated cells. With previous evidence of the reduction of ATP leading to apoptosis[40], the sub G1 cell population observed in the cell cycle histograms (Appendix A, Figure A.6), and the efficacy at which these HSC cell nucleus targeting (RGD/NLS) nanoparticles reduce ATP in HSC cells, it is imperative to assess the fate of these physiological changes and to determine if the outcome (*i.e.* apoptosis and/or necrosis) is dependent on the nanoparticle structure (*i.e.* solid sphere vs. hollow cage). In order to directly resolve whether or not the peptide-conjugated gold nanoparticles utilized in this study cause apoptosis and/or

necrosis, flow cytometric analysis of Alexa Fluor 488 conjugated annexin-V and propidium iodide (PI) in HSC cells was utilized. One of the earliest events that take place during apoptosis is the exposure of phosphatidylserine (PS) residues on the outer leaflet of the cell membrane. These PS residues have a high affinity for the phospholipid binding protein annexin-V. Therefore, by exposing cells to fluorescently labeled annexin-V, apoptosis can be quantified by the fluorescence intensity measured using flow cytometry.[42] The apoptotic population can be distinguished from the necrotic population with the addition of PI, which binds nucleic acids in cells only once the membrane becomes permeable (*i.e.* necrosis).

HSC cells were treated with 0.1 and 0.4 nM concentrations of peptide-conjugated gold nanoparticles and the percentages of apoptotic and necrotic cells were determined. The RGD/NLS-conjugated nanoparticles induce greater overall cell death than those conjugated with only RGD or only NLS (Appendix A, Figure A.7), which correlates well with the observed decrease in ATP for these nanoparticle formulations in particular. As shown in Figure 3.14, the AuNCs significantly induce more apoptosis (Fig. 3.14A) and necrosis (Fig. 3.14B) than the AuNSs. At higher treatment concentrations, the RGD/NLS-AuNCs induce apoptosis in HSC cells two times greater than RGD/NLS-AuNSs.

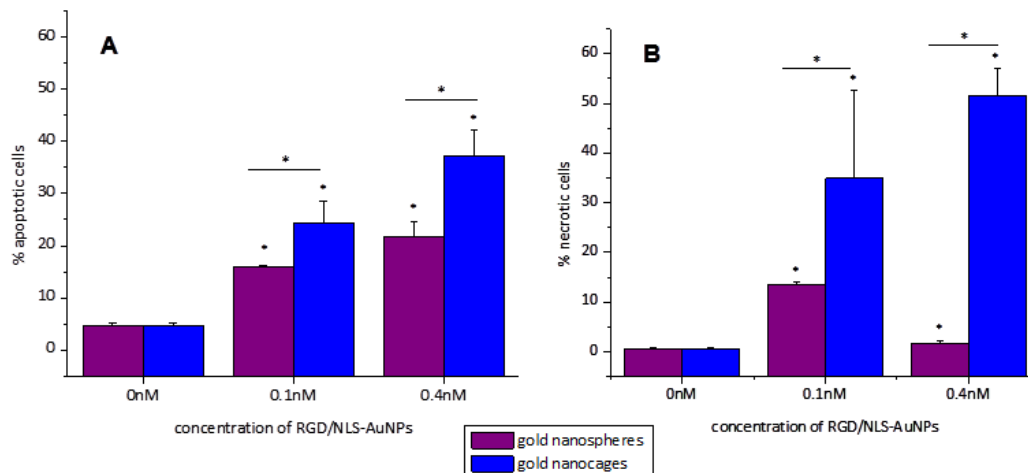


Figure 3.14. Cell death, via apoptosis (A) and necrosis (B), induced in HSC cells after 48 h treatment with 0, 0.1, and 0.4 nM peptide-conjugated AuNSs (purple) and AuNCs (blue). The RGD/NLS-AuNCs, at 0.4 nM treatment concentrations, induce the greatest amount of cell death. Values expressed as mean \pm standard deviation of three independent experiments. Statistical significance, with respect to control (above each bar) and between AuNSs and AuNSs (above each line) indicated by * ($p < 0.05$).

At higher concentrations, the RGD/NLS-AuNCs induce thirty times more necrosis than RGD/NLS-AuNSs. It is also important to note that these nanoparticles induce minimal cell death in a control (HaCat) cell line (Appendix A, Figure A.8), as these cells do not overexpress alpha beta integrins[43] and thereby are not effectively targeted with the RGD conjugated nanoparticle. The drastic differences in which the peptide-conjugated nanoparticles, solid gold spheres and hollow gold cages, induce cell death in HSC cells prompt an explanation for how two different gold nanoparticle formulations could have such different effects on these cells.

3.2.3.2. Possible mechanism for enhanced nanoparticle-induced cell death by the nanocages

Since it has been shown previously that nanoparticle conjugates exhibit enhanced cellular effects compared to the free ligands in solution,[44, 45] we therefore propose that

the RGD and NLS peptides conjugated to the nanoparticles are more effective than when free in solution. HSC cells were treated with the same concentration of NLS and RGD peptides as that which was added to the nanoparticles during conjugation (4 and 3.2 μM , respectively). The free NLS and RGD peptides induce much lower levels of apoptosis and necrosis, as seen in Figure 3.15, compared to that when conjugated to the AuNSs and AuNCs.

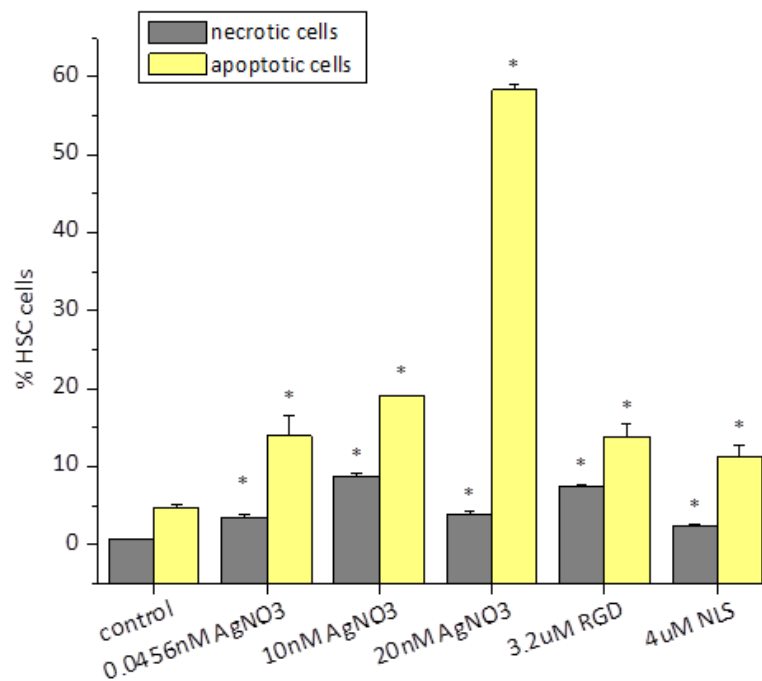


Figure 3.15. Cell death induced, via apoptosis (yellow) and necrosis (grey), in HSC cells after 48 h treatment with varying concentrations AgNO₃ (*i.e.* Ag⁺ ions), as well as free peptides in culture medium (3.2 μM RGD and 4 μM NLS). Values expressed as mean \pm standard deviation of three independent experiments. Statistical significance, with respect to control, indicated by * ($p < 0.05$).

This is possibly due to an RGD-dependent pathway. As was previously suggested by Salmon and coworkers, the RGD peptide activates pro-caspase-3, a pro-apoptotic protein,

via interactions with an RGD-binding motif and subsequent conformational changes in the protein.[19, 20] It is possible that multivalency (*i.e.* localized RGD peptides bound to the gold nanoparticle surface) can enhance the overall effect of RGD on the cell.

Another mechanism is proposed based on the confirmation that the RGD/NLS-AuNCs reduce ATP and induce apoptosis and necrosis in HSC cells to a greater extent than RGD/NLS-AuNSs. As expected, based on the method of AuNC synthesis (see Experimental section 3.3.2.2), ICP results show a 10% silver atom content in the metallic composition of the AuNCs used in this study. Therefore, we consider the possibility that there could be Ag^+ ions present in the nanoparticle solution used for the treatment of HSC cells. In order to quantify the amount of Ag^+ ions, NaCl was added to the 0.4 nM RGD/NLS-AuNC solution, such that the NaCl concentration is slightly below its K_{sp} . Upon dissolution of NaCl in the 0.4 nM RGD/NLS-AuNC solution, no AgCl white precipitate was observed, indicating that the concentration of Ag^+ in the AuNC solution must be below 0.0456 nM. Therefore, HSC cells were treated with 0.0456 nM AgNO_3 to represent the maximum concentration of Ag^+ ions that could be present in the 0.4 nM RGD/NLS-AuNC treatment, as well as 10 and 20 nM AgNO_3 , to represent the concentration of Ag^+ ions that would be needed in order to observe high levels of apoptosis or necrosis. Figure 3.15 displays the apoptotic and necrotic populations for cells treated with increasing concentrations of AgNO_3 (*i.e.* Ag^+ ions). It is obvious here that 0.0456 nM Ag^+ is not sufficient to induce apoptosis or necrosis to the extent at which the 0.4 nM RGD/NLS-AuNCs do. It is also apparent that the concentration of Ag^+ would have to be on the order of 20 nM for there to be significant apoptosis in HSC cells. Although the Ag^+ ions do not appear to induce apoptosis or necrosis, the residual silver

atoms remaining on the inner cavity of the AuNCs could possibly have been oxidized in the cell culture medium to silver oxide (Ag_2O).^[26, 46] To test this, AuNCs were left under physiological conditions, in cell culture medium, for 48 h, after which the UV-Vis spectrum was taken in order to detect any changes in the surface plasmon resonance of the AuNCs. Indeed, a 51 nm redshift in the AuNC surface plasmon resonance was observed after 48 h in cell culture medium, as shown in Figure 3.16, indicating the residual silver atoms on the inner cavity of the AuNC were oxidized to Ag_2O .^[47-49]

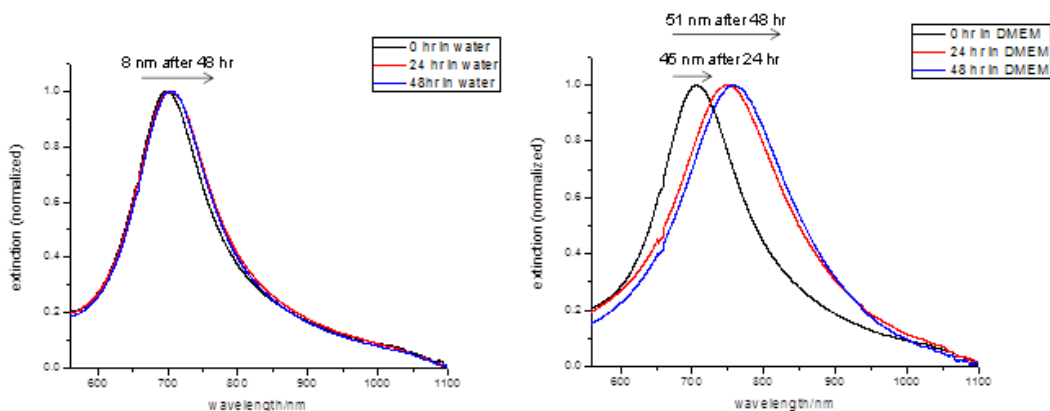


Figure 3.16. UV-Vis spectra of AuNCs in water (left) and DMEM, cell culture medium (right). A 51 nm shift in the surface plasmon of the AuNCs in DMEM is observed after 48 h at physiological conditions indicating the oxidation of silver atoms to Ag_2O on the inner cavity of the AuNC.

It has previously been shown, by Yen, *et. al.*,^[26] that when Ag_2O is formed on the inside of the gold nanocage, it has the ability to produce hydroxyl radicals (generally termed reactive oxygen species (ROS)). These ROS have shown to damage DNA, ultimately leading to apoptosis, especially when located near the DNA,^[27] as would be expected with the nuclear-targeted AuNPs studied here. Therefore, it is important to consider the possibility that ROS are generated by the RGD/NLS-AuNCs, which might

be causing the observed enhanced apoptosis and necrosis[50] above that observed with RGD/NLS-AuNSs. Confocal imaging was performed to detect the presence of ROS in HSC cells treated with 0.4 nM RGD/NLS-AuNCs and AuNSs, as shown in Figure 3.17.

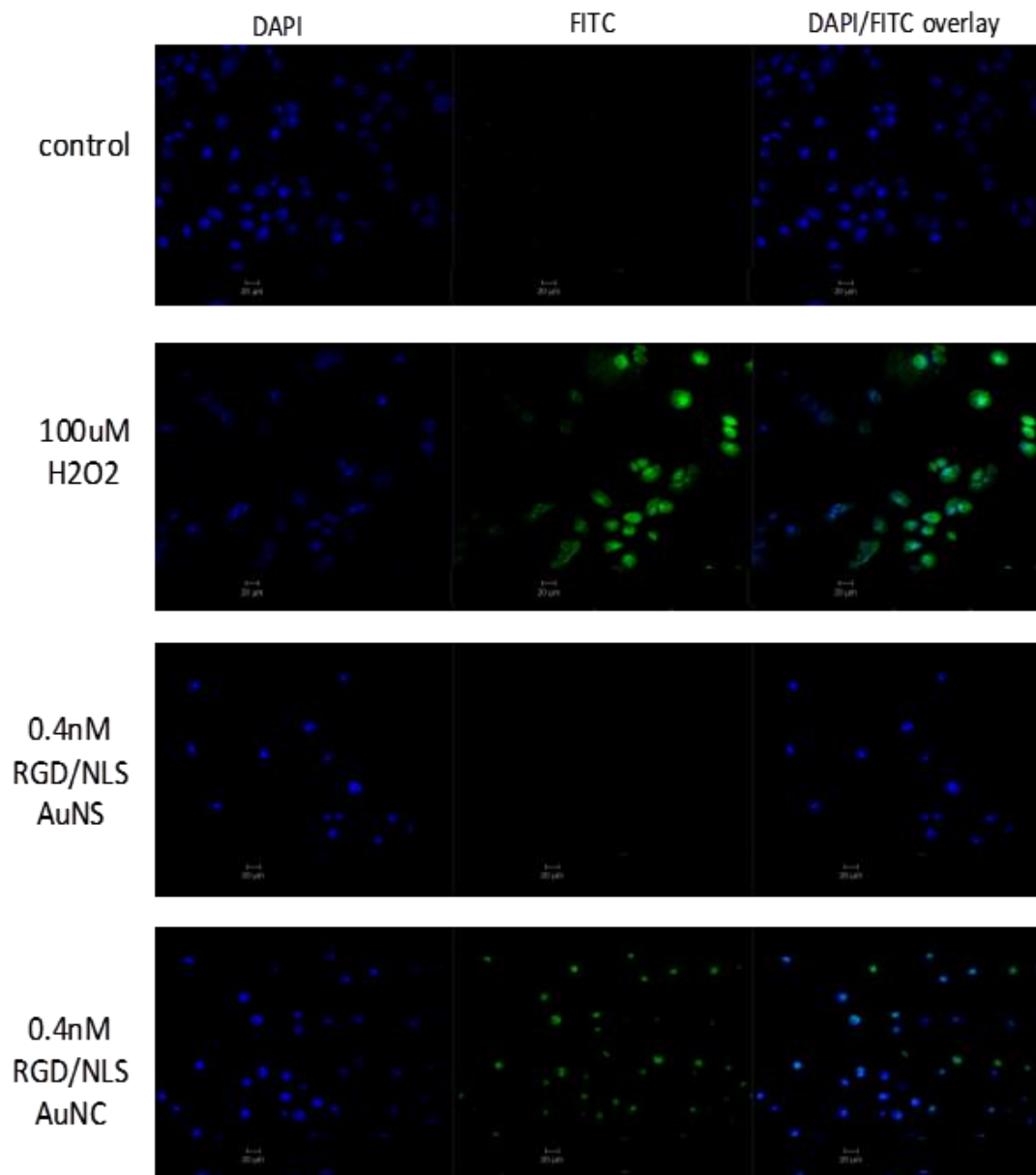


Figure 3.17. Reactive oxygen species (ROS) generation detected by confocal microscopy for 0.4 nM RGD/NLS-AuNSs and AuNCs. DAPI panel (left) shows the nuclei of HSC cells stained blue. FITC panel (middle) represents green fluorescence indicative of ROS generated inside cells. DAPI/FITC overlay (right) shows the combination of both nuclei and ROS. Control (cells treated with nanoparticle-free medium) exhibits minimal FITC fluorescence, along with the 0.4 nM RGD/NLS-AuNSs. 100 μ M H₂O₂ shows high FITC fluorescence, used as a positive control for ROS generation. The 0.4 nM RGD/NLS-AuNCs display FITC fluorescence, indicating ROS are generated in HSC cells with this nanoparticle treatment. Scale bar: 20 μ m.

HSC cells were stained with H2DCFDA after treatment with nanoparticles and a green fluorescent (FITC) signal is generated when the acetate groups of H2DCFDA are removed during intracellular oxidation via the generation of ROS. The confocal images shown in Figure 3.17 show that there are indeed ROS in the RGD/NLS-AuNC-treated HSC cells, which is not seen with the RGD/NLS-AuNS treatment. The presence of ROS is also detected with other peptide-conjugated AuNCs, but not the AuNSs (Appendix A, Figure A.9). Although the ROS seen with the AuNCs is not as apparent as the ROS seen with a positive control (100 μ M H₂O₂ for 3 h), it can still be concluded that the silver atom content on the inner cavity of the AuNCs has an impact on the enhanced apoptosis and necrosis observed for the RGD/NLS-AuNC-treated HSC cells.

3.2.4. Conclusions and Future Outlook

We have found here that hollow gold nanocages conjugated with nuclear targeting (NLS) and cancer cell penetration/pro-apoptotic (RGD) peptides induce apoptosis and necrosis in HSC cancer cells to a greater extent than solid gold nanospheres. The observed cell death is preceded by a number of different processes that also appear to be dependent on the concentration and shape/metallic composition of the peptide-conjugated gold nanoparticles. It is found that the 0.4 nM RGD/NLS-AuNCs and RGD/NLS-AuNSs induce cell cycle changes (*i.e.* G0/G1 phase accumulation, S phase depletion and G2/M phase depletion) (Fig. 3.12) and subsequently reduce ATP production in HSC cells (Fig. 3.13). The outcome of these cell cycle changes and reduction in ATP is apoptosis and necrosis (Fig. 3.14), with the greatest degrees of apoptosis and necrosis occurring when HSC cells are treated with the hollow gold nanocages. The increased apoptosis and

necrosis seen with hollow gold nanocages can be explained based on the metallic composition of the gold nanocage. As a result of the synthesis, the gold nanocage has residual silver atoms on its inner cavity, which can be easily oxidized to Ag_2O , as observed by a redshift in the AuNC surface plasmon resonance (Fig. 3.16),[47-49] which in turn produces ROS,[26, 50] as observed by confocal microscopy of HSC cells treated with 0.4 nM RGD/NLS-AuNCs (Fig. 3.17). In conclusion, it is clear here that the metallic composition and thus, the shape of gold nanoparticles have an impact on their intrinsic antineoplastic properties, which can possibly be exploited further in the treatment of cancer.

3.2.5. References

1. Mackey, M. A., Saira, F., Mahmoud, M. A., and El-Sayed, M. A. (2013) Inducing Cancer Cell Death by Targeting Its Nucleus: Solid Gold Nanospheres versus Hollow Gold Nanocages, *Bioconjugate chemistry* 24, 897-906.
2. Hirsch, L. R., Stafford, R. J., Bankson, J. A., Sershen, S. R., Rivera, B., Price, R. E., Hazle, J. D., Halas, N. J., and West, J. L. (2003) Nanoshell-mediated near-infrared thermal therapy of tumors under magnetic resonance guidance, *Proceedings of the National Academy of Sciences of the United States of America* 100, 13549-13554.
3. O'Neal, D. P., Hirsch, L. R., Halas, N. J., Payne, J. D., and West, J. L. (2004) Photo-thermal tumor ablation in mice using near infrared-absorbing nanoparticles, *Cancer Lett* 209, 171-176.
4. Dickerson, E. B., Dreaden, E. C., Huang, X. H., El-Sayed, I. H., Chu, H. H., Pushpanketh, S., McDonald, J. F., and El-Sayed, M. A. (2008) Gold nanorod assisted near-infrared plasmonic photothermal therapy (PPTT) of squamous cell carcinoma in mice, *Cancer Lett.* 269, 57-66.
5. Huang, X. H., El-Sayed, I. H., Qian, W., and El-Sayed, M. A. (2006) Cancer cell imaging and photothermal therapy in the near-infrared region by using gold nanorods, *J. Am. Chem. Soc.* 128, 2115-2120.
6. Huang, X. H., Jain, P. K., El-Sayed, I. H., and El-Sayed, M. A. (2007) Gold nanoparticles: interesting optical properties and recent applications in cancer diagnostic and therapy, *Nanomedicine* 2, 681-693.
7. Chen, J. Y., Wang, D. L., Xi, J. F., Au, L., Siekkinen, A., Warsen, A., Li, Z. Y., Zhang, H., Xia, Y., and Li, X. (2007) Immuno gold nanocages with tailored optical properties for targeted photothermal destruction of cancer cells, *Nano Lett.* 7, 1318-1322.
8. El-Sayed, I. H., Huang, X. H., and El-Sayed, M. A. (2006) Selective laser photothermal therapy of epithelial carcinoma using anti-EGFR antibody conjugated gold nanoparticles, *Cancer Lett.* 239, 129-135.

9. Kang, B., Mackey, M. A., and El-Sayed, M. A. (2010) Nuclear Targeting of Gold Nanoparticles in Cancer Cells Induces DNA Damage, Causing Cytokinesis Arrest and Apoptosis, *J. Am. Chem. Soc.* *132*, 1517-1519.
10. Austin, L. A., Kang, B., Yen, C. W., and El-Sayed, M. A. (2011) Nuclear Targeted Silver Nanospheres Perturb the Cancer Cell Cycle Differently than Those of Nanogold, *Bioconjugate Chem.* *22*, 2324-2331.
11. El-Sayed, I. H., Huang, X. H., and El-Sayed, M. A. (2005) Surface plasmon resonance scattering and absorption of anti-EGFR antibody conjugated gold nanoparticles in cancer diagnostics: Applications in oral cancer, *Nano Lett.* *5*, 829-834.
12. Zitzmann, S., Ehemann, V., and Schwab, M. (2002) Arginine-glycine-aspartic acid (RGD)-peptide binds to both tumor and tumor-endothelial cells in vivo, *Cancer Res.* *62*, 5139-5143.
13. Xue, H., Atakilit, A., Zhu, W. M., Li, X. W., Ramos, D. M., and Pytela, R. (2001) Role of the alpha v beta 6 integrin in human oral squamous cell carcinoma growth in vivo and in vitro, *Biochem. Biophys. Res. Commun.* *288*, 610-618.
14. Xue, H., Atakilit, A., Zhu, W. M., Sheppard, D., Ramos, D. M., and Pytela, R. (2000) Role of av beta 6 integrin in growth and migration of oral squamous cell carcinoma, *Mol. Biol. Cell* *11*, 1363.
15. Castel, S., Pagan, R., Mitjans, F., Piulats, J., Goodman, S., Jonczyk, A., Huber, F., Vilaro, S., and Reina, M. (2001) RGD peptides and monoclonal antibodies, antagonists of alpha(v)-integrin, enter the cells by independent endocytic pathways, *Lab. Invest.* *81*, 1615-1626.
16. Tkachenko, A. G., Xie, H., Liu, Y. L., Coleman, D., Ryan, J., Glomm, W. R., Shipton, M. K., Franzen, S., and Feldheim, D. L. (2004) Cellular trajectories of peptide-modified gold particle complexes: Comparison of nuclear localization signals and peptide transduction domains, *Bioconjugate Chem.* *15*, 482-490.
17. Tkachenko, A. G., Xie, H., Coleman, D., Glomm, W., Ryan, J., Anderson, M. F., Franzen, S., and Feldheim, D. L. (2003) Multifunctional gold nanoparticle-peptide complexes for nuclear targeting, *J. Am. Chem. Soc.* *125*, 4700-4701.

18. Escriou, V., Carriere, M., Scherman, D., and Wils, P. (2003) NLS bioconjugates for targeting therapeutic genes to the nucleus, *Adv. Drug Delivery Rev.* 55, 295-306.
19. Fischer, U., and Schulze-Osthoff, K. (2005) Apoptosis-based therapies and drug targets, *Cell Death Differ.* 12, 942-961.
20. Buckley, C. D., Pilling, D., Henriquez, N. V., Parsonage, G., Threlfall, K., Scheel-Toellner, D., Simmons, D. L., Akbar, A. N., Lord, J. M., and Salmon, M. (1999) RGD peptides induce apoptosis by direct caspase-3 activation, *Nature* 397, 534-539.
21. Huang, X. H., Kang, B., Qian, W., Mackey, M. A., Chen, P. C., Oyelere, A. K., El-Sayed, I. H., and El-Sayed, M. A. (2010) Comparative study of photothermolysis of cancer cells with nuclear-targeted or cytoplasm-targeted gold nanospheres: continuous wave or pulsed lasers, *J. Biomed. Opt.* 15.
22. Oyelere, A. K., Chen, P. C., Huang, X. H., El-Sayed, I. H., and El-Sayed, M. A. (2007) Peptide-conjugated gold nanorods for nuclear targeting, *Bioconjugate Chem.* 18, 1490-1497.
23. Chen, J. Y., Wiley, B., Li, Z. Y., Campbell, D., Saeki, F., Cang, H., Au, L., Lee, J., Li, X., and Xia, Y. (2005) Gold nanocages: Engineering their structure for biomedical applications, *Adv. Mater.* 17, 2255-2261.
24. Cho, E. C., Au, L., Zhang, Q., and Xio, Y. (2010) The Effects of Size, Shape, and Surface Functional Group of Gold Nanostructures on Their Adsorption and Internalization by Cells, *Small* 6, 517-522.
25. Mahmoud, M. A., Snyder, B., and El-Sayed, M. A. (2010) Surface Plasmon Fields and Coupling in the Hollow Gold Nanoparticles and Surface-Enhanced Raman Spectroscopy. Theory and Experiment, *J. Phys. Chem. C* 114, 7436-7443.
26. Yen, C. W., Mahmoud, M. A., and El-Sayed, M. A. (2009) Photocatalysis in gold nanocage nanoreactors, *J. Phys. Chem. A* 113, 4340-4345.

27. Cadet, J., Delatour, T., Douki, T., Gasparutto, D., Pouget, J. P., Ravanat, J. L., and Sauvaigo, S. (1999) Hydroxyl radicals and DNA base damage, *Mutat. Res.* 424, 9-21.
28. Siekkinen, A. R., McLellan, J. M., Chen, J. Y., and Xia, Y. N. (2006) Rapid synthesis of small silver nanocubes by mediating polyol reduction with a trace amount of sodium sulfide or sodium hydrosulfide, *Chem. Phys. Lett.* 432, 491-496.
29. Frens, G. (1973) Controlled nucleation for regulation of particle-size in monodisperse gold suspensions, *Nature (London), Phys. Sci.* 241, 20-22.
30. Olenych, S. G., Moussallem, M. D., Salloum, D. S., Schlenoff, J. B., and Keller, T. C. S. (2005) Fibronectin and cell attachment to cell and protein resistant polyelectrolyte surfaces, *Biomacromolecules* 6, 3252-3258.
31. Liu, X. O., Atwater, M., Wang, J. H., and Huo, Q. (2007) Extinction coefficient of gold nanoparticles with different sizes and different capping ligands, *Colloids Surf., B* 58, 3-7.
32. Chithrani, B. D., and Chan, W. C. W. (2007) Elucidating the mechanism of cellular uptake and removal of protein-coated gold nanoparticles of different sizes and shapes, *Nano Lett.* 7, 1542-1550.
33. Crouch, S. P. M., Kozlowski, R., Slater, K. J., and Fletcher, J. (1993) The Use of Atp Bioluminescence as a Measure of Cell-Proliferation and Cytotoxicity, *J. Immunol. Methods* 160, 81-88.
34. Gao, H. J., Shi, W. D., and Freund, L. B. (2005) Mechanics of receptor-mediated endocytosis, *P. Natl. Acad. Sci. U.S.A.* 102, 9469-9474.
35. Feldherr, C. M., and Akin, D. (1990) The permeability of the nuclear-envelope in dividing and nondividing cell-cultures, *J. Cell Biol.* 111, 1-8.
36. Feldherr, C. M., and Akin, D. (1993) Regulation of nuclear transport in proliferating and quiescent cells, *Exp. Cell Res.* 205, 179-186.

37. Feldherr, C. M., Lanford, R. E., and Akin, D. (1992) Signal-mediated nuclear transport in simian-virus-40-transformed cells is regulated by large tumor-antigen, *P. Natl. Acad. Sci. U.S.A.* 89, 11002-11005.
38. Feldherr, C. M., Lanford, R. E., and Akin, D. (1992) Signal-mediated nuclear transport in simian-virus 40-transformed cells is regulated by large tumor-antigen, *P. Natl. Acad. Sci. U.S.A.* 89, 11002-11005.
39. Nakielny, S., and Dreyfuss, G. (1999) Transport of proteins and RNAs in and out of the nucleus, *Cell* 99, 677-690.
40. Narayanan, B. A., Geoffroy, O., Willingham, M. C., Re, G. G., and Nixon, D. W. (1999) p53/p21(WAF1/CIP1) expression and its possible role in G1 arrest and apoptosis in ellagic acid treated cancer cells, *Cancer Lett.* 136, 215-221.
41. Sweet, S., and Singh, G. (1995) Accumulation of Human Promyelocytic Leukemic (HL-60) Cells at 2 Energetic Cell-Cycle Checkpoints, *Cancer Res.* 55, 5164-5167.
42. van Engeland, M., Nieland, L. J. W., Ramaekers, F. C. S., Schutte, B., and Reutelingsperger, C. P. M. (1998) Annexin V-affinity assay: A review on an apoptosis detection system based on phosphatidylserine exposure, *Cytometry* 31, 1-9.
43. Koivisto, L., Larjava, K., Hakkinen, L., Uitto, V. J., Heino, J., and Larjava, H. (1999) Different integrins mediate cell spreading, haptotaxis and lateral migration of HaCaT keratinocytes on fibronectin, *Cell Adhes. Commun.* 7, 245-257.
44. Tassa, C., Duffner, J. L., Lewis, T. A., Weissleder, R., Schreiber, S. L., Koehler, A. N., and Shaw, S. Y. (2010) Binding Affinity and Kinetic Analysis of Targeted Small Molecule-Modified Nanoparticles, *Bioconjugate Chem.* 21, 14-19.
45. Dreaden, E. C., Mwakwari, S. C., Sodji, Q. H., Oyelere, A. K., and El-Sayed, M. A. (2009) Tamoxifen-Poly(ethylene glycol)-Thiol Gold Nanoparticle Conjugates: Enhanced Potency and Selective Delivery for Breast Cancer Treatment, *Bioconjugate Chem.* 20, 2247-2253.

46. AshaRani, P. V., Low Kah Mun, G., Hande, M. P., and Valiyaveettil, S. (2009) Cytotoxicity and genotoxicity of silver nanoparticles in human cells, *ACS Nano* 3, 279-290.
47. Yin, Y. D., Li, Z. Y., Zhong, Z. Y., Gates, B., Xia, Y. N., and Venkateswaran, S. (2002) Synthesis and characterization of stable aqueous dispersions of silver nanoparticles through the Tollens process, *J. Mater. Chem.* 12, 522-527.
48. Kapoor, S. (1998) Preparation, characterization, and surface modification of silver particles, *Langmuir* 14, 1021-1025.
49. Chen, M., Wang, L. Y., Han, J. T., Zhang, J. Y., Li, Z. Y., and Qian, D. J. (2006) Preparation and study of polyacryamide-stabilized silver nanoparticles through a one-pot process, *J. Phys. Chem. B.* 110, 11224-11231.
50. Moustafa, M. H., Sharma, R. K., Thornton, J., Mascha, E., Abdel-Hafez, M. A., Thomas, A. J., Jr., and Agarwal, A. (2004) Relationship between ROS production, apoptosis and DNA denaturation in spermatozoa from patients examined for infertility, *Hum. Reprod.* 19, 129-138.

3.3. Varying the Silver Content of Gold Nanocages Impacts Apoptosis and Necrosis Induced in Cancer Cells [1]

We previously reported that cancer cell nucleus targeting gold nanocages (AuNCs) induce higher levels of apoptosis and necrosis than their gold nanosphere counterparts. We attributed this enhancement in cell death to the residual silver present on the inner cavity of the AuNC (inherent to its synthesis) being oxidized to Ag₂O in the cell culture and subsequently generating toxic reactive oxygen species. Based on these observations, we have examined this mechanism further, in the present work, by comparing the apoptosis and necrosis induced in cancer cells by AuNC containing varying ratios of Ag to Au, which can be controlled through the galvanic replacement method of synthesis. First, three different AuNC were synthesized such that they contained increasing ratios of Ag to Au. Second, the three different AuNCs were functionalized with cancer cell targeting (RGD) and nuclear targeting (NLS) peptides (RGD/NLS-AuNCs). The extent of Ag oxidation was estimated based on the redshift of the surface plasmon peak position for each of the three different RGD/NLS-AuNCs, with the greatest redshift occurring for AuNCs with highest Ag to Au ratio. The RGD/NLS-AuNCs were then tested for their ability to induce apoptosis and necrosis in cancer cells. The highest levels of apoptosis and necrosis were observed for AuNCs with the highest Ag to Au ratio. These results indicate that these particles induce cell death in a particle composition-dependent manner. More importantly, these results stress how crucial it is to consider the morphology, composition, and even the synthesis of nanostructures when utilizing them in cancer therapeutics.

3.3.1. Introduction

Gold nanostructures are becoming increasingly popular in the application of cancer therapeutics, either by utilizing them as contrast agents for photothermal therapy,[2-8] imaging contrast agents,[9-11] drug delivery vehicles[12, 13] or as intrinsic antineoplastic agents.[14-17] Specifically, gold nanocages (AuNCs) have received a great deal of attention with their ability to function in all of the above aspects of cancer therapeutics.[7, 17-19] In considering their growing popularity for use in nanomedicine, it is crucial to understand how the morphology and composition of these AuNCs might affect living cancer cells, specifically when targeted to the nucleus. We have already established that the synthesis of these nanostructures can impact how they interact with cells. This is mainly due to the presence of residual silver that remains on the inner cavity of the AuNC after synthesis via galvanic replacement.[20] The residual silver can be oxidized under certain conditions, such as in cell culture medium,[21] creating a layer of silver oxide on the inner cavity of the AuNC. Silver oxide is known to generate reactive oxygen species (ROS),[22] which are highly toxic to cells.[23, 24] Therefore, it is possible that the amount of Ag₂O present on the inner cavity of the AuNC could potentially influence the levels of apoptosis and necrosis induced when targeted to the cancer cell nucleus.

In the present work we synthesize three different AuNCs with varying Ag:Au ratios (*i.e.* varying amounts of silver) and functionalize them with peptides known to target alpha v beta integrins present on the cancer cell surface,[25-28] as well as nuclear targeting peptides to facilitate nuclear localization[29-31] of AuNCs within the cells of interest.[17] The extent of oxidation of the three different AuNCs, indicated by a redshift

in the surface plasmon peak position, is measured after a 48 h incubation period in cell-free culture medium. Further studies are conducted, in the presence of cells, to correlate the Ag: Au ratio, and subsequent silver oxidation, of the AuNCs to the levels of apoptosis and necrosis induced when these particles are localized at the nucleus of cancer cells.

3.3.2. Experimental Methods

3.3.2.1. Cell Culture

Human oral squamous cell carcinoma (HSC-3) cells were maintained in Dulbecco's modified Eagle's medium (DMEM, Mediatech) supplemented with 10% v/v fetal bovine serum (FBS, Mediatech) and 1% v/v antimycotic solution (Mediatech) in a 37°C, 5% CO₂ humidified incubator.

3.3.2.2. Gold Nanocage Synthesis and Peptide Conjugation

Gold nanocages (AuNCs) are synthesized via galvanic replacement method using silver nanocubes as a template. The silver atoms of the silver nanocube template are oxidized by Au³⁺, which is subsequently reduced and deposited onto the surface of the template.[20] The silver nanocube template is prepared by a previously reported method.[32] Briefly, 70 mL of ethylene glycol (EG) is heated to 145°C for 1 h, followed by addition of polyvinyl pyrrolidone (PVP, MW 55,000; 0.82 g dissolved in 5 mL EG). The temperature is then raised to 150°C and 0.7 mL of a 3 mM sodium sulfide solution (in EG) is added, followed by slow injection of 4 mL of a silver nitrate solution (0.48 g dissolved in 10 mL EG). [22, 33] The silver nanocubes are then purified by adding a 1:2 acetone:water mixture at a volume twice that of the nanocube solution, followed by centrifugation at 10,000 rpm for 5 min and redispersing the precipitate in 600 mL of DI

water. From the template of silver nanocubes, AuNCs of different morphologies (*i.e.* porosity) and Ag to Au ratios can be prepared. Briefly, the silver nanocube solution is brought to a boil and a 10 mg/L hydrogen tetrachloroaurate ($\text{HAuCl}_4 \cdot 3\text{H}_2\text{O}$) solution is slowly injected until the surface plasmon resonance peak of the solution shifts from ca. 442 nm (silver nanocubes) to ca. 600 nm (gold-silver nanoboxes). Upon initial peak shift, a 1 mg/L $\text{HAuCl}_4 \cdot 3\text{H}_2\text{O}$ solution is added drop wise until the peak shifts to ca. 650 nm (Fig. 3.18A, sample 1). A 200 mL volume of this solution is moved to another clean flask and left to cool to room temperature. The 1 mg/L $\text{HAuCl}_4 \cdot 3\text{H}_2\text{O}$ solution is further added to the remaining 400 mL of the nanoparticle solution until the peak shifts to ca. 700 nm (Fig. 3.18A, sample 2). A 200 mL volume is again removed and placed in another clean flask to cool to room temperature. Further addition of the 1 mg/L $\text{HAuCl}_4 \cdot 3\text{H}_2\text{O}$ solution to the remaining 200 mL until the peak shifts to ca. 760 nm (Fig. 3.18A, sample 3). These three different samples of AuNCs exhibit varying ratios of Ag to Au. The AuNCs are then purified by centrifugation at 10,000 rpm for 5 min and redispersed in DI water. TEM images revealed that the AuNCs synthesized here have a wall length of about 40 nm, as shown in Figure 3.18B-D. Because the amount of Ag present in each of the different AuNC samples can vary with the addition of Au salt, ICP analysis was done by dissolving 1 mL of a 1 nM solution of each sample in nitric acid. The Ag to Au ratio was then determined.

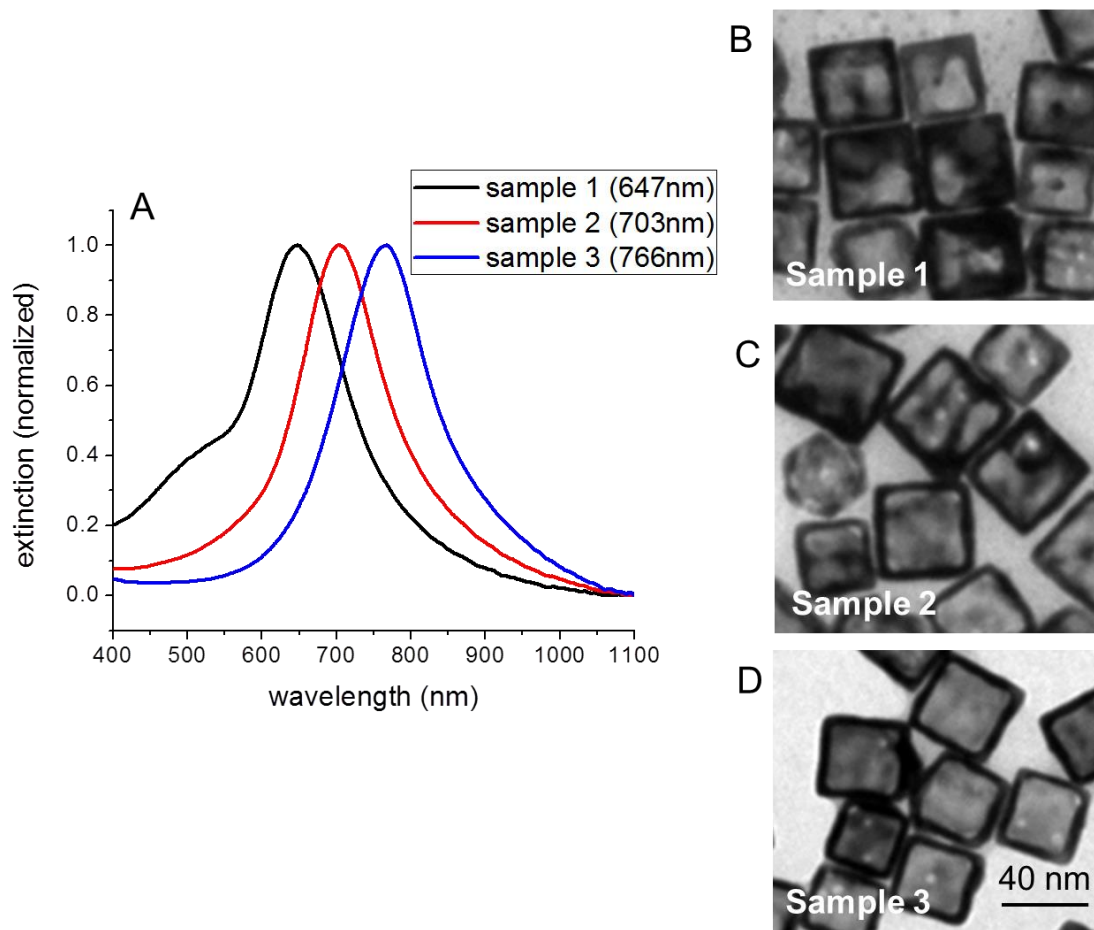


Figure 3.18. UV-Vis spectra (A) and TEM images of 40 nm AuNCs (B-D) synthesized with varying ratios of Ag to Au. As more gold salt is deposited onto the silver nanocube template, the surface plasmon peak redshifts (A). Scale bar: 40 μm .

Upon synthesis and purification of the various AuNCs, they were stabilized with polyethylene glycol (mPEG-SH, MW 5000, Laysan Bio, Inc.) by addition of a 1 mM aqueous solution of PEG to the AuNCs at 10^4 molar excess and shaking overnight. The PEG-AuNCs were then purified by centrifugation at 6000 rpm for 15 min and redispersed in water. After PEGylation, the particles are conjugated with custom peptides purchased from Genscript USA, Inc. as previously described.[17] Specifically, aqueous solutions of both an RGD peptide (RGDRGDRGDRGDPGC) and an NLS peptide

(CGGGPKKKRKVGG) were added to the PEG-AuNCs at a 10^4 molar excess and left on an orbital shaker overnight. The RGD/NLS-AuNCs were then purified by centrifugation at 6000 rpm for 15 min and redispersed in DI water.

3.3.2.3. Flow Cytometry Analysis of Apoptosis and Necrosis

Cell death, via apoptosis and necrosis, associated with the treatment of cells with the varying RGD/NLS-AuNCs, was quantified using the *ApoTarget*TM Annexin-V FITC Apoptosis Kit (Invitrogen, Inc. Cat. #PHN1010). The standard protocol was optimized for our experimental conditions. Briefly, HSC cells were plated in a 12-well tissue culture plate. Cells were allowed to grow overnight, after which they were treated with 0.1 nM RGD/NLS-AuNCs (samples 1-3). Upon treatment of cells, they are washed with PBS and collected by trypsinization and centrifugation. The cells are then washed again with cold PBS and collected by centrifugation, after which, 500 μ L of 1x Annexin binding buffer, 2 μ L of 100 μ g/mL PI and 5 μ L of Annexin-V-FITC are all mixed with the cells and left to incubate for 15 min at room temperature. Following cell staining with PI and Annexin-V-FITC, the remaining volume of 1x Annexin binding buffer was added (493 μ L) and the cell solution was passed through a 40 μ m sterile filter. Cells are then analyzed on a BD LSR II (BD Biosciences) with a 488 nm excitation. Flow cytometry data is analyzed using the flow cytometry analysis software, FlowJo. Results are reported as the average % of cells \pm standard deviation.

3.3.2.4. Statistical Analysis

Statistical significance was determined with the *t test calculator* (GraphPad Software, Inc.). Data is considered statistically significant when $p < 0.05$ and is indicated by *.

3.3.3. Results and Discussion

The presence of residual silver on the inner cavity of gold nanocages (AuNCs) is inherent to their synthesis via galvanic replacement.[34, 35] This method of synthesis begins with a silver nanocube template and, after oxidation of the silver atoms by Au^{3+} ions, results in a hollow cage structure with porous faces and residual silver remaining on the inner cavity, as displayed by the reaction and schematic shown in Figure 3.19.

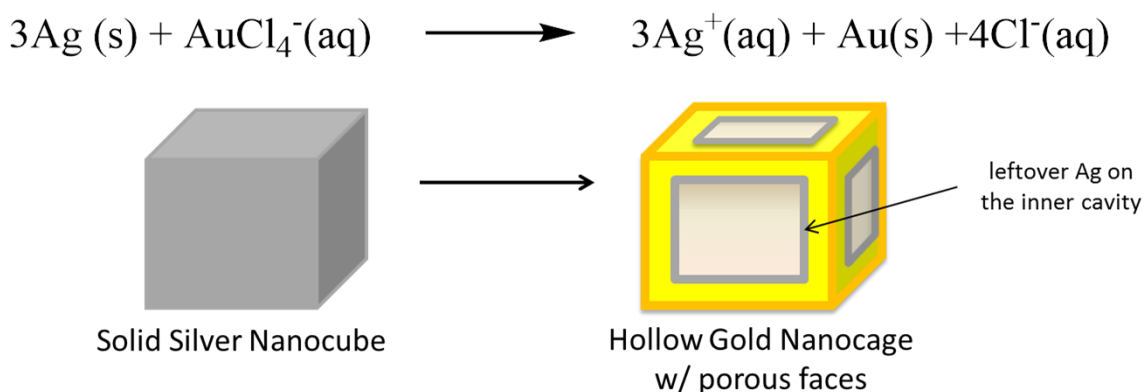


Figure 3.19. Synthesis of AuNCs via galvanic replacement. Stoichiometrically, three Ag atoms of the Ag nanocube template are oxidized by one Au^{3+} ion of the Au salt, which is subsequently reduced and deposited onto the Ag template. This results in hollow cage structure with porous faces and residual Ag on the inner cavity.

Using this method of synthesis, it is possible to vary the ratio of Ag to Au in the nanocage. Therefore, we have used this method to obtain three different samples of AuNCs, all having the same average wall length, but varying silver content. During the synthesis of AuNCs (see section 3.3.2.2), a redshift of the surface plasmon peak (Fig 3.18A) with increasing amounts of gold salt is an indication of the decrease in silver content.[34, 35] The actual ratio of Ag to Au for each AuNC synthesized in this work

was determined and is shown in Table 3.3 and it is clear that as the surface plasmon peak of the AuNCs is redshifted as the amount of silver present is slightly increased.

Table 3.2. Various AuNCs synthesized with different surface plasmon peak positions and their corresponding ratio of Ag to Au.

AuNC	Surface Plasmon Peak	Ag:Au
Sample 1	647 nm	2.56
Sample 2	703 nm	2.34
Sample 3	766 nm	1.78

With evidence that AuNC samples 1-3 have increasing Ag:Au ratios, it is important to assess the implications of these variations. It is especially important to determine how the change of structure and composition of AuNCs will affect how these nanoparticles function in a physiological environment. Therefore, we have investigated the oxidation of these AuNCs in cell culture medium, since it has been previously suggested that the silver, remaining on the inner cavity, of the AuNCs can be oxidized to silver oxide (Ag₂O) under these conditions.[17, 21] The oxidation of Ag to Ag₂O, in general, can be estimated by a redshift in the surface plasmon peak position, which has been previously demonstrated both theoretically and experimentally.[36] This has also been shown in the case of oxidizing AuNCs.[22] In order to estimate the oxidation of RGD/NLS-AuNCs in this work, a 0.2 nM concentration of particles in cell culture medium was placed at 37°C in a 5% CO₂ humidified incubator for up to 48 h. The surface plasmon peak position was determined for each of the samples at 0, 24, and 48 h. Figure 3.20 displays the peak shift observed for samples 1-3. It should be noted that the initial peak position (0 h) is shifted

with respect to that of the as-synthesized AuNCs, due to conjugation of peptides and dispersion in cell culture medium (*i.e.* change in dielectric of the medium surrounding the nanoparticle).

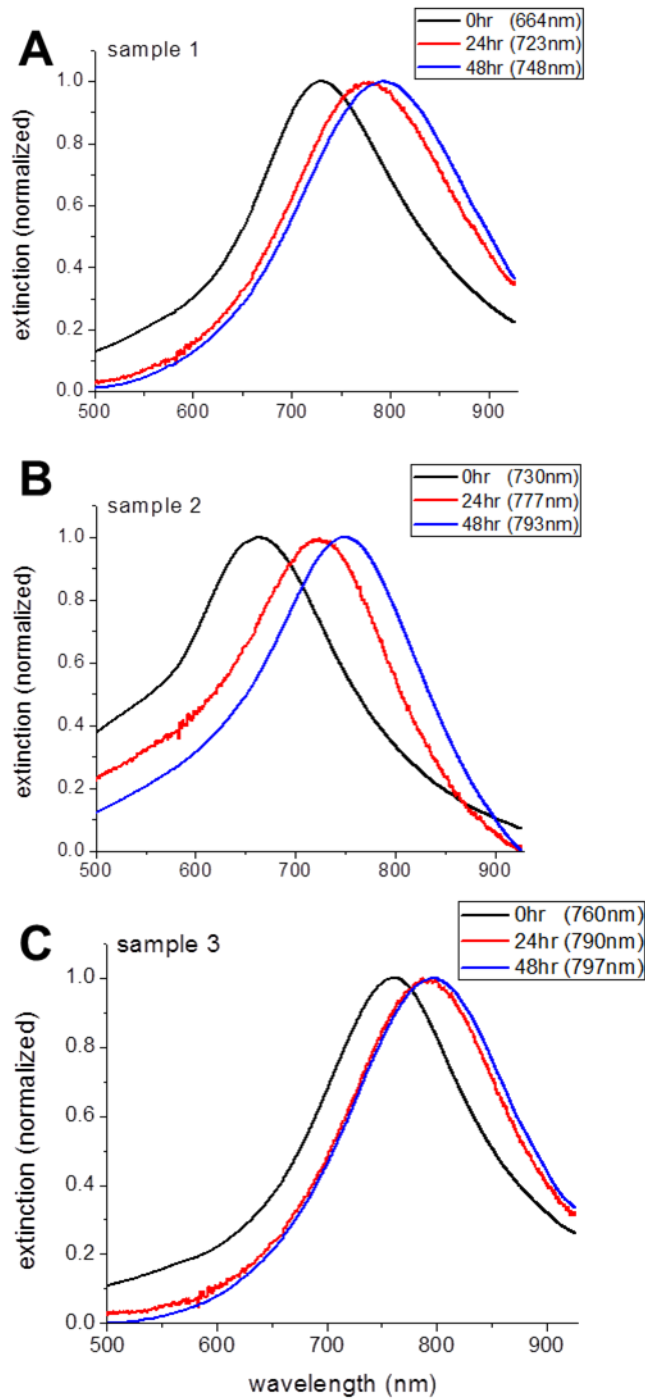


Figure 3.20. Surface plasmon peak shifts observed for the oxidation of various RGD/NLS-AuNCs incubated in cell culture medium for up to 48 h. (A) Sample 1 (2.56 Ag: Au) exhibits an 84 nm redshift after 48 h. (B) Sample 2 (2.34 Ag: Au) exhibits a 63 nm redshift after 48 h. (C) Sample 3 (1.78 Ag: Au) exhibits a 37 nm redshift after 48 h.

The peak shifts observed for the various RGD/NLS-AuNCs indicate that these particles are indeed oxidized under cell culture conditions at 24 h and further oxidized when remaining under these conditions up to 48 h. Based on previous reports of Ag being oxidized to Ag_2O , [36] it can be estimated that the greatest redshift in the plasmon peak position (sample 1, 2.56 Ag:Au, 84 nm redshift) would have the greatest amount of Ag_2O present on the inner cavity of the AuNC after oxidation of Ag in cell culture medium. We have previously reported that the oxidation of Ag remaining on the inner cavity of RGD/NLS-AuNCs can specifically induce cell death in HSC cells, via apoptosis and necrosis. [17] Because it has been established that Ag_2O causes the production of toxic reactive oxygen species (ROS) in cells, [22-24] the impact of varying the Ag content, and subsequent Ag_2O presence, on cell death is therefore assessed utilizing flow cytometry for the detection of apoptosis and necrosis (see section 3.3.2.3). Figure 3.21 displays the populations of apoptotic and necrotic cells induced in HSC cells after a 48 h treatment with RGD/NLS-AuNCs having increasing Ag content.

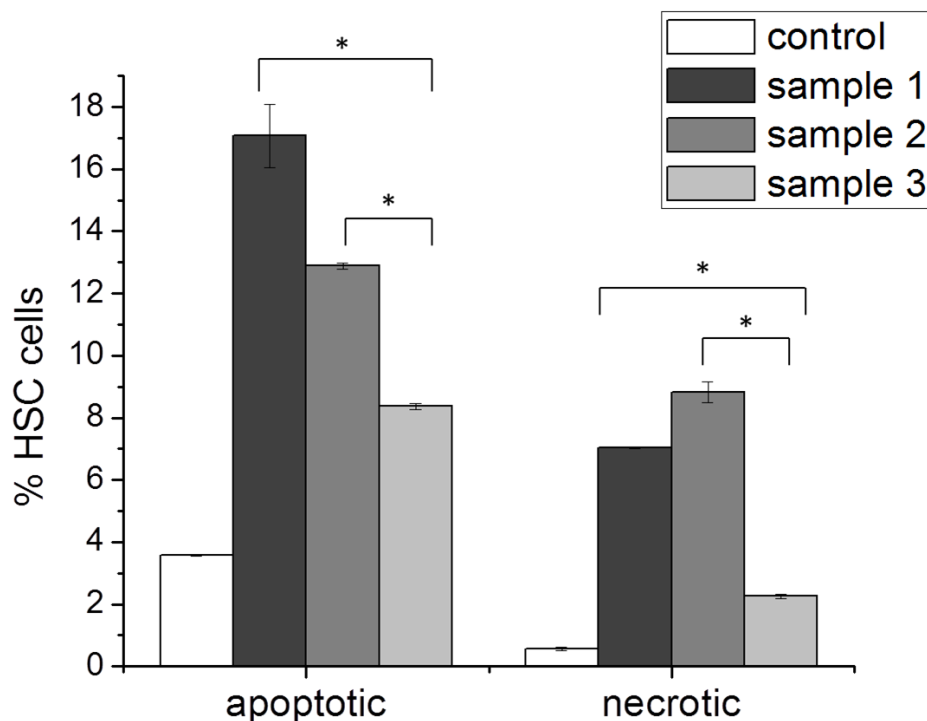


Figure 3.21. Apoptosis and necrosis induced in HSC cells by 48 h treatment of 0.1 nM RGD/NLS-AuNCs with varying porosity and Ag content (Samples 1-3). All nanocage-treated samples have statistically higher levels of apoptotic and necrotic cells ($p < 0.05$) than the untreated cells (control). Remaining data are considered statistically significant if $p < 0.05$, and is indicated by * above bars.

It appears that the greatest amount of apoptosis (~17%) is observed when HSC cells are treated with RGD/NLS-AuNCs having the highest amount of Ag (sample 1, 2.56 Ag:Au) and the difference between sample 1 and sample 2 (2.34 Ag:Au) is not significant. However, the RGD/NLS-AuNCs having the lowest amount of Ag (sample 3, 1.78 Ag:Au) do exhibit the least amount of apoptotic cells (~8%) when compared to the other treatments. In terms of necrosis, the RGD/NLS-AuNCs with the highest levels of Ag (sample 1 and sample 2) both induce significantly more (~7% and ~9%, respectively) than the particles containing the smallest amount of Ag (only ~2% necrotic cells).

3.3.4. Conclusions and Future Outlook

In conclusion, the specific targeting of AuNCs to the nucleus of HSC cells (RGD/NLS-AuNCs) induces apoptosis and necrosis in a silver content-dependent manner. We propose that the Ag remaining on the inner cavity of the AuNCs becomes oxidized to Ag₂O during the 48 h treatment period when in cell culture medium. The RGD/NLS-AuNCs exhibit redshifts in their surface plasmon peak positions, such that greater extent of Ag oxidation to Ag₂O is characterized by a larger redshift.[36] The extent to which Ag is oxidized to Ag₂O is said to be the basis of the observed trend of apoptosis and necrosis increasing with increasing Ag:Au ratio. The actual oxidation state of Ag can possibly be quantified (*i.e.* determine actual extent of Ag oxidation to Ag₂O) by X-Ray Photoelectron Spectroscopy (XPS), which should be the next step in assessing the effects of AuNC oxidation on cellular functions. These results have important implications in the use of these nanostructures in medicine, such that the amount of Ag present within the inner cavity of the AuNC must be taken into consideration before utilizing them as photothermal contrast agents or drug delivery vehicles.

3.3.5. References

1. Mackey, M. A., Bordley, J., Mahmoud, M.A., El-Sayed, M.A. (2013) Varying the Silver Content of Gold Nanocages Impacts Apoptosis and Necrosis Induced in Cancer Cells, *in progress*.
2. Hirsch, L. R., Stafford, R. J., Bankson, J. A., Sershen, S. R., Rivera, B., Price, R. E., Hazle, J. D., Halas, N. J., and West, J. L. (2003) Nanoshell-mediated near-infrared thermal therapy of tumors under magnetic resonance guidance, *Proceedings of the National Academy of Sciences of the United States of America* 100, 13549-13554.
3. O'Neal, D. P., Hirsch, L. R., Halas, N. J., Payne, J. D., and West, J. L. (2004) Photo-thermal tumor ablation in mice using near infrared-absorbing nanoparticles, *Cancer Lett* 209, 171-176.
4. Dickerson, E. B., Dreaden, E. C., Huang, X. H., El-Sayed, I. H., Chu, H. H., Pushpanketh, S., McDonald, J. F., and El-Sayed, M. A. (2008) Gold nanorod assisted near-infrared plasmonic photothermal therapy (PPTT) of squamous cell carcinoma in mice, *Cancer Lett.* 269, 57-66.
5. Huang, X., El-Sayed, I. H., Qian, W., and El-Sayed, M. A. (2006) Cancer cell imaging and photothermal therapy in the near-infrared region by using gold nanorods, *J Am Chem Soc* 128, 2115-2120.
6. Huang, X., Jain, P. K., El-Sayed, I. H., and El-Sayed, M. A. (2007) Gold nanoparticles: interesting optical properties and recent applications in cancer diagnostics and therapy, *Nanomedicine (Lond)* 2, 681-693.
7. Chen, J., Wang, D., Xi, J., Au, L., Siekkinen, A., Warsen, A., Li, Z. Y., Zhang, H., Xia, Y., and Li, X. (2007) Immuno gold nanocages with tailored optical properties for targeted photothermal destruction of cancer cells, *Nano Lett* 7, 1318-1322.
8. El-Sayed, I. H., Huang, X., and El-Sayed, M. A. (2006) Selective laser photothermal therapy of epithelial carcinoma using anti-EGFR antibody conjugated gold nanoparticles, *Cancer Lett* 239, 129-135.
9. Jain, P. K., Huang, X., El-Sayed, I. H., and El-Sayed, M. A. (2008) Noble metals on the nanoscale: optical and photothermal properties and some applications in imaging, sensing, biology, and medicine, *Acc Chem Res* 41, 1578-1586.
10. Sokolov, K., Follen, M., Aaron, J., Pavlova, I., Malpica, A., Lotan, R., and Richards-Kortum, R. (2003) Real-time vital optical imaging of precancer using

anti-epidermal growth factor receptor antibodies conjugated to gold nanoparticles, *Cancer Res* 63, 1999-2004.

11. Murphy, C. J., Gole, A. M., Stone, J. W., Sisco, P. N., Alkilany, A. M., Goldsmith, E. C., and Baxter, S. C. (2008) Gold nanoparticles in biology: beyond toxicity to cellular imaging, *Acc Chem Res* 41, 1721-1730.
12. Paciotti, G. F., Myer, L., Weinreich, D., Goia, D., Pavel, N., McLaughlin, R. E., and Tamarkin, L. (2004) Colloidal gold: a novel nanoparticle vector for tumor directed drug delivery, *Drug delivery* 11, 169-183.
13. Dreaden, E. C., Austin, L. A., Mackey, M. A., and El-Sayed, M. A. (2012) Size matters: gold nanoparticles in targeted cancer drug delivery, *Therapeutic delivery* 3, 457-478.
14. Kang, B., Mackey, M. A., and El-Sayed, M. A. (2010) Nuclear targeting of gold nanoparticles in cancer cells induces DNA damage, causing cytokinesis arrest and apoptosis, *J Am Chem Soc* 132, 1517-1519.
15. Mukherjee, P., Bhattacharya, R., Wang, P., Wang, L., Basu, S., Nagy, J. A., Atala, A., Mukhopadhyay, D., and Soker, S. (2005) Antiangiogenic properties of gold nanoparticles, *Clinical cancer research : an official journal of the American Association for Cancer Research* 11, 3530-3534.
16. Roa, W., Zhang, X., Guo, L., Shaw, A., Hu, X., Xiong, Y., Gulavita, S., Patel, S., Sun, X., Chen, J., Moore, R., and Xing, J. Z. (2009) Gold nanoparticle sensitize radiotherapy of prostate cancer cells by regulation of the cell cycle, *Nanotechnology* 20, 375101.
17. Mackey, M. A., Saira, F., Mahmoud, M. A., and El-Sayed, M. A. (2013) Inducing Cancer Cell Death by Targeting Its Nucleus: Solid Gold Nanospheres versus Hollow Gold Nanocages, *Bioconjugate chemistry* 24, 897-906.
18. Chen, J., Saeki, F., Wiley, B. J., Cang, H., Cobb, M. J., Li, Z. Y., Au, L., Zhang, H., Kimmey, M. B., Li, X., and Xia, Y. (2005) Gold nanocages: bioconjugation and their potential use as optical imaging contrast agents, *Nano Lett* 5, 473-477.
19. Yavuz, M. S., Cheng, Y., Chen, J., Cobley, C. M., Zhang, Q., Rycenga, M., Xie, J., Kim, C., Song, K. H., Schwartz, A. G., Wang, L. V., and Xia, Y. (2009) Gold nanocages covered by smart polymers for controlled release with near-infrared light, *Nature materials* 8, 935-939.
20. Chen, J. Y., Wiley, B., Li, Z. Y., Campbell, D., Saeki, F., Cang, H., Au, L., Lee, J., Li, X., and Xia, Y. (2005) Gold nanocages: Engineering their structure for biomedical applications, *Adv. Mater.* 17, 2255-2261.

21. AshaRani, P. V., Low Kah Mun, G., Hande, M. P., and Valiyaveetil, S. (2009) Cytotoxicity and genotoxicity of silver nanoparticles in human cells, *ACS Nano* 3, 279-290.
22. Yen, C. W., Mahmoud, M. A., and El-Sayed, M. A. (2009) Photocatalysis in gold nanocage nanoreactors, *J. Phys. Chem. A* 113, 4340-4345.
23. Moustafa, M. H., Sharma, R. K., Thornton, J., Mascha, E., Abdel-Hafez, M. A., Thomas, A. J., Jr., and Agarwal, A. (2004) Relationship between ROS production, apoptosis and DNA denaturation in spermatozoa from patients examined for infertility, *Hum. Reprod.* 19, 129-138.
24. Cadet, J., Delatour, T., Douki, T., Gasparutto, D., Pouget, J. P., Ravanat, J. L., and Sauvaigo, S. (1999) Hydroxyl radicals and DNA base damage, *Mutation research* 424, 9-21.
25. Zitzmann, S., Ehemann, V., and Schwab, M. (2002) Arginine-glycine-aspartic acid (RGD)-peptide binds to both tumor and tumor-endothelial cells in vivo, *Cancer Res.* 62, 5139-5143.
26. Xue, H., Atakilit, A., Zhu, W. M., Sheppard, D., Ramos, D. M., and Pytela, R. (2000) Role of α v β 6 integrin in growth and migration of oral squamous cell carcinoma, *Mol. Biol. Cell* 11, 1363.
27. Xue, H., Atakilit, A., Zhu, W. M., Li, X. W., Ramos, D. M., and Pytela, R. (2001) Role of the α v β 6 integrin in human oral squamous cell carcinoma growth in vivo and in vitro, *Biochem. Biophys. Res. Commun.* 288, 610-618.
28. Castel, S., Pagan, R., Mitjans, F., Piulats, J., Goodman, S., Jonczyk, A., Huber, F., Vilaro, S., and Reina, M. (2001) RGD peptides and monoclonal antibodies, antagonists of α (v)-integrin, enter the cells by independent endocytic pathways, *Lab. Invest.* 81, 1615-1626.
29. Tkachenko, A. G., Xie, H., Liu, Y., Coleman, D., Ryan, J., Glomm, W. R., Shipton, M. K., Franzen, S., and Feldheim, D. L. (2004) Cellular trajectories of peptide-modified gold particle complexes: comparison of nuclear localization signals and peptide transduction domains, *Bioconjugate chemistry* 15, 482-490.
30. Tkachenko, A. G., Xie, H., Coleman, D., Glomm, W., Ryan, J., Anderson, M. F., Franzen, S., and Feldheim, D. L. (2003) Multifunctional gold nanoparticle-peptide complexes for nuclear targeting, *J Am Chem Soc* 125, 4700-4701.
31. Escriou, V., Carriere, M., Scherman, D., and Wils, P. (2003) NLS bioconjugates for targeting therapeutic genes to the nucleus, *Advanced drug delivery reviews* 55, 295-306.

32. Mahmoud, M. A., Snyder, B., and El-Sayed, M. A. (2010) Surface Plasmon Fields and Coupling in the Hollow Gold Nanoparticles and Surface-Enhanced Raman Spectroscopy. Theory and Experiment, *J. Phys. Chem. C* 114, 7436-7443.
33. Siekkinen, A. R., McLellan, J. M., Chen, J. Y., and Xia, Y. N. (2006) Rapid synthesis of small silver nanocubes by mediating polyol reduction with a trace amount of sodium sulfide or sodium hydrosulfide, *Chem. Phys. Lett.* 432, 491-496.
34. Sun, Y., and Xia, Y. (2004) Mechanistic study on the replacement reaction between silver nanostructures and chloroauric acid in aqueous medium, *J Am Chem Soc* 126, 3892-3901.
35. Skrabalak, S. E., Au, L., Li, X., and Xia, Y. (2007) Facile synthesis of Ag nanocubes and Au nanocages, *Nature protocols* 2, 2182-2190.
36. Yin, Y. D., Li, Z. Y., Zhong, Z. Y., Gates, B., Xia, Y. N., and Venkateswaran, S. (2002) Synthesis and characterization of stable aqueous dispersions of silver nanoparticles through the Tollens process, *J. Mater. Chem.* 12, 522-527.

3.4. Enhancing 5-Fluorouracil Drug Efficacy by Gold Nanoparticle Cell Cycle Regulation [1]

We have previously shown that gold nanoparticles conjugated with nuclear-targeting and cytoplasm-targeting peptides (NLS and RGD, respectively) are capable of altering the cell cycle of human oral squamous carcinoma cells (HSC-3). In the present work, we show that this regulation of the cell cycle can be exploited to enhance the efficacy of a common chemotherapeutic agent, 5-Fluorouracil, by pre-treating cells with gold nanoparticles. Utilizing flow cytometry cell cycle analysis, we were able to quantify the 5-Fluorouracil efficacy as an accumulation of cells in the S phase with a depletion of cells in the G2/M phase. Nuclear-targeted gold nanoparticles (NLS-AuNPs, 30 nm in diameter) showed the greatest 5-Fluorouracil efficacy enhancement when compared to smaller NLS-AuNPs (15 nm in diameter) and particles that were targeted to the cytoplasm (RGD-AuNPs, 30 nm in diameter). Not only were these particles best at enhancing 5-Fluorouracil efficacy via cell cycle regulation, but this was further confirmed by cytotoxicity measurements. When 5-Fluorouracil treatment (500 μ M, 48 h) is preceded by a 24 h treatment with 30 nm NLS-AuNPs (0.4 nM), the cell viability is significantly reduced from 40% to 17%. In addition, modes of cell death induced by 5-Fluorouracil, namely late apoptosis and necrosis, were shown to be enhanced by the pre-treatment of cells with these 30 nm NLS-AuNPs. Overall, we show that nuclear-targeted 30 nm gold nanoparticles enhance 5-Fluorouracil drug efficacy in HSC-3 cells via regulation of the cell cycle, a chemosensitization technique that could potentially be expanded to different cell lines and different chemotherapies.

3.4.1. Introduction

Noble metal nanoparticles are becoming increasingly prominent in the treatment of disease due to their unique properties as both intrinsic antineoplastic agents[2-5] and extrinsic photothermal contrast agents.[6-12] Gold nanoparticles, in particular, are showing great promise as antineoplastic agents, especially with their ability to prohibit cell growth and regulate the cell cycle without external stimulation via radiation.[3, 5, 13-15] Specifically, cell cycle regulation by gold nanoparticles has been utilized for the sensitization of malignant cells to radiation. For example, Roa, et.al.[15] previously showed that glucose-capped gold nanoparticles caused accumulation of prostate cancer cells (DU145) in the G2/M phase of the cell cycle and subsequent radiation sensitization of these cells, as cells in the G2/M phase are most vulnerable to radiation. Another group later showed that peptide-capped gold nanorods were capable of sensitizing melanoma cells (A375) to radiation, also through a G2/M arrest.[16]

Cell cycle regulation by gold nanoparticles could also potentially be useful for sensitization of malignant cell lines to chemotherapeutic agents. For example, the antimetabolite drug 5-Fluorouracil (5-FU) specifically acts on cells present in the S phase of the cell cycle.[17] More specifically, a population of cells is resistant to 5-FU treatment when there is a depletion of cells in the S phase with an accumulation of cells in the G2/M phase.[18, 19] With the extensive research done on the use of 5-FU as a chemotherapeutic agent and its mode of action, it is possible to now enhance 5-FU chemosensitivity in cells, namely by regulating the cell cycle.

In the present work, we show that gold nanoparticles, specifically conjugated with nuclear-targeting peptides, are capable of regulating the cell cycle, such that they induce

an S phase accumulation and G2/M phase depletion. Subsequently, these gold nanoparticles enhance the chemosensitivity of a human oral squamous carcinoma cell line to 5-FU treatment, as shown by a cell viability assay. Along with the cell viability results, the mode of cell death is assessed by flow cytometry analysis of apoptotic and necrotic cells. With these results, it is again apparent that the pre-treatment of cells with nuclear-targeting gold nanoparticles, can enhance cell death pathways already predominant with 5-FU treatment. The cell cycle regulation and subsequent enhancement of 5-FU efficacy seen with the gold nanoparticles investigated in this work is dependent upon both nanoparticle size (30 vs. 15 nm) and nanoparticle functionalization with RGD peptides versus NLS peptides (*i.e.* location of nanoparticles within cells). Also interesting is that the gold nanoparticles are not inherently cytotoxic to the cells, potentially minimizing toxicity issues commonly presented with combination chemotherapies.

3.4.2. Experimental Methods

3.4.2.1. Cell Culture

Human oral squamous cell carcinoma (HSC-3) cells were maintained in Dulbecco's modified Eagle's medium (DMEM, Mediatech) supplemented with 10% v/v fetal bovine serum (FBS, Mediatech) and 1% v/v antimycotic solution (Mediatech) in a 37°C, 5% CO₂ humidified incubator.

3.4.2.2. Gold Nanoparticle Synthesis and Peptide Conjugation

Gold nanoparticles (AuNPs) were synthesized via citrate reduction of chloroauric acid (HAuCl₄), as developed by Frens[20] Briefly, 50 mL of a 0.01% (w/v) HAuCl₄ aqueous solution is brought to a boil, while stirring, followed by addition of a trisodium

citrate aqueous solution. The reaction is determined to reach completion when the solution color changes from clear to a deep red/purple. To obtain AuNPs with a 30 nm diameter (Figure 3.22A), 1 mL of 1% (w/v) trisodium citrate was added to the HAuCl_4 solution. To obtain AuNPs with a 15 nm diameter (Figure 3.22B) 1 mL of 2% trisodium citrate (w/v) was added. The AuNPs were then purified by centrifugation at 6000 rpm for 15 min and redispersed in water. The core nanoparticle diameters were determined using ImageJ software. Extinction coefficients used for the 30 and 15 nm AuNPs (3.0×10^9 and $3.6 \times 10^8 \text{ M}^{-1}\text{cm}^{-1}$, respectively) were based on previous reports.[21]

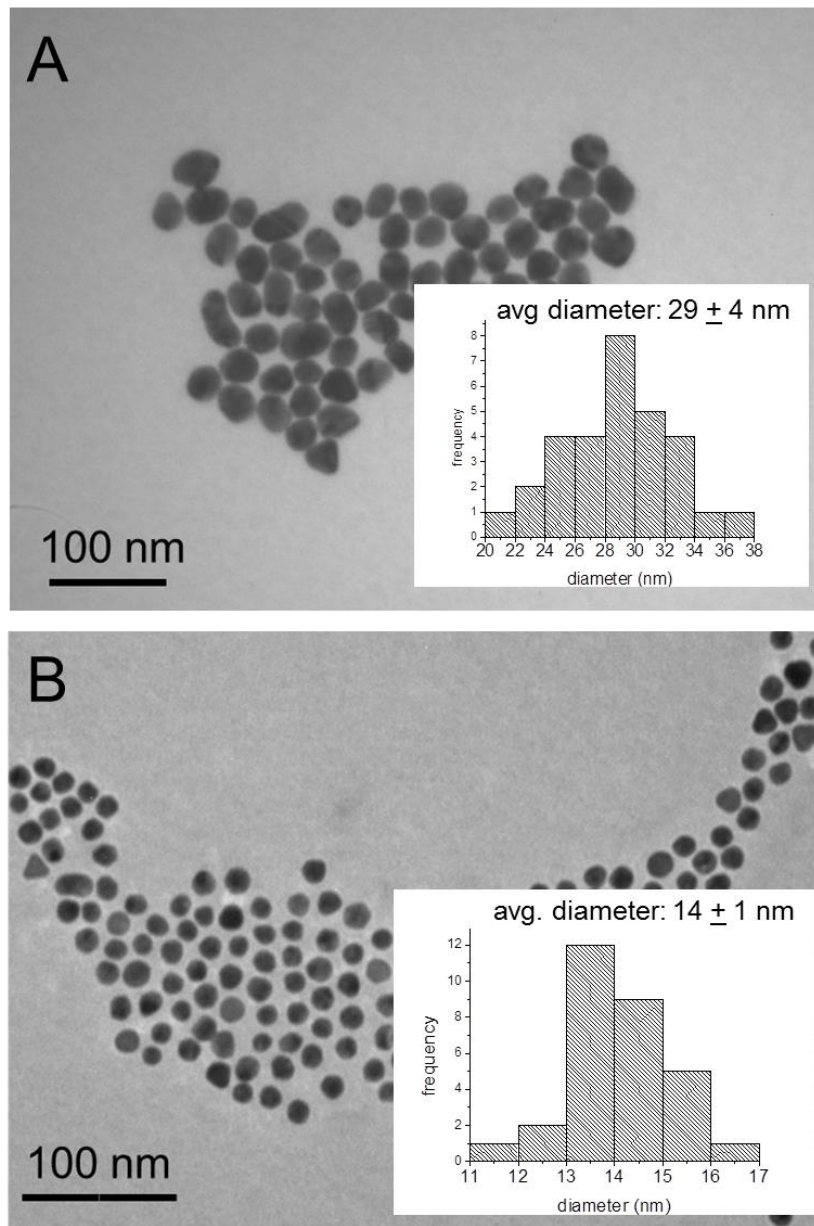


Figure 3.22. TEM images of AuNPs synthesized via citrate reduction of HAuCl_4 . (A) AuNPs with diameter of 29 ± 4 nm, inset showing size distribution histogram. (B) AuNPs with diameter of 14 ± 1 nm, inset showing size distribution histogram.

The as-synthesized AuNPs are first stabilized with polyethylene glycol (mPEG-SH, MW 5000, Laysan Bio, Inc.) to prevent nonspecific adsorption of proteins and other biological components in the physiological environment. Stabilization with PEG was achieved through addition of a 1 mM aqueous solution of PEG to the AuNP solution at a

molar excess of 10^4 and shaking on an orbital shaker overnight at room temperature. After PEG stabilization, the AuNPs were centrifuged at 6000 rpm for 15 min and redispersed in water.

The now PEG-stabilized AuNPs were functionalized with custom peptides purchased from GenScript USA, Inc, as we have previously demonstrated.[5] Specifically, an NLS (nuclear localization sequence) peptide with the sequence CGGGPKKKRKVGG and an RGD (Arg-Gly-Asp) peptide with the sequence (RGD)₄PGC were used throughout this work. Peptide conjugation was achieved through addition of a 5 mM aqueous solution of peptides to the PEG-AuNP solutions at a molar excess of 10^4 and shaking on an orbital shaker overnight at room temperature. The peptide-conjugated AuNPs were then purified by centrifugation at 6000 rpm for 15 min and redispersed in water. Three different nanoparticle formulations were utilized in this study; 15 nm NLS-AuNPs, 30 nm NLS-AuNPs and 30 nm RGD-AuNPs.

In order to confirm nanoparticle functionalization, the hydrodynamic diameter (HD) and zeta potential were measured via dynamic light scattering (DLS). Table 3.4 displays the increasing HD and neutralization of zeta potential upon conjugation of citrate-capped AuNPs with PEG and peptides.

Table 3.3. Dynamic light scattering measurements of the hydrodynamic diameter and zeta potential for various AuNPs used in this study.

Nanoparticle Core Size (diameter)	Surface Functionalization	Hydrodynamic Diameter	Zeta Potential
15 nm	Citrate	22 nm	-33 mV
	PEG+NLS	58 nm	-4 mV
30 nm	Citrate	49 nm	-33 mV
	PEG+RGD	73 nm	6 mV
	PEG+NLS	87 nm	- 3 mV

3.4.2.3. Treatment of Cells with AuNPs and 5-Fluorouracil

HSC-3 cells were treated with both AuNPs and 5-Fluorouracil (5-FU). Briefly, after cells were grown overnight, a 0.4 nM concentration of AuNPs (in cell culture medium) was added to the cells. Cells were treated with AuNPs for 24 h, after which, they were washed with PBS and subsequently treated with various concentrations of 5-FU. Cells were treated with 5-FU for 48 h before performing analyses. The control samples in this work are treated with an appropriate concentration of DMSO in cell culture medium (0.2%) corresponding to the highest percentage of DMSO that is introduced to cells by the 5-FU treatment.

3.4.2.4. Flow Cytometry Cell Cycle Analysis

In order to determine the percentages of cells that exist in specific phases of the cell cycle, flow cytometry cell cycle analysis was performed. Briefly, HSC cells were plated in a 12-well tissue culture plate. Cells were allowed to grow overnight after which treatment was administered according to method described in Section 3.4.2.3. Upon treatment of cells, they are washed with PBS, collected by trypsinization and centrifugation, and fixed in 70% ice cold ethanol and storage at -20 °C. For preparation of cells for flow cytometry cell cycle analysis, the fixed cell suspension is centrifuged and a cell pellet is obtained. The cells are then redispersed in PBS (750 uL) and 5 uL of 2 mg/mL RNase is added and the cells are incubated at 37 °C for 30 min. After RNase treatment, cells are stained with 75 uL of the fluorescent nucleic acid dye, Propidium iodide (PI, 1 mg/mL). Cells are then incubated at room temperature for 15 min, after which they are passed through a 40 um sterile filter. Cells are then analyzed on a BD LSR II (BD Biosciences) with a 488 nm excitation. Flow cytometry data is analyzed using the flow cytometry analysis software, FlowJo. Results are reported as the average % of cells in each phase of the cell cycle \pm standard deviation.

3.4.2.5. Cell Viability Assay

In order to determine cell viability, an XTT assay (Biotium, Inc. Cat# 30007) was utilized. Briefly, HSC cells were plated in a 96-well tissue culture plate. Cells were allowed to grow overnight, after which, treatment was administered according to method described in Section 3.4.2.3. Upon treatment of cells, they are washed with PBS and then incubated with the activated XTT reagent (prepared according to manufacturer's protocol) for 5 h. The cell viability is determined based on spectrophotometric

measurements of the XTT reagent with a Biotek Synergy H4 multi-mode plate reader. All treated groups are normalized to the control (HSC cells treated with 0.2% DMSO) and results are reported as the average % viability \pm % relative standard deviation.

3.4.2.6. Apoptosis and Necrosis Detection via Flow Cytometry

In order to quantify the various modes of cell death that are potentially involved with the combination treatment of AuNPs and 5-FU, the *ApoTarget*TM Annexin-V FITC Apoptosis Kit (Invitrogen, Inc. Cat. #PHN1010) was utilized. The standard protocol was optimized for our experimental conditions. Briefly, HSC cells were plated in a 12-well tissue culture plate. Cells were allowed to grow overnight after which treatment was administered according to method described in Section 3.4.2.3. Upon treatment of cells, they are washed with PBS and collected by trypsinization and centrifugation. The cells are then washed again with cold PBS and collected by centrifugation, after which, 500 μ L of 1x Annexin binding buffer, 2 μ L of 100 μ g/mL PI and 5 μ L of Annexin-V-FITC are all mixed with the cells and left to incubate for 15 min at room temperature. Following cell staining with PI and Annexin-V-FITC, the remaining volume of 1x Annexin binding buffer was added (493 μ L) and the cell solution was passed through a 40 μ m sterile filter. Cells are then analyzed on a BD LSR II (BD Biosciences) with a 488 nm excitation. Flow cytometry data is analyzed using the flow cytometry analysis software, FlowJo. Results are reported as the average % of cells \pm standard deviation.

3.4.2.7. Statistical Analysis

Statistical significance was determined with the *t test calculator* (GraphPad Software, Inc.). Data is considered statistically significant when $p < 0.05$ and is indicated by *.

3.4.3. Results and Discussion

3.4.3.1. Gold Nanoparticle Induced Cell Cycle Regulation

Cell cycle regulation can be advantageous, specifically for the sensitization of malignant cells to specific methods of cancer treatment.[15, 16] Particularly, some chemotherapeutic agents act on cells that are in a specific phase of the cell cycle (*e.g.* G0/G1, S, or G2/M). For example, 5-Fluorouracil (5-FU), a standard drug utilized in the clinical treatment of cancers of the head and neck,[22, 23] is most effective when cells are in the S phase of the cell cycle, as it is associated with the incorporation of fluoronucleotides (*e.g.* fluorodeoxyuridine triphosphate, FdUTP) in place of nucleotides (*e.g.* deoxyuridine triphosphate, dUTP) in the cell's DNA.[17-19] Since we have shown previously that AuNPs conjugated with NLS and RGD peptides have the ability to alter the cell cycle of HSC-3 cells[3, 5], we took this further by testing their ability to chemosensitize HSC-3 cells to 5-FU treatment *in vitro*. In order to first estimate the efficacy by which these nanoparticles chemosensitize HSC-3 cells to 5-FU treatment, we performed cell cycle analysis on cells after a 24 h treatment with various AuNPs (0.4 nM), as well as a subsequent treatment with 100 μ M 5-FU. In order to compare cell cycle regulation between nanoparticle size, 15 and 30 nm NLS-AuNPs, known to localize at the nucleus of HSC-3 cells,[5] were tested. In order to compare between the location of nanoparticles within cells (*i.e.* AuNP surface functionalization), the 30 nm NLS-AuNPs were also compared to RGD-AuNPs, known to localize in the cytoplasm of HSC-3 cells.[5] Figure 3.23 shows the cell cycle analysis of HSC-3 cells after various treatments. An interesting observation here is that all nanoparticles induce an increase in the S phase population and a decrease in the G2/M phase population of cells after a 24 h treatment.

Also shown by the cell cycle analysis is that 100 μM 5-FU itself induces an S phase accumulation with a G2/M phase depletion. The combination treatment of AuNPs and 5-FU causes an S phase increase with a G2/M phase decrease, but only in the case of the 30 and 15 nm NLS-AuNPs (Fig. 3.23A,B).

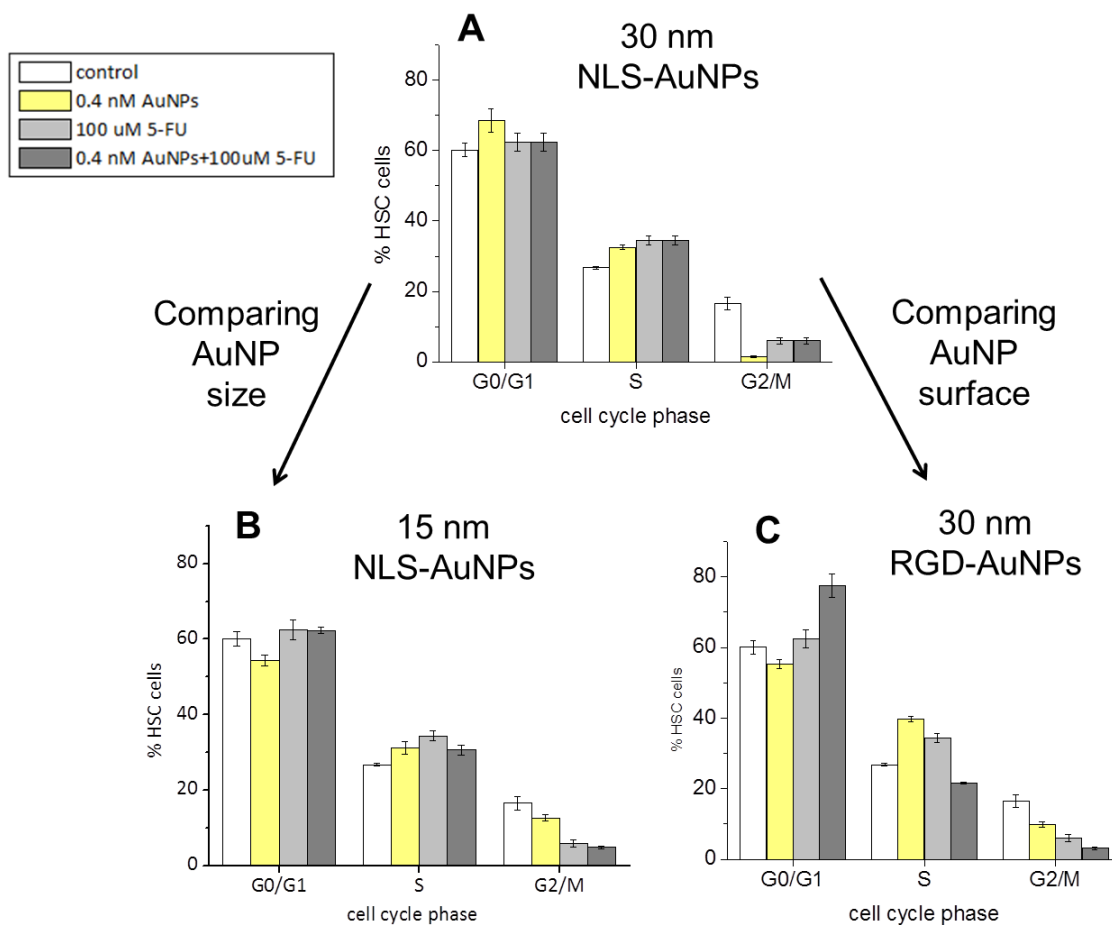


Figure 3.23. Cell cycle analysis of HSC-3 cells after treatment with various AuNPs (0.4 nM, 24 h) and 5-FU (100 μM , 48 h). Cells that were not treated (white), cells treated with AuNPs alone (yellow), cells treated with 5-FU alone (light gray) and cells treated with combination of AuNPs and 5-FU (dark gray). Comparison between AuNP size: (A) 30 nm NLS-AuNPs versus (B) 15 nm NLS-AuNPs. Comparison between AuNP surface functionalization: (A) 30 nm NLS-AuNPs versus (C) 30 nm RGD-AuNPs.

The cell cycle regulation observed for the combination of AuNPs and 5-FU suggests that the potency of 5-FU could be enhanced when administered after an initial 24 h

treatment with the AuNPs tested in this work. In order to assess this potency, we have calculated the 5-FU efficacy by dividing the S phase population by the G2/M phase population. This value is justified as the chemosensitivity factor since 5-FU itself causes an S phase accumulation with a G2/M phase depletion (Fig. 3.23), and previous reports have defined the resistance to 5-FU as a decrease in S phase with an increase in G2/M phase populations.[18] Figure 3.24 shows the 5-FU chemosensitivity factors for the various nanoparticle treatments alone (0.4 nM, 24 h), as well as in combination with 100 μ M 5-FU (48 h). The inherent 5-FU efficacy value for HSC-3 cells is around 1.6 and after treatment with 100 μ M 5-FU, this value is increased to 5.8. In terms of the various nanoparticles tested here, the 30 nm NLS-AuNPs have the greatest impact on 5-FU efficacy, increasing the value to 21.4 and when combined with 100 μ M 5-FU, the value is increased even more, to 29.8. The 15 nm NLS-AuNPs increase 5-FU efficacy to 2.5, and only up to 6.3 when combined with 5-FU. The 30 nm RGD-AuNPs increase 5-FU efficacy to 4.1, but only up to 6.9 when combined with 5-FU. It is clear here that 5-FU efficacy is influenced by AuNPs and is dependent on the size and location of nanoparticles within cells, with 30 nm nuclear-localized AuNPs being the most effective at enhancing 5-FU efficacy.

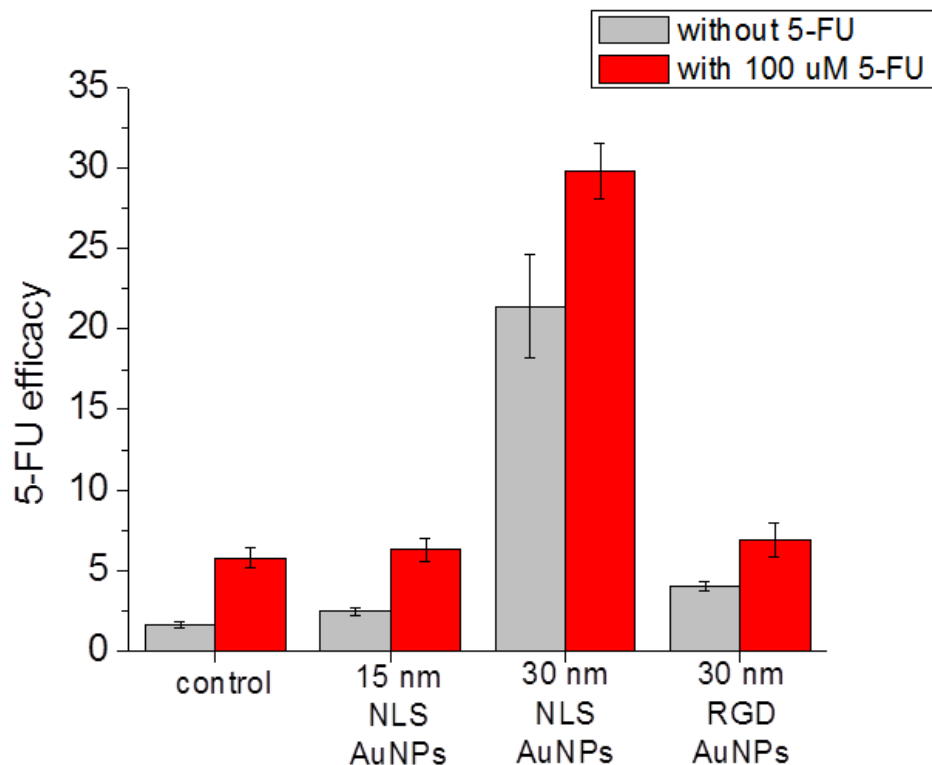


Figure 3.24. 5-FU efficacy in HSC-3 cells after treatment with various AuNPs (0.4 nM, 24 h) and 5-FU (100 μ M, 48 h). Control represents cells that were not treated with any AuNPs. Cells that were not treated with 5-FU (light gray) and cells that were treated with 5-FU (red). 5-FU efficacy defined as % cells in S phase divided by % cells in G2/M phase of the cell cycle.

3.4.3.2. Enhanced 5-Fluorouracil Chemosensitivity

Utilizing the various AuNPs and their ability to regulate the cell cycle, as shown above, we can now assess whether these nanoparticles actually sensitize HSC-3 cells to 5-FU treatment (*i.e.* chemosensitization). HSC-3 cells were initially treated with the different AuNPs (0.4 nM, 24 h) in order allow for accumulation of cells in the S phase and depletion of cells in the G2/M phase. Following AuNP treatment, 5-FU was introduced at increasing concentrations (10-500 μ M, 48 h) and the cell viability was determined. Figure 3.25 displays the results of the cell viability analysis comparing between both AuNP size and AuNP surface functionalization (*i.e.* nanoparticle location

within the cell). It should first be noted that none of the AuNP formulations shown here are inherently cytotoxic to the HSC-3 cells (no significant reduction in cell viability upon 24 h treatment with 0.4 nM AuNPs), possibly alleviating common toxicity issues presented with combination chemotherapies. As one would expect, cell viability decreases with increasing concentrations of 5-FU. The lowest cell viability observed for the control (no AuNPs) is about 40% when the cells are treated with 500 μ M 5-FU, but when pre-treated with 30 nm NLS-AuNPs (Fig. 3.25A), the cell viability is significantly reduced to 17%. In addition to the 500 μ M 5-FU treatment being more effective, sensitivities to concentrations as low as 100 μ M are also significantly enhanced by the pre-treatment of cells with the 30 nm NLS-AuNPs (Fig. 3.25A). When comparing AuNP size, the 15 nm NLS-AuNPs (Fig. 3.25B) do not appear to enhance the efficacy of 5-FU at any of the 5-FU treatment concentrations tested. In particular, at 5-FU concentrations of 10 and 100 μ M, the cell viability is significantly enhanced by pre-treatment of cells with 15 nm NLS-AuNPs. At increasing concentrations of 5-FU (200-500 μ M), pre-treatment of cells with 15 nm NLS-AuNPs has no significant effect on 5-FU efficacy. Another comparison here is the different effects induced when the nanoparticles are localized in the cytoplasm of the cell (RGD-AuNPs) as opposed to at the nucleus of the cell (NLS-AuNPs). When cells are pre-treated with 30 nm RGD-AuNPs (Fig. 3.25C), the efficacy of 10 μ M 5-FU is significantly enhanced (79% cell viability reduced to 43%). At higher 5-FU treatment concentrations (100-500 μ M), the pre-treatment of cells with 30 nm RGD-AuNPs does not have any significant effect on 5-FU efficacy.

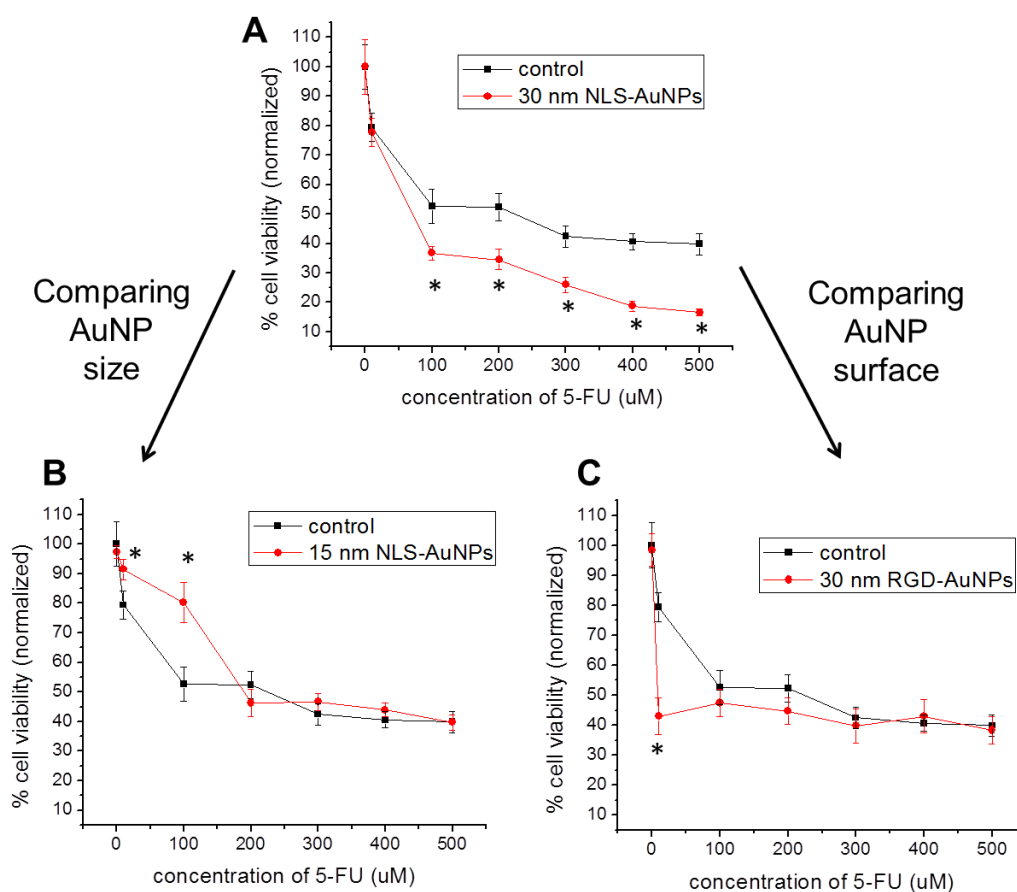


Figure 3.25. Cell viability determined by an XTT assay of HSC-3 cells after treatment with various AuNPs (0.4 nM, 24 h) and 5-FU (10-500 μ M, 48 h). Cells that were only treated with 5-FU (control, black) and cells treated with a combination of AuNPs and 5-FU (red). Comparison between AuNP size: (A) 30 nm NLS-AuNPs versus (B) 15 nm NLS-AuNPs. Comparison between AuNP surface functionalization: (A) 30 nm NLS-AuNPs versus (C) 30 nm RGD-AuNPs. Statistical significance between cells treated with only 5-FU and cells treated with combination of AuNPs and 5-FU is indicated by * ($p < 0.05$).

It is clear from the cell viability results shown in Figure 3.25 that there are definite differences in the 5-FU efficacy after cells are pre-treated with various AuNPs. The 30 nm NLS-AuNPs appear to be the most effective at sensitizing HSC-3 cells to 5-FU treatment, which is also confirmed by the high 5-FU efficacy values determined by cell cycle analysis (Fig. 3.23), and no apparent increase in 5-FU uptake by the presence of

nanoparticles was observed in this case (see Appendix A, Figure A10). Smaller AuNPs (15 nm NLS-AuNPs) and AuNPs localized at the cytoplasm (30 nm RGD-AuNPs) do not consistently enhance the efficacy of 5-FU, which is also confirmed by the lower 5-FU efficacy values determined by cell cycle analysis (Fig. 3.24).

In order to further assess the mode by which the 30 nm NLS-AuNPs chemosensitize HSC-3 cells to 5-FU, cell death was investigated by flow cytometry analysis of cells labeled with the nucleic acid dye, propidium iodide (necrotic cells), cells stained with a phosphatidylserine label, Annexin-V-FITC (early apoptotic cells), cells labeled with both (late apoptotic), and cells that are unlabeled (live cells). Figure 3.26 displays percentages of necrotic (red), late apoptotic (dark blue), early apoptotic (light blue) and live (green) cells after treatment with 0.4 nM 30 nm NLS-AuNPs alone (24 h), 150 μ M 5-FU alone (48 h), as well as 150 μ M 5-FU (48 h) after pre-treatment with 30 nm NLS-AuNPs (0.4 nM, 24 h). The primary mode of cell death upon treatment with 5-FU appears to be via early apoptosis. Interestingly, the 30 nm NLS-AuNP treatment also exhibits a higher degree of early apoptosis, compared to necrosis or late apoptosis. Although early apoptosis is the predominant mode of cell death, late apoptosis and necrosis also occur to a significant degree. In terms of late apoptosis, when cells are treated with the combination of 30 nm NLS-AuNPs (0.4 nM, 24 h) and 150 μ M 5-FU (48 h), the population is significantly enhanced compared to either treatment alone. In terms of necrosis, the population is also significantly enhanced for the combination treatment, compared to treatment with only 30 nm NLS-AuNPs or only 5-FU. In looking at the early apoptotic populations, which appear to be the dominant mode of cell death for both individual treatments, the pre-treatment with 30 nm NLS-AuNPs does not enhance the

amount of early apoptotic cells. It is interesting to note that this is the only population of dead cells in which this trend is observed, possibly due to the fact that the 30 nm NLS-AuNPs alone exhibit a smaller population of early apoptotic cells than the 5-FU alone, therefore not providing any enhancement in this mode of cell death.

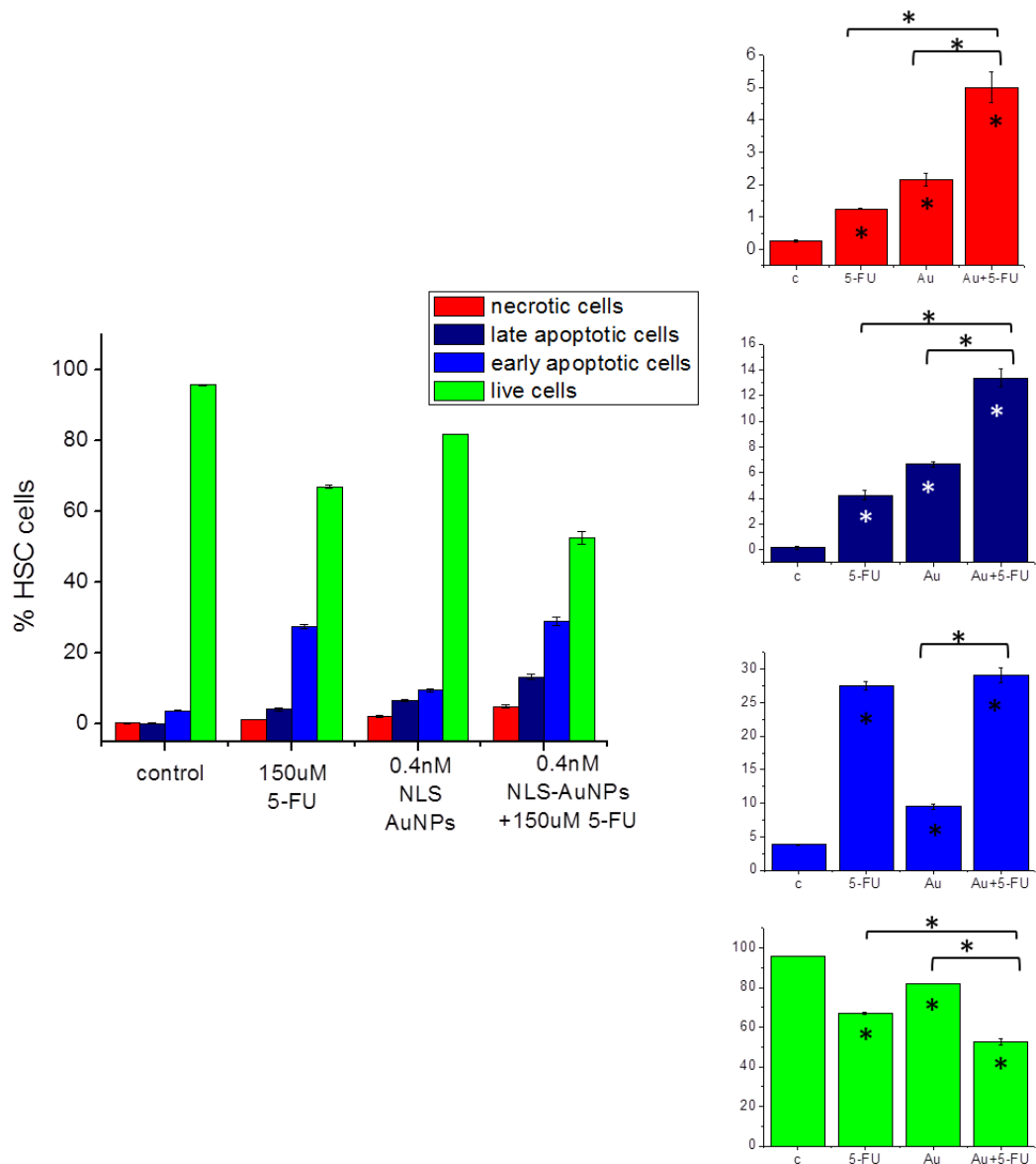


Figure 3.26. Flow cytometry analysis of HSC-3 cell death after treatment with 0.4 nM NLS-AuNPs (24 h), 150 µM 5-FU (48 h) or 0.4 nM NLS-AuNPs (24 h) followed by 150 µM 5-FU (48 h). Right panel shows necrotic cells (red), late apoptotic cells (dark blue), early apoptotic cells (light blue) and live cells (green) for cells that were untreated (c), treated with 150 µM 5-FU for 48 h (5-FU), treated with 0.4 nM 30 nm AuNPs for 24 h (Au) and treated with 150 µM 5-FU (48 h) after 24 h pre-treatment with 0.4 nM 30 nm NLS-AuNPs (Au + 5-FU). Statistical significance with respect to the control is indicated by * ($p < 0.05$) within the bars of the graph. Statistical significance with respect to different treatment groups indicated by * ($p < 0.05$) above graph.

3.4.4. Conclusions and Future Outlook

In conclusion, we have shown that nuclear-targeted gold nanoparticles (NLS-AuNPs), specifically 30 nm in diameter, regulate the cell cycle of HSC-3 cells by inducing an accumulation of cells in the S phase with a depletion of cells in the G2/M phase. The S phase accumulation and G2/M phase depletion can be used to quantify the efficacy of a common chemotherapeutic agent, 5-Fluorouracil (5-FU). Of all the nanoparticles tested in this work, the 5-FU efficacy value is highest when cells are treated with 30 nm NLS-AuNPs (0.4 nM, 24 h), compared with 15 nm NLS-AuNPs or 30 nm RGD-AuNPs (cytoplasm localized AuNPs). This high 5-FU efficacy value is made more apparent when testing the cytotoxicity of 5-FU after pre-treatment with the various AuNPs. The cell viability of 5-FU treated cells is significantly reduced when the cells are pre-treated with 30 nm NLS-AuNPs (0.4 nM, 24 h), compared with cells pre-treated with the smaller NLS-AuNPs or the RGD-AuNPs. More detailed analyses of the modes of cell death involved with 5-FU treatment revealed that these 30 nm NLS-AuNPs also enhance levels of late apoptosis and necrosis when introduced to the cells 24 h prior to 5-FU treatment. It is clear that cell cycle regulation plays a major role in enhancing drug efficacy in malignant cells. A detailed mechanism by which gold nanoparticles are capable of doing this will be essential. Once the molecular mechanisms involved in AuNP-induced cell cycle alterations are determined, chemosensitization via AuNPs can be exploited as a new technique for the treatment of various cancers with various chemotherapies.

3.4.6. References

1. Mackey, M. A., El-Sayed, M.A. (2013) Enhancing 5-Fluorouracil Drug Efficacy by Gold Nanoparticle Cell Cycle Regulation, *in progress*.
2. AshaRani, P. V., Low Kah Mun, G., Hande, M. P., and Valiyaveetil, S. (2009) Cytotoxicity and genotoxicity of silver nanoparticles in human cells, *ACS Nano* 3, 279-290.
3. Kang, B., Mackey, M. A., and El-Sayed, M. A. (2010) Nuclear targeting of gold nanoparticles in cancer cells induces DNA damage, causing cytokinesis arrest and apoptosis, *J Am Chem Soc* 132, 1517-1519.
4. Austin, L. A., Kang, B., Yen, C. W., and El-Sayed, M. A. (2011) Nuclear targeted silver nanospheres perturb the cancer cell cycle differently than those of nanogold, *Bioconjugate chemistry* 22, 2324-2331.
5. Mackey, M. A., Saira, F., Mahmoud, M. A., and El-Sayed, M. A. (2013) Inducing Cancer Cell Death by Targeting Its Nucleus: Solid Gold Nanospheres versus Hollow Gold Nanocages, *Bioconjugate chemistry* 24, 897-906.
6. Hirsch, L. R., Stafford, R. J., Bankson, J. A., Sershen, S. R., Rivera, B., Price, R. E., Hazle, J. D., Halas, N. J., and West, J. L. (2003) Nanoshell-mediated near-infrared thermal therapy of tumors under magnetic resonance guidance, *Proceedings of the National Academy of Sciences of the United States of America* 100, 13549-13554.
7. O'Neal, D. P., Hirsch, L. R., Halas, N. J., Payne, J. D., and West, J. L. (2004) Photo-thermal tumor ablation in mice using near infrared-absorbing nanoparticles, *Cancer Lett* 209, 171-176.
8. Huang, X., El-Sayed, I. H., Qian, W., and El-Sayed, M. A. (2006) Cancer cell imaging and photothermal therapy in the near-infrared region by using gold nanorods, *J Am Chem Soc* 128, 2115-2120.
9. El-Sayed, I. H., Huang, X., and El-Sayed, M. A. (2006) Selective laser photothermal therapy of epithelial carcinoma using anti-EGFR antibody conjugated gold nanoparticles, *Cancer Lett* 239, 129-135.
10. Huang, X., Jain, P. K., El-Sayed, I. H., and El-Sayed, M. A. (2007) Gold nanoparticles: interesting optical properties and recent applications in cancer diagnostics and therapy, *Nanomedicine (Lond)* 2, 681-693.

11. Chen, J., Wang, D., Xi, J., Au, L., Siekkinen, A., Warsen, A., Li, Z. Y., Zhang, H., Xia, Y., and Li, X. (2007) Immuno gold nanocages with tailored optical properties for targeted photothermal destruction of cancer cells, *Nano Lett* 7, 1318-1322.
12. Dickerson, E. B., Dreaden, E. C., Huang, X., El-Sayed, I. H., Chu, H., Pushpanketh, S., McDonald, J. F., and El-Sayed, M. A. (2008) Gold nanorod assisted near-infrared plasmonic photothermal therapy (PPTT) of squamous cell carcinoma in mice, *Cancer Lett* 269, 57-66.
13. Bhattacharya R., M. P., Xiong Z., Atala A., Soker S., Mukhopadhyay. (2004) *Nano Lett* 4, 2479-2481.
14. Mukherjee, P., Bhattacharya, R., Wang, P., Wang, L., Basu, S., Nagy, J. A., Atala, A., Mukhopadhyay, D., and Soker, S. (2005) Antiangiogenic properties of gold nanoparticles, *Clinical cancer research : an official journal of the American Association for Cancer Research* 11, 3530-3534.
15. Roa, W., Zhang, X., Guo, L., Shaw, A., Hu, X., Xiong, Y., Gulavita, S., Patel, S., Sun, X., Chen, J., Moore, R., and Xing, J. Z. (2009) Gold nanoparticle sensitize radiotherapy of prostate cancer cells by regulation of the cell cycle, *Nanotechnology* 20, 375101.
16. Xu, W., Luo, T., Li, P., Zhou, C., Cui, D., Pang, B., Ren, Q., and Fu, S. (2012) RGD-conjugated gold nanorods induce radiosensitization in melanoma cancer cells by downregulating alpha(v)beta(3) expression, *International journal of nanomedicine* 7, 915-924.
17. Longley, D. B., Harkin, D. P., and Johnston, P. G. (2003) 5-fluorouracil: mechanisms of action and clinical strategies, *Nature reviews. Cancer* 3, 330-338.
18. De Angelis, P. M., Svendsrud, D. H., Kravik, K. L., and Stokke, T. (2006) Cellular response to 5-fluorouracil (5-FU) in 5-FU-resistant colon cancer cell lines during treatment and recovery, *Molecular cancer* 5, 20.
19. Yoshida, S., Ito, D., Nagumo, T., Shirota, T., Hatori, M., and Shintani, S. (2009) Hypoxia induces resistance to 5-fluorouracil in oral cancer cells via G(1) phase cell cycle arrest, *Oral Oncol* 45, 109-115.
20. Frens, G. (1973) Controlled Nucleation for Regulation of Particle-Size in Monodisperse Gold Suspensions, *Nature-Phys Sci* 241, 20-22.
21. Liu, X., Atwater, M., Wang, J., and Huo, Q. (2007) Extinction coefficient of gold nanoparticles with different sizes and different capping ligands, *Colloids and surfaces. B, Biointerfaces* 58, 3-7.

22. Andreadis, C., Vahtsevanos, K., Sidoras, T., Thomaidis, I., Antoniadis, K., and Mouratidou, D. (2003) 5-Fluorouracil and cisplatin in the treatment of advanced oral cancer, *Oral Oncol* 39, 380-385.
23. Yoshitomi, I., Kawasaki, G., Yanamoto, S., and Mizuno, A. (2006) Orotate phosphoribosyl transferase mRNA expression in oral squamous cell carcinoma and its relationship with the dihydropyrimidine dehydrogenase expression and the clinical effect of 5-fluorouracil, *Oral Oncol* 42, 880-887.

CHAPTER 4

EXTRINSIC PROPERTIES OF GOLD NANOPARTICLE CONJUGATES

4.1. The Most Effective Gold Nanorod Size for Plasmonic Photothermal Therapy: Theory and Experiment [1]

The development of new and improved photothermal contrast agents for the successful treatment of cancer via plasmonic photothermal therapy (PPTT) is a crucial part of the application of nanotechnology in medicine. It is well established that as the size of a plasmonic nanoparticle decreases, the percentage of its extinction cross section that is converted to heat increases. But it is also known that the extinction cross section itself decreases as the size of the nanoparticle decreases. Taking these two factors into consideration, one expects that there is a gold nanorod (AuNR) with an optimum size that is most efficient in heat production when exposed to near-infrared (NIR) laser irradiation for the treatment of cancer via PPTT. In the present work, we utilize theoretical calculations as well as experimental techniques to determine this optimum AuNR size, by comparing plasmonic properties and the efficacy as photothermal contrast agents of three different sizes of AuNRs. The more conventional AuNRs used in PPTT are synthesized via seed-mediated growth, having dimensions of 38 x 11 nm. The smaller, less conventional, AuNRs are synthesized by a seedless growth method, described previously by our group, having dimensions of 28 x 8 nm and 17 x 5 nm. Our theoretical calculations showed that the absorbance:scattering ratio of the 28 x 8 nm AuNRs is 3 times greater than that of the commonly used larger (38 x 11 nm) AuNRs. We confirmed this experimentally in solution, by near-infrared (NIR) cw laser irradiation, where the optical density of the 38 x 11 nm AuNRs had to be 3 times that of the 28 x 8 nm AuNRs

in order to achieve an equivalent temperature increase. More theoretical calculations were carried out in order to determine the electromagnetic field intensity around the different AuNRs. The maximum field intensity for the 28 x 8 nm AuNRs is 1.5 times greater than that of the 38 x 11 nm AuNRs. We further confirmed this experimentally, by determining a parameter termed the photothermal heat conversion factor per particle. This value was found to be 1.4 greater for the 28 x 8 nm AuNRs than that of the 38 x 11 nm AuNRs. We also found that the field of the 17 x 5 nm AuNR extends a much shorter distance from its surface than that of the larger AuNRs, making it much less efficient at generated heat in solution. These results encouraged us to carry out *in vitro* experiments to compare the PPTT efficacy of the different sized AuNRs. The 28 x 8 nm AuNRs were found to be the most effective in PPTT of human oral squamous cell carcinoma because the cancer cell death induced by the plasmonic AuNR-induced hyperthermia is greatest when this size AuNR is used as the photothermal contrast agent.

4.1.1. Introduction

Plasmonic photothermal therapy (PPTT) for the treatment of cancer has received a great deal of attention in recent years, especially with the advent of new photothermal contrast agents.[2] In the past decade, specifically, there has been much progress in the development of plasmonic nanoparticles for photothermal therapy applications due to their unique optical properties, namely their localized surface plasmon resonance (LSPR),[3, 4] as well as their inherently low toxicities.[5-7] The unique plasmonic properties of the nanoparticles can be exploited in photothermal therapy by coherently photo-exciting their conduction electrons to induce surface plasmon oscillations. Upon surface plasmon formation, non-radiative relaxation occurs through electron-phonon and phonon-phonon coupling, efficiently generating localized heat that can be transferred to the surrounding environment.[4, 8, 9] This conversion of photon energy to thermal energy is useful in biomedical applications, such as plasmonic photothermal therapy of cancer.[10-14]

In PPTT, thermal energy generated can induce temperature increases of more than 20°C (*i.e.* hyperthermia), which can thereby induce tumor tissue ablation.[11, 12, 15-21] This was first demonstrated *in vitro*, by Lin and coworkers in 2003, using antibody-conjugated spherical gold nanoparticle-labeled lymphocytes and a nanosecond pulsed visible laser.[22] A few years later, El-Sayed and coworkers also used visible light and antibody-conjugated spherical gold nanoparticles for the selective photothermal ablation of epithelial carcinoma cells *in vitro*. [10] Although visible light is successful in destroying cells labeled with spherical gold nanoparticles, the need for radiation to penetrate deep into tissues, with minimal attenuation by water and hemoglobin, is desired

for the practical application of PPTT. Near-infrared (NIR) external radiation is capable of achieving this, such that it can penetrate up to 10 cm in soft tissues (termed the NIR tissue transmission window, 650-900 nm).[23] By changing the shape and composition of the nanoparticle, the surface plasmon absorption can be shifted into the NIR transmission window.[24-29] With this in mind, gold nanoparticles (AuNPs) that absorb in the NIR tissue transmission window were developed by Halas and coworkers (silica-gold core-shell nanoparticles),[12, 30] El-Sayed and coworkers (rod-shaped AuNPs),[13, 31] as well as Xia and coworkers (gold nanocages).[32] When comparing the different nanoparticle structures in terms of their application in PPTT, the most important plasmonic properties to consider are the absorption cross section, absorption efficiency, and thermal transduction per particle. Of all the plasmonic AuNPs developed, the rod-shaped AuNPs, or gold nanorods (AuNRs), exhibit the most ideal NIR absorption cross section[33] and demonstrate extremely efficient NIR photothermal heat conversion.[19] The most common size of AuNR utilized for use in successful PPTT now is around 40 nm in length and 10 nm in diameter, with a longitudinal plasmon resonance around 800 nm. Investigating various AuNR sizes, specifically those that have smaller dimensions, and their efficacy as photothermal contrast agents has important implications in the clinical applications of AuNRs in PPTT, especially since the accumulation and toxicity of smaller AuNRs in the tumor interstitium and the organs of the reticuloendothelial system (RES) could be more ideal than that of the larger AuNRs. Also, as previously shown theoretically by Jain *et.al.*, plasmonic absorption becomes dominant as the nanoparticle size is decreased.[34, 35] More specifically, the extinction of the AuNRs increases with the size of the AuNRs, while the contribution of scattering also increases, essentially

decreasing the absorbance:scattering ratio as the AuNR size increases. This ultimately suggests that as the particle size decreases, the absorbance:scattering ratio increases, allowing for greater photothermal heat conversion and therefore potentially enhancing PPTT efficacy with decreased particle size. Another plasmonic property associated with photothermal heat conversion is the electric field around the AuNRs. It has previously been shown that excitation at the plasmon wavelength creates very strong electromagnetic fields,[36, 37] and the field strength trends with absorbance, not scattering or extinction.[38] Since the field strength is derived from absorbance, not scattering, greater absorbance with smaller AuNRs would indicate a stronger field, which in turn would result in greater photothermal heat conversion and, again, enhanced PPTT efficacy.

In this work, we present both theoretical and experimental results, ultimately comparing AuNRs commonly used for PPTT (about 38 x 11 nm) and new, smaller AuNRs[39] (about 28 x 8 nm and 17 x 5 nm), in order to determine which would be the most effective photothermal contrast agent. The discrete dipole approximation (DDA), a theoretical technique for modeling the spectral properties of varying nanoparticle shapes, was utilized for the theoretical portion of this work. DDA has the advantage of being able to model particles of arbitrary shape.[34, 37, 40-43] In this method, the particle is represented by a three-dimensional finite lattice of point dipoles that is excited by an external field. The response of the point dipoles to the external field and to one another is solved self-consistently using Maxwell's equations. The DDSCAT 6.1 code offered publicly by Draine and Flatau[44] allows for the calculation of the absorbance and scattering spectra separately, enabling the assessment of the contributions from each to

the extinction spectra, which is ideal for comparing the absorbance:scattering ratio of the two different sizes of AuNRs. Furthermore, with modifications to the code by Goodman[45] and Schatz,[46] it is possible to calculate the electric field enhancement contours and the individual dipole orientations at a specific wavelength, allowing for the theoretical estimation of the potential heat generated by the different-sized AuNRs upon exposure to NIR radiation. Theoretical results show that the electromagnetic field around the particle and the absorbance:scattering ratio both increase with decreasing AuNR size, as expected. Experimental AuNR heating quantitatively agrees with the theoretical calculations for the 28 x 8 and 38 x 11 nm AuNRs, while the 17 x 5 nm particles do not experimentally trend with the theoretical results. We suggest that this is due to the fact that although the 17 x 5 nm AuNRs have the highest absorbance:scattering ratio and the most intense electromagnetic field, the field decays from the surface of the nanoparticle to a very short distance, suggesting that effective experimental heating of the solution, when exposed to NIR radiation, would be less likely.

We take our theoretical and experimental results a bit further by determining the efficacy of the different sized AuNRs as photothermal contrast agents, using an *in vitro* malignant cell model. The 28 x 8 nm AuNRs showed the greatest efficacy, exhibiting greater cell death upon NIR laser irradiation compared to the more conventional AuNRs (38 x 11 nm) as well as the smallest AuNRs (17 x 5 nm). These results suggest that the most ideal AuNR for the plasmonic photothermal treatment of disease is that of a median size (e.g. 28 x 8 nm).

4.1.2. Experimental Methods

4.1.2.1. Gold Nanorod (AuNR) synthesis and PEG conjugation

The large AuNRs were synthesized via the seed-mediated growth method.[47] Briefly, a seed solution consisting of 7.5 mL of 0.2 M CTAB, 2.5 mL of 1.0 mM HAuCl₄ and 600 μ L 0.01 M NaBH₄ is prepared, followed by a growth solution containing 100 mL of 1.0 mM HAuCl₄, 100 mL of 0.2 M CTAB, 5 mL of 4.0 mM silver nitrate and 1.4 mL of 78.8 mM ascorbic acid. A 240 μ L volume of the seed solution is added to the growth solution, producing AuNRs approximately 38 nm in length and 11 nm in width, as displayed in Figure 4.1A. The surface plasmon resonance (SPR) of these AuNRs is around 740 nm.

Two different, smaller, AuNRs were synthesized by a seedless growth method.[39] In this method, the growth solution was kept at an acidic pH and sodium borohydride was added instead of a seed solution, for simultaneous seed formation and AuNR growth. To obtain AuNRs approximately 28 nm in length and 8 nm in width (Fig. 4.1B), 300 μ L of 0.01 M NaBH₄ was prepared and added to an acidic growth solution containing 160 μ L of 37% HCl, 100 mL of 1.0 mM HAuCl₄, 100 mL of 0.2 M CTAB, 5 mL of 4.0 mM silver nitrate and 1.4 mL of 78.8 mM ascorbic acid. The SPR of these AuNRs is around 770 nm. To obtain AuNRs approximately 17 nm in length and 5 nm in width (Fig. 4.1C), 150 μ L of 0.01 M NaBH₄ was prepared and added to an acidic growth solution containing 160 μ L of 37% HCl, 50 mL of 1.0 mM HAuCl₄, 100 mL of 0.2 M CTAB, 5 mL of 4.0 mM silver nitrate and 700 μ L of 78.8 mM ascorbic acid. The SPR of these AuNRs is around 755 nm. All CTAB-stabilized AuNRs were also purified by centrifugation and redispersed in dI H₂O.

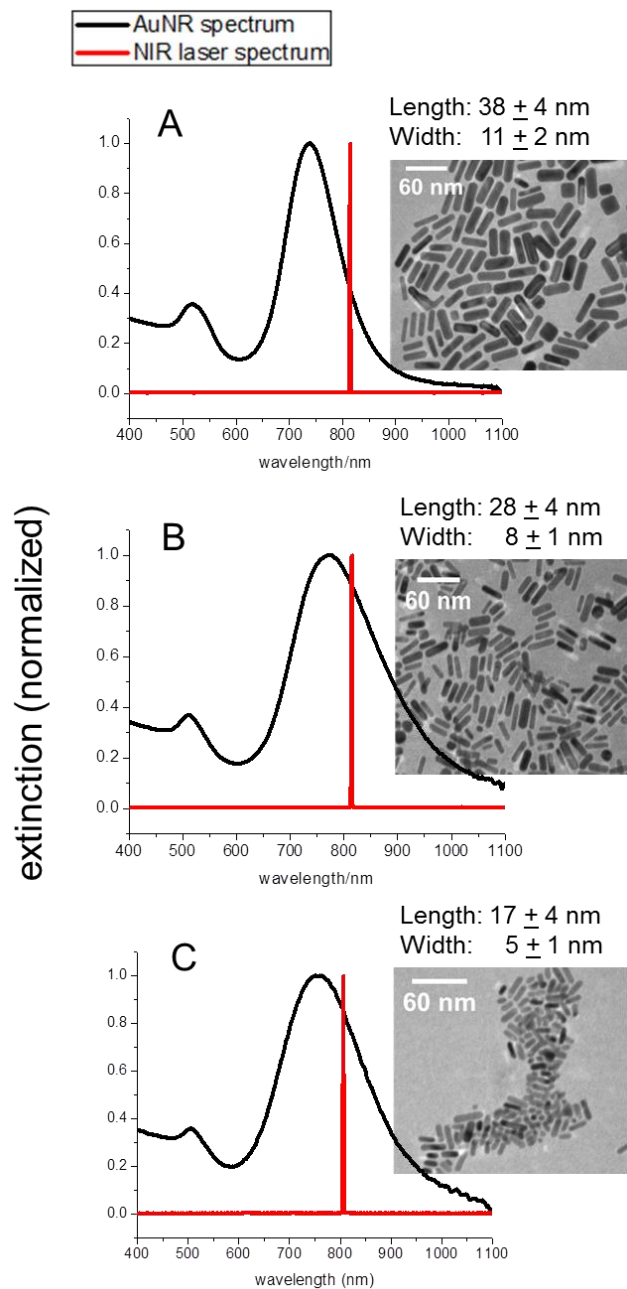


Figure 4.1. UV-Vis spectra of AuNRs (black) as well as the NIR cw laser spectrum (red) (with corresponding TEM images, scale bar: 60 nm). (A) 38 x 11 nm AuNRs with longitudinal plasmon resonance at 740 nm. (B) 28 x 8 nm AuNRs with longitudinal plasmon resonance at 770 nm (C) 14 x 5 nm AuNRs with longitudinal plasmon resonance at 755 nm.

After purification, the various AuNRs were functionalized with polyethylene glycol (mPEG-SH, MW 5000, Laysan Bio, Inc.) and left on a shaker overnight, after which, they were centrifuged and redispersed in dI H₂O.

4.1.2.2. Photothermal heating of AuNRs in solution

The as-synthesized (*i.e.* CTAB capped) AuNRs were diluted in dI H₂O, such that the three AuNR solutions had either the same concentration of particles or the same optical density (OD). The AuNR concentrations were calculated based on the previously determined extinction coefficients for the 17 x 5 nm AuNRs ($7.9 \times 10^7 \text{ M}^{-1} \text{ cm}^{-1}$), 28 x 8 nm AuNRs[39] ($1.5 \times 10^8 \text{ M}^{-1} \text{ cm}^{-1}$) and the 38 x 11 nm AuNRs[48] ($4.0 \times 10^9 \text{ M}^{-1} \text{ cm}^{-1}$). A 500 uL volume of AuNRs, in a microcentrifuge tube, was exposed to a near-infrared (NIR) cw laser (808 nm) at 5.8 W/cm^2 (spot size around 5.6 mm) at increasing irradiation times. The temperature increase of the solution was measured by placing a 33 gauge hypodermic thermocouple (Omega) directly into the AuNR solution. A 500 uL solution of dI H₂O was also measured and the temperature increase of the H₂O was subtracted from that of the AuNR solutions in order to account for any heat generated from the laser itself. For normalization purposes, all initial temperatures were $24 \pm 1 \text{ }^\circ\text{C}$. TEM images and UV-Vis spectra indicate that photothermal heating did not alter the structure or spectra of the AuNRs (data not shown).

4.1.2.3. AuNR heating in cell culture and cell viability assay

Human oral squamous cell carcinoma (HSC-3) cells were maintained in Dulbecco's modified Eagle's medium (DMEM, Mediatech) supplemented with 10% v/v fetal bovine serum (FBS, Mediatech) and 1% v/v antimycotic solution (Mediatech). The cell culture

was kept in a 37°C, 5% CO₂, humidified incubator. HSC-3 cells were grown in 96-well tissue culture plates overnight. After which, the growth media was removed and replaced with growth media containing PEG-AuNRs at optical densities of 0.5 (17 x 5, 28 x 8 and 38 x 11 nm AuNRs) and 1.5 (38 x 11 nm AuNRs). After a 2 h incubation time, the cells were exposed to a NIR cw laser (808 nm) at 5.8 W/cm² (spot size around 5.6 mm) at increasing irradiation times. The temperature increase was measured by placing a 33 gauge hypodermic thermocouple (Omega) directly into the culture medium. For normalization purposes, all initial temperatures were 32 ± 1 °C. The cell viability was determined via an XTT cell viability assay kit (Biotium, Inc), according to the manufacturer's protocol.

4.1.2.4. Statistical analysis

Results are expressed as the mean ± standard deviations of three independent experiments. Statistical significance (*i.e.* p-value) was calculated by a *t-test calculator* (GraphPad Software, Inc.). Statistically significant data is indicated by * (p-value < 0.05).

4.1.2.5. DDA calculations

The optical response of a gold nanorod with varying dimensions (38 x 10 nm, 25 x 7 nm, and 18 x 4 nm) was calculated using the DDA method with the DDSCAT 6.1 code offered publicly by Draine and Flatau[44] with modifications by Goodman[45] and Schatz.[46] The dielectric values for gold reported by Johnson and Christy[49] were used. The incident light is always polarized along the length of the particle (*i.e.* longitudinal mode) in this report, and the medium surrounding the particle was

represented as water with a refractive index of 1.333. The nanorods were modeled as cylinders with hemispherical end caps.

4.1.3. Results and Discussion

4.1.3.1. Size-Dependent Photothermal Heat Conversion: Experiment

Gold nanorods (AuNRs) were synthesized with lengths of around 38 nm (Fig. 4.1A), 28 nm (Fig. 4.1B) and 17 nm (Fig. 4.1C). The longitudinal plasmon resonances of the different AuNRs are around 740, 770 and 755 nm, respectively. With the knowledge that plasmonic absorption dominates as nanoparticle size is decreased,[34, 35] we expect that the smaller AuNRs would generate more heat than the larger AuNRs when exposed to near-infrared (NIR) cw laser irradiation (808 nm). Therefore, we determined the photothermal heat conversion factor, per particle, in order to directly compare the difference in heat generated by the different AuNRs upon NIR irradiation at increasing time intervals. This was done by preparing 10 nM solutions of the three different AuNRs (see Experimental Methods for details). The solutions were each then exposed to NIR radiation at 5.8 W/cm^2 (spot size around 5.6 mm). Upon determining the increase in temperature for the AuNR solutions, the change in temperature per AuNR was calculated and multiplied by a factor (10^{11}) in order to simplify the values being compared. Figure 4.2 compares the photothermal heat conversion factor of each different AuNR tested in this work. As the NIR laser irradiation time is increased, the photothermal heat conversion factor increases, especially for AuNRs that are 28 nm in length. At an exposure time of 2 min, the photothermal heat conversion factor for the 17, 28 and 38 nm

AuNRs is 1.21, 2.48 and 1.77, respectively. This indicates that the 28 nm AuNRs exhibit the greatest photothermal heat conversion, which was unexpected since we predicted that the smaller the AuNRs would generate more heat upon NIR laser irradiation. Therefore, a thorough investigation of the plasmonic properties of these three different nanoparticles, as well as their efficacy in plasmonic photothermal therapy, is warranted.

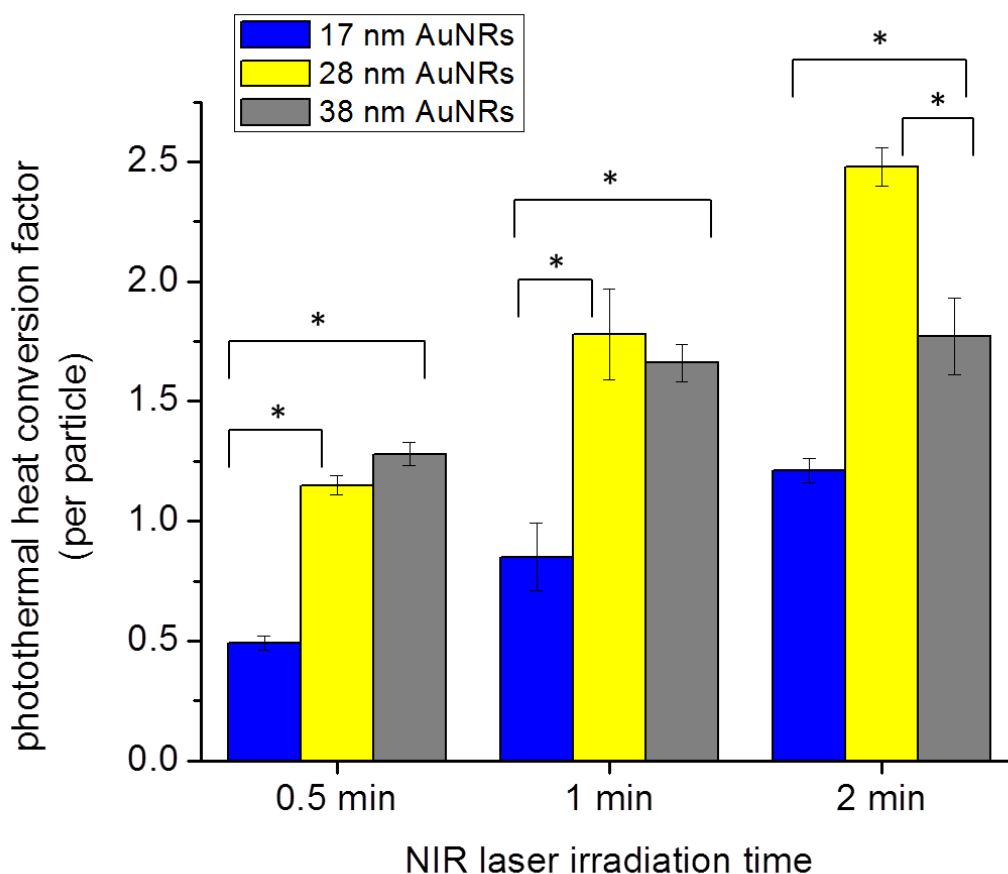


Figure 4.2. Photothermal heat conversion factor determined, per particle, for 17 x 5 nm AuNRs (17 nm, blue), 28 x 8 nm AuNRs (28 nm, yellow) and 38 x 11 nm AuNRs (38 nm, gray) at increasing NIR laser irradiation time. All initial temperatures were 24 ± 1 °C. Statistical significance ($p < 0.05$) indicated by *.

4.1.3.2. Size-Dependent Electromagnetic Field: Theory

Since the experimental photothermal heat conversion factor per particle could potentially be related to the field enhancement around the particle, the Discrete Dipole Approximation (DDA) was used to generate field contour plots for three different AuNRs (38 x 10 nm, 25 x 7 nm and 18 x 4 nm) shown in Figure 4.3. The laser wavelength (808 nm) used for experimental heating did not exactly correspond to the plasmon resonances of the AuNRs, therefore in the DDA calculations the AuNRs were similarly excited off resonance. We also compared the field enhancement values for the three AuNRs (38 x 10, 25 x 7 and 18 x 4 nm) on resonance, at their respective resonance wavelengths (786, 757 and 865 nm), which can be seen in Figure B.1 of Appendix B. Experimentally, the particles were excited at 808 nm (i.e. off resonance), at which point the extinction value of the AuNRs was decreased by 15% (18 x 4 nm), 6% (25 x 7 nm) and 46% (38 x 10 nm), compared to their maximum value (Fig. 4.1). In order to account for this theoretically, we calculated the electromagnetic field contours at 804 nm for the 38 x 10 nm AuNR, 761 nm for the 25 x 7 nm AuNR and 875 nm for the 18 x 4 nm AuNR, which are the wavelengths where the DDA calculated extinction decreased by 46%, 6% and 15% from its maximum value, respectively. As shown in Figure 4.3, the maximum fields generated are 3500, 5220 and 5480 for the 38 x 10, 25 x 7 and 18 x 4 nm AuNRs, respectively. It should also be noted that the field maximum for the 25 x 7 nm AuNRs is 1.5 times that of the 38 x 10 nm AuNRs, which is consistent with their experimentally determined photothermal heat conversion factor being 1.4 times greater than that of the 38 nm AuNRs.

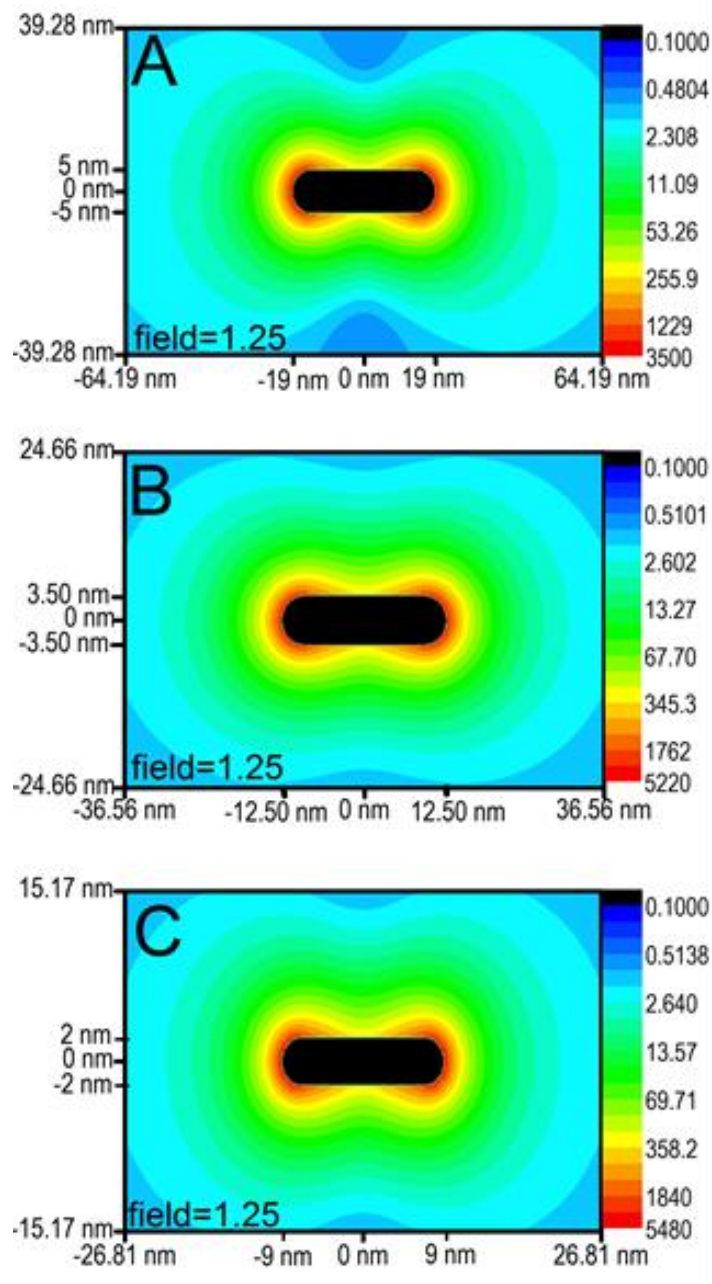


Figure 4.3. Field contour plots for the longitudinal mode of the different AuNRs, with particle dimensions indicated and the field decaying to 1.25 at the extremities of each plot. (A) The field maximum of the 38 x 10 nm AuNR (calculated at 804 nm) is 3500. (B) The field maximum of the 25 x 7 nm AuNR (calculated at 761 nm) is 5220. (C) The field maximum of the 18 x 4 nm AuNR (calculated at 875 nm) is 5480.

This trend of increasing electromagnetic field with decreasing particle size is expected, but does not necessarily correlate with what was seen experimentally for the photothermal heat conversion factor (Figure 4.2). The smallest AuNRs had the smallest photothermal heat conversion factor, suggesting that they would have the weakest electromagnetic field, but they in fact have the strongest field according to our calculations. Therefore, another factor involved in the photothermal heat conversion could be the distance at which the field decays. In order to achieve overall heating of the surrounding medium, as opposed to local heating around the particle, the field needs to extend a certain distance away from the particle surface. Because the field decays exponentially from the particle surface, both the maximum field enhancement value and particle size play a role in how far the enhanced field extends away from the particle. Therefore, also shown in Figure 4.3 are the distances at which the field has decayed to a value of 1.25. The smallest AuNR (18 x 4 nm) does indeed have the strongest field, but it only extends 15.17 nm from the nanoparticle surface before it has decayed to a value of 1.25, while the 25 x 7 nm AuNR has a slightly weaker field maximum, but the field extends out to 24.66 nm from the nanoparticle surface. The largest AuNR (38 x 10 nm) has the weakest field maximum, but has the largest distance at which the field decays to 1.25 (39.28 nm).

The distance at which the field decays is relevant in terms of the experimental photothermal heat conversion determined for these AuNRs, such that although the smallest AuNR (18 x 4 nm) has the strongest field, it does not extend far enough from the nanoparticle surface to achieve sufficient overall experimental heating of the 10 nM

AuNR solution. The concentration of the smallest AuNRs must be at least 20 nM in order for the solution temperature to reach that which is comparable to the other AuNRs at 10 nM concentrations (see Appendix B, Table B.1). The necessity for this prohibitively high concentration of the smallest AuNRs renders these particles impractical for applications in which overall heating of a solution is desired.

4.1.3.3. Size-Dependent Absorbance:Scattering Ratio: Theory

To further investigate the plasmonic properties of the different sized AuNRs, which influence their differences in photothermal heat conversion, DDA calculations were done to determine the contributions of absorbance and scattering to the total extinction of the particles. In Figure 4.4, the DDA spectra show that the plasmon resonance for the longitudinal mode of the 38, 25 and 18 nm AuNRs are at 786, 757 and 865 nm, respectively. Additionally, the total extinction decreases with increasing particle size, with the contribution from scattering also decreasing with particle size, as expected.[34, 35] The absorbance:scattering ratio for the 38, 25 and 18 nm is 63.8, 204 and 921, respectively. Therefore, comparing the smaller AuNRs to the 38 nm AuNRs, the absorbance:scattering ratio is 3.2 times greater for the 25 nm AuNRs and 14.4 times greater for the 18 nm AuNRs. This suggests that the experimental photothermal heating of AuNR solutions would be equivalent when the optical density of 38 nm AuNRs is about 3 times that of the 28 nm AuNRs and about 14 times that of the 17 nm AuNRs.

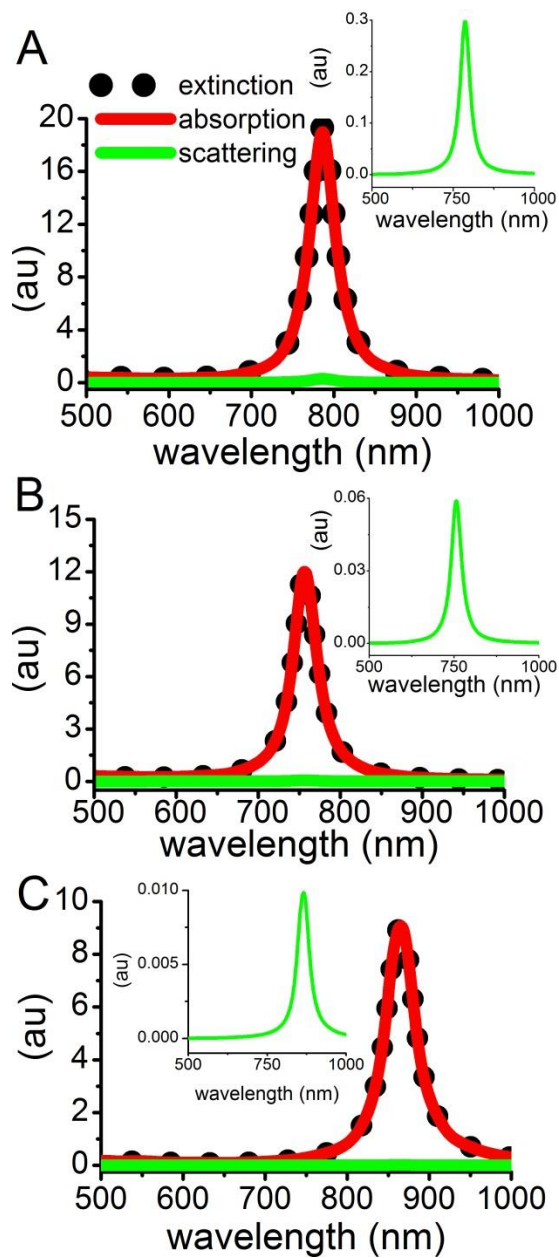


Figure 4.4. DDA extinction (black dots), absorption (red line) and scattering (green line, and shown in inset) spectra for the longitudinal mode of the different AuNRs in water. (A) The 38 x 10 nm AuNR has an absorbance:scattering ratio of 63.8. (B) The 25 x 7 nm AuNR has an absorbance:scattering ratio of 204. (C) The 18 x 4 nm AuNR has an absorbance:scattering ratio of 921.

4.1.3.4. Size-Dependent Absorbance:Scattering Ratio: Experiment

In order to experimentally correlate the calculated absorbance:scattering ratio to photothermal heat conversion, we looked at the NIR photothermal heating of the different sized AuNRs at varying extinctions (optical densities). Specifically, as shown in Figure 4.5, the smaller AuNRs (17 and 28 nm) with an OD of 0.5 demonstrate statistically significant enhanced photothermal heating (increase by 15 °C) compared to that of the 38 nm AuNRs at OD 0.5 after 2 min of NIR laser exposure. Interestingly, the small AuNRs (17 and 28 nm) at OD 0.5 and the large AuNRs (38 nm) with OD 1.5, exhibit about the same change in temperature after 2 min of NIR laser exposure. This shows that a 3-fold increase in the optical density, the same difference in the absorbance:scattering ratio predicted by DDA, was needed to achieve the same temperature increase. Again, the 28 x 8 and 38 x 11 nm AuNRs experimentally agree with the theoretical calculations for the 25 x 7 nm and 38 x 10 nm AuNRs, while the 17 x 4 nm AuNRs do not experimentally correlate with the theoretical predictions, since they are limited by a threshold solution concentration of 20 nM (OD 1.6) for sufficient overall experimental heating to be observed (see Appendix B, Table B.1).

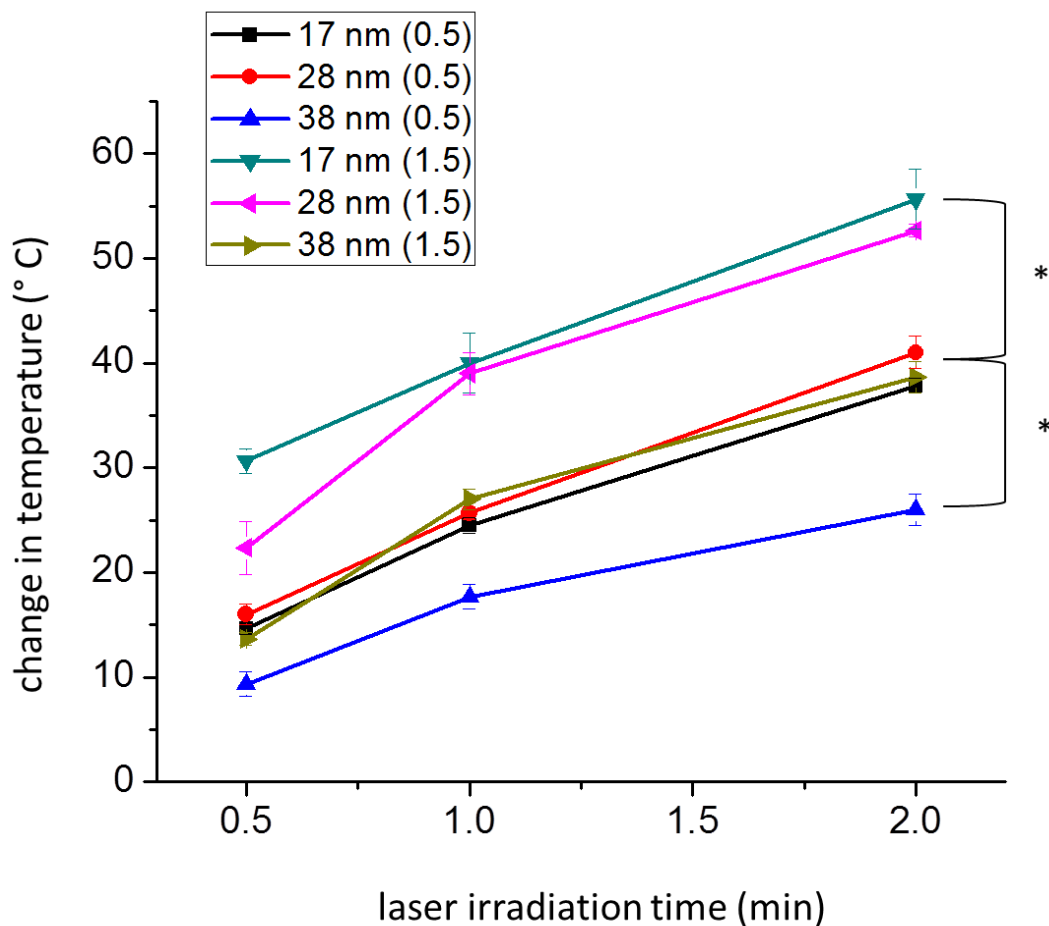


Figure 4.5. Temperature change induced by plasmonic photothermal heating of different AuNRs (17, 29=8 and 38 nm in length) at different optical densities (0.5 and 1.5) and increasing NIR laser irradiation times. All initial temperatures were 24 ± 1 °C. Statistical significance between different sized AuNRs and optical densities at 2 min laser irradiation ($p < 0.5$) is indicated by *.

4.1.3.5. Size-Dependent in vitro Plasmonic Photothermal Efficacy in HSC-3 Cancer Cells

The enhanced photothermal heat conversion observed with the 28 nm AuNRs suggests that these nanoparticles would have great potential as photothermal contrast agents in Plasmonic Photothermal Therapy (PPTT). Therefore, we used HSC-3 cells (oral squamous cell carcinoma), *in vitro*, to compare the efficacy of the three different PEG-AuNRs for photothermal ablation. Our *in vitro* experiments essentially represent a situation in which the malignant cells are surrounded by a solution containing the photothermal contrast agents (*i.e.* PEG-AuNRs). These *in vitro* results can perhaps be expanded to the *in vivo* regime, in which a tumor is directly injected with AuNRs. HSC-3 cells were treated with the three different PEG-AuNRs for 2 h before exposure to NIR radiation. The cells were irradiated at 5.8 W/cm^2 for 0.5, 1 and 2 min, and the temperature increase was directly measured in the cell culture using a hypodermic thermocouple. The change in temperature observed for the different PEG-AuNRs in the cell culture is shown in Figure 4.6.

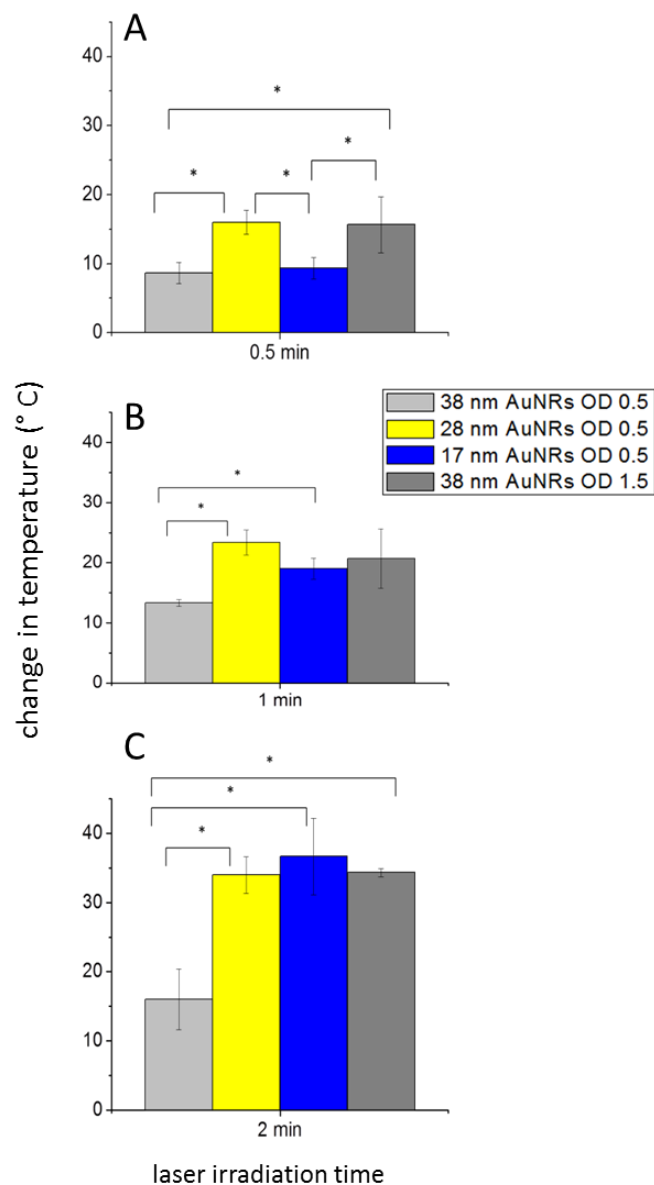


Figure 4.6. Temperature change of cell culture medium containing different AuNRs. AuNRs 38 nm in length at OD 0.5 (light gray), AuNRs 28 nm in length at OD 0.5 (yellow), AuNRs 17 nm in length at OD 0.5 (blue) and AuNRs 38 nm in length at OD 1.5 (dark gray) were all exposed to upon NIR laser irradiation at increasing lengths of time. All initial temperatures were 32 ± 1 °C. . Statistical significance between different sized AuNRs and optical densities ($p < 0.5$) is indicated by * above bars.

It is clear that at the same OD, the temperature increase is greater for the smaller PEG-AuNRs (17 and 28 nm) than for the large PEG-AuNRs (38 nm). When the optical density of the large PEG-AuNRs was made to be 3 times that of the smaller PEG-AuNRs, as suggested by the absorbance:scattering ratios determined with DDA (Fig. 4.4) and the photothermal heating in solution (Fig. 4.5), the temperature increase was similar to that of both smaller PEG-AuNRs. These temperature increases indicate hyperthermia, which is a well-established mode of tumor tissue ablation.[11-13] Therefore, it is important to assess the outcome of these temperature increases by determining the cell death associated with the AuNR-induced plasmonic photothermal hyperthermia. As shown in Figure 4.7, the cell viability decreases with increasing NIR laser irradiation times, as would be expected. Also interesting here is that the greatest amount of cell death, at any exposure time, is observed for the 28 nm PEG-AuNRs with an OD of 0.5. The 17 nm PEG-AuNRs with an optical density of 0.5 and the 38 nm PEG-AuNRs with an optical density of 1.5 show a higher cell viability, but not statistically significant enough to claim it as different from that of the 28 nm PEG-AuNRs (OD 0.5). The 38 nm PEG-AuNRs at OD 0.5 do not show any significant change in cell viability upon NIR laser exposure at any of the exposure times tested here.

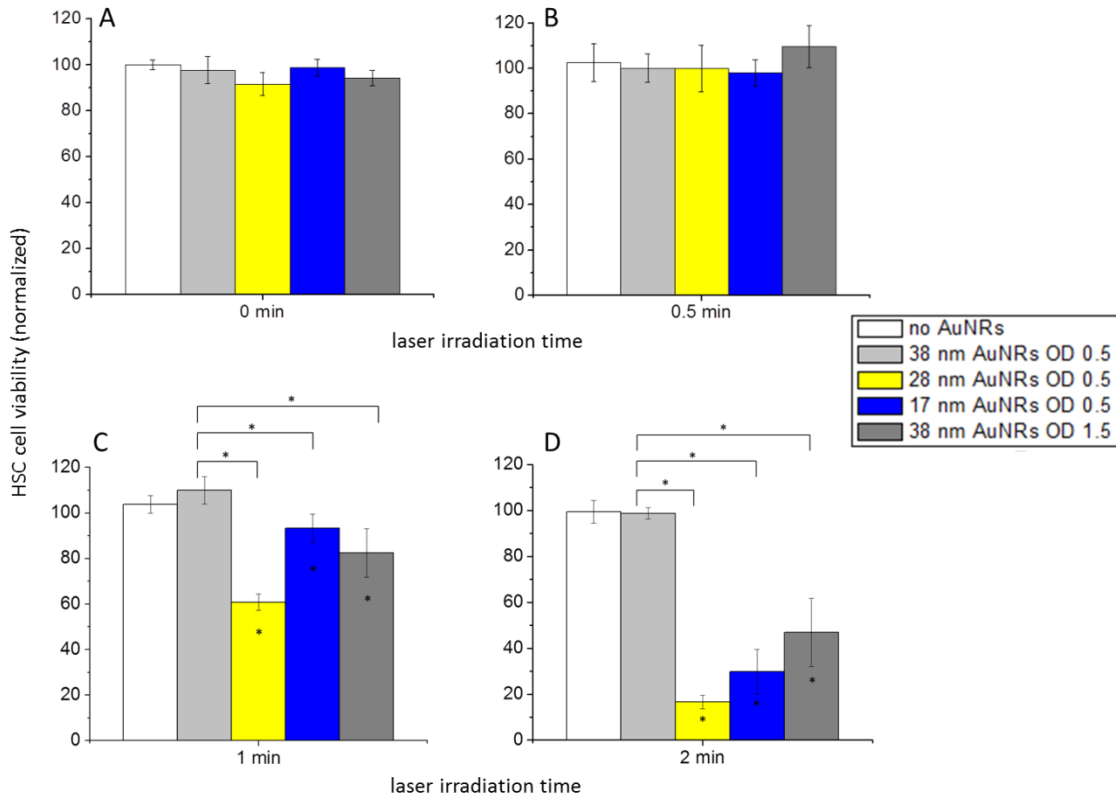


Figure 4.7. Cell viability determined for HSC cells treated with different AuNRs and subjected to PPTT via NIR laser irradiation. Cells treated with AuNRs 38 nm in length at OD 0.5 shown in light gray, AuNRs 28 nm in length at OD 0.5 shown in yellow, AuNRs 17 nm in length at OD 0.5 shown in blue and AuNRs 38 nm in length at OD 1.5 shown in dark gray. Statistical significance ($p < 0.05$) indicated by *. Statistical significance with respect to control (no AuNRs) indicated inside bars. Statistical significance between different treatments indicated above bars.

4.1.4. Conclusions and Future Outlook

We have clearly shown, both theoretically and experimentally, that there are limitations in the AuNR size when choosing the best photothermal contrast agent for use in Plasmonic Photothermal Therapy (PPTT). It is clear from the agreement between

experimental and theoretical results presented above, that the 28 nm AuNR are capable of producing more heat via NIR cw laser irradiation than the larger more conventional (38 nm) AuNRs. The disagreement between theory and experiment for the smallest AuNR investigated (17 nm) suggests that there is a lower limit in the size of the AuNR needed to achieve sufficient experimental photothermal heating. With AuNRs having dimensions around 17 x 5 nm, the particle is so small that although it has an extremely intense electromagnetic field at its surface, this field does not extend far enough from the surface to allow for overall experimental heating of a solution. With AuNRs having dimensions around 38 x 11 nm, the particle is so large that although it exhibits a high extinction cross-section, the majority of the extinction comes from scattering instead of absorption, thus less heat is generated upon experimental NIR laser irradiation. The AuNR having dimensions of around 28 x 8 nm exhibits the most ideal size for its application as a photothermal contrast agent. This size nanorod has an intense electromagnetic field that extends far enough from the particle surface in order to achieve sufficient experimental photothermal heating. This size nanorod, although having a low extinction cross-section, the majority of the extinction comes from absorption, allowing for high photothermal heat conversion upon experimental NIR laser irradiation. These theoretical and experimental observations lead to the conclusion, and is shown in our *in vitro* experiments, that the 28 x 8 nm AuNRs are more effective photothermal contrast agents than the 38 x 11 or 17 x 5 nm AuNRs, for the photothermal ablation of cancer cells. A full assessment of these newly investigated AuNRs should be done in order to determine their efficacy *in vivo* as well as their toxicity, compared with more conventional

photothermal contrast agents. This work has the potential to aid in the development of a more effective PPTT for the treatment of disease.

4.1.5. References

1. Mackey, M. A., Near, R.D., Ali, M.R.K., Austin, L.A., El-Sayed, M.A. (2013) The Most Effective Gold Nanorod Size for Plasmonic Photothermal Therapy: Theory and Experiment, *Journal of Physical Chemistry B*, submitted.
2. Huang, X. H., Jain, P. K., El-Sayed, I. H., and El-Sayed, M. A. (2008) Plasmonic photothermal therapy (PPTT) using gold nanoparticles, *Laser Med Sci* 23, 217-228.
3. El-Sayed, M. A. (2001) Some interesting properties of metals confined in time and nanometer space of different shapes, *Acc Chem Res* 34, 257-264.
4. Link, S., and El-Sayed, M. A. (2000) Shape and size dependence of radiative, non-radiative and photothermal properties of gold nanocrystals, *Int Rev Phys Chem* 19, 409-453.
5. Connor, E. E., Mwamuka, J., Gole, A., Murphy, C. J., and Wyatt, M. D. (2005) Gold nanoparticles are taken up by human cells but do not cause acute cytotoxicity, *Small* 1, 325-327.
6. Khan, J. A., Pillai, B., Das, T. K., Singh, Y., and Maiti, S. (2007) Molecular effects of uptake of gold nanoparticles in HeLa cells, *Chembiochem : a European journal of chemical biology* 8, 1237-1240.
7. Shukla, R., Bansal, V., Chaudhary, M., Basu, A., Bhonde, R. R., and Sastry, M. (2005) Biocompatibility of gold nanoparticles and their endocytotic fate inside the cellular compartment: a microscopic overview, *Langmuir* 21, 10644-10654.
8. Jain, P. K., Huang, X. H., El-Sayed, I. H., and El-Sayed, M. A. (2008) Noble Metals on the Nanoscale: Optical and Photothermal Properties and Some Applications in Imaging, Sensing, Biology, and Medicine, *Accounts Chem Res* 41, 1578-1586.
9. Hartland, G. V. (2011) Optical Studies of Dynamics in Noble Metal Nanostructures, *Chem Rev* 111, 3858-3887.
10. El-Sayed, I. H., Huang, X. H., and El-Sayed, M. A. (2006) Selective laser photothermal therapy of epithelial carcinoma using anti-EGFR antibody conjugated gold nanoparticles, *Cancer Letters* 239, 129-135.
11. Nolsoe, C. P., Torp-Pedersen, S., Burcharth, F., Horn, T., Pedersen, S., Christensen, N. E., Olldag, E. S., Andersen, P. H., Karstrup, S., Lorentzen, T., and

- et al. (1993) Interstitial hyperthermia of colorectal liver metastases with a US-guided Nd-YAG laser with a diffuser tip: a pilot clinical study, *Radiology* 187, 333-337.
12. O'Neal, D. P., Hirsch, L. R., Halas, N. J., Payne, J. D., and West, J. L. (2004) Photo-thermal tumor ablation in mice using near infrared-absorbing nanoparticles, *Cancer Lett* 209, 171-176.
 13. Dickerson, E. B., Dreaden, E. C., Huang, X. H., El-Sayed, I. H., Chu, H. H., Pushpanketh, S., McDonald, J. F., and El-Sayed, M. A. (2008) Gold nanorod assisted near-infrared plasmonic photothermal therapy (PPTT) of squamous cell carcinoma in mice, *Cancer Letters* 269, 57-66.
 14. Gobin, A. M., Lee, M. H., Halas, N. J., James, W. D., Drezek, R. A., and West, J. L. (2007) Near-infrared resonant nanoshells for combined optical imaging and photothermal cancer therapy, *Nano Lett* 7, 1929-1934.
 15. Dreaden, E. C., Alkilany, A. M., Huang, X. H., Murphy, C. J., and El-Sayed, M. A. (2012) The golden age: gold nanoparticles for biomedicine, *Chem Soc Rev* 41, 2740-2779.
 16. Dreaden, E. C., Mackey, M. A., Huang, X. H., Kang, B., and El-Sayed, M. A. (2011) Beating cancer in multiple ways using nanogold, *Chem Soc Rev* 40, 3391-3404.
 17. Dickerson, E. B., Dreaden, E. C., Huang, X. H., El-Sayed, I. H., Chu, H. H., Pushpanketh, S., McDonald, J. F., and El-Sayed, M. A. (2008) Gold nanorod assisted near-infrared plasmonic photothermal therapy (PPTT) of squamous cell carcinoma in mice, *Cancer Lett.* 269, 57-66.
 18. Chen, J. Y., Glaus, C., Laforest, R., Zhang, Q., Yang, M. X., Gidding, M., Welch, M. J., and Xia, Y. (2010) Gold Nanocages as Photothermal Transducers for Cancer Treatment, *Small* 6, 811-817.
 19. von Maltzahn, G., Park, J. H., Agrawal, A., Bandaru, N. K., Das, S. K., Sailor, M. J., and Bhatia, S. N. (2009) Computationally guided photothermal tumor therapy using long-circulating gold nanorod antennas, *Cancer Res* 69, 3892-3900.
 20. Hirsch, L. R., Stafford, R. J., Bankson, J. A., Sershen, S. R., Rivera, B., Price, R. E., Hazle, J. D., Halas, N. J., and West, J. L. (2003) Nanoshell-mediated near-infrared thermal therapy of tumors under magnetic resonance guidance, *Proceedings of the National Academy of Sciences of the United States of America* 100, 13549-13554.

21. Lu, W., Xiong, C., Zhang, G., Huang, Q., Zhang, R., Zhang, J. Z., and Li, C. (2009) Targeted photothermal ablation of murine melanomas with melanocyte-stimulating hormone analog-conjugated hollow gold nanospheres, *Clinical cancer research : an official journal of the American Association for Cancer Research* 15, 876-886.
22. Pitsillides, C. M., Joe, E. K., Wei, X. B., Anderson, R. R., and Lin, C. P. (2003) Selective cell targeting with light-absorbing microparticles and nanoparticles, *Biophys J* 84, 4023-4032.
23. Weissleder, R. (2001) A clearer vision for in vivo imaging, *Nat Biotechnol* 19, 316-317.
24. Burda, C., Chen, X. B., Narayanan, R., and El-Sayed, M. A. (2005) Chemistry and properties of nanocrystals of different shapes, *Chem Rev* 105, 1025-1102.
25. Loo, C., Lowery, A., Halas, N. J., West, J., and Drezek, R. (2005) Immunotargeted nanoshells for integrated cancer imaging and therapy, *Nano Lett* 5, 709-711.
26. Chen, J. Y., Wang, D. L., Xi, J. F., Au, L., Siekkinen, A., Warsen, A., Li, Z. Y., Zhang, H., Xia, Y. N., and Li, X. D. (2007) Immuno gold nanocages with tailored optical properties for targeted photothermal destruction of cancer cells, *Nano letters* 7, 1318-1322.
27. Murphy, C. J., San, T. K., Gole, A. M., Orendorff, C. J., Gao, J. X., Gou, L., Hunyadi, S. E., and Li, T. (2005) Anisotropic metal nanoparticles: Synthesis, assembly, and optical applications, *J Phys Chem B* 109, 13857-13870.
28. Nikoobakht, B., and El-Sayed, M. A. (2003) Preparation and growth mechanism of gold nanorods (NRs) using seed-mediated growth method, *Chem Mater* 15, 1957-1962.
29. Wiley, B., Sun, Y. G., and Xia, Y. N. (2007) Synthesis of silver nanostructures with controlled shapes and properties, *Accounts Chem Res* 40, 1067-1076.
30. Hirsch, L. R., Stafford, R. J., Bankson, J. A., Sershen, S. R., Rivera, B., Price, R. E., Hazle, J. D., Halas, N. J., and West, J. L. (2003) Nanoshell-mediated near-infrared thermal therapy of tumors under magnetic resonance guidance, *P Natl Acad Sci USA* 100, 13549-13554.
31. Huang, X. H., El-Sayed, I. H., Qian, W., and El-Sayed, M. A. (2006) Cancer cell imaging and photothermal therapy in the near-infrared region by using gold nanorods, *Journal of the American Chemical Society* 128, 2115-2120.

32. Chen, J., Wang, D., Xi, J., Au, L., Siekkinen, A., Warsen, A., Li, Z. Y., Zhang, H., Xia, Y., and Li, X. (2007) Immuno gold nanocages with tailored optical properties for targeted photothermal destruction of cancer cells, *Nano Lett* 7, 1318-1322.
33. Hu, M., Chen, J., Li, Z. Y., Au, L., Hartland, G. V., Li, X., Marquez, M., and Xia, Y. (2006) Gold nanostructures: engineering their plasmonic properties for biomedical applications, *Chem Soc Rev* 35, 1084-1094.
34. Jain, P. K., Lee, K. S., El-Sayed, I. H., and El-Sayed, M. A. (2006) Calculated absorption and scattering properties of gold nanoparticles of different size, shape, and composition: Applications in biological imaging and biomedicine, *J Phys Chem B* 110, 7238-7248.
35. Lee, K. S., and El-Sayed, M. A. (2005) Dependence of the enhanced optical scattering efficiency relative to that of absorption for gold metal nanorods on aspect ratio, size, end-cap shape, and medium refractive index, *J Phys Chem B* 109, 20331-20338.
36. Hao, E., and Schatz, G. C. (2004) Electromagnetic fields around silver nanoparticles and dimers, *J Chem Phys* 120, 357-366.
37. Kelly, K. L., Coronado, E., Zhao, L. L., and Schatz, G. C. (2003) The optical properties of metal nanoparticles: The influence of size, shape, and dielectric environment, *J Phys Chem B* 107, 668-677.
38. Near, R., Hayden, S., and El-Sayed, M.A. (2012) Extinction vs Absorption: Which is the Indicator of Plasmonic Field Strength for Silver Nanocubes?, *Journal of Physical Chemistry C* 116, 23019-23026.
39. Ali, M. R. K., Snyder, B., and El-Sayed, M. A. (2012) Synthesis and Optical Properties of Small Au Nanorods Using a Seedless Growth Technique, *Langmuir* 28, 9807-9815.
40. Halas, N. J. (2005) Playing with plasmons. Tuning the optical resonant properties of metallic nanoshells, *Mrs Bull* 30, 362-367.
41. Olson, T. Y., Schwartzberg, A. M., Orme, C. A., Talley, C. E., O'Connell, B., and Zhang, J. Z. (2008) Hollow gold-silver double-shell nanospheres: Structure, optical absorption, and surface-enhanced Raman scattering, *J Phys Chem C* 112, 6319-6329.
42. Sun, Y. G., Mayers, B., and Xia, Y. N. (2003) Metal nanostructures with hollow interiors, *Adv Mater* 15, 641-646.

43. Wan, D. H., Chen, H. L., Lin, Y. S., Chuang, S. Y., Shieh, J., and Chen, S. H. (2009) Using Spectroscopic Ellipsometry to Characterize and Apply the Optical Constants of Hollow Gold Nanoparticles, *Acs Nano* 3, 960-970.
44. Draine, B. T., and Flatau, P. J. (1994) Discrete-Dipole Approximation for Scattering Calculations, *J Opt Soc Am A* 11, 1491-1499.
45. Goodman, J. J., Draine, B. T., and Flatau, P. J. (1991) Application of Fast-Fourier-Transform Techniques to the Discrete-Dipole Approximation, *Opt Lett* 16, 1198-1200.
46. Shuford, K. L., Ratner, M. A., and Schatz, G. C. (2005) Multipolar excitation in triangular nanoprisms, *J Chem Phys* 123.
47. Huang, X. H., Neretina, S., and El-Sayed, M. A. (2009) Gold Nanorods: From Synthesis and Properties to Biological and Biomedical Applications, *Advanced Materials* 21, 4880-4910.
48. Orendorff, C. J., and Murphy, C. J. (2006) Quantitation of metal content in the silver-assisted growth of gold nanorods, *J Phys Chem B* 110, 3990-3994.
49. Johnson, P. B., and Christy, R. W. (1972) Optical Constants of Noble Metals, *Phys Rev B* 6, 4370-4379.

4.2. Decreasing Gold Nanorod Size for Plasmonic Photothermal Therapy in a Mouse Model

Plasmonic photothermal therapy (PPTT) is a non-invasive and highly effective method of cancer treatment. Optimizing current PPTT treatment methods by determining the most efficient photothermal contrast agents is important for transitioning from *in vivo* experiments to a clinical setting. We have previously shown by theoretical calculations and experimental evaluation *in vitro*, that the most efficient gold nanorod size for plasmonic photothermal heat conversion is around 28 nm in length and 8 nm in width. Therefore, in the present work, we determine how effective these gold nanorods are as photothermal contrast agents for the photothermal ablation of tumors in a mouse model. Since these particles are new for this type of application, we also determined their pharmacokinetic properties as well as their biodistribution profile, comparing between targeting (head and neck cancer) and non-targeting AuNRs (27 x 8 nm). These particles are stable *in vivo*, as demonstrated by their long blood circulation half-lives, and exhibit accumulation in organs of the reticuloendothelial system (RES), which is common to nanoparticle-based therapies. The targeting AuNRs do exhibit enhanced tumor accumulation in squamous cell carcinoma of the head and neck as well as dramatic tumor growth suppression upon exposure to laser radiation. These results suggest a new and improved AuNR-based photothermal contrast agent for tumor ablation via PPTT.

4.2.1. Introduction

The plasmonic photothermal therapy (PPTT) treatment of cancer is a burgeoning field in medicine, especially with the use of noble metal nanoparticles, since they exhibit optical properties that can be exploited for their use as photothermal contrast agents.[1-4] The localized surface plasmon, associated with various gold nanostructures, especially gold nanorods (AuNRs),[1, 5] can be photo-excited by external radiation with coherent laser frequencies to generate local heating around the particle, which is transferred to the surrounding environment.[1, 5, 6] The heat generated by externally activating AuNRs is specifically useful in the treatment of cancer, since hyperthermia induces tumor tissue ablation. [2, 3, 7-14]

In order for PPTT to be effective *in vivo*, external radiation must be able to penetrate deep into tissues. The most ideal radiation for this application is therefore in the near-infrared (NIR) region (650-900 nm), where minimal attenuation of water and hemoglobin occurs.[3] Since the surface plasmon resonance of the photothermal contrast agent (*i.e.* AuNR) must be coherent with the laser radiation, its shape and composition can be tuned in order to achieve NIR surface plasmon resonance.[15-20]

AuNRs have already shown to have high NIR absorption cross-sections as well as high photothermal heat conversion, [11, 21] but efficient PPTT for the suppression of tumor growth has mainly only been shown for AuNRs with dimensions of 40 x 10 nm.[9] Since we previously showed, both theoretically and experimentally *in vitro* (see Chapter 4.1), that the ideal AuNR for the most efficient plasmonic photothermal heat conversion has dimensions of 28 x 8 nm, it is imperative that these particles are tested in their ability to suppress tumor growth *in vivo* via PPTT. Therefore, in the present work, we determine

the pharmacokinetics as well as the biodistribution of these smaller AuNRs in tumor-bearing mice, comparing between particles that target cancer of the head and neck and non-targeting particles. After assessing their biocompatibility *in vivo*, the smaller AuNRs were utilized as photothermal contrast agents for us in PPTT and demonstrated dramatic tumor growth suppression.

4.2.2. Experimental Methods

4.2.2.1. Gold Nanorod Synthesis and Conjugation

Relatively small gold nanorods (AuNRs) were synthesized by a seedless growth method.[22] In this method, the growth solution was kept at an acidic pH and sodium borohydride was added instead of a seed solution, for simultaneous seed formation and AuNR growth. To obtain AuNRs with a length of 27 ± 4 nm and a width of 8 ± 1 nm, as shown in Figure 4.8, 300 μ L of 0.01 M NaBH₄ was prepared and added to an acidic growth solution containing 160 μ L of 37% HCl, 100 mL of 1.0 mM HAuCl₄, 100 mL of 0.2 M CTAB, 5 mL of 4.0 mM silver nitrate and 1.4 mL of 78.8 mM ascorbic acid. The surface plasmon resonance of these AuNRs is around 760 nm (Fig. 4.8). The CTAB-stabilized AuNRs were purified by centrifugation and redispersed in dI H₂O. The extinction coefficient used for the particles (1.5×10^8 M⁻¹ cm⁻¹) is based on previous reports.[22]

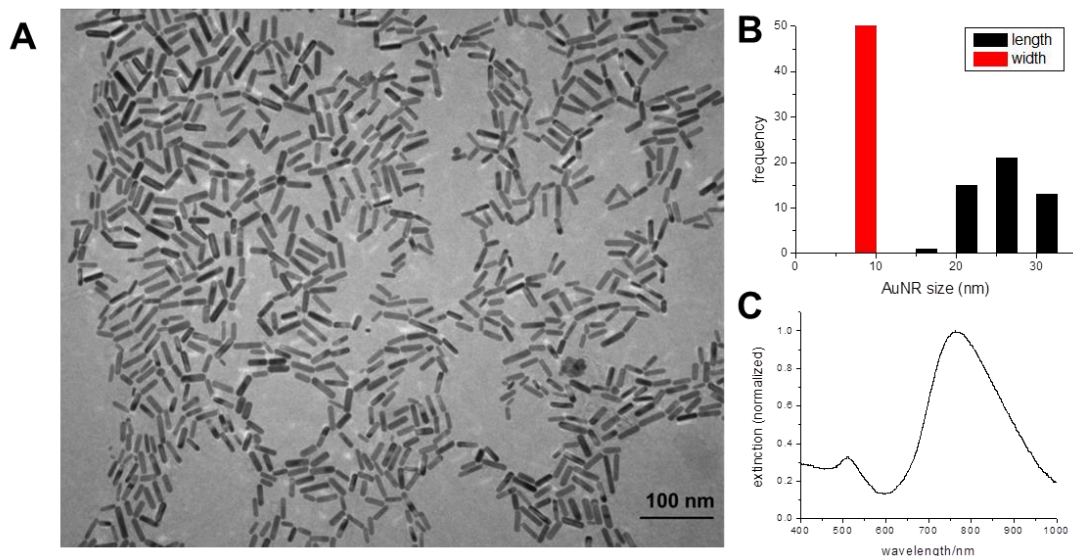


Figure 4.8. TEM image (A), size distribution (B), and UV-Vis spectrum (C) of AuNRs about 27 nm in length and 8 nm in width, with a surface plasmon resonance around 760 nm.

To obtain non-targeting AuNRs, the purified AuNRs were functionalized with polyethylene glycol (mPEG-SH, MW 5000, Laysan Bio, Inc.) by addition of a 1 mM aqueous solution of PEG to the AuNR solution at a ratio of 10,000 PEGs per AuNR and left on a shaker overnight, after which, they were centrifuged and redispersed in dI H₂O. These particles are referred to as PEG-AuNRs.

To obtain targeting AuNRs, the purified AuNRs were functionalized with PEG and a thiol-modified peptide (HNSCP, synthesized by the Oyelere Group at Georgia Tech), with a peptide sequence known to specifically target squamous cell carcinoma of the head and neck (SCCHN).[23] The peptide structure is shown in Figure 4.9 below. Functionalization of AuNRs with PEG and HNSCP was achieved by simultaneous

addition of a 1 mM aqueous solution of PEG, at 5000 PEGs per particle, and a 1 mM aqueous solution of HNSCP, at 5000 HNSCPs per particle. They were left to shake overnight, after which they were centrifuged and redispersed in DI H₂O. These particles are referred to as HNSCP-AuNRs.

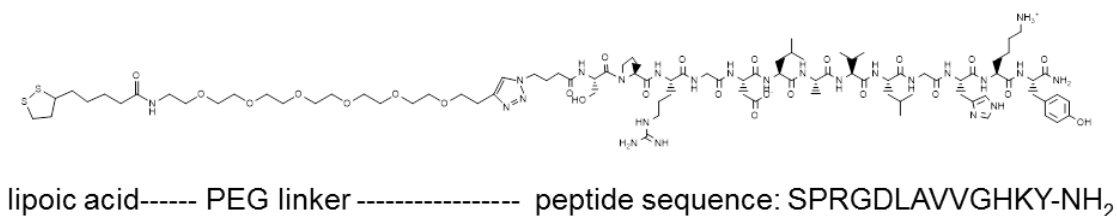


Figure 4.9. Structure of HNSCP peptide conjugated to AuNRs for specific targeting of squamous cell carcinoma of the head and neck. Peptide provided by Raftery, E. and Sotimehin, A. (Georgia Tech).

4.2.2.2. Circulation Half-Life and Biodistribution

The animal experiments have been approved by the Institutional Animal Care and Use Committee (IACUC) of Emory University. The circulation half-life experiments were carried out on BALB/c mice, 6-7 weeks of age. The animals, 3 per group, were injected via the tail vein with a 200 μ l solution of 2.5mg/kg AuNRs. A control group of 3 mice received saline alone. At specified time points of 5 min, 10, 30 min, 2h, 4, 8, 12, 24h and 72h, blood (10 μ l) was collected from the tail vein in pre-weighed heparinized capillary tubes. The blood samples were dissolved with 70% nitric acid and assayed for Au mass using ICP-MS. The mass of Au in the blood at different time points was calculated, taking into consideration that the blood constitutes 7% of the body weight.

Blood circulation half-life was calculated based on a one phase decay model using GraphPad Prism Version 6.02 (GraphPad Software, Inc.).

Biodistribution analysis was carried out on nude mice bearing human SCCHN tumors. Tu212 cells (1×10^6) were injected subcutaneously into 4-6-week old nude mice, and when the tumors develop to about 150 mm^3 , mice were divided into groups at random (3 mice per group) and were then injected via the tail vein with a 200 μl solution of 2.5 mg/kg AuNRs. A control group of 3 mice received saline alone (200 μL). At specified time points mice ($n = 3$) were euthanized by pressurized CO_2 asphyxiation. Blood samples (1000 μl) and other tissues (tumor, liver, spleen, kidney, lung, heart, brain, pancreas, stomach, intestine, bladder and muscle) were harvested for tissue distribution studies. The mass of Au in the various dried tissues was measured by ICP-MS.

4.2.2.3. Tumor Inoculation and Nanorod Injection

Animal studies have been approved by the Institutional Animal Care and Use Committee (IACUC) of Emory University. Tumor inoculation was achieved by subcutaneously injecting 1×10^6 Tu212 cells into 4-6 week old female nude mice. When the tumors reached about 200 mm^3 , the mice were divided into groups at random for each of the different treatment methods ($n = 3$). Intratumoral injection of either PBS (100 μL) or HNSCP-AuNRs (100 μL) was administered 2 min prior to laser exposure. The concentration of AuNRs injected into the tumor was adjusted according to the tumor volume, in order to achieve an overall AuNR concentration of 2.25 nM within the tumor, which was determined by preliminary experiments.

4.2.2.4. Near-Infrared (NIR) Laser Exposure

After the intratumoral injection of HNSCP-AuNRs, or PBS, tumors were extracorporeally exposed to NIR cw laser radiation (5.8 W/cm^2 for 2 min). The different treatment methods in this study are as follows: (1) control, 100 μL PBS only, (2) laser control, 100 μL PBS followed by 2 min NIR laser exposure, (3) HNSCP-AuNR control, 100 μL HNSCP-AuNRs only, and (4) HNSCP-AuNR laser treatment, 100 μL HNSCP-AuNRs followed by 2 min NIR laser exposure. After treatment, the tumor sizes were measured twice per week. The tumor volume was calculated using the formula $V = (\text{width})^2 \times (\text{length}/2)$. The data is displayed as the average tumor volume \pm standard deviation.

4.2.3. Results and Discussion

Based on our previous observations that the most effective gold nanorod (AuNR) size for plasmonic photothermal therapy (PPTT) is around 25 nm in length (see Chapter 4.1), we can now determine how effective this size AuNR is in a mouse model, particularly utilizing AuNRs that target SCCHN (Tu212 xenografts). In order to achieve targeting of SCCHN, AuNRs are conjugated with PEG and an HNSCP peptide (HNSCP-AuNRs) and non-targeting AuNRs are conjugated with PEG only (PEG-AuNRs). When transitioning from an *in vitro* model to an *in vivo* model, many more factors are involved, such as pharmacokinetic parameters, uptake of particles by the reticuloendothelial system (RES) and tumor accumulation/extravasation. The pharmacokinetic properties of the PEG-AuNRs and HNSCP-AuNRs were determined by measuring the blood circulation half-life of the particles in healthy mice. After tail vein injection of the particles, ICP-MS

measurements of Au content in the blood were taken at specified time points (0-24 h). The experimental data was fit to a one-phase decay. Figure 4.10 displays the blood circulation half-life for the PEG-AuNRs is 12.8 h (Fig. 4.10A) and for the HNSCP-AuNRs is 8.5 h (Fig. 4.10B).

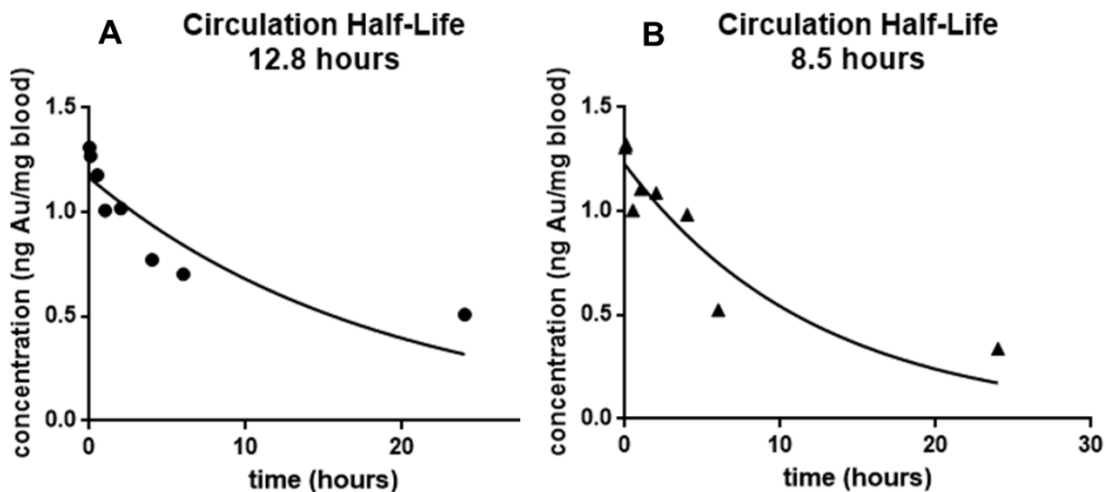


Figure 4.10. Pharmacokinetic properties, in terms of the blood circulation half-life ($t_{1/2}$) in healthy mice. (A) The $t_{1/2}$ is 12.8 h for PEG-AuNRs and (B) 8.5 h for HNSCP-AuNRs, as calculated by fitting the data to a one-phase decay model. Conjugated particles were provided by Mackey, M.A. and Ali, M.R.K. (Georgia Tech). Circulation half-life measurements were provided by Peng, X. (Emory University).

The decreased circulation half-life observed when functionalizing the AuNRs with HNSCP, indicate that blood clearance is increased when a targeting ligand is conjugated to the surface of the AuNR, which has been shown previously.[24-26] In addition to the circulation half-life, RES uptake and tumor accumulation are also important to assess before utilizing these AuNRs as photothermal contrast agents *in vivo*. Therefore, biodistribution in RES organs, as well as other tissues/organs were determined in nude

mice bearing Tu212 xenografts. Figure 4.11 displays the biodistribution for both PEG-AuNRs and HNSCP-AuNRs 24 h post tail vein injection.

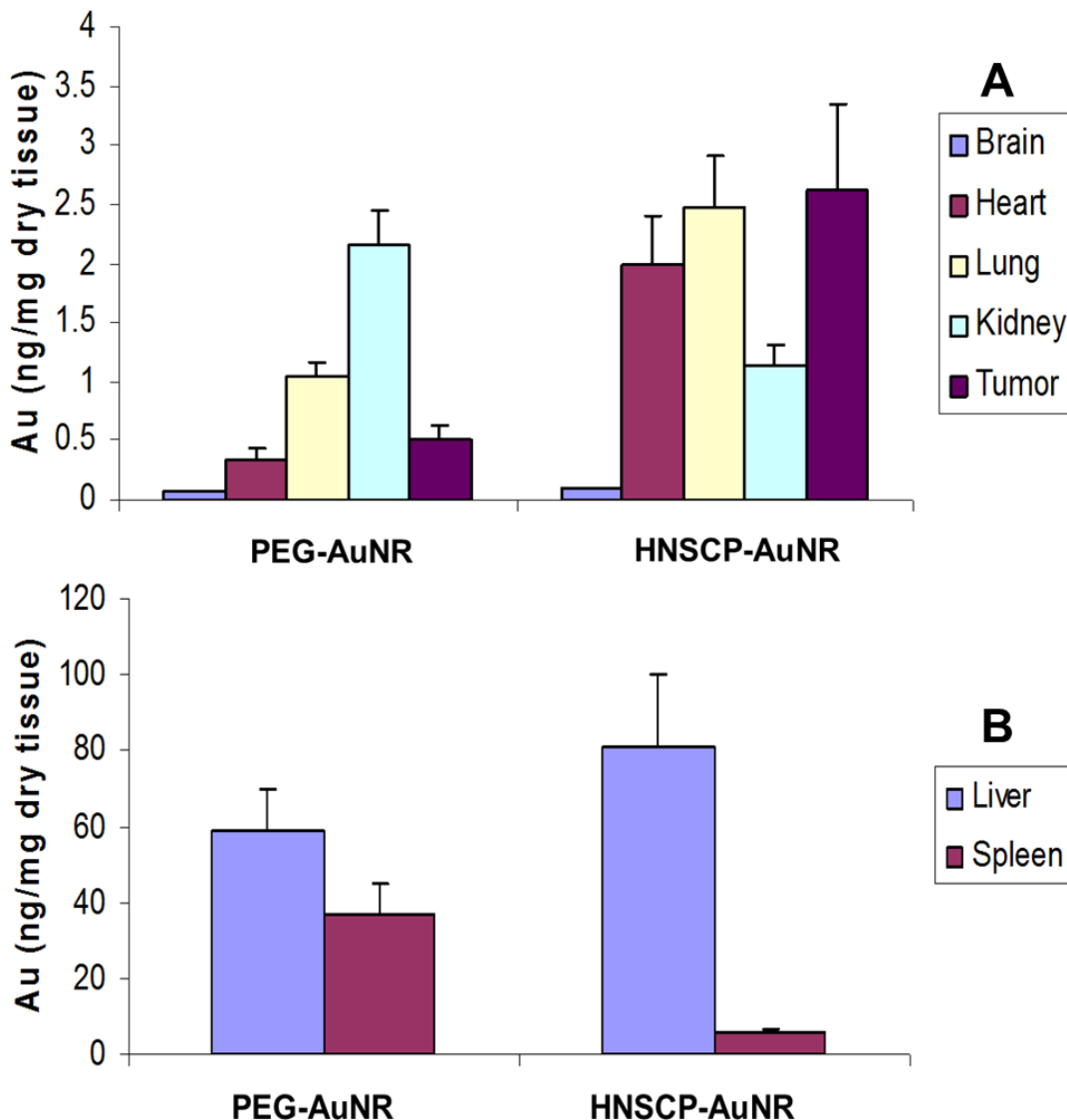


Figure 4.11. Biodistribution profile of PEG-AuNRs and HNSCP-AuNRs 24 h following iv injection to nude mice bearing Tu212 xenografts. (A) Accumulation of AuNRs in brain, heart, lung, kidney and tumor. (B) Uptake of AuNRs by RES (*i.e.* accumulation in the liver and spleen). Conjugated particles were provided by Mackey, M.A. and Ali, M.R.K. (Georgia Tech). Biodistribution profile was provided by Peng, X. (Emory University).

The HNSCP-AuNRs exhibit enhanced tumor accumulation when compared with the PEG-AuNRs (Fig. 4.11A), as expected. The surface functionalization (targeting vs. non-targeting) also appears to have an effect on the accumulation of AuNRs in tissues such as brain, lung, kidney, and RES organs (liver and spleen). Specifically, the HNSCP-AuNRs exhibit a much lower accumulation in the spleen, compared to the PEG-AuNRs. The pharmacokinetic parameters and biodistribution profile of the targeting and non-targeting AuNRs suggests that the surface functionalization of the AuNRs has an impact on how these AuNRs behave *in vivo*.

The HNSCP-AuNRs were chosen as the AuNR to be tested as a photothermal contrast agent in Tu212 tumor xenografts, due to their established targeting abilities, as shown in Figure 4.11. Optimal treatment conditions were established in preliminary studies. First, the tumor volume was measured and an HNSCP-AuNR solution (100 μL) was prepared from a concentrated stock solution of particles, such that the final concentration of these particles within the tumor volume is 2.25 nM. Second, the HNSCP-AuNRs were directly injected into the tumor. After 2 min, the tumors were extracorporeally exposed to NIR laser radiation at 5.8 W/cm^2 for 2 min. After laser treatment, tumor volumes were measured twice per week for up to 33 days. Figure 4.12 displays the tumor volume over the course of about 4 weeks, for the various treatments. It should be noted that the control, laser control, and HNSCP-AuNR control tumors could only be measured up to 16 days, due to tumor size reaching a limit at which animals had to be sacrificed.

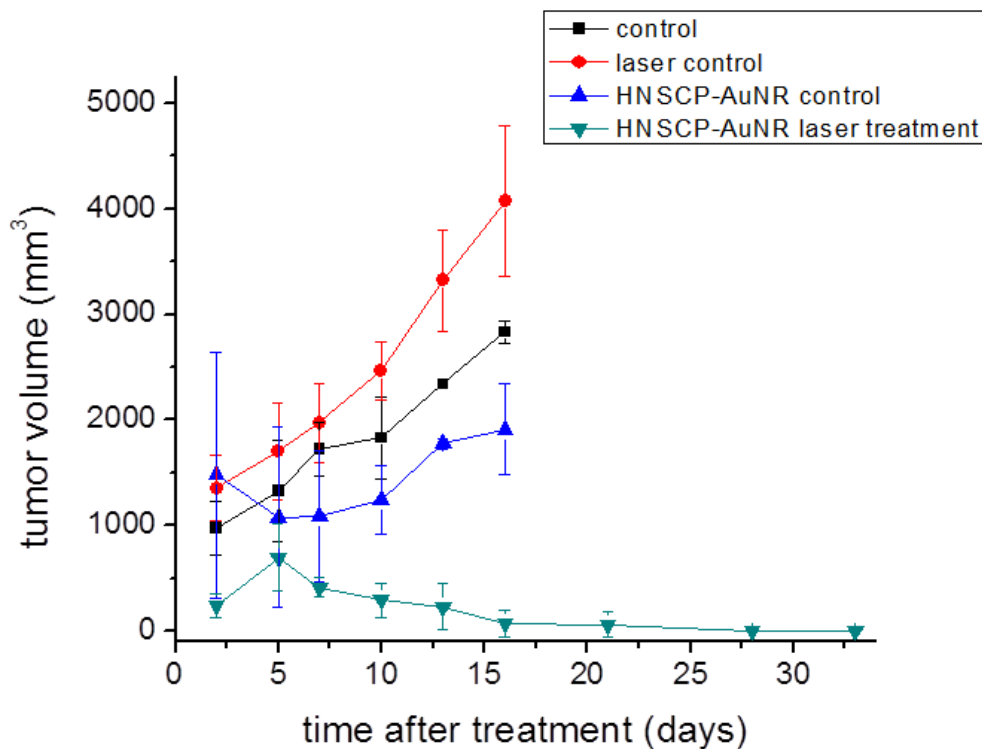


Figure 4.12. Tumor volume measurements with respect to time after treatment of nude mice bearing Tu212 xenografts. Control (black) mice ($n = 3$) were directly injected with 100 μL of PBS. Laser control (red) mice ($n = 3$) were directly injected with 100 μL of PBS and exposed to NIR radiation ($5.8 \text{ W}/\text{cm}^2$, 2 min). HNSCP-AuNR control (blue) mice ($n = 3$) were directly injected with 100 μL of HNSCP-AuNRs, such that final concentration in tumor was 2.25 nM. HNSCP-AuNR laser treatment (green) mice ($n = 6$) were directly injected with 100 μL of HNSCP-AuNRs, such that final concentration in tumor was 2.25 nM and exposed to NIR radiation ($5.8 \text{ W}/\text{cm}^2$, 2 min). Conjugated particles were provided by Mackey, M.A. and Ali, M.R.K. (Georgia Tech). Photothermal treatment and tumor size were provided by Mackey, M.A. (Georgia Tech) and Peng, X. (Emory University).

It is clear from the tumor volume measurements that the HNSCP-AuNR laser treatment suppresses tumor growth, such that the tumors disappeared two weeks after treatment and complete resorption was observed for up to 33 days. The drastic decrease in tumor growth observed for the HNSCP-AuNR laser treatment group is attributed to

efficient PPTT-induced hyperthermia. This has been demonstrated *in vitro* for AuNRs of similar size and concentration (see Chapter 4.1), where a rapid increase in temperature (after 30 sec laser exposure) is observed. The hyperthermia induced by the 27 nm HNSCP-AuNRs after external NIR laser activation dramatically suppresses tumor growth by ablating tumor tissue through various disruptions of biochemical processes within in the tumor cells, as well as physical destruction of the tumor structure.[27-32] Dickerson, et.al. previously demonstrated tumor growth suppression of nude mice bearing HSC-3 xenografts after PPTT with 40 nm PEG-AuNRs.[9] Specifically, 15 uL (10 nM, optical density 40) of 40 nm PEG-AuNRs were directly injected into tumors, followed by 10 min NIR laser radiation (1 W/cm^2). Although in the present work, we irradiate tumors at 5.8 W/cm^2 , we were able to decrease the laser exposure time to 2 min and still see complete tumor growth suppression, without causing severe skin burning, as well as observe tumor growth suppression for up to 1 month, as opposed to only 2 weeks. The decrease in laser irradiation time is possible, owing to the enhanced photothermal heat conversion exhibited by these 27 nm AuNRs, compared to that of the 40 nm AuNRs (see Chapter 4.1).

4.2.4. Conclusions and Future Outlook

In conclusion, we have demonstrated the use of a new, smaller AuNR (27 x 8 nm) as an efficient photothermal contrast agent in PPTT. These smaller AuNRs can be conjugated with non-targeting ligands (PEG-AuNRs) as well as peptides that specifically target squamous cell carcinoma of the head and neck (SCCHN) for Tu212 xenograft

targeting *in vivo* (HNSCP-AuNRs). Both PEG-AuNRs and HNSCP-AuNRs are stable *in vivo*, as shown by the 12.8 and 8.5 h blood circulation half-lives, respectively. The two different AuNRs exhibit different tumor accumulation and biodistribution profiles, such that the HNSCP-AuNRs show higher tumor accumulation and are distributed in the RES organs (liver and spleen) differently (higher liver accumulation, lower spleen accumulation) than the PEG-AuNRs. Although HNSCP-AuNRs accumulate in the liver and spleen after 24 h, they still remain in the circulation long enough to allow for the accumulation in the tumor. With the ability for these HNSCP-AuNRs to target Tu212 xenograft tumors in mice, as well as their size being the most efficient for photothermal heat conversion via NIR laser irradiation (see Chapter 4.1), they were tested for their efficacy as photothermal contrast agents for the suppression of tumor growth. About 16 days after directly injecting HNSCP-AuNRs into the tumor and extracorporeally irradiating with a NIR cw laser for 2 min (5.8 W/cm^2), tumors were almost completely resorbed, while control tumors continued to increase in volume. Up to 1 month after HNSCP-AuNR laser treatment, complete tumor resorption was still evident. Since these smaller AuNRs demonstrate such great potential as photothermal contrast agents for the clinical photothermal treatment of head and neck cancer, further examination of their long-term toxicity within the RES organs should be carried out and compared with the toxicity associated with the larger, more conventional AuNRs (40 x 10 nm).

4.2.5. References

1. Jain, P. K., Huang, X., El-Sayed, I. H., and El-Sayed, M. A. (2008) Noble metals on the nanoscale: optical and photothermal properties and some applications in imaging, sensing, biology, and medicine, *Acc Chem Res* 41, 1578-1586.
2. Dreaden, E. C., Alkilany, A. M., Huang, X., Murphy, C. J., and El-Sayed, M. A. (2012) The golden age: gold nanoparticles for biomedicine, *Chem Soc Rev* 41, 2740-2779.
3. Dreaden, E. C., Mackey, M. A., Huang, X., Kang, B., and El-Sayed, M. A. (2011) Beating cancer in multiple ways using nanogold, *Chem Soc Rev* 40, 3391-3404.
4. Huang, X., Jain, P. K., El-Sayed, I. H., and El-Sayed, M. A. (2007) Gold nanoparticles: interesting optical properties and recent applications in cancer diagnostics and therapy, *Nanomedicine (Lond)* 2, 681-693.
5. Link, S., and El-Sayed, M. A. (2003) Optical properties and ultrafast dynamics of metallic nanocrystals, *Annual review of physical chemistry* 54, 331-366.
6. Hartland, G. V. (2011) Optical Studies of Dynamics in Noble Metal Nanostructures, *Chem Rev* 111, 3858-3887.
7. Nolsoe, C. P., Torp-Pedersen, S., Burcharth, F., Horn, T., Pedersen, S., Christensen, N. E., Olldag, E. S., Andersen, P. H., Karstrup, S., Lorentzen, T., and et al. (1993) Interstitial hyperthermia of colorectal liver metastases with a US-guided Nd-YAG laser with a diffuser tip: a pilot clinical study, *Radiology* 187, 333-337.
8. O'Neal, D. P., Hirsch, L. R., Halas, N. J., Payne, J. D., and West, J. L. (2004) Photo-thermal tumor ablation in mice using near infrared-absorbing nanoparticles, *Cancer Lett* 209, 171-176.
9. Dickerson, E. B., Dreaden, E. C., Huang, X. H., El-Sayed, I. H., Chu, H. H., Pushpanketh, S., McDonald, J. F., and El-Sayed, M. A. (2008) Gold nanorod assisted near-infrared plasmonic photothermal therapy (PPTT) of squamous cell carcinoma in mice, *Cancer Letters* 269, 57-66.
10. Chen, J. Y., Glaus, C., Laforest, R., Zhang, Q., Yang, M. X., Gidding, M., Welch, M. J., and Xia, Y. (2010) Gold Nanocages as Photothermal Transducers for Cancer Treatment, *Small* 6, 811-817.

11. von Maltzahn, G., Park, J. H., Agrawal, A., Bandaru, N. K., Das, S. K., Sailor, M. J., and Bhatia, S. N. (2009) Computationally guided photothermal tumor therapy using long-circulating gold nanorod antennas, *Cancer Res* 69, 3892-3900.
12. Hirsch, L. R., Stafford, R. J., Bankson, J. A., Sershen, S. R., Rivera, B., Price, R. E., Hazle, J. D., Halas, N. J., and West, J. L. (2003) Nanoshell-mediated near-infrared thermal therapy of tumors under magnetic resonance guidance, *Proceedings of the National Academy of Sciences of the United States of America* 100, 13549-13554.
13. Lu, W., Xiong, C., Zhang, G., Huang, Q., Zhang, R., Zhang, J. Z., and Li, C. (2009) Targeted photothermal ablation of murine melanomas with melanocyte-stimulating hormone analog-conjugated hollow gold nanospheres, *Clinical cancer research : an official journal of the American Association for Cancer Research* 15, 876-886.
14. El-Sayed, I. H., Huang, X. H., and El-Sayed, M. A. (2006) Selective laser photothermal therapy of epithelial carcinoma using anti-EGFR antibody conjugated gold nanoparticles, *Cancer Letters* 239, 129-135.
15. Burda, C., Chen, X. B., Narayanan, R., and El-Sayed, M. A. (2005) Chemistry and properties of nanocrystals of different shapes, *Chem Rev* 105, 1025-1102.
16. Loo, C., Lowery, A., Halas, N. J., West, J., and Drezek, R. (2005) Immunotargeted nanoshells for integrated cancer imaging and therapy, *Nano Lett* 5, 709-711.
17. Chen, J. Y., Wang, D. L., Xi, J. F., Au, L., Siekkinen, A., Warsen, A., Li, Z. Y., Zhang, H., Xia, Y. N., and Li, X. D. (2007) Immuno gold nanocages with tailored optical properties for targeted photothermal destruction of cancer cells, *Nano letters* 7, 1318-1322.
18. Murphy, C. J., San, T. K., Gole, A. M., Orendorff, C. J., Gao, J. X., Gou, L., Hunyadi, S. E., and Li, T. (2005) Anisotropic metal nanoparticles: Synthesis, assembly, and optical applications, *J Phys Chem B* 109, 13857-13870.
19. Nikoobakht, B., and El-Sayed, M. A. (2003) Preparation and growth mechanism of gold nanorods (NRs) using seed-mediated growth method, *Chem Mater* 15, 1957-1962.
20. Wiley, B., Sun, Y. G., and Xia, Y. N. (2007) Synthesis of silver nanostructures with controlled shapes and properties, *Accounts Chem Res* 40, 1067-1076.
21. Hu, M., Chen, J., Li, Z. Y., Au, L., Hartland, G. V., Li, X., Marquez, M., and Xia, Y. (2006) Gold nanostructures: engineering their plasmonic properties for biomedical applications, *Chem Soc Rev* 35, 1084-1094.

22. Ali, M. R. K., Snyder, B., and El-Sayed, M. A. (2012) Synthesis and Optical Properties of Small Au Nanorods Using a Seedless Growth Technique, *Langmuir* 28, 9807-9815.
23. Hong, F. D., and Clayman, G. L. (2000) Isolation of a peptide for targeted drug delivery into human head and neck solid tumors, *Cancer Res* 60, 6551-6556.
24. Huang, X., Peng, X., Wang, Y., Wang, Y., Shin, D. M., El-Sayed, M. A., and Nie, S. (2010) A reexamination of active and passive tumor targeting by using rod-shaped gold nanocrystals and covalently conjugated peptide ligands, *ACS Nano* 4, 5887-5896.
25. Montet, X., Funovics, M., Montet-Abou, K., Weissleder, R., and Josephson, L. (2006) Multivalent effects of RGD peptides obtained by nanoparticle display, *Journal of medicinal chemistry* 49, 6087-6093.
26. McNeeley, K. M., Annapragada, A., Bellamkonda, R.V. (2007) Decreased Circulation Time Offsets Increased Efficacy of Pegylated Nanocarriers Targeting Folate Receptors of Glioma, *Nanotechnology* 2, 249-255.
27. Li, G. C., Mivechi, N. F., and Weitzel, G. (1995) Heat shock proteins, thermotolerance, and their relevance to clinical hyperthermia, *International journal of hyperthermia : the official journal of European Society for Hyperthermic Oncology, North American Hyperthermia Group* 11, 459-488.
28. Coleman, M. L., Sahai, E. A., Yeo, M., Bosch, M., Dewar, A., and Olson, M. F. (2001) Membrane blebbing during apoptosis results from caspase-mediated activation of ROCK I, *Nature cell biology* 3, 339-345.
29. Falk, M. H., and Issels, R. D. (2001) Hyperthermia in oncology, *International journal of hyperthermia : the official journal of European Society for Hyperthermic Oncology, North American Hyperthermia Group* 17, 1-18.
30. Hildebrandt, B., Wust, P., Ahlers, O., Dieing, A., Sreenivasa, G., Kerner, T., Felix, R., and Riess, H. (2002) The cellular and molecular basis of hyperthermia, *Critical reviews in oncology/hematology* 43, 33-56.
31. Sebbagh, M., Renvoize, C., Hamelin, J., Riche, N., Bertoglio, J., and Breard, J. (2001) Caspase-3-mediated cleavage of ROCK I induces MLC phosphorylation and apoptotic membrane blebbing, *Nature cell biology* 3, 346-352.
32. Kowal-Vern, A., McGill, V., Walenga, J. M., and Gamelli, R. L. (2000) Antithrombin III concentrate in the acute phase of thermal injury, *Burns : journal of the International Society for Burn Injuries* 26, 97-101.

APPENDIX A

CHAPTER 3 ADDITIONAL FIGURES

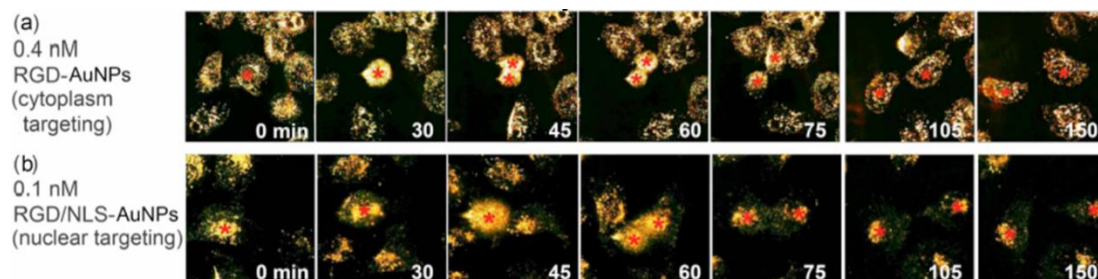


Figure A.1. Real time imaging of cancer cells incubated with 0.4 nM cytoplasm targeting gold nanoparticles (RGD-AuNPs) (a) and 0.1 nM nuclear targeting gold nanoparticles (RGD/NLS-AuNPs) (b) show no apparent cytokinesis arrest.

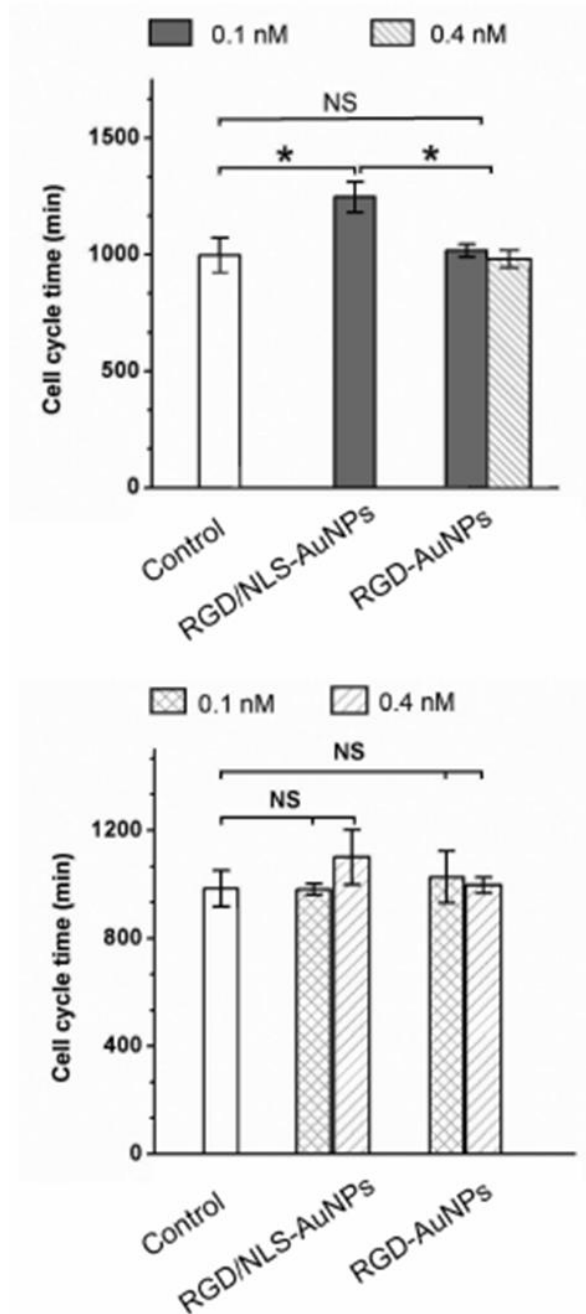


Figure A.2. Cell cycle time of cancer cells and normal cells with treatment of AuNPs. The cell cycle of cancer cells was extended by about 4 h with treatment of 0.1 nM RGD/NLS-AuNPs; but no changes with RGD-AuNPs treatment. The cell cycle time of normal cells have no change under both RGD-AuNPs and RGD/NLS-AuNPs. For cancer cells, 0.4 nM RGD/NLS-AuNPs induced cell cycle arrest, which make the whole cell cycle observation unavailable. The cell cycle time here is defined from the division of parent cells to the division of 2nd generation cells (daughter cells). Four individual cell cases were taken for each data point to obtain an average value. The * indicates $p < 0.05$ and NS indicates *not significant*.

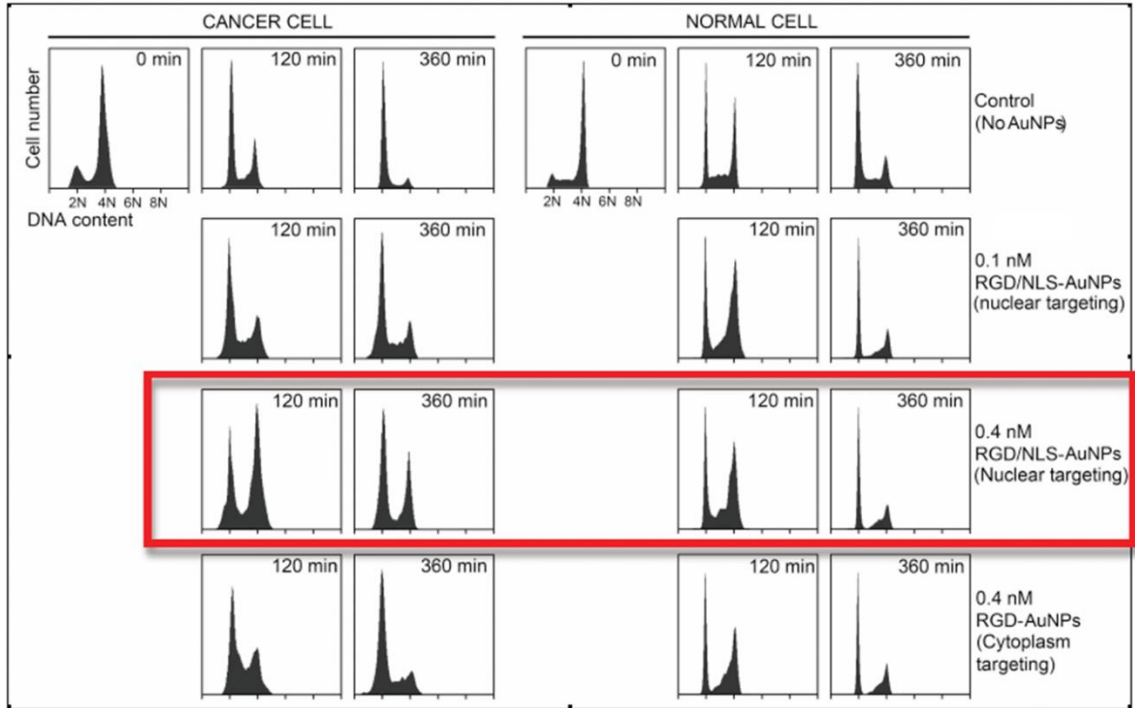


Figure A.3. Release dynamics of cancer cells (left) and normal cells (right) initially synchronized at prometaphase. Cells are synchronized to prometaphase with nocodazole and then released in fresh medium. At different time points of release, DNA content was measured using flow cytometry.

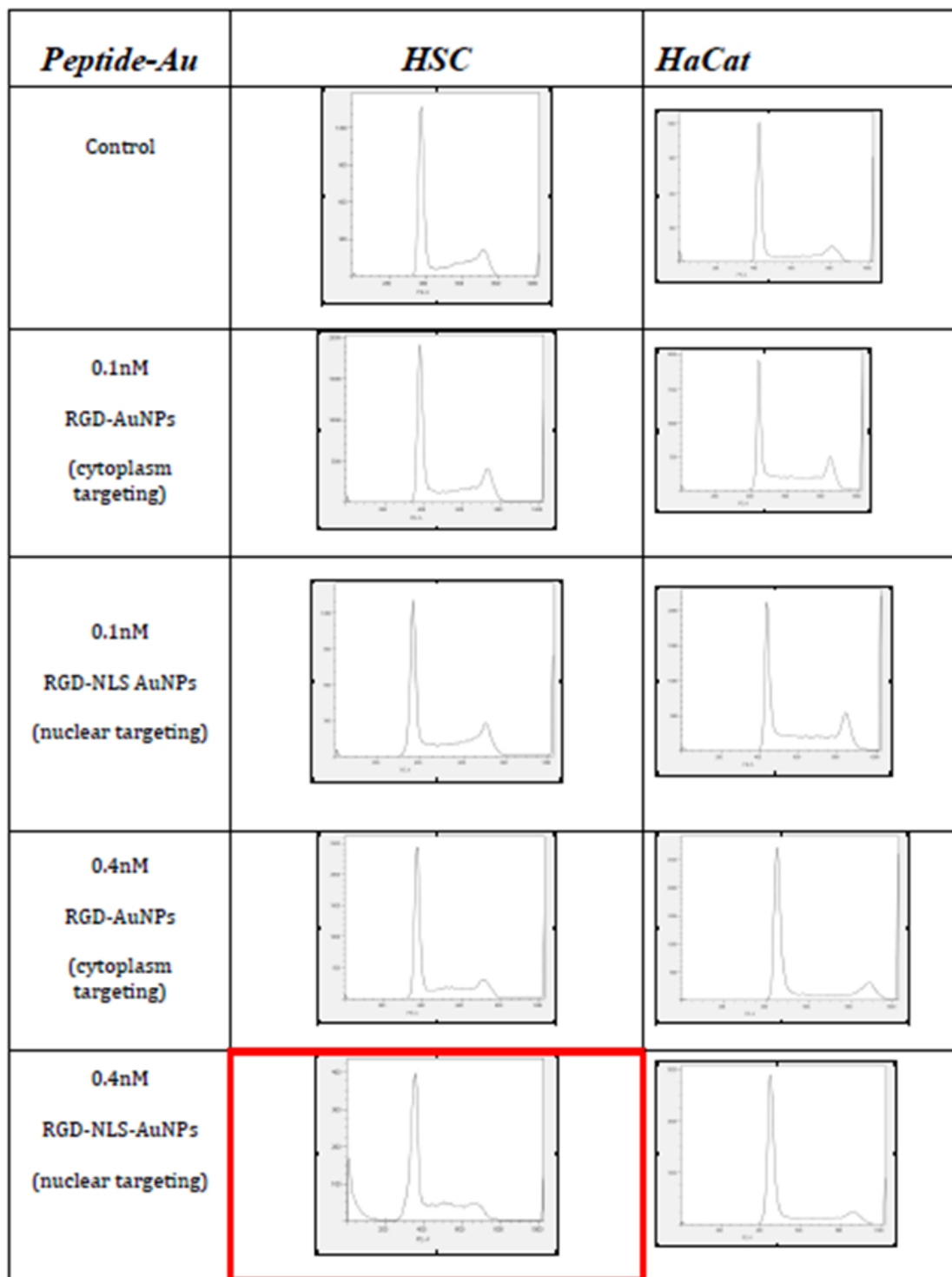


Figure A.4. Apoptosis induced by the presence of AuNPs at the nucleus of cancer cells. Cells were incubated with AuNPs for 24 h before analysis. The red box indicates sample with subG1 cell population (i.e. apoptotic cells).

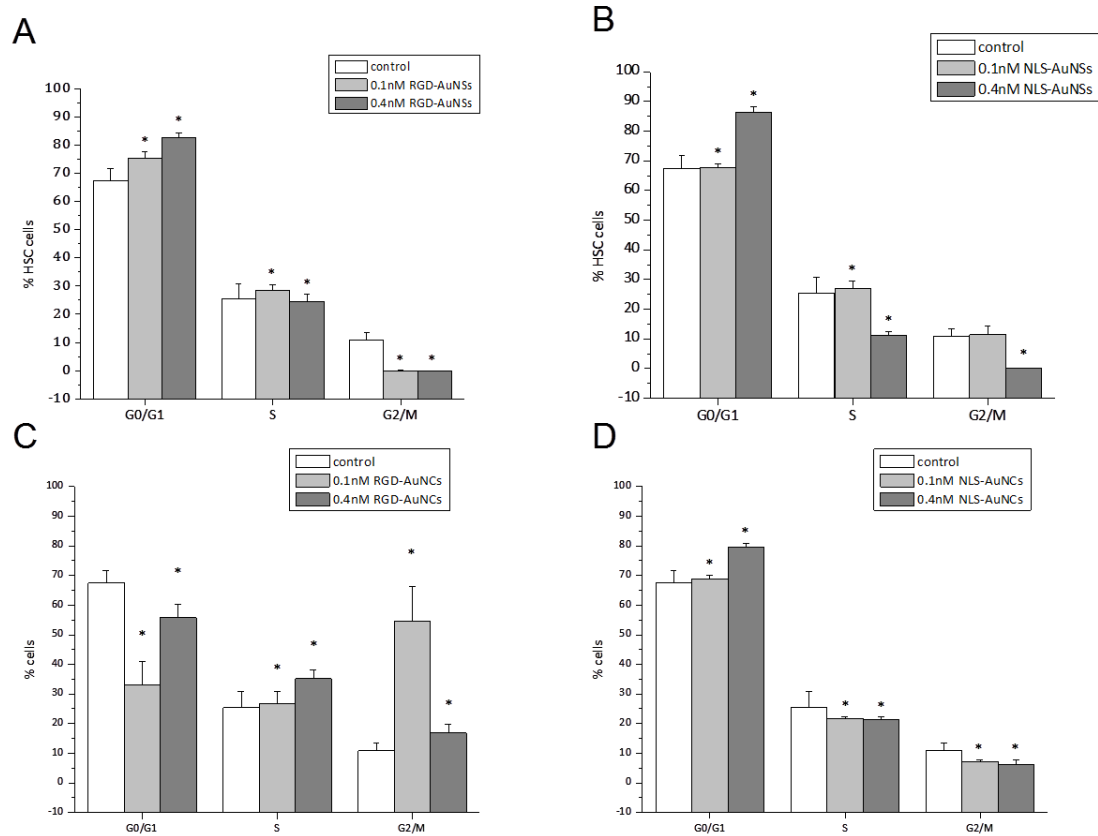


Figure A.5. Cell cycle changes induced by 0.1 and 0.4 nM peptide-conjugated gold nanoparticles in HSC cells after 48 h treatment with RGD-AuNSs (A), NLS-AuNSs (B), RGD-AuNCs (C) and NLS-AuNCs (D). Values expressed as mean \pm standard deviation of three independent experiments. Statistical significance, with respect to control, indicated by * ($p < 0.05$).

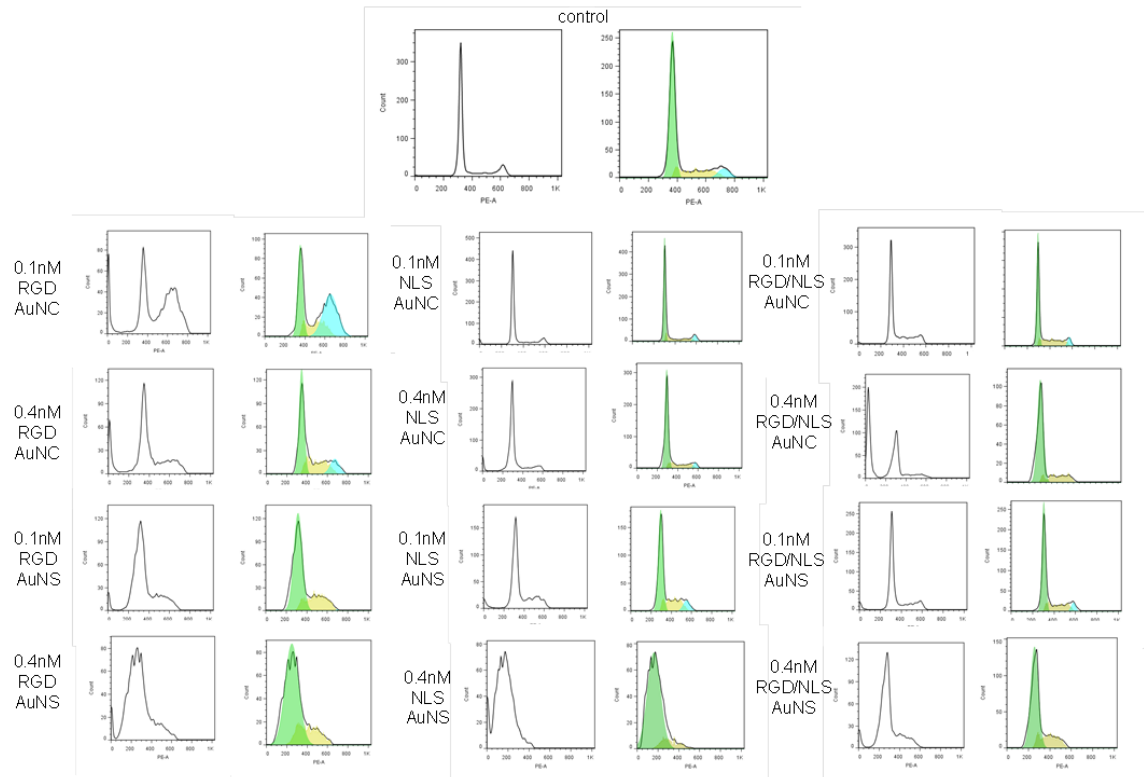


Figure A.6. Raw data obtained from flow cytometry cell cycle analysis for all nanoparticle treatments tested in this work. Cell cycle histograms, not filled in, represent the raw data, including the subG1 population, indicative of an apoptotic population. SubG1 populations appear in HSC cells treated with 0.1 nM RGD-AuNC, 0.4 nM RGD-AuNC, 0.4 nM RGD-AuNS, 0.4 nM NLS-AuNS, 0.4 nM RGD/NLS-AuNS, and the greatest subG1 population in 0.4 nM RGD/NLS-AuNC. Cell cycle histograms, filled in, represent how the data was fit, after gating single cells and eliminating the subG1 populations, to obtain G0/G1 (green), S (yellow) and G2/M (blue) phase populations.

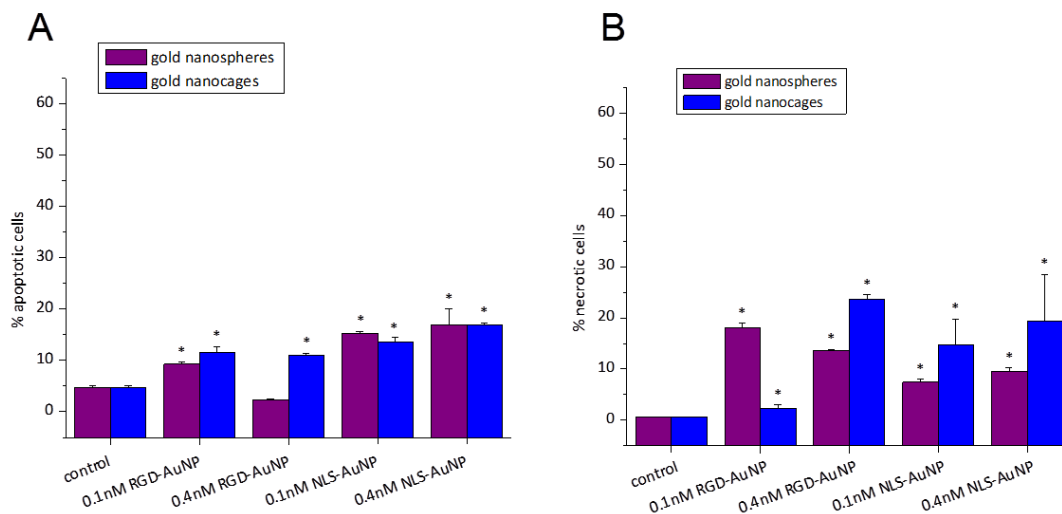


Figure A.7. Peptide-conjugated gold nanoparticle-induced cell death, via apoptosis (A) and necrosis (B), in HSC cells after 48 h treatment with RGD-AuNSs, RGD-AuNCs, NLS-AuNSs, and NLS-AuNCs. Values expressed as mean \pm standard deviation of three independent experiments. Statistical significance, with respect to control, indicated by * ($p < 0.05$).

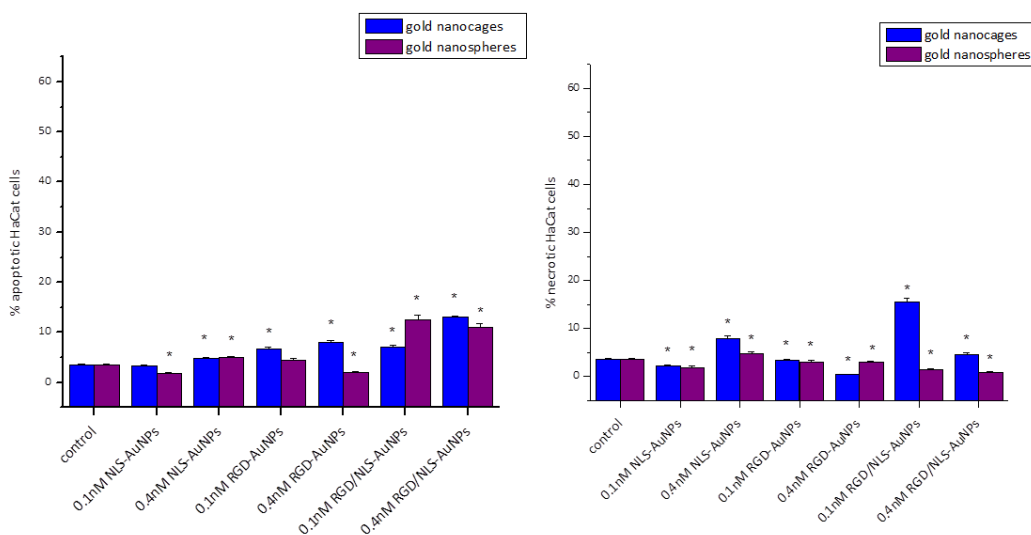


Figure A.8. HaCat cell death via apoptosis (left) and necrosis (right) induced by all nanoparticle formulations. All nanoparticle formulations induce minimal cell death in the HaCat cells compared with the HSC cells. This was expected, as the HaCat cells do not overexpress the alpha beta integrins on their surface.¹ Values expressed as mean \pm standard deviation of three independent experiments. Statistical significance, with respect to control, indicated by * ($p < 0.05$).

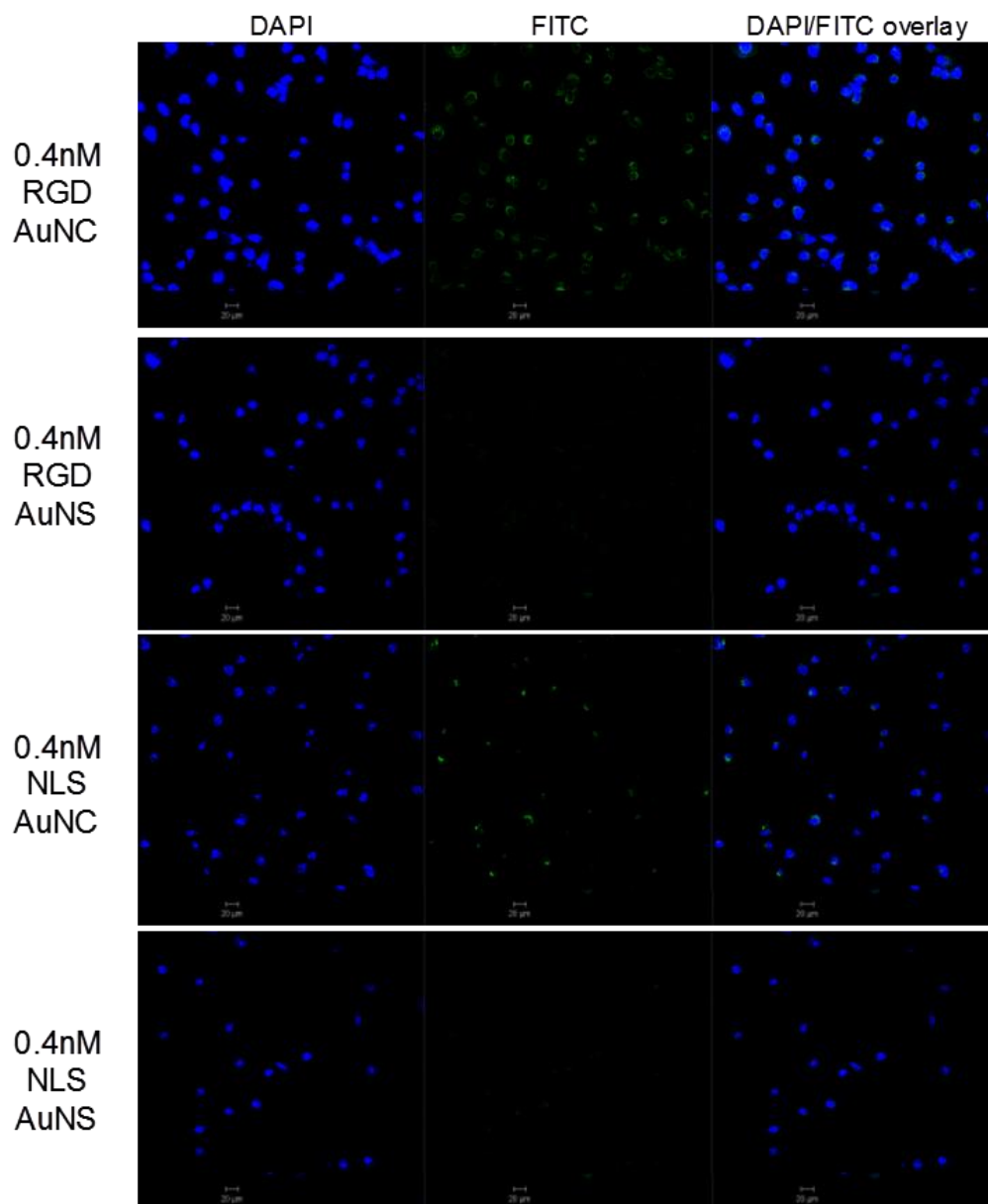


Figure A.9. ROS generation detected by confocal microscopy for 0.4 nM RGD-AuNCs, RGD-AuNSs, NLS-AuNCs, and NLS-AuNSs. DAPI panel (left) shows the nuclei of HSC cells stained blue. FITC panel (middle) represents green fluorescence indicative of ROS generated inside cells. DAPI/FITC overlay (right) shows the combination of both nuclei and ROS. The 0.4 nM RGD-AuNCs and NLS-AuNCs display FITC fluorescence, indicating ROS are generated in HSC cells with this nanoparticle treatment. Scale bar: 20 μm .

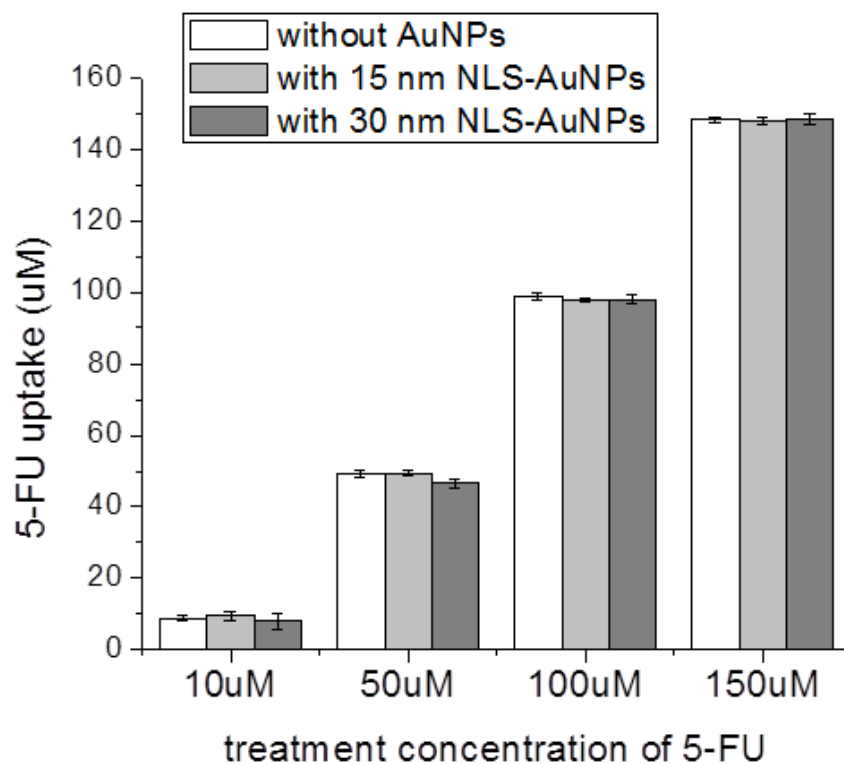


Figure A.10. Uptake analysis of 5-Fluorouracil (5-FU) in HSC-3 cells after cells were pre-treated with 15 nm NLS-AuNPs (light gray) or 30 nm NLS-AuNPs (dark gray). 5-FU uptake was determined by measuring the optical density (OD) of cell culture medium containing 5-FU, after 48 h treatment, with a Biotek Synergy H4 multi-mode plate reader. The measured OD was converted to a concentration by multiplying by the extinction coefficient, $39,290 \text{ M}^{-1} \text{ cm}^{-1}$ (determined by measuring various concentrations of 5-FU in cell culture medium). This concentration was then subtracted from the treatment concentration initially added to cells. Pre-treatment with NLS-AuNPs does not appear to enhance the uptake of 5-FU by HSC-3 cells.

APPENDIX B

CHAPTER 4 ADDITIONAL FIGURES

Table B.1. Additional temperature measurements taken for experimental photothermal heat conversion.

	T_i	T_f 30 sec irradiation	T_i	T_f 1 min irradiation	T_i	T_f 2 min irradiation
38 nm 10 nM	26 ± 3	69 ± 3	23 ± 3	80 ± 0	23 ± 1	82 ± 5
28 nm 10 nM		65 ± 3		85 ± 5		103 ± 1
17 nm 10 nM		40 ± 2		49 ± 3		62 ± 2
17 nm 20 nM		48 ± 5		65 ± 5		81 ± 2

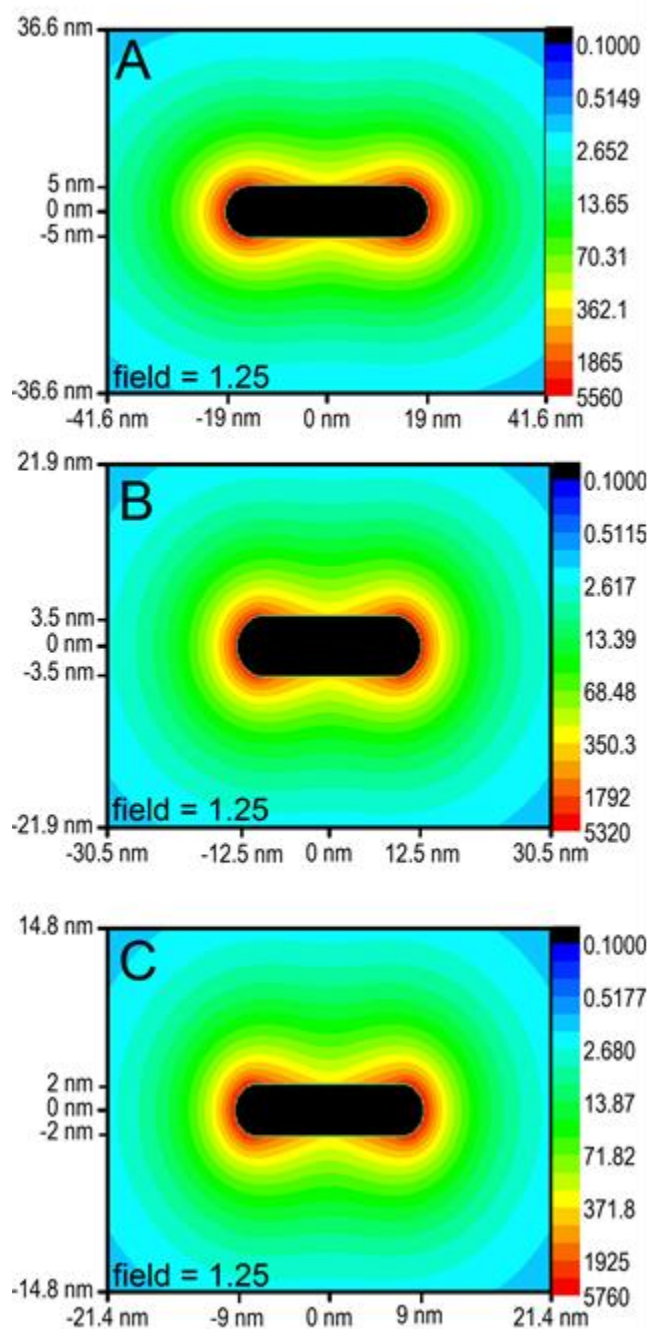


Figure B.1. Field contour plots at the resonance wavelength for the longitudinal mode of (A) a 38 x 10 nm AuNR at a wavelength of 786. The field maximum is 5560. (B) A 25 x 7 nm AuNR at a wavelength of 757 nm. The field maximum is 5320. (C) An 18 x 4 nm AuNR at a wavelength of 865 nm, The field maximum is 5760. For all cases, the particle dimensions are indicated on the axes and the field has decayed to a value of 1.25 at the extremities of the plot. At the resonance condition, there is less than 10% difference between the maximum field enhancement values for the different sized AuNR, not corresponding to the experimental results.

CURRICULUM VITAE

MEGAN A. MACKEY

EDUCATION

Georgia Institute of Technology, Atlanta

Dissertation Completed: August 2013

PhD, Chemistry and Biochemistry

GPA: 3.20

State University of New York at New Paltz, New Paltz, NY

May 2007

B.A., Chemistry, Minors in Biochemistry and Mathematics

GPA: 3.15

RESEARCH EXPERIENCE

Georgia Institute of Technology, Atlanta, GA

11/2007-8/2013

Research Assistant to Dr. Mostafa A. El-Sayed

Nanoparticle synthesis, functionalization and characterization

- Mastered the synthesis of spherical gold nanoparticles via citrate reduction method and rod-shaped gold nanoparticles via seed-mediated growth.
- Established and carried out methods for functionalizing gold nanoparticles with various ligands.
- Trained and qualified to use TEM, SERS, DLS and optical spectrometers for the use of nanoparticle characterization.
- Served in supervisory roles, including mentoring graduate and undergraduate students, visiting scholars and high school students through
 - Training in various laboratory techniques
 - Designing detailed experiment plans

Fundamental studies of the use of various gold nanoparticles in cancer treatment

- Developed protocols for the testing of gold nanoparticles as anticancer agents.
- Established a dark-field microscopy method for live-cell imaging of gold nanoparticles in cells.
- Mastered flow cytometry cell cycle analysis to assess the potency of various gold nanoparticle cancer treatments.
- Performed bioassays to detect apoptosis, cytotoxicity and metabolic changes in cells upon treatment with various gold nanoparticle composites.
- Developed, designed, and carried out *in vivo* studies for the use of gold nanoparticles in photothermal therapy.

- Liased with fellow scientists and medical doctors to assess and enhance clinical applications of gold nanoparticles.

State University of New York at New Paltz, New Paltz, NY

05/2005-05/2007

Undergraduate Research Assistant to Dr. Pamela St. John

- Optimized gel electrophoresis protocols for structural studies of DNA hairpin structures.

James Madison University, Harrisonburg, VA

05/2006-08/2006

Summer Research Assistant (NSF-REU) to Dr. Debra L. Mohler

- Optimized agarose gel electrophoresis methods to determine DNA cleavage products of DNA hydrolysis.

TEACHING EXPERIENCE

General Chemistry Teaching Assistant, Georgia Tech, Atlanta, GA

08/2007-05/2008

- Trained students in analytical techniques and communicated advanced chemical concepts.
- Designed lesson plans for pre-lab and recitation lectures.
- Assessed student progress through grading laboratory reports.

Physical Chemistry Teaching Assistant, SUNY New Paltz, New Paltz, NY

01/2007-05/2007

- Assisted students in experimental physical chemistry methods and concepts.

LEADERSHIP

Women in Chemistry Executive Board, Georgia Tech, Atlanta, GA

01/2011-Present

- Served an administrative role and mentored female graduate students.
- Initiated new procedures and policies for the organization through writing the Women in Chemistry handbook.
- Organized a faculty advisory board for the organization to gain support and advice from faculty members in the School of Chemistry and Biochemistry.
- Established a professional development seminar series for graduate and undergraduate students.

- Designed and organized a travel grant fellowship to be awarded to two students in the School of Chemistry and Biochemistry each semester.

**Graduate Student Forum, Georgia Tech, Atlanta, GA
05/2008-05/2009**

- Organized seminars and various graduate student-specific events for the School of Chemistry and Biochemistry.

PUBLICATIONS

15. “Varying the Silver Content of Gold Nanocages Impacts Apoptosis and Necrosis Induced in Cancer Cells.” **Mackey, Megan A.**; Bordley, J.; *Mahmoud, M.A.; El-Sayed, M.A., in preparation.*

14. “Gold Nanoparticle-Sensitized 5-Fluorouracil Treatment of Cancer by Regulation of the Cell Cycle.” **Mackey, Megan A.**; El-Sayed, Mostafa A., *in preparation, Cancer Letters, 2013.*

13. “The Most Effective Gold Nanorod Size for Plasmonic Photothermal Therapy: Theory and Experiment.” **Mackey, Megan A.**; Ali, Moustafa R.K.; Austin, Lauren A.; Near, Rachel D.; El-Sayed, Mostafa A., *submitted to Journal of Physical Chemistry B, 2013.*

12. “Antimicrobial Activity of Some Novel Water Soluble Phenazines.” Hayden, Steven C.; Bryant, Jonny B.; **Mackey, Megan A.**; Hofer, Katharina; Lindner, Benjamin; Nguyen, Vanessa P.; Jaschke, Andres; Bunz, Uwe H.F., *submitted to JACS, 2013.*

11. “Surface Enhanced Raman Spectroscopy for the Real Time Monitoring of Molecular Events Associated with Reactive Oxygen Species-Induced DNA Damage and its Prevention by Platinum Nanocages.” Panikkanvalappil, Sajanlal; **Mackey, Megan A.***; Mahmoud, Mahmoud A.*; El-Sayed, Mostafa A., *under review, ACS Nano, 2013.*

*equal contributions

10. “XAV939: From a Small Inhibitor to a Potent Drug Bioconjugate When Delivered by Gold Nanoparticles.” Afifi, Marwa A.; **Mackey, Megan A.***; Austin, Lauren A.*; El-Sayed, Mostafa A., *under review, Bioconjugate Chemistry, 2013.*

*equal contributions

9. “Inducing Cancer Cell Death by Targeting Its Nucleus: Solid Gold Nanospheres versus Hollow Gold Nanocages.” **Mackey, Megan A.**; Farhat Saira; Mahmoud, Mahmoud A.; El-Sayed, Mostafa A., *Bioconjugate Chemistry, 2013, 24, 897-906.*

8. “Probing the Unique Dehydration-Induced Structural Modifications in Cancer Cell DNA using Surface Enhanced Raman Spectroscopy.” Panikkanvalappil, Sajanlal;

Mackey, Megan A.; El-Sayed, Mostafa A., *JACS Communications*, **2013**, 135, 4815-4821.

7. “Size Matters: Gold Nanoparticles in Targeted Cancer Drug Delivery”. Dreaden, Erik C.; Austin, Lauren A.; **Mackey, Megan A.**; El-Sayed, Mostafa A. *Therapeutic Delivery*, **2012**, 3, 457-478.
6. “Remote Triggered Release of Doxorubicin in Tumors by Synergistic Application of Thermosensitive Liposomes and Gold Nanorods.” Agarwal, Abhiruchi; **Mackey, Megan A.**; El-Sayed, Mostafa A.; Bellamkonda, Ravi V. *ACS Nano*, **2011**, 5, 4919-4926.
5. “Beating Cancer in Multiple Ways Using Nanogold.” Dreaden, Erik C.; **Mackey, Megan A.**; Huang, Xiaohua; Kang, Bin; El-Sayed, Mostafa A. *Chemical Society Reviews*, **2011**, 40, 3391-3404.
4. “A comparative study of photothermolysis of cancer cells with nuclear-localized or cytoplasm-distributed gold nanoparticles: Continuous wave or pulsed lasers.” Huang, Xiaohua; Kang, Bin; Qian, Wei; **Mackey, Megan A.**; Chen, Po; Oyelere, Adegboyega; El-Sayed, Ivan; El-Sayed, Mostafa A. *Journal of Biomedical Optics*, **2010**, 15 (5).
3. “Nuclear targeting of gold nanoparticles in cancer cells induces DNA damage, causing cytokinesis arrest and apoptosis.” **Mackey, Megan A.***; Kang, Bin*; El-Sayed, Mostafa A. *JACS Communications*, **2010**, 132, 1517-1519.
*equal contributions
2. “Formal DNA Hydrolysis by Mono- and Dinuclear Iron Complexes.” Shell, Thomas A.; Glass, Jessica E.; **Mackey, Megan A.**; Layman, Kathryn A.; Mohler, Debra L. *Inorganic Chemistry*, **2007**, 46, 8120-8122.
1. “Increase in Hybridization Rates with Oligodeoxyribonucleotides Containing Locked Nucleic Acids.” Ormond, Thomas K.; Spear, Daniel; Stoll, Jacqueline; **Mackey, Megan A.**; St. John, Pamela M. *Journal of Biomolecular Structure and Dynamics*, **2006**, 24, 171-182.

PRESENTATIONS

8. “Gold Nanoparticle-Induced Cell Death: Solid Gold Nanospheres versus Hollow Gold Nanocages.” American Chemical Society National Meeting (April 2013) New Orleans, Louisiana.
7. “The Effects of Size and Surface Coating of Gold Nanorods on Biodistribution and Associated Toxicity in Mouse Models.” National Cancer Institute Alliance for Nanotechnology in Cancer Meeting (November 2012) Houston, Texas.

6. “Biodistribution and Antitumor Efficacy of Tumor-Targeted Gold Nanorods in a Mouse Model.” National Cancer Institute Alliance for Nanotechnology in Cancer Meeting (November 2012) Houston, Texas.
5. “Gold Nanoparticle-Induced Apoptosis in Cancer: Nanoparticle Shape Dependence.” Georgia Life Sciences Summit (September 2011) Atlanta, Georgia.
4. “Inducing Programmed Cancer Cell Death with Nuclear-Localizing Gold Nanoparticles: Nanoparticle Shape Dependence.” American Chemical Society National Meeting (August 2011) Denver, Colorado.
3. “Potential for Nuclear Localization of Gold Nanoparticles in Cancer Therapy.” Georgia Life Sciences Summit (October 2010) Atlanta, Georgia.
2. “Nuclear Targeting of Gold Nanoparticles in Cancer Cells.” Invited talk. State University of New York (April 2010) New Paltz, New York.
1. “Nuclear Targeting of Gold Nanoparticles in Cancer Cells Induces DNA Damage, Causing Cytokinesis Arrest and Apoptosis.” Integrative BioSystems Institute (IBSI) poster session (March 2010), Atlanta, Georgia.

PROFESSIONAL MEMBERSHIPS

American Chemical Society

08/2011-Present

Student Affiliates of the American Chemical Society

01/2006-05/2007

TECHNICAL SKILLS

Mammalian Cell Culture

Flow Cytometry

SDS PAGE

In vitro and *in vivo* Laser-Ablative Therapeutics

Microplate Assay Techniques

Laser Scanning Confocal Fluorescence Microscopy

Agarose gel electrophoresis

Colloidal Noble Metal Nanoparticle Synthesis

Colloidal Bio-Conjugation Techniques

Surface-Enhanced Raman Spectroscopy

Dynamic Light Scattering

Optical Microscopy

UV-Vis Spectroscopy

Raman Spectroscopy

Transmission Electron Microscopy